MODELLING THE SPATIAL RELATIONSHIP BETWEEN BUILT-UP VOLUMES AND SURFACE URBAN HEAT ISLANDS IN UPPER HILL, NAIROBI CITY COUNTY, KENYA

PATRICIA WANJIKU MWANGI (MSc, BSc)

N85/33297/2015

DEPARTMENT OF ENVIRONMENTAL PLANNING AND MANAGEMENT

A Thesis Submitted in Fulfilment of the Requirements for the Award of the Degree of Doctor of Philosophy in Environmental Planning and Management in the School of Environmental Studies of Kenyatta University

JULY 2020

DECLARATION

This thesis is my original work and has not been presented for a degree in any other University or for any other award. No part of work should be reproduced without prior permission of the author or Kenyatta University.

Signature..... Date.....

Patricia Wanjiku Mwangi
Registration No. N85/33297/2015
Department of Environmental Planning and Management, Kenyatta University

Declaration by the Supervisors:

We, as university supervisors, confirm that this thesis was carried out by the candidate under our supervision.

Signature..... Date……..

Dr. Peter K. Kamau, PhD
Department of Spatial Planning and Urban Management, Kenyatta University

Signature ……... Date……

Dr. Faith N. Karanja, PhD
Department of Geospatial Engineering and Space Technology, University of Nairobi

Signature ……. Date…….

Dr. Sammy Letema, PhD
Department of Environmental Planning and Management, Kenyatta University

DEDICATION

This thesis is dedicated to my parents Mr. & Mrs. Mwangi and my siblings for their support and encouragement.

ACKNOWLEDGEMENTS

I am sincerely grateful to my supervisors Dr. Faith Karanja, Dr. Sammy Letema and Dr. Peter Kamau for the incredible guidance, encouragement and supervision throughout my study. My appreciation also goes to the staff in the Department of Spatial Planning and Urban Management for understanding and support during the period of my studies.

I would like to thank Ramani Geosystems Ltd. for availing 3D digital aerial imagery and ready support. For Oakar Services Limited and David Manzano for entrusting me with their Geodetic survey equipment and providing technical support. I would like to specially thank Mr. Peter Wachira, Ms. Anne Ndung'u and members of staff at Survey of Kenya, Photogrammetry Department for giving their time, expertise and technical support in obtaining 3D aerial imagery and data. Mr. Wachira, working together on setting the images within the tight time schedules, your encouragement and guidance was invaluable.

I would like to specially thank Professor Christian Heipke of Leibniz University, Hannover, Germany for his supervision and guidance during my six month stay at the university. His insights and opening up opportunities for growth in conferences was highly invaluable. I would also like to thank other members of staff in Leibniz University for their support and insights. I would like to thank the DAAD team for the scholarship which made this PhD a success.

I appreciate my friends David Mugendi, Godwin Opinde and Purity Muthoni for their contribution, insights and encouragement. The friends made along this journey and are not mentioned by name are truly appreciated.

TABLE OF CONTENTS

LIST OF TABLES

LIST OF FIGURES

ABBREVIATIONS AND ACRONYMS

AICc	Akaike Information Criterion
ARDA	Association of Religion Data Archives
ASTER	Advanced Spaceborne Thermal Emission & Reflection Radiometer
AU	African Union
BVD	Built-up Volume Density
CBD	Central Business District
CEHI	Children's Environmental Health Initiative
CoM	City of Melbourne
DEM	Digital Elevation Model
DN	Digital Number
DSM	Digital Surface Model
DTM	Digital Terrain Model
ETM	Enhanced Thematic Mapper
FAR	Floor Area Ratio
GCP	Ground Control Point
GCR	Ground Coverage Ratio
GWR	Geographically Weighted Regression
HDE	Humanitarian Data Exchange
JICA	Japan International Cooperation Agency
LCC	Land Cover Change
LoD	Level of Detail
LPS	Leica Photogrammetric Station
LSE	Land Surface Emissivity
LST	Land Surface Temperature
MODIS	Moderate Resolution Imaging Spectroradiometer
NASA	National Aeronautics and Space Administration
NCC	Nairobi City Council
NDBI	Normalized Difference Built-up Index
NDVI	Normalized Difference Vegetation Index

NIR	Near infra-red
NTPLC	Nairobi Town Planning Liaison Committee
OLI	Operational Land Imager
OLS	Ordinary Least Square
PR	Plot Ratio
RoK	Republic of Kenya
RPC	Rational Polynomial Coefficient
SDG	Sustainable Development Goals
SGM	Semi Global Matching
TIR	Thermal Infra-Red
UBL	Urban Boundary Layer
UCL	Urban Canopy Layer
UHDA	Upper Hill District Association
UHI	Urban Heat Island
UMC	Urban Mass Concentration
UNEP	United Nations Environment Programme
UN-Habitat	United Nations Human Settlements Programme
USGS	United States Geological Survey
WGS	World Geodetic System

ABSTRACT

Urban heat island refers to the thermal temperature differences between rural and urban areas. The factor that has been attributed to this phenomenon is urbanization, where natural land cover is replaced by concrete and other man-made impervious surfaces. Causes and effects of heat islands and urban climates are varied. The urbanization process dislocates the natural solar and hydrologic balances by transforming the radiative, thermal, moisture and aerodynamic characteristics of a region. Lack of indicators and frameworks on three dimensional development in urban environment possess a challenge to urban authorities when formulating policies on thermal comfort, pollution, assessing health-related risks such as heat stress, respiratory diseases and vector-borne diseases. Therefore, this study aims at modelling the relationship between built-up morphology and topographical features with land surface temperatures using time series data in Upper Hill, Nairobi. Upper Hill, Nairobi, Kenya has rapidly developed over the years, transforming to commercial, office blocks and high-rise flats from low density residential area. Changes in zoning regulations is informed by businesses choosing to locate their offices away from the Central Business District because of traffic jams, inadequate parking space and high costs of renting office space. The research uses case study and correlational research design. Random sampling is used to collect ground control points and verify analysed data. Land surface temperature, land cover, NDVI and albedo is analysed for the years 1986, 1995, 2000, 2005, 2011 and 2017. Road and building information is extracted from stereo-aerial photographs for the period 1978, 1998 and 2017, which is utilized to obtain building height, ground coverage ratio and built-up volume density index. The spatial relationship of land surface temperature with built-up morphology is modelled using geographically weighted regression and ordinary linear regression. Findings show that land surface temperature is influenced by type of land cover and albedo; with sparse grassland having an albedo of 0.18 and mean surface temperature of 28 ^{0}C while water has an albedo of 0.09 and mean surface temperature of 25 ^{0}C during the day. At night, water and sparse grassland have mean surface temperatures of 18.62 ^{0}C and 18 ^{0}C respectively. Contribution index of built-up and forest areas has reduced with increased impervious surfaces. Mean built-up volume density and ground coverage ratio in Upper Hill in 1978, 1998 and 2017 is low density while mean building heights are low-rise. Geographically weighted regression model findings indicate that building height in 1978 has an r^2 of 70% and built-up volume density in 1998 and 2017 have r^2 of 72% therefore having a great relationship with land surface temperature. Combined modelling tools capture the physical dynamics and interaction built-up forms have with land surface temperature. Built-up volume densities should be integrated in the development control frameworks, with building heights being an important variable in urban development. It further recommends that green design strategies be made an integral part of urban development with percentage vegetation cover specified in the zoning policy as surface urban heat islands is a spatial temporal phenomena.

CHAPTER ONE: INTRODUCTION

1.0 Background to the Study

Global warming above preindustrial levels of between 0.8 ^{0}C to 1.2 ^{0}C have been caused by human activities, with estimations of further increases by 1.5 ^{0}C between 2030 and 2050; with past and ongoing emissions are estimated to cause an increase in anthropogenic global warming of 0.2 ^{0}C per decade (Masson *et al*., 2018). Climate related risks resulting from increased global warming depend on factors such as geographic location, warming rate and magnitude, development levels and vulnerability, and implementation of mitigation and adaptation options *(*Masson *et al*., 2018).

Surface temperatures of urban structures are higher than ambient air temperatures as solar energy is absorbed into roads and rooftops (Gorsevski *et al*., 1998). During the day, heat is absorbed by buildings, roads and other constructions and re-emitted after sunset in urban areas, creating temperature differences between urban and rural areas (Shahmohamadi *et al*., 2012). Oke (2014) notes that urban heat island intensity varies throughout the day where villages that have a population size of 1000 people also experience heat islands, indicating that city size is a factor that affects heat island intensity. Large cities with inhabitants of approximately one million people can have annual mean temperatures that are 1 ^{0}C to 2 ^{0}C warmer than before development and up to 12 ^{0}C on individual clear and calm nights (Oke, 2014). Very strong winds remove urban to rural thermal differences hence heat island intensities are most sensitive to wind speeds (Voogt, 2007).

Sustainable Development Goal 13 (SDG 13) specifies urgent actions required in addressing climate change and its impacts and they include strengthening adaptive capacity and resilience in dealing with natural disasters and climate-related hazards (Allen *et al*., 2018). Adaptation options for urban areas in reducing climate-related risks include sustainable water management, sustainable land use management and green infrastructure (Masson *et al*., 2018). Limiting global warming to 1.5 ^{0}C would necessitate a change in land and urban planning practices together with reducing transport and building emissions (Masson *et al*., 2018). Practices that lead to sustainable intensification of land-use are mitigation options which limit the demand of land, with their implementation requiring overcoming barriers such as institutional, technological, environmental, financial and socio-economic (Masson *et al*., 2018). When considering threats and opportunities for sustainable development climate mitigation-adaptation strategies that include synergies and trade-offs are important (Allen *et al*., 2018).

Compact city morphology is considered a sustainable solution for urbanization pressures though compact city urban forms may potentially expand and intensify the already established urban heat island (UHI) experienced in many cities worldwide (Argent *et al*., 2012). Disadvantages that accompany high densities include high property prices and rent, low air quality, transportation system congestion and a discomforting urban microclimate (Krehl *et al*., 2016). The Intergovernmental Panel on Climate Change (IPCC) has asserted that persistent anthropogenic changes in land use may be leading to climate change (Guzmán *et al*., 2009). Compared to vegetated areas, urban materials such as paving and building materials have lower albedo hence having less reflection and more absorption of sunlight, causing high air and surface temperatures (Bouyer *et al*., 2009).

Low density areas in close proximity to the central business district (CBD) in Nairobi have been re-zoned due to the increased population and demand for office space such as Upper Hill, Kilimani and Kileleshwa areas. Rezoning reviews undertaken in 2004 and 2012 (NCC *et al*., 2014) proposed that the plot ratios for Zones 3, 4 and 5 be increased from 100 to 200% as these areas were facing intense developmental pressures (Kiai, 2008). Consequently, Upper Hill has undergone transformation from residential to commercial, office blocks and high-rise flats (Appendix 15) due to re-zoning policies. Redevelopment challenges have resulted from lack of strategies to guide densification, regeneration such as proper guidelines and coordination between agencies (Kiai, 2009). Little is known on the impact of rezoning policies on built-up volumes and urban heat island effect, which this study attempts to explore for sustainable city development.

1.1 Statement of the Problem

The current densification trends and land utilization do not address issues of straining existing infrastructure and vulnerability to climate change (Kiai, 2009). Lack of suitable policy guidelines on densification further compounds the problem. Cities that are more compact and have higher densities tend to have unprecedented problems and issues to policy makers, planners and other urban designers (Ng & Ren, 2015). It is therefore imperative that professionals in the built environment analyze current policies with a view to provide sustainable densification guidelines in cities and towns (Kiai, 2009).

Increase in urbanization rates in Nairobi impacts on land surface temperatures. This is based on analysis by Ongoma *et al*., (2013a) who investigated temperature changes in selected parts of

Nairobi and determined that minimum and maximum land surface temperatures are increasing. Makokha & Shisanya (2010) studied air temperature differences for Aga Khan walk, Uhuru Park and Kenyatta University with results showing that urban geometry leads to higher nocturnal minimum temperatures and the development of urban heat island (UHI). Nairobi depicts low albedo due to dense building regions that have a canyon effect, limiting the solar energy reflected back to the atmosphere due to the multiple reflections of solar photons of urban surfaces such as concrete material (Ongoma *et al*., 2013a; Nyaga, 2014)

Upper Hill is considered an extended or secondary commercial area without a defined development plan and implementation of the zoning provisions are not being implemented on the ground (Macharia, 2012). Concreted areas in Upper Hill were investigated by Karanja & Matara (2013) between the years 2002 and 2012 with results showing an increase of 4% of concreted areas and a corresponding decrease of 4% in green areas. Human and vehicular traffic increased with open plots being converted into large-scale office blocks and old residential buildings giving way to high-rise office or commercial blocks (Karoki, 2004). Infrastructure challenges were not adequately taken into consideration resulting to increased traffic snarl ups due to the increased number of people driving into these areas, which then contributed to volume of greenhouse gases emitted in the urban environment (Opiyo, 2009).

Analyzing the horizontal development of urban spaces without considering its vertical development does not adequately demonstrate the interactions that changing landscape patterns are having on the built environment. Impacts that built-up volumes have on the solar energy potential of an urban area and its effects on current energy use is important for developing

mitigative and adaptive measures. Therefore this study addresses scientific lacuna of three-dimensional (3D) studies and the effects of built-up volumes on urban heat using Upper Hill, Nairobi, Kenya as a case study.

1.2 Research Questions

1. What is the relationship between land cover changes and land surface temperature changes over time space continuum between 1986 and 2017 in Upper Hill, Nairobi?
2. What are the effects of built-up morphology on land surface temperature between 1986 and 2017 in Upper Hill, Nairobi?
3. Which model can best simulate the relationship between built-up volumes and land surface temperature in Upper Hill, Nairobi?

1.3 Research Objective

The general objective of this to develop a model that simulates' the impact of built-up morphology on land surface temperature in Upper Hill, Nairobi.

The specific objectives of this study are namely to:

1. Determine the relationship between land cover and land surface temperature changes in time space continuum between 1986 and 2017 in Upper Hill, Nairobi.
2. Evaluate the effects of built-up morphology on land surface temperature between 1986 and 2017 in Upper Hill, Nairobi.
3. Model the spatial relationship between built-up volumes and land surface temperature in Upper Hill, Nairobi.

1.4 Justification of the Study

Climate change has been a major issue of concern as it affects both people and the environment. Different biophysical properties of urban landscapes have different thermal responses such as vegetation and buildings (Liu *et al.,* 2015). An important measuring index of the process of urbanization is urban expansion which is a phenomenon of urban space expansion (Longyu *et al.,* 2009) and is a 3D process of horizontal and vertical expansion. Assessing the geometric and urban parameters of buildings is crucial in promoting sustainable growth through urban plans and land regulations (Diego *et al*., 2013).

SDGs have a 2030 agenda for sustainable development which aims at ensuring that cities develop without straining their land and resources (UN, 2015). Goal 11 aims at ensuring that despite the challenges cities are facing such as pollution, poverty and poor resource use; they can reduce and overcome them while continuing to thrive and grow (UN, 2015). Goal 13 aims at tackling climate change issues and its impacts by improving and integrating climate change measures within national strategies, policies, planning and institutional capacities (UN, 2016). These two main goals, together with others, will ensure that our cities are inclusive, safe, resilient and sustainable.

Previous studies on land surface temperatures in Nairobi have not analyzed urban developments from a 3D perspective and related this to land surface temperature. 3D studies helps to understand the implications of built-up densities on the population that reside in this area and its impacts in other sectors of the economy such as transport, health, architecture and urban planning. Data from areas transforming in policy and land use act as baselines to effectiveness to

adopted methods in dealing with climate change and environmental sustainability. The findings can inform architects in designing passive buildings that are important in tackling climate change and inform planners in designing sustainable cities using 3D models while making informed decisions using simulated designs. The study is crucial to environmentalists in advocating for mitigative and adaptive actions when looking at the interaction between rising temperatures brought about by changing landscapes and the need to localize solutions to geographic location.

1.5 Significance of the Study

The study provides an assessment of the climate risk and opportunities in Upper Hill, Nairobi associated with the built environment and temperature changes in determining adaptation needs to become a resilient and sustainable city. The findings of this study has progressed climate policy discussions by assessing impacts of the city at a local scale (Hunt & Watkiss, 2011) as activities in Nairobi do have a negative impact on the environment and its hinterlands (UNEP *et al*., 2009). This will enable both private and public stakeholders deliberate and implement responses.

The study enhances a change in the current zoning policy since planning in Nairobi has been undertaken without consideration of impacts of urban processes and 3D urban forms on land surface temperature. The need to integrate planning for sustainable development has been considered in this research. The study promotes better informed practices and policies on land use within cities by the use of a model that considers heterogeneous land cover and identifying areas that are more susceptible to increases in surface temperatures. The current land use policy provides guidelines on zoning in urban areas with climate change issues still remaining a salient

feature. Quality data and information on the environment at city level enables success in implementing sound policies to achieve sustainable development (UNEP *et al*., 2009). The study supports guidelines targeted at urban renewal with the promotion of high-rise buildings and the expansion of existing roads to allow more human and vehicular traffic (NEMA, 2011) without increasing pollution and environmental stressors due to development.

The study determines possible adaptation options as Upper Hill is growing faster than its physical infrastructure capacity which creates an adaptation deficit in relation to the climatic changes, as developing countries tend to be more vulnerable (Hunt & Watkiss, 2011).

1.6 Theoretical Framework

The framework is derived from the ecologic economic theory and the institutional theory.

1.6.1 Ecologic Economic Theory

The ecologic economic theory initially emerged under the term eco-development where natural and economic processes are interwoven (Gowdy, 2000). The economic ecological theory emerged to bridge the gap between natural science and economics. The theory is a subset of the neoclassical model, which failed to consider social and environmental aspects as it focusses on market exchange (Gowdy, 2000). The ecologic economic theory is referred to as “strong” sustainability while the neoclassical theory is the “weak” sustainability concept. The “weak” sustainability concept assumes the capital stock, comprising of “human capital”, “manufactured capital” and “natural capital” can be substituted with each other while the “strong” sustainability concept assumes that substitution amongst each of these capitals is limited (Gowdy, 2000). This

implies that if we destroy that which nature provides not only is our wellbeing threatened but also our very existence (Gowdy, 2000). The concept of "strong sustainability" is that natural capital, which are the non-renewable resources remain constant over time and that it is undesirable to limitlessly substitute natural capital with manufactured capital, which is the human-created machines (Gowdy, 2000).

The distinctive character of land, which come from its ecological, physical and institutional properties, has to be considered while investigating the economics of land use changes (Hubacek & Vazquez, 2014). Limits on what can be done using and resources are defined by the nature, availability, quantity and characteristics of land resources. Human interactions defined by unconscious habits and human devised constraints are established by institutions (Hubacek & Vazquez, 2014). Operationalizing the ecologic economic theory, various concepts have been identified including: 1) adopting a no-substitution stance between economic and ecological sustainability; 2) the ability to respond to changing physical and biological conditions is a complex relationship which life on earth depends on; 3) defining social sustainability as social systems have evolved under specific environmental and biological constraints; 4) delineating and defining the conditions for sustainability of the economy; 5) delineating conflict points between ecosystems and markets (Gowdy, 2000). For this to be viable, policies need to be developed that will enable humans to live within the requirements of long-run sustainably according to social and biological requirements (Gowdy, 2000).

1.6.2 Institutional Theory

The institutional theory was founded on the ideas from Philip Selznick in 1948 who likened organizations to organisms that adapted to environmental threats. The theory was further developed by Meyer and Rowan in 1977 who argued that institutional norms and beliefs of the larger organizational environment were adhered to by organizations (ARDA, 2018). Advanced scholarly work fronted the concepts of neo-institutional theory by DiMaggio and Powell in 1983 who described organizations as isomorphic, where they are similar in practice and form (Lawrence & Shadnam, 2008).

Institutional theory is a theoretical framework that views the social world as one that comprises of institutions that set conditions on actions (Lawrence & Shadnam, 2008). Institutions comprise of the norms, cultural, social and legal rules that are prevalent in society (Bass *et al*., 2013). Institutions are viewed as the constants determining rules of variation (Lawrence & Shadnam, 2008). The institutional theory examines how actions of organizations and individuals are affected and affect historical and social forces that range from cultural understanding to explicit laws. Institutions determine the opportunities in society, which organizations are created to take advantage of (Bass *et al*., 2013). Departures from conditions set by institutions are counteracted by social controls that can be costly if they deviate from the social order (Lawrence & Shadnam, 2008). Nonconformity is associated with increased risks leading to increased costs or it can lead to reduction in legitimacy and resources that accompany the controls (Lawrence & Shadnam, 2008). There have been critics to this theory due to its short-comings from the assumption that an organization's behavior, whose outcomes are different from what was predicted in the theory and lack of incorporation of an organization's individual dynamic (ARDA, 2018).

1.7 Conceptual Model

The ecologic economic theory emphasize on human induced environmental stressors such as land conversion and resource use so that effective policies are developed for a sustainable environment. The ecologic economic theory influences the green economy term. The ecological models of urban form describe and explain the spatial patterns taken by the distribution of buildings, their form and activities across a city's terrain and relate this with land surface temperature. Development of cities should ensure that resources such as land, water and air are sustainably managed. The institutional theory looks at current policies on development in urban areas and ensures that resources are sustainably managed. That policies that are in existence could act as triggers to the urban heat island phenomenon. It also considers adaptation that institutions can make to tackle challenges and changes occurring within a local scale for sustainable development.

Oke (2014) stated that UHI occurs when the air in the urban canopy is warmer than the surrounding countryside, which is an indicator of climate modification. This phenomenon varies due to locational, meteorological and urban characteristics, which vary in space and time. The urbanization process leads to the transformation of the moisture, thermal, radiative and aerodynamic characteristics and this change the hydrologic and natural solar balances (Oke, 2014). The surface energy balance (Equation 1.1) within a volume is given as:

$$Q^{*}=QH+QE+QG+\Delta QS \quad \text{Equation 1.1}$$

Where:

Q^{*} Surface energy

QH Sensible heat

QE Latent heat

QG Conduction to or from underlying soil

ΔQS Changes in energy storage as a result of changes in energy absorption or release by the volume

Surface urban heat island (SUHI) is the dependent variable and influenced by land surface temperatures, which is a result of interactions of incoming radiation from the sun with different land cover types, urban form and structure. These are the independent variables since mitigative and adaptive measures can be developed based on human activity. Changes in average patterns of climate parameters like temperature, wind, pressure, rainfall and others can be used to detect climate change (RoK, 2013). This study assumes that urban morphological changes and land use have contributed to development of heat islands. Policies and regulations lay out the structure in how development will occur. Any conflict within the urban space can be investigated starting from the framework and addressing challenges that are occurring. The conceptual model is illustrated in figure 1.1.

The study identifies surface urban heat island as a result of land use and land cover changes and built- up morphology, which are independent variables, where vegetated areas are replaced by impervious surfaces including buildings, roads and pavements. Developmental changes that occur on land, driven by policies and systems within institutions, affect both day and night time land surface temperatures. Their relationship is expressed using a model that addresses all factors simultaneously.

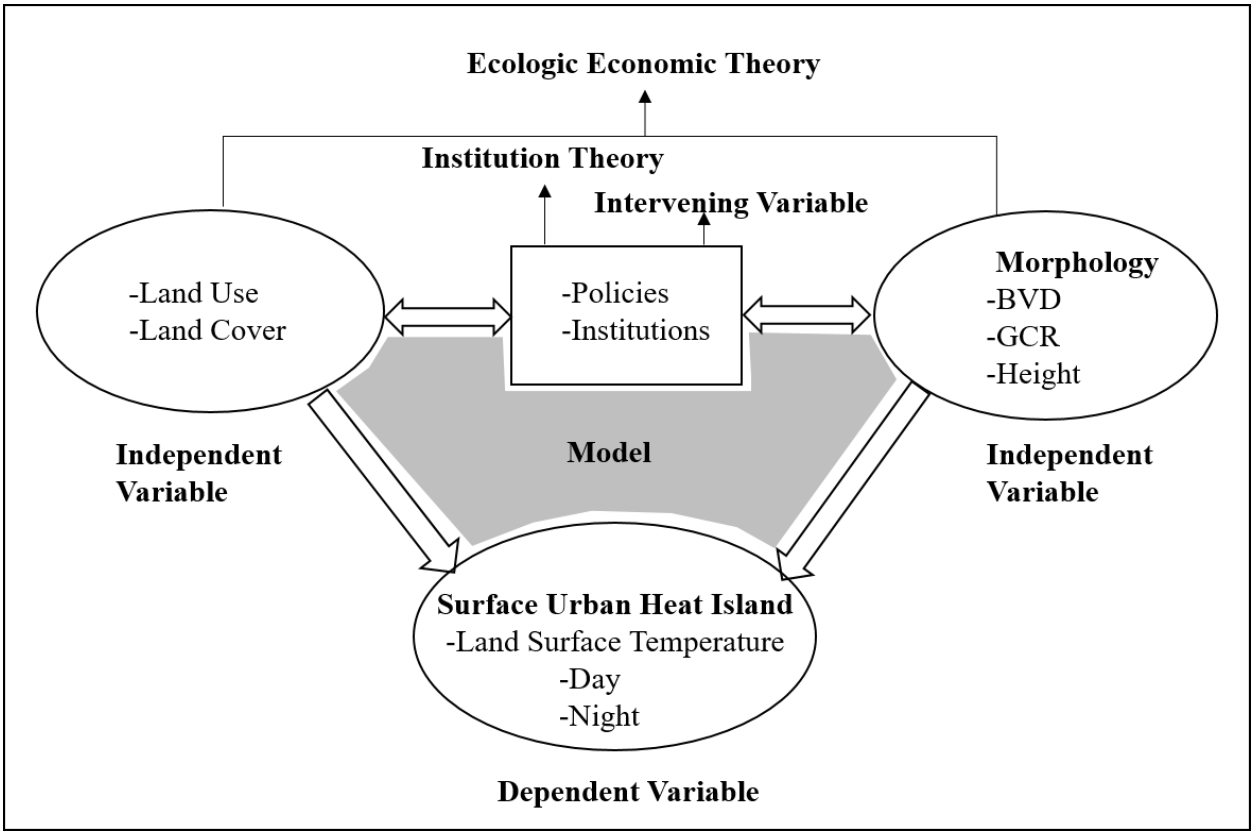

Figure 1.1: Surface Urban Heat Island as a Function of Morphology and Land Cover

1.8 Limitation of the Study

A limitation of the study was availability of thermal data in the same period that stereo-aerial imagery was collected.

1.9 Definition of Terms

The following terms are used in the study in the context of the definitions below:

1. Adaptation- refers to changing from existing attributes due to new climatic attributes. It previously referred to animals and plants but has now been fronted to ensure sustainable development occurs through policy (Schipper *et al*., 2010).

2. Coping- they are actions that are short-term that hold off risks that occur immediately. It does not focus on changing threats that are continuous or that are permanent. They can compromise adaptations that are long-term (Schipper *et al.,* 2010).
3. Maladaptation- are changes that increase the vulnerability of human or natural systems to climatic changes. Maladaptation occurs when changes made have positive impacts on one generation but eventually have negative effects on future generations or different groups (Schipper *et al.*, 2010).
4. Vulnerability- also described as exposure, it indicates the level of sensitivity a system or an organism is to a hazard. Factors considered to define vulnerability include age, livelihood, gender, political affiliation, entitlements, geographical location and other factors (Schipper *et al.,* 2010).
5. Vulnerability assessment- it involves determining factors that cause vulnerability and also assessment of capacity. This is done by mapping baseline data against future scenarios (Schipper *et al.*, 2010).
6. Impact assessment- this is identifying climate change effects in a certain location. This requires a baseline that acts as a reference and another climate change scenario that is projected. A comparison is done between the projected scenario and baseline or actual situation to determine the impact in part or as a whole (Schipper *et al.,* 2010).
7. Green economy- reducing the environmental impact while prosperity is increasingly generated (Mccormick *et al*., 2015).

1.10 Study Outline

The research is structured into five chapters. Chapter one gives an introduction, background to the study, problem statement, research questions and objectives, significance and justification of the study and conceptual framework. Chapter two reviews literature on urban heat island, frameworks for managing urban areas, built-up volumes, technologies for dealing with climate change, urban spatial models and research gaps. Chapter three describes the study area, data collection and processing, generation of data-sets and data analysis. Chapter four begins by giving an introduction, presents results of analyzed data and discusses the results: land surface temperature, land cover, NDVI, albedo, building heights, built-up volume densities, ground coverage ratio and aspect. Chapter five is a summary of findings, conclusion, recommendations, references and appendix.

CHAPTER TWO: LITERATURE REVIEW

2.1 Introduction

This chapter is a review of literature regarding urban heat island, urbanization, spatial management and technologies used in urban heat island studies. These focuses on the global, regional and national frameworks.

2.2 Urban Heat Island

Climate change is here and in the coming decades people will need to deal with this challenge. Irreversible changes by human activities to the ecosystem has occurred and further damage is likely (Schipper *et al*., 2010). Many cities around the world have reported perceived changes in sea level, temperature, precipitation or natural hazards that they attribute to climate change (Carmin *et al*., 2012). The differences in the climates in the rural areas and the urban areas, which tend to be warmer and more polluted is due to the replacement of crops and natural vegetation with non-evaporating and non-transpiring surfaces such as metal, asphalt and concrete (Zhan *et al*., 2015). Past studies reveal how much and how quickly climate can change even without the potential effects of human actions (USGS, 2013). Whether or not climate changes are due to anthropogenic causes, it is clear that new weather and climate patterns are emerging and that these changes are putting urban residents and assets at risk (Carmin *et al*., 2012). They have the potential to place stress on infrastructure, buildings, environment and other assets, affecting the health and wellbeing of local population *(*Carmin *et al*., 2012).

UHI is a combination of preexisting geographical factors including altitude, local climatic conditions, and urbanization processes that create artificial conditions such as urban tissue morphology, land cover, building percentage coverage and others (Inostroza, 2014). Human

activities that change the land surface properties and pollution emissions affect the earth's energy budget (Wu & Lung, 2016). UHI has been the most intensively studied climatic feature of cities and has been quantified by calculating air or surface temperature differences between urban and nearby rural areas *(*Zhan *et al*., 2015). Voogt (2007) when studying UHI used the term urban heat island (UHI) to refer to the relative warmth of air temperature near the ground i.e. canopy layer. Three main types of UHI have been identified namely, boundary layer urban heat island (BLUHI), canopy layer urban heat island (CLUHI) and surface urban heat island (SUHI) with surface urban heat island (SUHI) being large both day and night (James, 2000). Urban heat (UH) therefore tends to form in the air due to the difference in cooling between urban and rural areas (Voogt, 2007) (Figure 2.1).

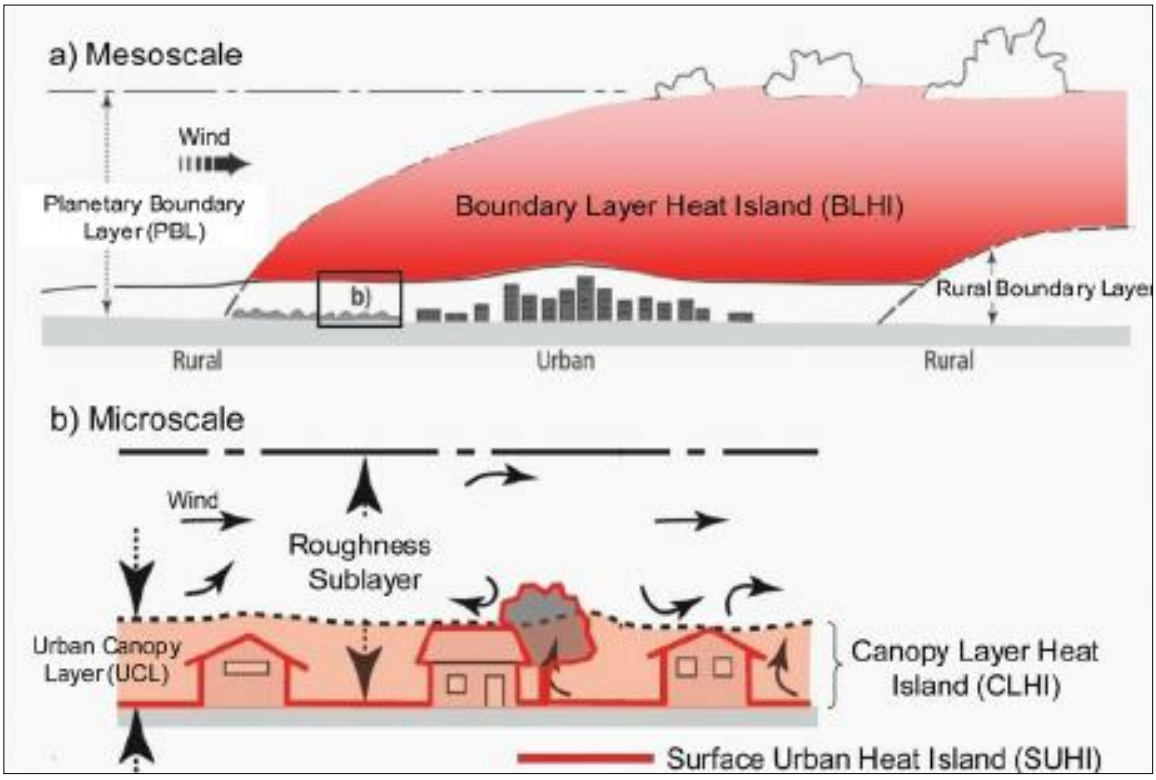

Figure 2.1: Urban Heat Island Boundary Layers

(Source: Oke, 2014)

In the urban atmosphere, two layers can be distinguished. Firstly, urban canopy layer (UCL) which is the layer between the urban roughness elements that is mainly buildings. Its climate is modified by the nature of the immediate surroundings and is dominated by geographical factors. Secondly, urban boundary layer (UBL) which is normally directly above the first layer. The nature of the whole urban area affect its characteristics (Voogt, 2007) . The urban heat island (UHI) effect is directly controlled by the land surface temperature (LST), which is an important parameter in urban climate (Feizizadeh & Blaschke, 2013). Since local environments modify the conditions in the thin air stratum above the ground, generally referred to as the atmospheric boundary layer, urban areas cannot be viewed in isolation. The local energy exchanges that take place within the boundary layer are affected by the changing character of the natural landscape in the city-building process (Gorsevski *et al*., 1998).

Voogt (2007) identified various factors that affect UHI such as the geographic location, time, synoptic weather, city form, city function and city size. Voogt stipulated that the surface energy balance which affects the surface temperature is governed by the properties of a surface. The properties include orientation and openness to sun, sky and wind, the radiative ability to reflect solar and infrared and to emit infrared, the availability of surface moisture to evaporate, the ability to conduct and diffuse heat and the surface roughness (Voogt, 2007). Decreased long-wave radiation loss, decreased total turbulent heat transport and increased absorption of shortwave radiation are some factors seen to cause UHI and are related to urban street geometry (Yang & Li, 2015).

UHI peak development is related to the different urban surfaces (Bottyan *et al*., 2005). The simulation of the real factors and the physical processes of maximum UHI is difficult. The modification of energy balances and radiation in urban areas due to different building materials, air pollution, heat production using air conditioners and differences in built-up surface geometry make simulation of maximum UHI development, factors and processes difficult to model (Bottyan *et al*., 2005). Different approaches such as energy balance, sensible heat flux, water balance, radiation models have been developed to study small scale climatic variations in cities. In using different urban surface parameters, quantitative information on spatial features in relation to maximum UHI intensity are generated from statistical models (Bottyan *et al*., 2005).

Bottyan *et al*., (2005) studied the seasonal mean maximum UHI intensity spatial distribution in Debrecen city. Basing on the built-up ratio, the spatial distribution of the thermal excess was estimated using linear statistical modelling. Built-up areas were extracted from Landsat imagery using NDVI indices. The percentage of built-up areas had a positive correlation with the mean maximum UHI intensity, in both the heating period where artificial heat sources are used as well as during non-heating periods. Investigations were also carried out with the distance from the city center where a negative linear relationship was observed with mean maximum UHI intensity. This investigation was undertaken in a model by using the percentage of built-up per cell in exponentially distance-weighted scale. Predictors were determined on the surface built-up ratio.

2.3 Urban Spatial Management

Urbanization is a term referring to political forces, social, cultural, demographic, environmental and economic processes that act on the physical geography proportionally to resource consumption and the population in urban settlements (Wapwera, 2013). It is a transition that is ongoing that provides social, economic and environmental opportunities (Satterthwaite & McGranahan, 2014).

Forces that shape urban growth and different extensions include: natural environment e.g. slope, water availability, climate and others; economy such as global exposure and economic development level; transportation systems such as private vehicle dependency and access; demographics such as growth of natural population and rural migration levels; consumer preferences such as home ownership and open space proximity; property or land markets such as cost and availability of land; governance such as level and type of development enforcement, amount of metropolitan land in public ownership (UN-Habitat, 2012). A significant part of urbanization is the growth of urban populations due to an increase in towns and cities (Nyaura, 2014). Therefore the key to sustainable urban forms is in being able to manage natural and human systems to maximize the benefits accrued from natural systems while reducing the city's ecological footprint (UN-Habitat, 2012).

Urban planning designs regulates the use of space by considering the location of different activities occurring in an area. It impacts access to light and solar heating through urban geometry, as well as overshadowing between buildings through zoning laws which control the height-to-distance ratios between buildings as well as the proportions of streets (Strømann &

Sattrup, 2011). Urban planning also focuses on the economic functions, social impacts and the physical form of the urban environment where at the city level, planning should target environmental planning and management (Nyaura, 2014). Many aspects of urban planning, development and management makes use of spatial information which is indispensable. Spatial information has gained importance due to advancement in data capture, management and access as well as analytical techniques (Potsiou *et al*., 2010). Issues such as climate change can be resolved using spatial information systems in supporting land administrative functions (Potsiou *et al*., 2010).

Climate change responses can be categorized broadly into mitigation of green-house gases or adaptation to changing weather conditions (UN-Habitat, 2012). Urbanization and climate change effects converge dangerously and threaten to have negative impacts on quality of life, and economic and social stability (Hebbert, 2012). Blakely (2007) stated that previous research had mainly focused on environmentally sustainable urban forms. However, research was needed to bring current knowledge about temperature rises and 'heat island effects', air pollution, sea level rise, storms, flooding and wild fires to bear on the design of disaster resistant communities (DRCs) that are much better able to withstand extreme events (Blakely, 2007). Research on design of cities and natural hazards induced by climate change should correspond to the geographical location of the area, the development scale and threats by climate changes on the settlement (Blakely, 2007).

Growing cities are experiencing a modification of climate and it is affecting human comfort and the environment. In 2003 during a summer excessive heat event (EHE), over 15,000 people died

in France (Wang *et al*., 2016). By the end of the century, with the ongoing concentrations and greenhouse gas emissions, it is estimated that global temperatures will exceed 1.5 ^{0}C (UN, 2015). To make cities environmentally sustainable proper urban planning and management is needed (Ongoma *et al*., 2013b).

2.4 Frameworks for Sustainable Urban Development

Cities are important drivers to sustainable urban development and transitioning into greener economies. They are associated with major environmental issues such as greenhouse gas emissions, air pollution, waste, poverty and have a dominant role in global consumption. Cities also have great potential for change and are great centers for innovation and creativity (Mccormick *et al*., 2015). Realizing opportunities that enhance local natural resources and that enhance human well-being while reducing ecological scarcities and environmental risks is referred to as the green urban economy, which is interconnected with sustainable urban transformations (Mccormick, *et al*., 2012).

Sustainable urban transformation directs development of urban areas towards sustainable development, focusing on three key areas: lifestyles and consumption, business and innovation and governance and planning. Integration of policy instruments and strategic planning in governance is essential and can be accomplished where policies are developed quickly and with flexibility for urban conditions that are rapidly changing, policies are economically and politically realistic and where policies that are contradictory are eliminated (Mccormick *et al*., 2015). Sustainable urban transformation therefore focuses on changes of urban areas while sustainable urban development mainly looks at development in urban areas (Mccormick *et al*.,

2013). Visualization of future sustainable cities requires identification of actions that need to be taken so as to realize these visions and move sustainably. Action that has been taken that involves changes in systems and technology are green-roofs, which are known to reduce impact of heavy rain, cool buildings through insulation in summer and keep buildings warm in winter (Mccormick *et al*., 2015).

Technological development is a force often tied to city evolution (DuPuis & Stahl, 2016). Smart cities make use of real-time data to improve the lives of its residents and it constitutes three major components: information and communication technologies for data aggregation; analytical tools that are useful for converting data into useful information; and organizational structures that make use of collected information to resolve community problems (DuPuis & Stahl, 2016). Cities such as San Francisco have endeavored to make the city smart and sustainable by reducing their greenhouse gas emissions and improving their public transportation by directing their initiatives around smart developments. With the use of internet of things (IoT) and big data, smart cities become environmentally sustainable (Joshi *et al*., 2016). Big data analytics has been applied in climate change research studies on smart urban planning, energy efficiency, forecasting weather, intelligent agriculture and others (Hassani *et al*., 2019). Extracting hidden valuable information from big data requires knowledge on the purpose of data and data collection techniques (Hassani *et al*., 2019). Big data is the technology where models are discovered through the process of data exploration with tools including R, Storm, Massive On-line Analysis and others. The main data analysis techniques include classification, clustering, association rule mining and regression (Hassani *et al*., 2019). Clustering involves grouping closely related or similar data sets together by exploring data, such that dissimilar data objects

are separated. Classification is the categorization of data sets into groups that are predefined and this is done using techniques such as decision trees. Regression is important as it explores the relationship between two or more variables for purposes of decision making and forecasting (Hassani *et al*., 2019).

2.4.1 Sustainable Development Goals

A spatial planning role is to meet sustainable development challenges (Wapwera, 2013). Sustainable development happens when the ability of future generations to meet their own needs is not compromised by meeting the present (Kanuri *et al*., 2016). The three dimensions of sustainable development are economic, social and environmental (Satterthwaite & McGranahan, 2014). Urbanization has created great opportunities in relation to advancing sustainable development but has also brought about some of the world's greatest development challenges (Kanuri *et al*., 2016). Development challenges have driven the green economy concept which is anchored on three key areas: valuing the environment, environmental protection policies and environmental accounting (Mccormick *et al*., 2015). Urban sustainability problems have been considered to be results from poor planning and governance and not necessarily from urbanization (Mccormick *et al*.,2013).

It is projected that by 2050 two thirds of the global population will be living in cities (Kanuri *et al*., 2016). Cities today are responsible for 70% of global carbon emissions, are key contributors to environmental degradation and climate change, while they generate 80% of the global gross domestic product (GDP) (Kanuri *et al*., 2016). Higher per capita incomes are associated with higher urbanization levels (Satterthwaite & McGranahan, 2014). The biggest per capita drivers

of climate change are the wealthiest countries which also have the largest global environmental footprints. Cities in middle-income countries that are industrialized and motorized have the worst ambient air pollution problems. The worst environmental health conditions are in the poorest countries amongst the poorest urban populations but have the lowest greenhouse gas emissions around themselves (Satterthwaite & McGranahan, 2014). The living standards of the world's population can be improved through proper management of urbanization (Wapwera, 2013).

The infrastructure that urbanization is putting in place in cities will determine whether people will be protected from further local environmental burdens or will contribute to climate change adaptation or mitigation (Satterthwaite & McGranahan, 2014). Adaptation to climate change has been talked about frequently as a way of dealing with climate change. Adaptation has been defined as a process of adjusting to new conditions, stresses and natural hazards that result from climate change (Schipper *et al*., 2010). Lives and assets and will be at risk and infrastructure adaptation limited if zoning and building codes are not adjusted for future needs in urban planning (Hebbert, 2012). Climate change responses can be contributed to or impeded by sustainable strategies and choices while sustainable development can also be influenced, that is contributed to or impeded by adaptation and mitigation strategies (Allen *et al.*, 2018). Climate-resilient pathways that strengthen sustainable development can be considered at different scales such as at the global level, rural areas or even at city scale (Allen *et al.*, 2018).

SDGs can provide more resources for local governments and strengthen outcomes of development if they are aligned with development priorities and planning frameworks that are currently existing (Kanuri *et al*., 2016). This can be achieved through a process referred to as

localization which involves adapting, implementing and monitoring SDGs at the local level. Therefore, local governments define policies and must be partners in implementing and monitoring progress of the SDG agenda against goals and targets (Kanuri *et al*., 2016).

2.4.2 Africa 2063 Framework

Major development frameworks in Africa include the sustainable development goals and Africa 2063. African Union (AU) in 2013 formulated a plan for Africa's transformation referred to as Africa Agenda 2063, which seeks to implement and accelerate initiatives of the past and present for sustainable development and growth (AU, 2014). One of the aspirations targets Africa's inclusive growth and sustainable development, one of which is through economies and communities that are environmentally sustainable and climate resilient. Despite Africa's minor role in contributing to the accumulation of greenhouse gases, production systems are geared towards minimizing climate risk vulnerability and related natural disasters (AU, 2014).

In Durban, the Environmental Management Department initiated the development of a climate protection programme in 2004 which comprised of three phases. The third phase involved the incorporation of climate change into long-term city planning where strategic urban development plans were simulated, compared and evaluated through development of models (Satterthwaite, 2008). Some of the interventions formulated to adapt to climate risks are (Satterthwaite, 2008):

a) Developing an information base on current conditions in each city or town. This would include events that would be classified as 'small disasters' as well as more significant events;
b) Initiate risk or vulnerability assessments for the city or town with as much geographic detail. One would need to ink hard maps with details of what is currently located within

the hazardous zones i.e. Population groups or settlements most at risk and activities that that may pose particular risk;

c) Discuss on how the above findings can be incorporated into the different aspects of the local governments.

2.4.3 National Frameworks in Kenya

Urban morphology is determined by urban planning, which influences the modes of living and impacts urban climate (Srivanit & Kazunori, 2011). Concentrations of large and small scale industries, commercial, administrative and financial set-ups in different parts of Kenya have led to urbanization (Nyaura, 2014). According to Kenya Vision 2030, it is estimated that 54% of the population in the country will be living in urban areas (RoK, 2016). Population, social issues, economics and the environment are some of the driving forces that have been identified that may influence development in Nairobi (UNEP *et al*., 2009). Competition of resources intensifies when depletion and degradation of a resource occurs, thus causing migration to less stressed areas to avert conflict. The management of assets sustainably would occur if strategies are employed that would reduce risks posed by threats which would then allow the environment to support development (UNEP *et al*., 2009).

Since Kenya's independence, policies have been created to adequately handle urban development issues (JICA, 2014). Action on climate and development go hand-in-hand (RoK, 2013). National policies and legislation that address and provide a framework to deal with the issue of climate change within the country include: The Constitution of Kenya (2010) which provides for policies and strategies so as to guarantee a right to a clean and healthy environment

under the Bill of Rights; The National Policy for the Sustainable Development of Northern Kenya and other Arid Lands; The National Disaster Management Policy, 2012; The Environmental Management and Coordination Act, 1999; The Integrated National Land Use Guidelines, 2011; The National Climate Change Action Plan, 2010; The National Climate Response Plan, 2013 (RoK, 2013).

Institutional frameworks that tackle urban development in Kenya include: The Physical Planning Act 1996, revised in 2012, was created to define the urban development management; The Building Code 1968 which specifies conditions of building constructions and it supplements development controls in the Physical Planning Act; The Urban Areas and Cities Act 2011 which defines the management of urban areas and cities (JICA, 2014); The Sessional Paper No. 3 of 2009 on National Land Policy provides a framework that is consistent with other policies to address necessary land reforms for equitable, sustainable and efficient use of land resources (RoK, 2009b). In the New Urban Agenda (RoK, 2017), Kenya committed itself in ensuring that it would develop environmentally sustainably and have resilient urban and human settlements through the use of sustainable construction materials, renewable and affordable energy and natural resources amongst other ways. The impact of climate change on human health is evident in Nairobi where there have been indications that malaria is spreading due to warmer temperatures and variation of rainfall patterns, which are suitable conditions for malaria causing mosquitos. Through the National Climate Change Response Strategy, RoK (2013) recommended within urban areas, planning to take into consideration the high growth rate of urban population due to climate-induced migration from rural to urban centers.

2.5 Built-up Volumes

A key concept considered in describing a city's urban spatial structure is urban density (Krehl *et al*., 2016). Sustainable urban forms are best determined using density where built-forms reflect the spatial layout of space (Sokido, 2016). Various notions have been given when using the term 'density' in reference to urban areas. Density has been defined as the number of units in a given area where the intensity of building development is used when referring to how much area is built-up within a specified area (Forsyth, 2003). Concentrations of urban masses can be described by physical quantifiable elements of urban space-buildings (Wurm *et al*., 2014). A key variable in characterizing the city's structure and shape is the volume density or urban mass concentration (UMC) (Wurm *et al.,* 2014). Using earth observation data one can identify and differentiate these urban masses. Building volume densities or floor space index, also known as floor-area-density or floor-area-ratio can be used to derive physical polycentricity. However, deriving floor-area- ratios is a complex process as building surveys are not typically available (Wurm *et al.,* 2014). Depending on the vast area of study, an appropriate stereo-image can be used. Urban morphology analysis have focused on planar physiognomies. Indices and methods frequently used include spatial metrics, sprawl intensity, fractal dimensions, gradient analysis and compactness index (Qin *et al*., 2015). They enable analysis of speed and intensity of urban expansion and its heterogeneity.

Creating affordable, efficient, comfortable, attractive and sustainable buildings is a challenge in the building and construction sector as these buildings should help occupants reduce their contribution to climate change, consumptions of excessive materials while being able to adapt to realities of the changing environment (Mccormick *et al.*, 2013). Very dense developed cities

serve socioeconomic purposes where population densities are concentrated in very tall buildings but they also have challenges in developing sustainably (Schläpfer *et al*., 2015). There is also high energy use within such cities for driving electrical appliances, heating, cooling, and lighting. In different parts of cities, building heights tend to be clustered around different height values partly due to restrictions in building height by city laws (Schläpfer *et al*., 2015).

Qin *et al.,* (2015) studied urban expansion in 3D where four indices were used to quantify urban expansion namely volume of buildings, weighted average height of buildings, 3D fractal dimension and 3D expansion intensity. The weighted average height of buildings and volume of buildings illustrated the 3D urban morphology temporal changes while 3D expansion intensity and 3D fractal dimension, which were developed from the previous indices, indicated the crucial aspects of spatial change of urban 3D morphology. Koomen *et al*., (1998) studied the third dimension in Dutch cities where the building volume was taken as a proxy for urban density. Building density is not only an indicator of a city's evolution but an important issue in urban planning in land management as the buildings are constructed in different styles and vary greatly in how the land is used (Alhaddad *et al*., 2004).

2.5.1 Influence of Urban Forms on Urban Heat Island

Three dimensional urban index was developed to analyse the correlation between urban volumes and SUHI in Taipei and Yilan cities in northern Taiwan (Wu *et al*., 2013). MODIS day and night-time land surface temperature indicated that during heat-waves, SUHI intensity in large and medium sized cities would be enhanced. Further analysis undertaken using air temperature

observations from weather stations indicated a high correlation with building volumes within 1000 meter distance from the weather stations(Wu & Lung, 2016).

The use of 3D information will assist in analyzing dense building structures. Chun & Guldmann (2014) used 2D and 3D data collected from LiDAR to analyze the effect of urban geometry on UHI development. They divided the study area into grid sizes of 120 m, 320 m and 480 m to integrate the data which included building ground floor area (BGFA), sky view factor (SVF), solar radiation, normalized differential vegetation index (NDVI), land surface temperature (LST) and water bodies. A spatial regression model was used to determine the relationship and effects between geometric characteristics of the area and the surface temperature within each of these grids. Impervious surfaces tend to have higher air temperatures than vegetated areas of up to 2 ^{0}C (Chun & Guldmann, 2014). Argent *et al*., (2012) used ENVI Met to simulate how different UHI mitigation strategies affect the outdoor thermal comfort. Results showed that within urban canyons, reflective surfaces and microclimatic green roofs had little effect in improving thermal comfort of humans. The physiological equivalent temperature (PET) reduced significantly with the introduction of street trees in bare canyons which had a lower height or width ratios. Irrigation practices on urban greening further reduced the PET due to cooling effect brought about by evaporation. Overall, streets trees contribute to cooling efficiency of a site by 80% and also reduces pedestrian exposure to solar incoming radiation and are the most effective greening strategy (Argent *et al*., 2012).

The effect of other impervious surfaces, besides buildings are an important factor to consider. In terms of the impact on urban heat, pavements and roofs are not equal. Roofs readily transfer heat

into a dwelling because they are thin, hence increasing the need for air conditioning. Whether a pavement is dark or reflective there is little discernible difference in air temperature even eight feet above the pavement. Adjacent buildings are heated up by reflective pavements, thus more energy is required in cooling the buildings during summer (Marks, 2009). While comparing the different pavement thicknesses, Stempihar *et al*., (2013) noted that the surface temperature decreased as the pavement thickness increased. For a thicker pavement, the maximum surface temperature decreases during the day but during the night may cause an undesired increase in minimum temperature.

The characteristics of urban forms and their interactions with climatic surface parameters are indicated in table 2.1. Urban environmental variables such as micro-climatic factors, wind speed and ventilation paths within cities are subject to both horizontal and vertical properties such as orientation, arrangement, height and density of buildings (Berger *et al*., 2012). Decreased sky view factor and massive construction materials cause huge quantities of solar radiations to be stored and re-radiated in urban areas (Memon *et al*., 2008). Surface temperatures are increased when the sky view factor is decreased, which is a measure of the visible sky. Closely compacted buildings reduces wind speeds within the canyon thus reducing the dispersion of heat, decreases terrestrial radiation loss while increasing the absorption of solar radiation on surfaces, which leads to increased surface temperatures (Chun & Guldmann, 2014). Surface temperatures can also be explained by the shape and size of buildings structures (Chun & Guldmann, 2014). Critical typologies for sustainable urban forms have been compactness and density whose purpose is to assign a degree of urban sustainability. Effective measurement tools for characterizing urban forms are spatial metrics in large study extents (Shirowzhan & Lim, 2014).

Urban sustainability indexes were developed using spatial metrics such as complexity, compactness and density (Shirowzhan & Lim, 2014).

The effective albedo or urban albedo, which is the ability of urban canyons to absorb solar radiation, depends on the surface albedo and urban geometry. Surface albedo is the reflecting power of a surface in the shortwave region of the electromagnetic spectrum (Yang & Li, 2015).

Table 2.1: Urban Spatial Characteristics and Climate Surface Parameters

Urban Spatial Characteristics	**Climate Surface Parameters**			
	Temperature	**Wind Speed**	**Humidity and Precipitation**	**Air Quality**
Building structure	•	•	•	•
H/W ratio of street canyons	•	•		
Sky view factor	•			
Land cover	•	•	•	•
Albedo	•			
Emissivity	•			
Thermal inertia	•			
Impervious area	•	•	•	
Vegetation fraction	•	•	•	
Surface water	•			•
Land use	•		•	•
Traffic density	•		•	•
Industrial areas	•		•	•

(Source: Heldens *et al*., 2012).

Albedo ranges are 0.10 to 0.5 with higher values being metallic surfaces. The albedo of individual reflecting surfaces and geometrical arrangement of building-air volumes influence short-wave radiation reflection (Oke, 2014). Albedo and emissivity are non-dimensional (Mills, 2004) (Table 2.2).

Table 2.2: Radiative Properties of Selected Materials

Surface	**α**	**ε**
Asphalt	0.05-0.20	0.95
Concrete	0.10-0.35	0.71-0.91
Urban Areas	0.10-0.27	0.85-0.96
Soils: wet to dry	0.05-0.40	0.98-0.90
Grass: long to short	0.16-0.26	0.90-0.95

(Source: Mills, 2004)

Urban heat island effect occurs due to urbanization which changes the surface albedo resulting in higher urban air temperatures than rural areas (Bhargava & Bhargava, 2018).

2.6 Technologies for Dealing with Urban Heat Islands

2.6.1 Aerial Photogrammetry

Photogrammetry was invented by Colonel Aime Laussedat in 1851. Over time, it has progressed from plane-table photogrammetry, analogue photogrammetry, analytical photogrammetry to presently digital photogrammetry (Kinani, 2015). Photogrammetry is used to extract topographic information such as contour lines, elevation data and height information and producing or updating of topographical maps (McWilliam *et al*., 2005). Collecting accurate and precise measurements from photographs is the science behind photogrammetry. To facilitate stereo viewing, aerial photographs are taken with some considerable overlap between images to enable

one to view the area in 3-Dimensions (Schenk, 1999). Stereo imagery can also be acquired from satellites.

Digital photogrammetry refers to the analysis of imagery in digital form, whether its source is scanned analogue aerial photo or digital imagery (Schenk, 1999). Automatic processes refer to processes that need minimal human intervention (Schenk, 1999). A digital representation of the earth's surface comprising of manmade and natural features in an urban area is referred to as a 3D city model (Singh, 2013). Datasets used in extracting building footprints include satellite stereo-imagery, aerial stereo-photos and LiDAR data. Laser scanned data provides automated data analysis and interpretation and also wide-area data capture (Neidhart & Brenner, 2003). Determination of building outlines has many application areas such as insurance, town planning, tax assessment and 3D modelling (Wang, 2016).

Climate vulnerability of cities can be addressed through 3D maps. Three dimensional (3D) visualization of built up areas is crucial for understanding building density (Peng *et al*., 2016). Spatiotemporal representation of land use processes and production of geographic knowledge has been aided by 3D dynamic geo-visualization models, which reflect changes in urban land areas (Gadal *et al*., 2009). Neidhart & Brenner (2003) used laser scanned data to determine the heat requirements by calculating the individual building volumes and their distributions, with additional information such as date of construction or renovation, building type, materials of construction, age of building and others. Gadal *et al*., (2009) identified some limitations associated in representation of data in 3D environment: (i) problems in managing geographic

databases and their size (ii) data and database quality which in turn determines representation accuracy and potential for producing geographic knowledge.

High resolution imagery is important in planning or planning during natural disasters and can be used to determine the severity and intensity of the damage (Eckert, 2008). This helps in improving the response to disasters. This data is also useful in creating smart cities or in determining suitable buildings for generating solar power (Eckert, 2008). Global elevation data can be obtained from various sources, the most common being Shuttle Radar Topography Mission (SRTM) at 90 meters. Other companies have developed higher resolution elevation grids such as Advanced Land Observing Satellite (ALOS) at 30 meters, Advanced Spaceborne Thermal Emission and Reflection Radiometer (ASTER) Global Digital Elevation Map (GDEM) at 60 meters. However this is coarse especially in urban areas in situations of disaster management and planning (Eckert, 2008).

Stereo-aerial photos tend to have smaller resolutions that are determined by the flying height at the time of acquisition. Digital surface models derived from very high resolution data, either from stereo-satellite imagery or aerial photos provide highly detailed topographical information that provides critical data for planning or disaster management (Eckert, 2008). The physical characteristics of buildings can be extracted from very high resolution imagery. Topography, climate, culture, technology and affluence are some of the aspects that characterize a built-up area (Eckert, 2008). Understanding the vulnerability of constructed buildings in a geographic area can be informed by the generation of 3D information especially informal buildings which tend to be more fragile (Eckert, 2008). Information that can be derived from analyzing 3D data

includes number of floors within a building which can be used to estimate the population within an area.

The realm of urban mapping has significantly and rapidly changed with urban planners challenged to analyze cities in three dimensions. Data sources for constructing 3D urban maps are 2D GIS databases, architectural plans, different remote sensing data as well as building component libraries (Esri, 2014). The accuracy of a digital surface model is also determined by the orthorectification of the stereo imagery (Eckert, 2008). Detection of buildings manually can be a tedious process. Alobeid *et al*., (2011) generated DSM's from aerial, IKONOs and GeoEye-1 stereo imagery to detect changes in buildings from 2007 to 2009. Semi-global matching tends to provide better building shapes (Alobeid *et al*., 2011). The rational polynomial coefficient (RPC) information available for satellite images are based on sensor information generated by an onboard Global Positioning System (GPS) receiver on the satellite, star and gyros sensors but are not supported by ground control points (GCPs) (Alobeid *et al*., 2011).

2D footprints of buildings from cadastral data or topographical maps constrain the shape of the building during 3D building reconstruction (Tack *et al*., 2012). Tack *et al*., (2012) used 2D building footprints from ground plans to extract building elevation from DSM generated from high resolution satellite imagery. The DSM was edited to remove any artifacts and features captured in the imagery to obtain a DTM of the study area. Despite the wide range of applications of 3D information, the accuracy requirements for each area differs (Tack *et al*., 2012). City Geography Markup Language (CityGML) has been adopting different level of detail (LoD) for modelling 3D urban objects by the Open Geospatial Consortium, Inc. (OGC) (Tack *et*

al., 2012).

The surface of the earth can be represented by a digital elevation model (DEM). Other terms used to describe the earth‘s terrain include: digital height model (DHM), digital terrain model (DTM) which represents the terrain’s surface, digital surface model (DSM) which represents all features including vegetation, man-made features such as buildings (Kinani, 2015) and triangulated irregular network (TIN) (Mathews & Weigle, 2015). There are several researches that have been undertaken that involve the generation of digital surface models (DSMs) from high resolution satellite and aerial imagery (Alobeid *et al*., 2009; Alobeid *et al*., 2011; Tack *et al*., 2012). Extraction of features such as buildings and roads from historical gray scale aerial imagery was mostly carried out by manual digitization. Compared to digital aerial or high resolution satellite imagery, historical aerial photographs have had limited application in the automatic extraction of features due to factors such as reduced signal-to-noise-ratio, limited radiometric resolution and lack of color information (Nebiker *et al*., 2014).

2.6.2 Earth Observing Satellites

The National Aeronautics and Space Administration (NASA) together with United States Geological Survey (USGS) jointly embarked in developing and launching earth observing satellites (EOS) that would help resource managers and earth scientists (USGS, 1997). These were designed to provide global and repetitive coverage of earth’s land masses and comprise of eight satellites, some of which have ceased operating. The first satellite named Landsat 1 was launched on 23rd July 1972 and ceased operation in January 6, 1978. Other satellites were subsequently launched including Landsat 2, Landsat 3, Landsat 4, Landsat 5, Landsat 6, Landsat 7 and Landsat 8 in 1975, 1978, 1982, 1984, 1993, 1999 and 2013 respectively. Landsat 1, 2 and

3 had an MSS sensor which had a spatial resolution of approximately 80 meters and worked within the green to near-infrared (IR) spectral bands (USGS, 1997). Landsat 3 had a thermal-IR sensor which was damaged during launch hence thermal data was not available until the launch of other satellites. Landsat 4 and 5 have an MSS sensor and a thematic mapper (TM) sensor with improved spatial and spectral resolution allowing them to sense wider bands i.e. six (6) bands from red to reflected near-infrared and see the ground in greater details (NASA, 2018a; Parcher, 2012). Landsat 6 failed at launch and did not reach orbit (NASA, 2018b). Landsat 1, 2, 3, 4 and 5 were decommissioned but the data they collected is available for use. Landsat 7 has an Enhanced Thematic Mapper plus (ETM+) which has a higher spatial resolution and nine spectral bands comprising of a panchromatic band, two thermal bands and five bands from green to mid-infrared (Appendix 1). In 2003 it experienced loss of its scan line corrector (SLC) leaving data gaps in the imagery it acquired. Landsat 8 consists of two sensors i.e. the Operational Land Imager (OLI) and a Thermal Sensor (TIRS) and has eleven bands (Appendix 1). All Landsat satellites have sun-synchronous orbits and cross the equator at 10.00am. They have temporal resolutions of 16 days which means that they return to the same place to capture data after 16 days.

Sentinel-2 has been a result of close collaboration between the European Commission, European Space Agency (ESA), industry, service providers, and data users. It's comprised of two satellites, Sentinel 2A and 2B launched in 2015 and 2017 respectively. It has a multispectral instrument (MSI) that captures 13 bands, with different spatial resolutions (USGS, 2015). Sentinel sensors have twelve (12) bands with four bands having a spatial resolution of 10 meters i.e. bands 2, 3, 4 and 8 (Appendix 2).

Advanced Spaceborne Thermal Emission and Reflection Radiometer (ASTER) satellite was a collaborative effort between NASA and Japan's Ministry of Economy Trade (Abrams & Hook, 2002). ASTER satellite system was launched in December 1999 and it crosses the equator at 10:30 am having a north-south orbit. It has the same temporal resolution as Landsat of 16 days. When first launched it comprised of fourteen (14) bands, three (3) very near infra-red (VNIR) at 15 meter spatial resolution, five (5) short-wave infra-red (SWIR) at and four (4) thermal infra-red bands (TIR) at 90 meter resolution (Appendix 3). In 2008 the SWIR sensor became non-functional and hence only seven bands are available (Caltech & JPL, 2004).

Moderate Resolution Imaging Spectroradiometer (MODIS) is a sensor upon two satellites which are Terra and Aqua satellites and cross the equator at different times. Terra was launched in 1999, crossing the equator in the morning and passes from north to south. Aqua was launched in 2002, crossing the equator in the afternoon and passes from south to north (Noi *et al*., 2016). Both Aqua and Terra have 36 spectral bands with a spatial resolution of 1 kilometer and a temporal resolution of 1 to 2 days. MODIS LST processed data sets are freely downloadable from the USGS website for both day and night- time LST analysis (Wan & Barbara, 2006) (Appendix 4).

2.6.3 Thermal Remote Sensing

UHI intensity and magnitude are widely used in thermal remote sensing to quantify thermal effects of urban built environment (Zhang *et al*., 2016). Though air temperatures in the urban canopy do not equal wall temperatures, previous studies have shown that near ground air temperature is highly related to land surface temperatures (LST) and it has been used to examine the relationship between urban surface biophysical parameters and UHI (Guo *et al*., 2016). Land

surface temperatures vary in response to the surface energy balance (Voogt & Oke, 2003). The energy balance within the urban climatic studies (UCL) is governed by the LST and it modifies the air temperature of the lowest layer in an urban area (Wang *et al*., 2016). Resulting surface temperature incorporates effects of the radiative input from the sun and atmosphere at the surface, the effects of surface radiative and thermodynamic properties, surface moisture, thermal admittance and surface emissivity, effects of the near surface atmosphere and its relation to turbulent transfer from the surface (Voogt & Oke, 2003).

Mishra (2009) used satellite imagery to extract environmental indicators such as land surface temperature, vegetation, building density and orientation, to develop an environmental quality index in relation to urban poverty and deprivation. A DSM was developed using Cartosat-1 stereo pair imagery to obtain an advanced view of the urban environmental quality. Zhang *et al*., (2016) studied the urban fabric of Shanghai by quantifying the relationship between fine-scale urban fabric properties and their thermal effect. The thermal effect was deduced from land surface temperature (LST), intra-UHI intensity, blackbody flux density (BBFD) and blackbody flux (BBF). They utilized resampling methods on Landsat 8 thermal infra-red (TIR) and used QuickBird imagery at 0.61m to obtain land parcels. The coarse resolution of LST was resampled to 1 meter resolution.

Using predictors of higher spatial resolution, one can ‘improve’ the spatial resolution of an image by using methods known as downscaling, image fusion, spatial sharpening and disaggregation (Bechtel *et al*., 2012). Mohajeri *et al*., (2015) explored the effects of urban form, particularly the density of the built environment, on the potential for solar energy production in

urban areas where building and street densities had large impacts on the solar energy potential. There was a negative correlation between building density and solar irradiance whereby dense parts of the city received less solar radiation than dispersed parts, presumably because the façades were under shadow during the day.

2.7 Spatial Models

2.7.1 Spatial Metrics

Spatial metrics are important in correct interpretation of pattern change as they provide additional information about the structure of changes e.g. fragmentation of the landscape, changes is patch size etc. However, inferring the causal factors of these changes and proceeding with the modelling of land use and land cover change dynamics is still difficult (Koukoulas *et al*., 2008). Indicators for the landscape that could be used for comparing the structure and form of various cities have been defined using spatial metric techniques. They provide a framework for examining the dynamics of change and unique spatial components of intra- and inter-city urban structure (Prastacos *et al*., 2011). The art of expressing mathematically the interaction of people and activities in the urban environment has been described as urban modelling (Prastacos *et al*., 2011). When coupled with remote sensing, spatial metrics have been argued as one impactful tool to link urban land-use pattern and dynamic processes (Zhao & Murayama, 2011). Spatial metrics can provide a link between the physical landscape structure and urban form (Pham *et al*., 2011).

Responses of people, as mediated by institutional factors, to economic opportunities drive land-cover changes (Lambin *et al*., 2001). Land use decisions vary across spatial scales from policies

and economic forces that change land use regionally and globally to households decisions that impacts local land use. Lambin *et al*., (2003) discussed some of the factors that cause land-use changes including technological and economic factors, variability of natural environment, globalization, demographic, cultural and institutional factors. When referring to the type of land cover, two important factors that contribute to temperature differences in urban fabric include decreased evapotranspiration rate and differences in thermal properties of impervious surfaces. In developing mitigation strategies, assessing consequences of climate change on the local climate brought about by changes in city structure and land use is important (Heldens *et al*., 2012). The local climate is determined by the regional climate, local surface and characteristics of morphology for example number, orientation and shape of buildings and urban objects, size, materials used and volume or type of vegetation (Heldens *et al*., 2012).

Vegetation is important because of its effects on air temperature, quality and air humidity (Mishra, 2009). Trees along street canyons could, due to many variables such as wind speed, building heights and traffic levels, cause increased localized exposure to traffic emission and other air pollution sources (Zupancic *et al*., 2015). Natural vegetation and tree cover have a cooling effect on the surroundings through the process of evapotranspiration (Grover & Singh, 2015). Sodoudi et al., (2018) studied attenuation effects and allometric properties of nine (9) individual trees of different species located in Uhuru and Central park in Nairobi City namely: *Ficus benjamina* (weeping fig), *Warburgia ugandensis* (East African greenheart), *Dypsis decaryi* (triangle palm), *Calistemon citrinus* (bottle brush), *Ficus religiosa* (pippala tree), *Terminalia mantaly* (Madagascar almond), *Cassia spectabilis* (cassia, yellow shower), *Bambusa vulgaris* (bamboo), *Schinus molle* (Peruvian pepper) and one type of grass, *Pennisetum clandestinum*

(Kikuyu grass). *Ficus benjamina,* having the most significant crown width, tree height and canopy, presented the most significant attenuation of mean ambient temperature by 20.07% and mean surface temperature by 40.26%. In the city the density and spatial configuration of urban forest affects land surface temperature. However it is difficult, using modelling scenarios to determine reliable air pollution mitigation estimates (Zupancic *et al*., 2015). While urban forests face threats that include extreme weather, diseases and pests, management of vulnerability will ensure maximization of tree benefits are realized (CoM, 2012).

2.7.2 Geographically Weighted Regression

Only by monitoring and modelling changes and impacts, which are two-way processes, can our knowledge increase on their relationships (Koukoulas *et al*., 2008). Identifying new rules, principles and making discoveries becomes difficult when one has data and tries to apply theories and models constructed in one's head to them (Murayama & Rajesh, 2011). Tobler in 1970 stated that " Everything is related to everything else, but near things are more related than distant things", which is referred to as "The First Law of Geography" (Murayama, 2011). The spatial dependence and association of geographic objects is described as spatial autocorrelation. Positive spatial autocorrelation occurs if features within a geographic space have a homogenous spatial pattern, while negative spatial autocorrelation occurs when features represent a heterogeneous spatial pattern. When values of attributes are independent of location, zero autocorrelation is said to exist. In natural systems, objects have some degree of spatial clustering (Murayama, 2011).

Global and local spatial autocorrelation tests are methods used to analyze patterns of spatial attributes. Moran's I and Geary's c are examples of global spatial autocorrelation tests that can

verify relationships between location of spatial objects and their attribute values through statistical tests of significance. This statistical test is effective in measuring spatial autocorrelation over an entire region, but not for searching for heterogeneous patterns or local clusters in a region. *Gi (d)* is a statistic that was developed as a local spatial autocorrelation statistic where *d* is a distance parameter to a weight coefficient w_{ij} to measure spatial proximity of objects (Murayama & Rajesh, 2011). A technique developed to analyze spatially varying relationships between variables is geographically weighted regression (GWR) which allows local rather than global parameters to be estimated (Murayama & Rajesh, 2011) and enables exploration of spatial nonstationarity (Mennis, 2006). It is based on a non-parametric technique in which differential weighting system is used to generate a separate model for each spatial location in a study area. Weights are calculated representing spatial dependencies between observations. Conventional regression can be expressed as equation 2.1:

$$y_i = \beta_0 + \sum_t \beta_t x_{it} + \mathcal{E}_i \ldots\ldots\ldots\ldots\ldots\ldots\ldots\ldots\ldots\ldots \text{ Equation 2.1}$$

Where y_i if the value estimated of the dependent variable for observation i, β_0 is the intercept, β_t is the estimated parameter for variable *t*, x_{it} is the value of the t^{th} variable for i and $\mathcal{E}_i$ is the error term. This is a single regression equation generated for simple linear model, usually fitted by ordinary least squares methods (OLS) (Propastin *et al*., 2008). For GWR, it the can be expressed as equation 2.2:

$$y_i = \beta_0(m_i, n_i) + \sum_t \beta_t(m_i, n_i) x_{it} + \mathcal{E}_i \ldots\ldots\ldots\ldots\ldots\ldots\ldots\ldots\ldots \text{ Equation 2.2}$$

Where m_i, n_i captures the coordinate location of i. this can be represented diagrammatically as shown in figure 2.2.

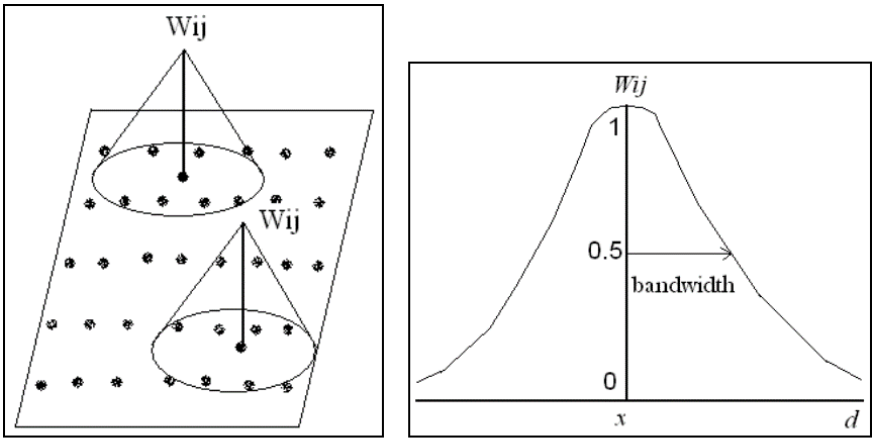

Figure 2.2: GWR with Fixed Kernels (a) and the Spatial Kernel (b)

(Source: Propastin *et al*.,2008)

The spatial points with fixed spatial kernels, where a region is described around a regression point that is located at the center of a moving window (Figure 2.2 a). The model is then calibrated using all the data points within the window. The spatial kernel (Figure 2.2 b) where the regression point is represented by *x*, the distance between regression point *i* and data point *j* is represented as *d* and the weight of data is *w* of point *j* at regression *i*. Depending on the density of the observations in a certain point, the size of the moving window can be varied from one point to another since it is also smaller in size than the study area (Propastin *et al*., 2008). In areas with low density points the size of the moving window can be increased. Since in GWR the weight of a data point depends on its distance from the regression point closer points have more weights. There are different methods for calculating the spatial weighting function, with the fixed kernel size being used for data sets that have regular distribution such as raster datasets. These can be calculated by using the Gaussian function in equation 2.3:

$$w = exp[\frac{1}{2(\frac{d_{mn}}{b})}]^2 \quad \text{Equation 2.3}$$

Where d_{mn} is the distance between the regression point *m* and the data point *n*, while *b* is the bandwidth. The Gaussian weighting function are most appropriate for regularly distributed data as continuous weighting function are provided from a regression point up to a distance b and data points beyond distance b are given zero weights (Propastin *et al*., 2008).

GWR has been used in various fields such as land surface temperature (Zhao *et al*., 2018), mapping diseases (Ge *et al*., 2017), land cover analysis (Georganos, 2016; Propastin *et al*., 2008); air pollution (Fang *et al*., 2015). Ordinary least squares (OLS) model, spatial lag (Autoregressive) model (SAR) and general spatial model (GSM), which is a combination of the SAR and the spatial error model (SEM) was used to analyze the relationship between the land surface temperature and the variables included in the grid. LST in adjacent grid cells was spatially correlated with the close-by cell locations, which was estimated using the GSM and SAR models.

2.8 Research Gap

Upper Hill's re-zoning, built-up developments and land use changes have not been analysed in relationship to changes in land surface temperature. Karanja & Matara (2013) cited the need to study the effect of urban heat islands in Upper Hill as the area which was formerly heavily vegetated, has transformed to high-rise urban developments. The study of using three-dimensional data using high resolution imagery to study surface urban heat islands has not been carried out in this study area. Previous studies by Msoffe *et al.,* (2014); Ongoma *et al*., (2014) and Nyaga (2014) analysed land surface temperature and urbanization effects on air pollution but the contribution that urban form and volumes have on land surface temperature have not been

adequately studied. The use of high resolution satellite imagery in urban studies provides additional details on built-up developments compared to the use of low-resolution satellite imagery which would not give a clear picture on urban development changes in the area. Results from this study are important in determining the energy use based on the heat capacities of buildings. Three dimensional data is important even as the country heads towards use of renewable sources of energy as potential areas of harnessing energy on buildings can easily be identified using this data. The study focuses on urbanization and land surface temperature though there are various factors that contribute to UHI. Ordinary least squares and geographical weighted regression analysis are used to model the spatial relationships of different urban spatial metrics and land surface temperature to understand the dynamics of UHI and built-up morphology.

CHAPTER THREE: METHODOLOGY

3.1 Introduction

This chapter introduces the study area and gives a detailed account of the adopted methodology used in collection of data, analysis and processing.

3.2 Study Area

The study covers Upper Hill, Nairobi, Kenya. The area covers 4.2 square kilometers and extends between latitudes 1^0 17' and 1^0 18' South and longitude 36˚48' and 36˚49' East, having an average altitude of 1700 meters above sea level (Figure 3.1). The 2009 population census indicates there were 3,138,295 inhabitants in Nairobi and it's estimated to increase to 5,468,000 by 2030 (NCC *et al*., 2014). The boundaries indicate Upper Hill is in two constituencies: a) Dagoretti North constituency, Kilimani location, Kilimani sublocation which is north of Ngong road; b) Kibra constituency, Kenyatta/Golf Course location, Kenyatta sublocation which is the south of Ngong road and bounded by the railway line, Mbagathi road and Uhuru highway (HDE, 2019). Population in Kenyatta sublocation was 10,050 with a population density of 3,448 people per Km^2 while population in Kilimani sublocation was 32,505 with a population density of 3,550 people per Km^2 . Land ownership in Upper Hill comprises of: Government, private (lease-hold) and Kenya Railways Corporation (Karoki, 2004). Upper Hill, known as the capital's financial hub is home to diverse organizations such as government institutions, hospitals, commercial centers, multinational companies and embassies. It also includes residential areas and educational centers such as a secondary school (UHDA, 2017).

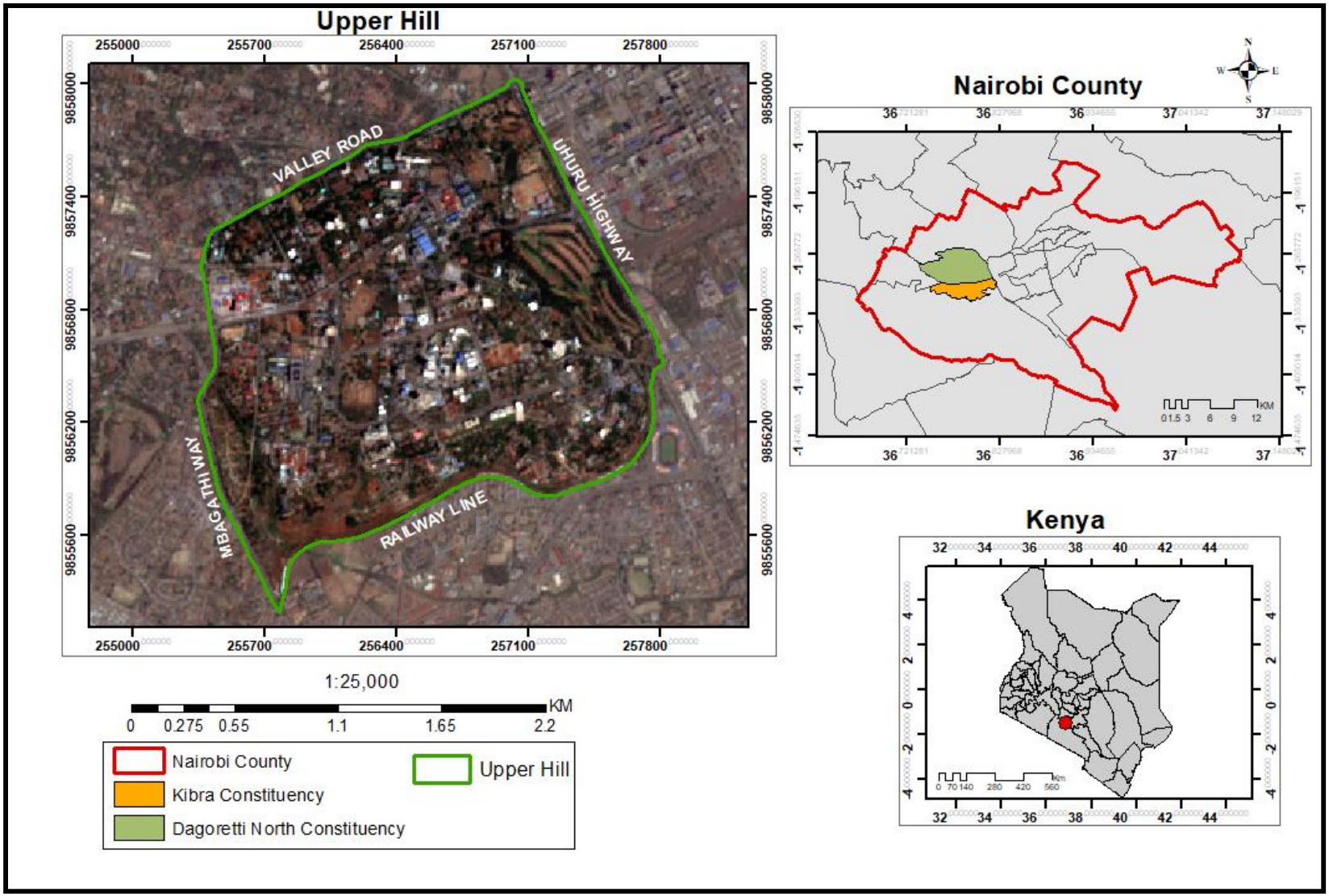

Figure 3.1: Location of Upper Hill in Nairobi City County, Kenya

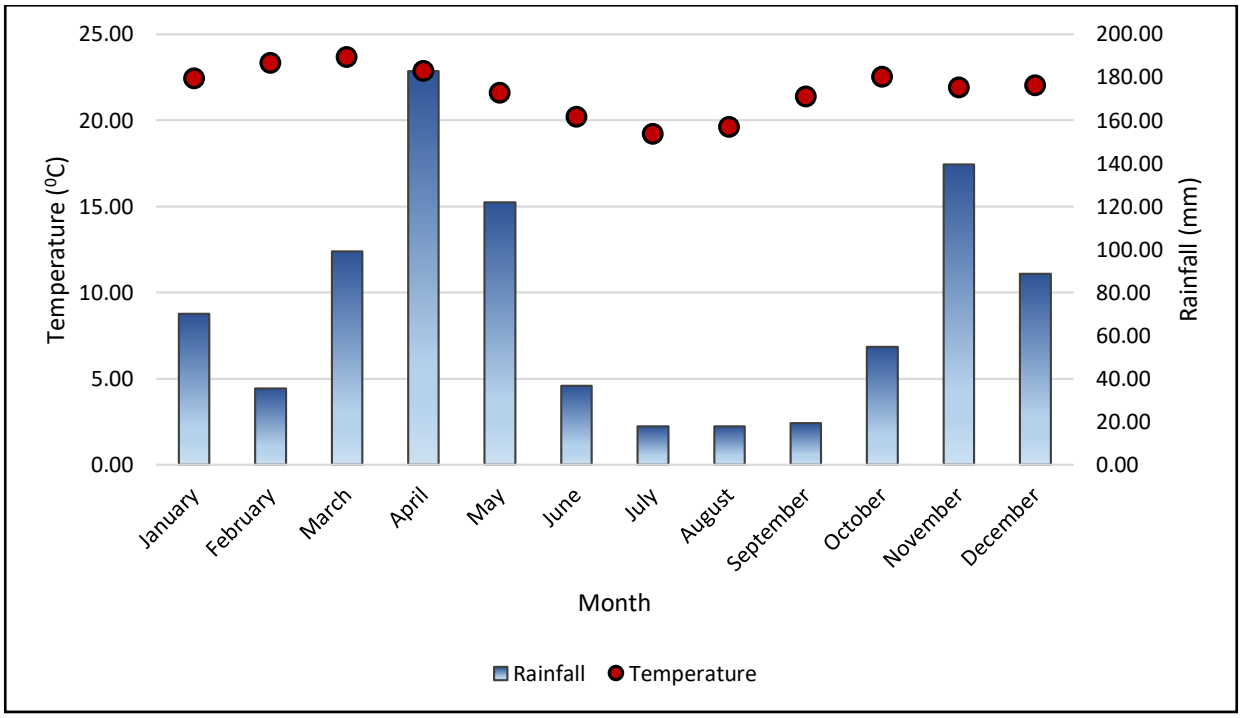

Figure 3.2: Mean Monthly Temperature and Rainfall from Nairobi Wilson Station (Source: Author, 2019)

Figure 3.2 illustrates the mean monthly temperature and rainfall measured at Wilson Station from the years 1984 to 2013 as it is the closest meteorological station to Upper Hill. April and November received the highest amounts of rainfall as they are in the long and short rainy seasons respectively. Low rainfall and temperatures were in the months of July and August and are cold periods in the year. High temperatures were recorded in the months of February and March with February receiving low amounts of rainfall thereby having low cloud cover. Mean annual air temperature (Figure 3.3) for the period 1984 to 2017 indicate that air temperatures have steadily risen with peaks as indicators of severe climatic events or natural disasters occurring in Kenya. Notable droughts or dry conditions have occurred in 1987, 1991 to 1992, 1997, 1999 to 2000, 2005 and 2010 to 2011 and 2015 (UNDP, 2015; Mbogo *et al*., 2015).

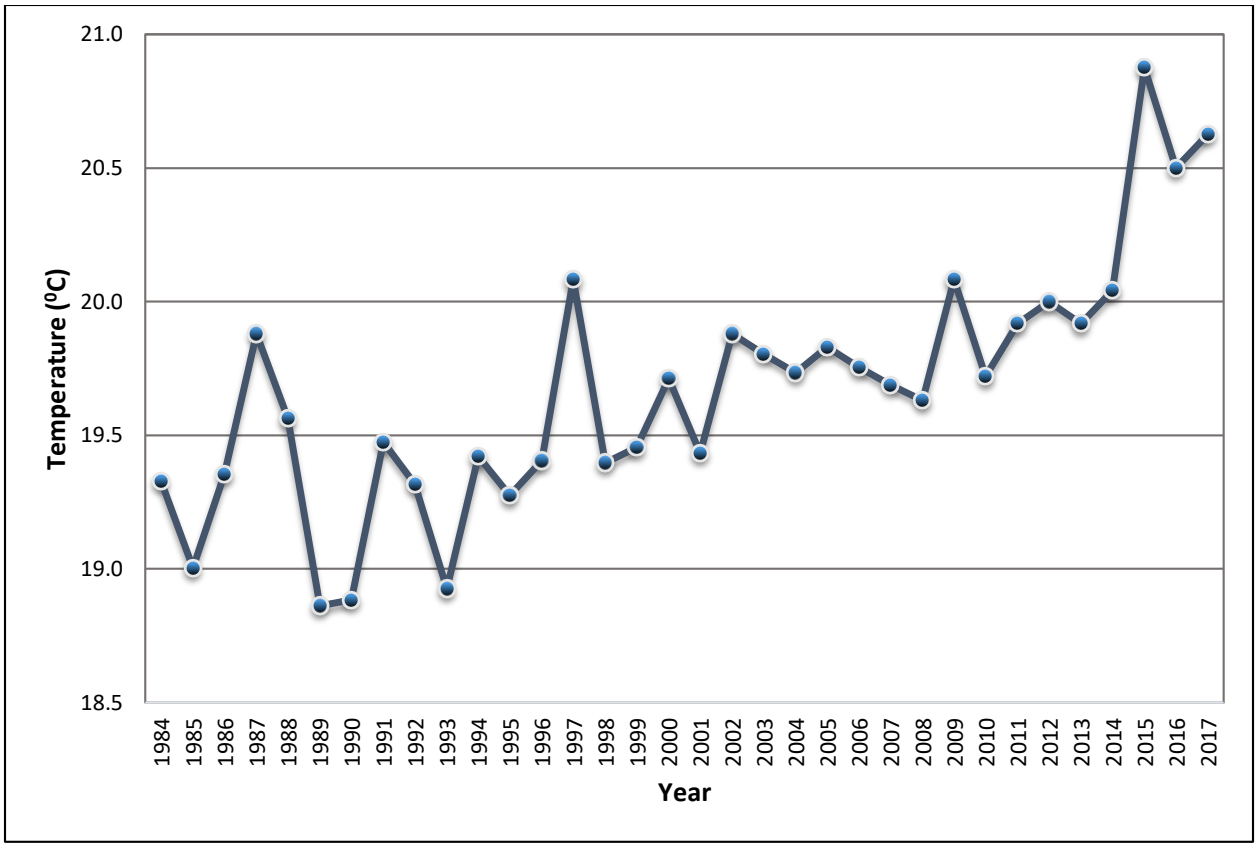

Figure 3.3: Mean Annual Temperature in Upper Hill from Nairobi Wilson Station

(Source: Author, 2019)

Nairobi's history dates back to the 19th Century when the Mombasa-Uganda railway was being built by the British. The first plan for Nairobi was drawn in 1898 by an assistant railway engineer, Arthur Fredrick Church, so as to prepare a town layout for the railway depot. It was followed by a second plan in 1927 as a settle capital (JICA, 2014). By 1927 the city area was expanded to 77 km^2 due to the growing population. A plan was drawn by F. Walton James and planned by Eric Dutton, which focused on regulating buildings and density, improving drainage and clearing swamps. Residential areas were segregated by racial groups.

A master plan for the colonial capital was prepared in 1948 whose goal was to make Nairobi more attractive for industrial investments (Figure 3.4). The plan introduced twenty (20) zones for railway, industry, business & commercial, residential, official housing, open space, forest reserves and parks (JICA, 2014). In 1968 the new zoning scheme was introduced that tried regulating minimum plot size and land use.

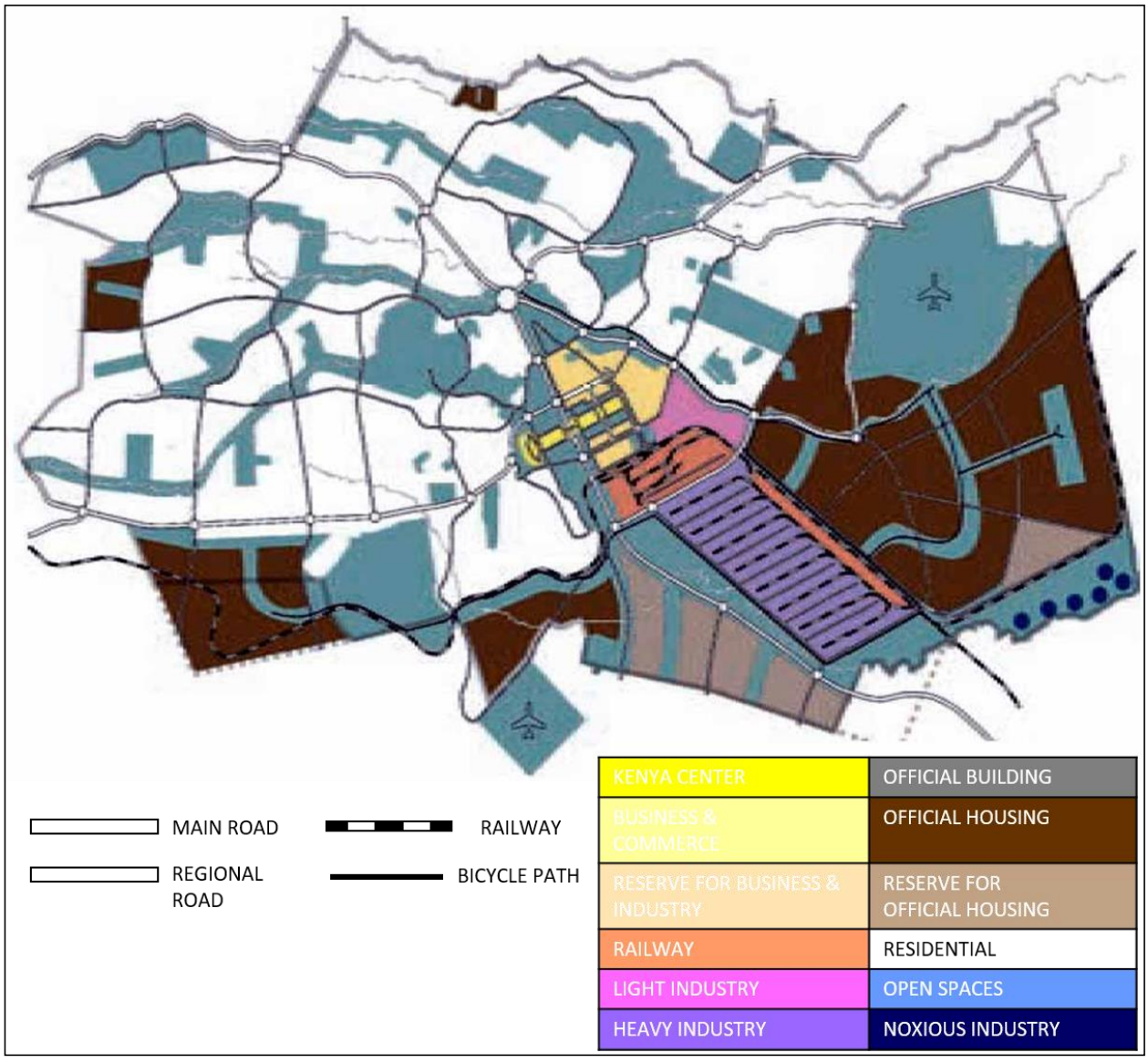

Figure 3.4*:* Nairobi Master Plan of 1948

(Source: JICA, 2014)

The only office development that existed in the late sixties was Ministry of Works building. A Nairobi Metropolitan Growth Strategy was published in 1973 which brought together UN experts, urban planners in the City Council of Nairobi and urban planning consultants. It was developed as a long-term planning policy intending to provide strategies and guidelines for Nairobi City's development by rezoning and creating a land use rationalization strategy for up to the year 2000 for CBD (UNEP *et al*., 2009). This influenced the character of the area to change in the 1980s from low-density residential buildings to high-rise office buildings (Karoki, 2004).

Upper Hill area's rezoning and re-planning policy was approved in 1995 by the former Nairobi City Council, currently the Nairobi City County, together with the Physical Planning department (Karoki, 2004; UNEP *et al*., 2009) which designated and expanded the designated commercial centers (UNEP *et al*., 2009). Rapid developments and modern offices motivated the rezoning plan however, the infrastructure services still remained the same (JICA, 2014).

Table 3.1: Zoning Regulations for Zone 1E in Upper Hill, Nairobi

Blocks in Upper Hill Area	**GCR%**	**PR%**	**Area (Ha)**	**Type(s) of Development Allowed**	**Min Area (Ha)**
Block 1- Offices (Community)	60	300	109		
Block 2- Commercial or Offices	60	250	44		
Block 3- Offices	60	300	34	Commercial/	
Block 4- Residential	35	150	52.8	Offices/	0.05
Block 5- Institutional (KNH)			97.9	Residential	
Block 6- Mixed: Institutional; Hotels; Offices	60	200	80		

(Source: Nairobi City County, 2006; Karoki, 2004)

The 2004 rezoning review was carried out on the whole of Nairobi where the 20 zones created in 1948 were subdivided into smaller zones, with ground coverage ratios (GCR), plot ratios (PR), block area and minimum plot sizes (Table 3.1) (NCC *et al*., 2014; Karoki, 2004). Areas such as Westlands, Kilimani, Kileleshwa, Parklands and Westlands allowed developers a maximum of four floors. However, these regulations were not followed, where high rise buildings of more than five (5) floors and land mixture in residential areas could be seen (NCC *et al*., 2014).

The Integrated Urban Development Master Plan for Nairobi was created with the specification of the Urban Areas Cities Act under the framework of the County Government Act (JICA, 2014). The National Spatial Plan, launched in 2017, provides comprehensive strategies and policy guidelines to address issues of balanced development by providing a coordinating framework for various sectors involved in spatial planning and implementation while also addressing climate change (RoK, 2016). It was created to guide development over a 30 year period from 2015 to 2045 to support projects that are in the Kenya Vision 2030 and give a framework for absorbing the spatial impacts of these projects (RoK, 2016).

3.3 Research Design

The study used case study and correlation research design. Case study design using quantitative analysis is used as it is characterized by data collection from different sources on Upper Hill, which is a case study of rapidly urbanizing areas. The correlation research design is used in analyzing relationships between the dependent variables as indicated in the objectives. It explores and observes relationships between the variables to determine if correlations exist between them. Land use changes have seen highly vegetated parts of Upper Hill being

transformed to built-up areas. 3D building reconstruction is extracted using data fusion techniques. This technique involves determining the volume of buildings so as to obtain urban mass concentrations (UMCs) for the study area. All data is transformed into Transverse Mercator projection with Arc 1960 Datum and UTM 37 as the projected coordinate system. Time series archive satellite and aerial imagery were analyzed for the period 1978, 1986, 1995, 2000, 2005, 2011 and 2017. Landsat Satellite imagery has a spatial resolution of 30m while aerial stereo-photos have a resolution of 10cm. The use of grids improves analytical results, easing visual interpretation of both built-up densities and land surface temperature. Statistical modelling was performed to determine spatial relationships across Upper Hill using time series data. A schematic summary of the research methodology is indicated in Figure 3.5.

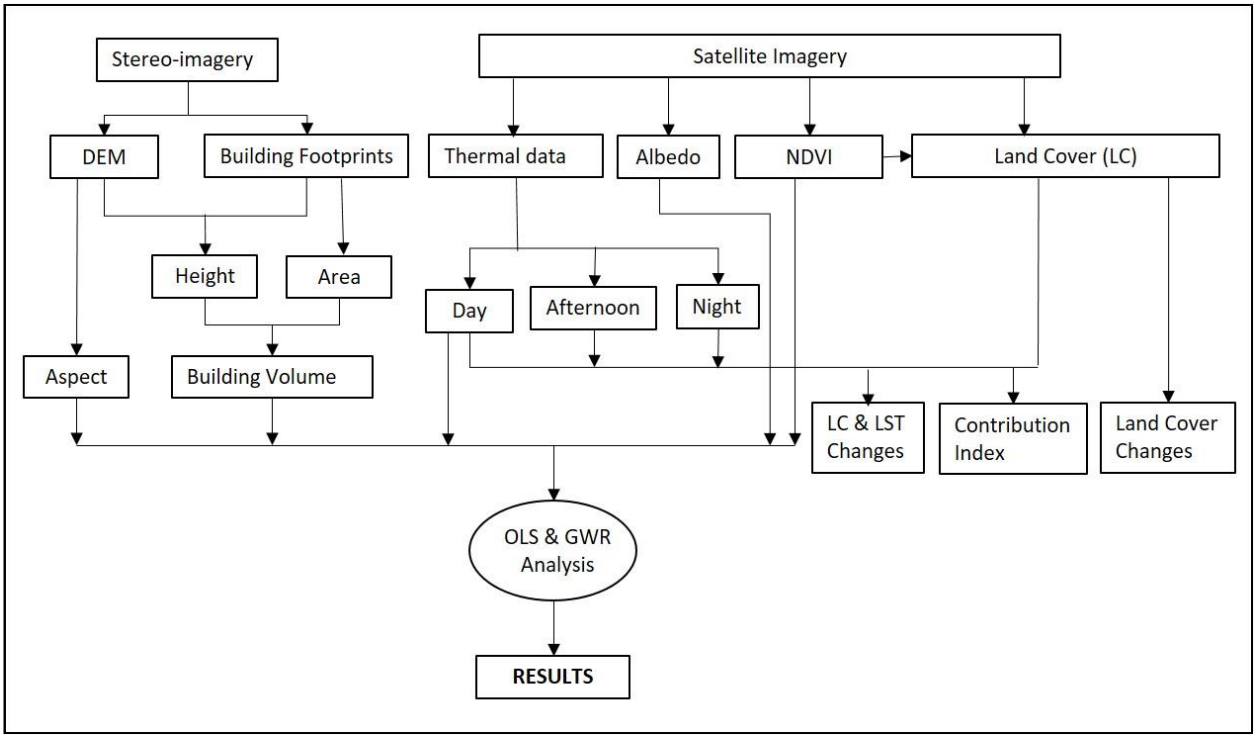

Figure 3.5: Schematic Summary of Methodological Approach

3.4 Relationship between Land Cover and Land Surface Temperature Change

3.4.1 Rainfall and Air Temperature Meteorological Data

Meteorological data from Wilson airport was used to validate the LST trend in the months collected as it is the nearest station to Upper Hill, where minimum and maximum air temperatures were obtained from the year 1984 to 2017 for the months of January and February. Minimum temperatures are measured before sunrise i.e. between 6:00 am and 7:00 am while the maximum temperatures are measured after sunset i.e. any time from 6:00pm to 9:00pm. Mean rainfall data was available from Dagoretti meteorological station for the period 1984 to 2017. The meteorological station details and datasets (Table 3.2).

Table 3.2: Meteorological Stations in Nairobi

Station	**Altitude (m)**	**Longitude (dd)**	**Latitude (dd)**	**Data Length**	
				From	**To**
Wilson Airport	1676	36.820	- 1.320	1984	2017
Dagoretti	1798	36.750	-1.300	1955	2013

(Source: Ongoma *et al., 2013a*)

3.4.2 Preprocessing of Satellite Imagery

Satellite imagery was used to determine land cover changes and calculate land surface temperature for different years. Cloud-free data was not available within the specified years and time-interval of study during the coldest months which are also rainy within the months of January and February, which are the warmest months. Therefore cloud-free datasets were available data Satellite imagery from Sentinel-2A, ASTER, MODIS and Landsat 5 TM, Landsat 7 ETM+ and Landsat 8 OLI/ TIRS were downloaded from the USGS website earth explorer with less than 10% cloud cover on each scene. All Landsat and ASTER imagery are geometrically

processed to a high level and data quality and are referred to as level-1 tier products. All imagery were transformed from UTM WGS84 Zone 37 N/S projection system to UTM Arc1960 37 South using the project raster tool in ArcGIS 10.7. This is the final coordinate system that is used for all imagery in the analysis.

A. Landsat

Landsat imagery was downloaded for Landsat 5 TM, Landsat 7 ETM+ and Landsat 8 OLI/TIRS sensors at UTM WGS 84 Zone 37 South coordinate system. The various sensors and dates are listed:

a) 5th January 1986 and 30th January 1995 are acquired using Landsat 5 TM sensor;

b) 21st February 2000 is acquired using Landsat 7 ETM+ sensor;

c) 11th February 2017 day-time and 16th February 2017 night-time acquired using Landsat 8 OLI/TIRS sensor.

Band information for each sensor are in Appendix 1. Night-time imagery only has the thermal band from which thermal data can be calculated. Composite images were created for each sensor in ArcMap 10.4 according to the band information needed for the land cover classification process. Composite bands are useful in differentiating land cover based on the reflection of different materials. Useful band combinations in Landsat include bands 432 for vegetation, bands 543 and bands 754 for built-up areas. Seven bands at 30 meter resolution in Landsat 5 TM were combined to create a composite image. Landsat 7 TM bands 1 to 7 at 30 meters were used to create a composite image, while band 8, which is a panchromatic band at 15 meter spatial resolution, was used to pan-sharpen the composite band when identifying training sites. Landsat 8 OLI/ TIRS bands 1 to 7 and band 10 at 30 meter resolution were used to create a composite

image. Panchromatic band (band 8), cirrus band (band 9) and thermal band (band 11) were not used due to the higher resolution of band 8, identification of cirrus clouds in band 9 and the overexposure of band 11 thermal sensor. However, band 8 was used in pan-sharpening.

Indices such as NDVI were created by carrying out band ratios for easy identification of certain features during analysis over the study area. Normalized differenced vegetation index (NDVI) analyses the photosynthetic activity of vegetation thus indicating vegetation vitality. NDVI is a dimensionless variable, with variables ranging from -1, which indicate no vegetation to +1 indication dense and healthy vegetation (Cottbus, 2013). The range of actual values is about 0.1 for bare soils to 0.9 for dense, healthy vegetation. Healthy vegetation reflects highly in near infra-red (NIR). For Landsat 5 TM and 7 ETM+, bands 4 and band 3 are used to calculate NDVI while in Landsat 8 OLI/TIRS bands 5 and band 4 are used.

B. ASTER

ASTER satellite imagery and datasets downloaded in WGS 84 zone 37 South coordinate system were:

a) 18th February 2005 having VNIR bands, SWIR bands and thermal bands
b) 25th January 2011 having VNIR bands and thermal bands

ASTER datasets are in the form of header files (.hdr) and image datasets were viewed in ENVI 5.1. Composite imagery, comprising of VNIR bands 123N, similar to Landsat 7 ETM+ band 234 were directly exported into an ArcMap window and the image file saved as .tiff image.

C. Sentinel

Sentinel-2A dataset for composite imagery was created using blue (band 2), green (band 3), red (band 4) and infrared bands (band 8) at UTM WGS84 zone 37 south coordinate system. Sentinel sensors do not have a thermal camera, therefore it is used for land cover and land use analysis. Sentinel dataset downloaded for 8th February 2017 was processed to determine land cover (Appendix 2).

D. MODIS

Averaged 8-day per-pixel MODIS surface temperature and emissivity data-sets were downloaded for afternoon at 1:30 pm and night at 10:30 pm. Afternoon imagery, acquired using Aqua satellite, was downloaded from the period 18th February 2005, 25th January 2011 and 10th February 2017 while night-time imagery, acquired using Terra satellite, was downloaded from the period 26th February 2000, 18th February 2005, 25th January 2011 and 10th February 2017. LST data-sets are ready for use and do not need further processing (Appendix 4).

3.4.3 Land Cover Classification

The satellite imagery were all in UTM WGS84 zone 37 N/S while the local coordinate system over the study area is UTM Arc 1960 zone 37 South. A polygon area of interest (AOI) defined using the Landsat was used to crop all the composite satellite imagery created for Landsat, ASTER and Sentinel, then projected into the local coordinate system of Upper Hill. Land cover classes were identified based on Food and Agricultural Organization (FAO) land cover classification system (LCCS). Five land cover classes were identified: (1) built-up, (2) forest, (3) sparse grassland, (4) water and (5) open grassland. The term sparse refers to a land cover that has 1 to 4% cover while open refers to a land cover that has 4 to 20% cover over an area (Di

Gregorio & Jansen, 1998). In respect to Upper Hill, the land cover that is described by these two terms is grassland, referred to as forbes in the FAO land cover classification system. Forests in urban areas as defined by FAO (2018) refers to all woodlands, trees that are in groups or individual that form a network or system.

Training sites were digitized using on-screen digitization over areas identified as having pure pixels on the colour composite imagery. Indices such as NDVI, NDBI were also used in identifying pure land cover pixels within the study area. Mean NDVI values were obtained from the statistics filed in the raster image properties in ArcMap. Class breaks for NDVI were created to ease identification of features. Generally, water has indice values of between -1 to 0, bare soil/urban area at 0 to 0.2, shrubs/ grassland at 0.2 to 0.5 and dense vegetation at 0.6 to 0.9. These values vary since NDVI indicates the health of vegetation and this is dependent on the season of the year. For Landsat 7 and Landsat 8 satellites, the panchromatic band 8 on both satellites at 15 meter resolution was used to pan sharpen the cropped composite imagery. Pan sharpening is the aspect of using the high resolution of a panchromatic band, which has a higher spatial resolution and assigning the colour information from the other bands of higher resolution. This helps to increase the spatial resolution of the imagery hence, different features can be better distinguished. The number of training sites per land cover class depended on the visibility of the classes on the imagery. A challenge during the classification process was the identification of pure pixels that represent forest and grassland from 2005 to 2017. This was seen in NDVI during classification in later years where the NDVI range of forest pixels reduced.

Land cover classification was carried out in R studio using Random Forests (Appendix 6) as it does not have the problem of over-fitting compared to Support Vector Machines (SVM). R is a

robust programming language which is used for statistical analysis and is increasingly being used in remote sensing data analysis (Lowe & Kulkarni, 2015). Landsat composite and NDVI imagery for each respective year were read and stacked in R studio and a new raster image created. The NDVI image was included in the analysis to provide a variance since it is an indice compared to the reflectance values from the bands. For Sentinel imagery no NDVI imagery was created hence only the composite imagery is used in the analysis.

Training sites created in ArcMap were read in R studio, and the values of the stacked raster corresponding to the vectors extracted and each of the land classes plotted to determine the scatter plot of their spectral values. Any two bands e.g. NIR and red band were chosen to view the scatter plot. This is a visual aid in determining whether there are mixed pixels in the land cover classes digitized. Visual inspection was undertaken using the 2017 orthophoto and scanned aerial photos for 1978 and 2003 as base maps.

A confusion matrix was calculated to determine the level of accuracy of the classes digitized in relation to other classes (Appendix 5). The confusion matrix shows the number of pixels classified in the specified class and those pixels within that class that have similar reflectance as other classes and this is used as an accuracy assessment. Producer accuracy indicates how well classification of reference pixels of the ground is done while user accuracy indicates the probability of classification of a pixel representing the actual class on the ground. Kappa statistics range between -1 and +1 where 0 represents a random agreement between the ground and classified pixels, -1 indicates no agreement and +1 indicates perfect agreement between the ground and classified pixels (Martensson, 2004). Classification results were saved as a .tif image

and imported into ArcMap for further analysis. Challenges encountered during the classification processes was the confusion of pixels between sparse grassland and built-up areas as the spectral signature between the two land covers is similar, creating a challenge in reducing misclassification. The sensor type was another challenge as Landsat 8 has clearer imagery than Landsat 7, which is much clearer than Landsat 5.

3.4.4 Land Cover Change Analysis

The land cover changes between the years was undertaken using the intersection tool in ArcMap. The datasets analyzed were between 1986 and 1995, 1995 and 2000, 2000 and 2005, 2005 and 2011, 2011 and 2017. The results had a salt and pepper effect hence a minimum mapping unit was used whereby datasets smaller than a certain area in hectares (Ha) are eliminated. For Landsat datasets i.e. 1986 and 1995, 1995 and 2000, 2000 and 2005 a minimum mapping unit of 0.09 Ha was used, despite 2005 imagery being ASTER at 15 meter resolution. The larger resolution of February 2000 at 30 meter resolution was used as the basis of eliminating smaller pixels of January 2005 image. For ASTER datasets of between 2005 and 2011, a minimum mapping unit of 0.045 Ha was used. Between 2011 and 2017 i.e. ASTER and Sentinel datasets, a minimum mapping unit of 0.0225 Ha was used. Six major land cover classes were identified as: 1) forest to built-up; 2) open grassland to built-up; 3) sparse grassland to built-up; 4) forest to open grassland; 5) forest to open grassland; 6) No change. The class ‘no change’ are classes that were classified as the same class between the two years, or there was a change in vegetative land cover between the two years due to seasonality such as open to sparse grassland and vice versa.

3.4.5 Land Surface Temperature Analysis

Thermal bands used to calculate the land surface temperature were extracted from Landsat and ASTER satellites. Processing of Landsat and ASTER thermal band was undertaken using ArcMap 10.4 and ENVI 5.1 respectively. Landsat 7 ETM+ sensor had a scan line error on May 2002 therefore analyzing this imagery to obtain LST would result to errors. Therefore none of its datasets were used in both land cover and LST datasets. Equations and processes for calculating land surface temperature for Landsat 5, Landsat 7 ETM+ and Landsat 8 OLI/TIRS was carried out using the spatial modeler in ArcMap 10.4. Method used to calculate the LST in Landsat is referred to as the 'single channel method' where one band is used to determine the value of LST in each pixel (Cristóbal *et al*., 2018).

A. Converting Landsat 5 TM to Landsat 7 ETM+

Landsat 5 TM data for the year January 1986 and January 1995 was converted to Landsat 7 ETM+ equivalent data to compute the top of atmosphere (TOA). The procedure of converting to Landsat 5 TM from Landsat 7 ETM+ is elaborated by Vogelmann *et al*., (2001). Firl & Carter (2011) describes how to compute to Landsat 7 ETM+ from Landsat 5 TM (Equation 3.1):

$$DN7 = (slope_\lambda * DN5) + intercept_\lambda \ldots\ldots\ldots\ldots\ldots\ldots\ldots \text{ Equation 3.1}$$

Where DN7 is the DN data of Landsat 7 ETM+ and DN5 is the DN data of Landsat 5 TM

The intercept and slope are band specific and are inverse of that described by (Vogelmann *et al*., 2001). The thermal band 6 was not recalculated. The values calculated by (Firl & Carter, 2011) are (Table 3.3).

Table 3.3: Intercept and Slope Values for Landsat 5

Band	Intercept	Slope
1	4.21	0.943
2	2.58	1.776
3	2.50	1.538
4	4.80	1.427
5	6.96	0.984
7	5.76	1.304

B. Converting to Top of Atmosphere (TOA) from DN Values

Digital number (DN) spectral information was transformed to reflectance values. Landsat 7 ETM+ and Landsat 8 OLI/TIRS equation for conversion to Top of Atmosphere (TOA) are different (Mwangi *et al*., 2018). Band 6a and band 6b are the two thermal bands in Landsat 7 ETM+, resampled to 30 meters. The low radiance variance of band 6a makes it suitable to use in the analysis compared to band 6b. Equation 3.2 is the conversion to Top of Atmosphere (TOA) radiometric values from DN for all bands Landsat 7 bands (Mwangi *et al*., 2018).

$$L_{\lambda'} = \left(\frac{L_{max} - L_{min}}{Q_{calmax} - Q_{calmin}}\right) * (Q_{cal} - Q_{calmin}) + L_{min} \ldots\ldots\ldots\ldots\ldots \text{ Equation 3.2}$$

Where,

$L_{\lambda'}$ is the spectral radiance

Q_{calmin} in DN is minimum quantized calibrated pixel value

Q_{calmax} in DN is maximum quantized calibrated pixel value

Q_{cal} is pixel DN value

L_{min} is minimum radiance detected by the sensor

L_{max} is maximum radiance detected by the sensor

Landsat 8 is comprised of band 10 and band 11 thermal bands. Band 10 is recommended for quantitative data analysis as stray light contaminates band 11 making it unsuitable (USGS & NASA, 2016). The split window algorithm is a process that uses both bands to calculate the land surface temperature (Mwangi *et al*., 2018). The 16-bit Landsat 8 Level 1 satellite imagery were converted to TOA spectral radiance using scaling factors (USGS & NASA, 2016) available in the metadata as (Equation 3.3):

$$L_{\lambda''} = M_L Q_{cal} + A_L \text{.....Equation 3.3}$$

Where:

$L_{\lambda''}$ Top of Atmosphere (TOA) radiance ($W/(m^2 * sr * \mu m)$)

M_L Multiplicative rescaling factor (RADIANCE_MULT_BAND_m where x is the band number) which is band-specific

Q_{cal} Digital number (DN)

A_L Additive rescaling factor (RADIANCE_ADD_BAND_m where x is the band number) which is band-specific

L_λ (Equation 3.2 & Equation 3.3) is not the true TOA as it does not have the correction of solar elevation angle. Conversion to true TOA is done using solar elevation angles from metadata which is the TOA reflectance values for Landsat 7 (NASA, 2009) (Equation 3.2) and Landsat 8 (USGS & NASA, 2016) (Equation 3.3). This was carried out for all bands except the thermal bands in each satellite (USGS, 2016).

$$R_{TOA_\lambda} = \frac{\pi L_\lambda d^2}{E_{sun\lambda} Sin\theta_{SE}} \text{.....Equation 3.4}$$

Where:

R_{TOA} TOA planetary reflectance for band r and is unitless

π 3.141592654

d Earth_Sun_distance in astronomical units

$E_{sun\lambda}$ Band specific mean solar exoatmospheric irradiance

θ_{SE} Sun elevation angle in degrees from the metadata and converted to radians

Top of atmosphere reflectance for Landsat 8 was similarly calculated using scaling factors (USGS & NASA, 2016) available in the metadata as (Equation 3.5):

$$\rho_{\lambda'} = M'_L Q_{cal} + A'_L \ldots\ldots\ldots\ldots\ldots\ldots\ldots\ldots\ldots\ldots\ldots\ldots\ldots\ldots\text{Equation 3.5}$$

Where:

$\rho_{\lambda'}$ Top of Atmosphere (TOA) reflectance and is unitless

M_L Multiplicative rescaling factor (REFLECTANCE_MULT_BAND_m where x is the band number) which is band-specific

Q_{cal} Digital number (DN)

A_L Additive rescaling factor (REFLECTANCE_ADD_BAND_m where x is the band number) which is band-specific

Correction for sun angles for TOA reflectance produces true TOA reflectance (Equation 3.6):

$$\rho\lambda = \frac{\rho\lambda\prime}{Sin\theta} \ldots\ldots\ldots\ldots\ldots\ldots\ldots\ldots\ldots\ldots\ldots\ldots\ldots\ldots\ldots\text{Equation 3.6}$$

Where:

ρ_λ TOA planetary reflectance and is unitless in Landsat 8

$\boldsymbol{\theta}$ Solar elevation angle from the metadata and converted to radians

At-satellite-brightness is the effective temperature that is viewed by a satellite with the assumption of having unity emission and was calculated as (Equation 3.1) for Landsat 7 and Landsat 8 on thermal bands only.

$$T_B = K_2/ln(\frac{K_1}{L_\lambda} + 1) \ldots\ldots\ldots\ldots\ldots\ldots\ldots\ldots\ldots\ldots\ldots\ldots\ldots\ldots\text{Equation 3.7}$$

Where:

T_B At-satellite-brightness temperature in degrees Celsius

K_1 Thermal conversion constant (K1_CONSTANT_BAND_t, where t is band 6a and 10) and is band-specific

K_2 Thermal conversion constant (K2_CONSTANT_BAND_t, where t is band 6a and 10) and is band-specific

L_λ TOA radiance for Landsat 7 or Landsat 8

C. Emissivity

NDVI was calculated (Equation 3.8) using the resulting reflectance values of the red and infra-red bands from equation 3.4 for Landsat 7 and Landsat 8.

$$NDVI = \frac{NIR-R}{NIR+R} \ldots\ldots\ldots\ldots\ldots\ldots\ldots\ldots\ldots\ldots\ldots\ldots\ldots\ldots\text{Equation 3.8}$$

The vegetation portion was calculated as (Equation 3.9):

$$P_v = \left(\frac{NDVI-NDVI_{min}}{NDVI_{max}-NDVI_{min}}\right)^2 \ldots\ldots\ldots\ldots\ldots\ldots\ldots\ldots\ldots\text{Equation 3.9}$$

Where:

P_v vegetation portion

NDVI normalized difference vegetation index

$NDVI_{min}$ minimum NDVI for pure soil

$NDVI_{max}$ maximum NDVI for pure vegetation

where the minimum and maximum NDVI is normally given as 0.2 and 0.5 respectively.

Land surface emissivity (LSE) was computed as (Equation 3.10):

$$LSE = 0.004 * P_v + 0.986 \ldots\ldots\ldots\ldots\ldots\ldots\ldots\ldots\ldots\ldots \text{Equation 3.10}$$

D. Land Surface Temperature

Land surface temperature was computed in degrees Celsius using the at-satellite brightness temperature and the Land Surface Emissivity (Equation 3.11)

$$LST = \left[\frac{T_B}{\left(1+\left(\lambda*\frac{T_B}{\rho}\right)*ln(LSE)\right)}\right] - 273.15 \ldots\ldots\ldots\ldots\ldots\ldots\ldots\ldots\ldots\ldots\ldots \text{Equation 3.11}$$

Where:

LST Land surface temperature

T_B At-satellite brightness temperature

λ Wavelength of emitted radiance (λ=11.5μm)

ρ $h * \frac{c}{\sigma}$ ($1.438*10^{-2}$ m K)

σ Bolzmann's constant ($1.38 * 10^{-23}$ J K^{-1})

h Planck's constant ($6.26 * 10^{-34}$ J s)

c velocity of light ($2.998 * 10^{-8}$ m s^{-1})

Once LST was determined, the study area was cropped using the polygon AOI at UTM WGS84 37 North, and then projected to the local coordinate system.

The ASTER thermal band was processed in ENVI 5.1 using a three step method with all four thermal bands processed together to obtain the LST. In the first step, a radiometric calibration was carried out on all four bands where the radiance was calculated. The second step was where

the thermal atmospheric correction was undertaken with the gain/ offsets information in the header file. The emissivity reference channel method was used to calculate the temperature in Kelvin and the emissivity. This method is different from the emissivity normalization method as it makes the assumption that all pixels in one band have the same emissivity. Using the Planck function, the emissivity values in all images was calculated by using the temperatures calculated using the constant emissivity (HGSI., 2019). The temperature calculated in Kelvin was converted to degrees by subtracting it by 273.15 ^{0}C. The temperature imagery results were not in a format that could be read by ArcMap and were changed to .dat format. The study area was cropped using the polygon AOI and then projected into the local coordinate system. The spatial resolution of ASTER LST is 90 meters and the grids of the composites and thermal bands do not overlap along common lines. Night-time LST for Landsat 8 was processed using the same procedure in ENVI 5.1 and imported into ArcMap and cropped using Upper Hill AOI boundary.

3.4.6 Albedo Calculation

Albedo which is the surface material type of an area was calculated for the years 1986, 2000 and 2017 which is the period buildings were digitized. The formula for calculating data from Landsat TM and ETM+ is the same (Odunuga & Badru, 2015) (Equation 3.12), while Landsat 8 OLI is calculated as equation 3.13. Values range between 0 and 1.

$$A_7 = \frac{0.356\alpha_1+0.130\alpha_3+0.373\alpha_4+0.085\alpha_5+0.072\alpha_7-0.0018}{0.356+0.130+0.373+0.085+0.072} \quad \text{.....Equation 3.12}$$

$$A_8 = \frac{0.116\alpha_2+0.321\alpha_4+0.355\alpha_5-0.027\alpha_6+0.150\alpha_7-0.0037}{0.116+0.321+0.355-0.027+0.150} \quad \text{.....Equation 3. 13}$$

Where:

A_7 and A_8 are the calculated Surface Albedo values of Landsat 7 and 8

α_x are TOA reflectance values for bands *x* as specified (Equation 3.2 to Equation 3.3).

The mean albedo for 1986, 1995, 2000, 2005, 2011 and 2017 in the five land covers were averaged and the mean compared to the mean morning LST to determine the relationship between albedo and LST.

3.4.7 Calculation of Contribution Index in Land Cover

To determine the LST of the land cover across the study area, the land cover were split using polygon grids created corresponding to the land surface temperature raster grids. Converting the LST images into point data, a spatial join was done with the polygon grid created for each dataset at 90 meters for Landsat and ASTER thermal data. Though Landsat has a spatial resolution of 30 meters, the grids were created at 90 meters, where the mean of nine pixels at 30 meters were averaged to obtain the LST in one grid cell. Since Sentinel satellite does not have thermal data, Landsat 8 OLI/TIRS for February 2017 at 30 meters was used to determine the LST of the land covers which were at 10 meter spatial resolution.

The split land cover datasets were merged and a spatial join was carried out with the gridded polygon LST data. This was analyzed in R studio to generate box plots that showed the statistical variance of each land cover in each year. Zonal statistics between land cover datasets and LST of corresponding years were analyzed in ArcMap to determine the minimum, maximum, mean and range temperature in each land cover for both day and night-time data-sets. LST for Landsat and ASTER was used to determine the contribution index of each land cover with the overall mean temperature in Upper Hill (Equation 3.14).

$$CI = S * D_T \ldots\ldots\ldots\ldots\ldots\ldots\ldots\ldots\ldots\ldots\ldots\ldots\ldots\ldots \text{ Equation 3.14}$$

Where: S is the ratio of the area covered by the land cover by the total study area while D_T is the temperature difference between the land cover and the mean temperature in Upper Hill. The contribution index can have positive values indicating that the land cover contributes positively to increasing the temperature over the study area. A negative contribution index shows that the land cover negatively contributes to LST and therefore lowers the temperature over a land surface.

Changes in LST in the land-cover change data-sets between consecutive years was done by subtracting the LST raster datasets for each period in study using the raster calculator tool. These were then spatially joined with the land cover change data set and zonal statistics done to calculate the average LST change in each of the changed land cover. These were then exported into excel.

3.5 Generation of Topology and Urban Morphology Datasets

3.5.1 Stereo-Aerial Photogrammetry

Stereo-aerial imagery was acquired for two different years: 1978 and 2017. Five aerial imageries at 1:25000 scale and two stereo-aerial imageries at 1:50000 scale for 1978 were scanned using Epson paper scanner. Forty digital stereo-aerial imageries at 10 cm accuracy for 2017 were acquired that cover the study area and other parts of the city. Georeferencing stereo-aerial images was undertaken using ground control points which were collected using geodetic GPSs, which provide X, Y and Z coordinates. The 1978 image was georeferenced after georeferencing the 2017 image and identifying common points in both images.

3.5.2 Ground Control Points Preparation and Collection

To determine where the GCP points were to be collected and that they are equally distributed within Upper Hill, orthorectification of the 2017 digital stereo-aerial imagery was done using aerial triangulation and generating tie points (Appendix 9). Twelve different locations were identified that comprise of culverts, road junctions and features that were easily identifiable on the image (Appendix 7). Obstacles such as close proximity to trees, tall buildings and high tension wires were avoided. A control point in Survey of Kenya's grid network, located next to Nyayo National Stadium was used to set up the base static GPS throughout the data collection process. Static GPS survey was undertaken with observations at each point done between 10 to 15 minutes (Appendix 10). Geodetic survey equipment used for the data collection was Trimble R8s GNSS receiver as the base and rover and Spectra Precision SP80 GNSS receiver as a rover. Data from the Geodedic GPS's was downloaded in Rinex format and post-processed using Regional Center for Mapping & Regional Development (RCMRD) CORs data for differential correction. RCMRD base station carrier phase data at 30 sec is available from the internet for download and is updated daily. Data was post processed at 10 sec phase and final coordinates presented in table 3.7.

3.5.3 Project Set-up 1978

The analogue aerial photographs were scanned using an Epson scanner at 1600 dpi to be converted into digital images. The camera used to collect the aerial stereo photos was RC30, lens type 15/4 UAG-S. After the model was set for 2017, points were identified in the 1978 image which were identifiable in the 2017 imagery and these points were used as GCPs in the imagery. The camera file name and the coordinates of the fiducial marks of the scanned analogue

photo were entered during the interior orientation process. Measuring the fiducial marks was done in a sequential order based on the camera measuring system as each image has four fiducial marks located on its four corners. The system computes and approximates the location of next fiducial mark as each fiducial mark is measured. A determination of the translation vector is calculated with the first fiducial mark. Using the second fiducial mark, the rotational angle can be computed (Schenk, 2005). After all the fiducial marks were measured, statistical values were computed including residual and standard deviations and transformation parameters.

3.5.4 Project Set-up 2017

The digital aerial imagery was acquired on February 24th 2017 using UltracamX large format Digital Aerial Camera, UCX-SX-1-60911016 by Ramani Geosystems. Setting-up the model involved the following process:

a) Defining the project- The reference horizontal coordinate system during acquisition was UTM WGS 84, Zone 37 South (32E – 42E) while the spheroid and datum was WGS84. The project coordinate system and datum is according to the Kenyan local system, which is UTM Arc 1960 as the coordinate system and Clarke 1880 as the spheroid.

b) Model setup & interior orientation- The reconstruction of objects in digital form in three dimensions is the primary purpose of photogrammetry. It creates a relationship between the object space and the image space. Every image ray in a 3D space can be defined if the camera imaging geometry and the object space imaging location are known (Luhmann *et al*., 2006). The internal geometric camera model is described by the interior orientation parameters. The interior orientation parameters are defined by the perspective center where all image rays pass, the image departures from the ideal image center which are referred to as image distortions and the principal distance (focal length) which is the

distance between the image plane and the perspective center (Luhmann *et al*., 2006). The orientation and spatial position of the camera in the global coordinate system is defined by the exterior orientation parameters. The coordinates of the perspective center in the global system and three rotational angles of the image coordinate system with respect to the global system define the exterior coordinate system (Luhmann *et al*., 2006). The geometric model has to be defined depending on the camera that is used in collecting the imagery. For 1978 model set-up, the camera was defined as frame camera while the 2017 model setup was defined as digital camera (Table 3.4).

c) Block Property Setup- The project was created where the projection was set as UTM zone 37 South, spheroid as Clark 1880 RGS and Datum Arc 1960. Frame specific information was input for the process. The rotation systems for the axes was set as Omega (X axis), Phi (Y axis) and Kappa (Z axis) where the angle units are degrees. The direction of the photo was considered the same as the optical axis of the camera. The flying height used was 1391.136m, which was determined by subtracting the average height of Upper Hill from the average heights of all the photos within the strip. The average height of Upper Hill was derived from studying the contours of toposheets at a scale of 1:2500 that cover the area.

d) Interior orientation files- Due to changes in temperatures and pressure of an airborne camera, some of the interior orientation elements might change (Schenk, 2005). Elements of interior orientation include: 1) calibrated focal length of the camera; 2) image quality measures such as resolution; 3) perspective center position with respect to the fiducial marks; 4) coordinates of the fiducial marks; 5) dis-centering and radial distortion of lens assembly, which also includes the radial distortion origin with respect to the fiducial

system. Interior orientation is carried out so as to establish a relationship between the photo-coordinate system and the measuring system (Schenk, 2005). The measured features are transformed into 3D Cartesian coordinates that have their origin in the perspective center of the camera (Schenk, 1999). The origin of the image coordinate system is the perspective center. Interior orientation involves setting up the parameters of the camera. For the interior parameters used the pixel size was specified and applied for all active frames which refer to all images used for the analysis. Camera information at the point of data acquisition was contained in the calibration report which was part of the data acquired from Ramani Geosystems (Table 3.4).

Table 3.4**:** Summary of Interior Orientation Process of Upper Hill Imagery

Model setup	Frame Camera	1978 stereo- image
	Digital Camera	2017 stereo-image
Block property setup	Projection	UTM Zone 37 South
	Datum	Arc 1960
	Spheroid	Clarke 1880 RGS
	Rotation System	Omega, Phi, Kappa

This contained the interior orientation parameters that were important in setting up the block file which included the focal length of the camera, principal point of collimation and the radial lens distortion. Images were then loaded into the block setup and pyramid files computed. These enabled the software to load and read the files easily as they were compressed.

e) Exterior orientation files- This defines the relationship between the image space and the object space, where the camera position is determined in the object coordinate system

(Schenk, 2005). Full control points are points whose three coordinates are known. Planimetric control points are those whose X and Y coordinates are only known. An elevation control point is one where the Z coordinates is only known (Schenk, 2005). The exterior orientation parameters for each stereo-image were imported as ASCII format (Appendix 11). The exterior orientation files were given by the vendor together with the image files and camera information. Exterior orientation defines the relationship between the image and object space and the orientation and position associated with an image is defined. It consists of six variables i.e. X_0, Y_0, Z_0 that define the perspective center of the camera and Omega (ω), Phi(ϕ), and Kappa (Ķ) which define the rotation of the perspective center (Table 3.5).

Table 3.5: Summary of Interior and Exterior Orientation Parameters of Cameras

Orientation	**Particulars**	**Values**
Interior	Focal length	100.4470 mm
	Pixel size	7.2 µm
	Principal point of	X: -0.0290 mm
	autocollimation (PPA)	Y: 0.1330 mm
	Lens distortion	Less than 0.002mm
	Average flying height	1476 m
Exterior	GNSS position (m)	X: 0.1000
		Y: 0.1000
		Z:: 0.1500
	IMU rotations (deg)	Omega: 0.00800
		Phi: 0.00800
		Kappa: 0.01600

Once the model was set, ground control points that were collected on the ground needed to be entered into the image to ensure that the image space and object space corresponded. Automatic tie point measurement was undertaken and auto-triangulation was performed on the images. The process of using a DSM to generate an orthophoto as approximate locations and coordinates was needed to identify the identified points on the ground.

f) Image matching- This has also been defined as correlation or automatic stereo matching (Schenk, 1999). There are three main methods used in image matching as shown in table 3.6. When working with multiple stereo-imagery, it is important to match adjacent imagery when undertaking aerial triangulation. When using high resolution stereo imagery, image matching accuracy is a limitation when automatically generating a DSM. When automatically generating a DSM from high resolution stereo imagery, image matching accuracy is a limitation brought about by the matching algorithm used. The algorithm produces height models from conjugate points identified in stereo pairs (Alobeid, 2011).

Table 3.6**:** Relationship between Matching Methods and Entities

Matching Method	**Similarity Measure**	**Matching Entities**
Area-based	Correlation, least-squares	Gray levels
Feature-based	Cost function	Edges, regions
Symbolic	Cost function	Symbolic description

(Source: Schenk, 1999)

g) Bundle-block adjustment- A 3D bundle-block adjustment can be used to process all images together as it uses tie-points which help reduce the number of GCPs to be used for the entire block (Eckert, 2008). The theoretical minimum that is recommended is twice the image resolution. In determining suitable locations for collecting GCPs within the stereo-image,

location along the edges will avoid extrapolation in geometry and they should also cover the full elevation range of the terrain (Eckert, 2008). Despite having an image that covers an area wider than the study area, GCPs should cover the full image size. Two types of GCPs can be used: tie points with unknown cartographic coordinates and full control GPCs with known XYZ coordinates. Tie points are important because they help in improving the stereo-geometry by filling in the gaps where there are no XYZ GCP points that were collected (Eckert, 2008).

h) GCP point input- This processes were carried out using ORIMA which is a robust interactive setup for bundle adjustment.

Table 3.7: Ground Coordinate Points Collected in Upper Hill and Environs

ID	Easting	Northing	Height	Type
GCP_1	255596.934	9856744.867	1731.295	GCP
GCP_2	254019.554	9857295.422	1754.223	GCP
GCP_3	256714.145	9858699.791	1671.642	GCP
GCP_4	255368.774	9855203.219	1712.703	GCP
GCP_6	257655.073	9855187.222	1655.644	GCP
GCP_8	258504.009	9856178.674	1652.597	GCP
GCP_10	256205.567	9856165.566	1721.129	GCP
GCP_11	257413.816	9856568.528	1685.805	GCP
GCP_12A	256764.481	9857785.006	1671.763	GCP
GCP_12B	256764.555	9857784.954	1671.641	GCP
GCP_13	254979.801	9857971.062	1734.980	GCP
GCP_14	254465.493	9856563.465	1754.623	GCP
V6	257722.890	9856148.250	1661.840	Base
RCMN	265499.483	9865267.660	1607.244	Base

The images were setup and the points where the GCP points were collected were selected and GCP coordinates entered (Table 3.7). Ten points were entered using the stereo measurement tool. Automatic tie-point measurement was done and an error report generated. This was used to adjust the location of each of the points to reduce the RMSE error which should be less than one pixel.

i) Digital Surface Model (DSM) - A digital elevation model (DEM) is a representation of the bare ground. LPS enhanced Automatic Terrain Extraction (eATE) was used to generate the DSM of all imagery, both analogue and digital stereo aerial imagery. For the analogue stereo-imagery, the output for the model was a raster while for the digital stereo-imagery a dense point cloud was produced. The set-up for obtaining the point-cloud layer was done in the eATE manager while for scanned aerial imagery was done using classic ATE. The output settings were used as ‘default’ while the file directory was ‘defined’. The classification was set to ‘all’ where a DSM would be generated. The setup detected the minimum and maximum height of the model. If set too high or too low it results to outliers and problems occur in the dataset. The scale of the output was defined in the strategy manager. To edit the DSM, the point cloud was reclassified and also colour coded for easy identification of points, with red areas indicating high elevation and blue areas indicating lower altitude areas.

Generation of an orthophoto was carried out using the Mosaic Pro tool in ERDAS Imagine. The seam lines were adjusted to ensure that there would be a smooth transition between the overlapping imagery.

3.5.5 Digital Elevation Model Generation and Accuracy Assessment

The best resolution of a DEM is three times the resolution of the stereo-image resolution. The DEM for 1998 and 2017 was generated from the stereo- aerial imagery in ArcMap 10.4. A TIN was first created using the data from the GCP and the tie points generated during the orientation process. A DEM was generated at 5 meter resolution and later resampled to 2 meter resolution due to the size of building footprints in the study area. Contour data was extracted from the 1998 topological data set. These contours were at 2 meter interval and were edited where contour lines crossed each other or were isolated and incomplete without particular adjacent lines connected to it. The resolution for determining the DEM to be generated was based on the contour interval as well as the mapping resolution. The 2 meter DEM was generated in ERDAS Imagine, from the edited contour dataset. The DEM accuracy shows how accurately the generated DEM represents the ground truth (Guo *et al*., 2001). A value that is calculated to determine DEM accuracy is the root mean square error (RMSE) as shown in equation 3.15.

$$RMSE = \sqrt{\frac{\sum_{j=1}^{z}(Q_j - P_j)^2}{z}} \quad \text{Equation 3.15}$$

Where Q_j is the DEM cell value at j and P_j is the corresponding sample point elevation at j, z is the number of sample points.

Accuracy assessment of the DEM generated in each of the years was undertaken before building height extraction. The reference points used were those collected in the field on October 2017 (Table 3.8). Verification was carried out for DEMs generated in 1978 and 2017 from photogrammetric processes and 1998 DEM generated from contours. An RMSE of 1.453, 0.910

and 0.685 meters was obtained for the years 1978, 1998 and 2017 respectively. The RMSE result was less than the resolution of the DEM, hence they were acceptable for further analysis. Aspect was created from 30 meter DEM for each year i.e. 1978, 1998 and 2017.

Table 3.8: Accuracy of 1978, 1998 and 2017 DEM in Upper Hill, Nairobi

	Elevation (m)			GCP
Point No.	**Yr. 1978**	**Yr. 1998**	**Yr. 2017**	**Yr. 2017**
GCP_1	1728.607	1731.253	1731.075	1731.295
GCP_10	1720.718	1721.437	1720.741	1721.129
GCP_11	1684.781	1684.517	1684.929	1685.805
GCP_12	1671.832	1670.228	1671.748	1671.763
V2	-	1662.000	1663.015	1661.840
RMSE	**1.453**	**0.910**	**0.685**	**-**

3.5.6 Editing of Buildings and Roads

In each of the datasets, a visual inspection was carried out of the footprints of buildings to ensure that they were well digitized. The 2017 orthophoto was used as a background image to determine whether the buildings which were existing in 1978 and 1998 were digitized correctly. The digitized 2017 building polygons were used to compare the digitized buildings of 1978 and 1998. Building parts that were within other buildings and needed to be excluded were edited. Road center line data was acquired for the whole Upper Hill region, which had road width information. Only main roads within the study area were analyzed for each of the years but roads that led into or were located within an organization's boundary were not included as they had not been constructed by Kenya Urban Roads Authority (KURA). Therefore, specifics on the width and roads type and thickness could not be verified from KURA as the main roads in this projects were those that are constructed and supervised by KURA. In each of the years, digitized road

edges were used to verify and determine road widths as some roads had undergone reconstruction and widening from the year 1978 to 2017 (Figure 3.6).

Road edges were obtained for each of the years from the digitized shape files. The digitized road center lines and road edges of major roads in 1978, 1988 and 2017 did not overlap due to changes in road width with time and shifts during generation of the block files. Digitized roads that led into plot boundaries were not included into the final road file that would be used for analysis. Roads that converged at round-abouts were edited to ensure uniformity in all years for purposes of analysis. Over-shoots and under-shoots were eliminated. Road buffers were generated for all roads in the three years using the center line. The buffer was created on both sides of the center line so that it coincided with the digitized road edges.

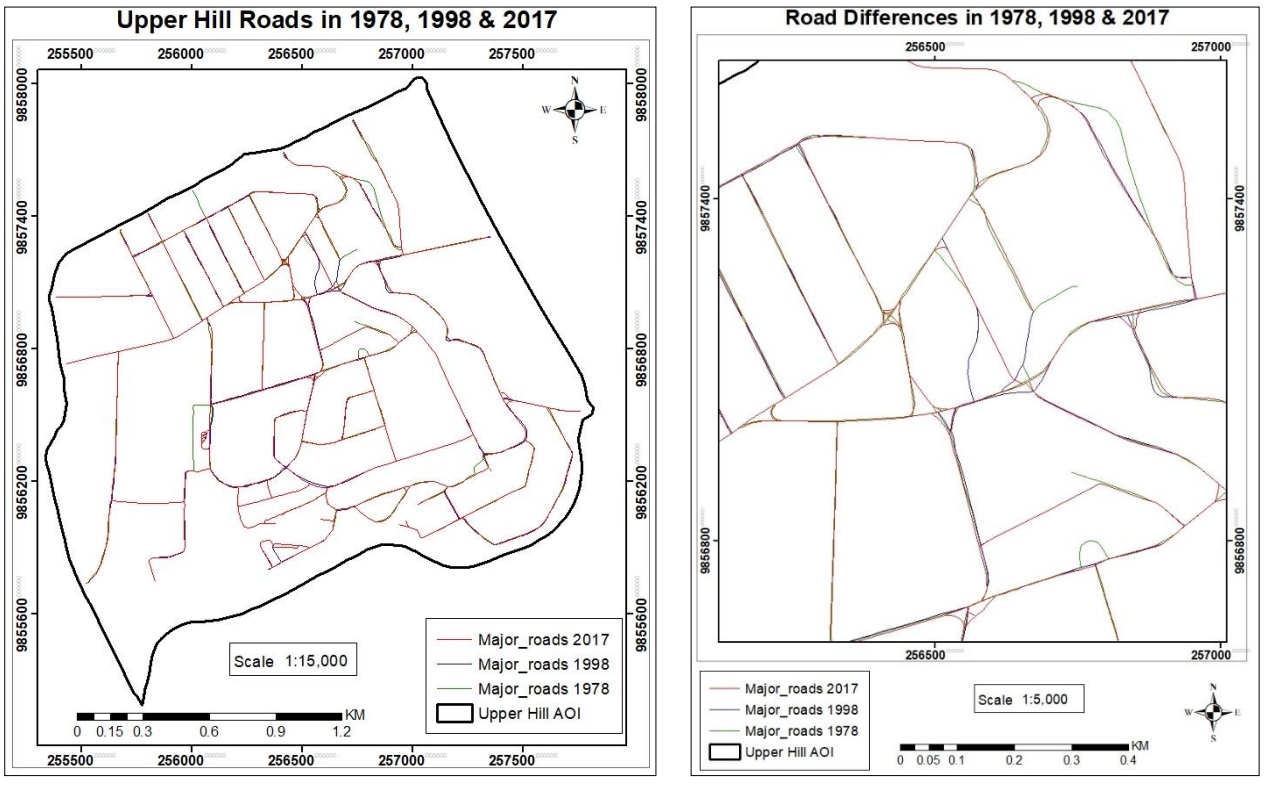

(a) **(b)**

Figure 3.6: Road Center Lines (a) and Edge Lines (b) in Upper Hill, Nairobi

3.5.7 Generation of Building Heights and Accuracy Assessment

The 2 meter raster DEMs for 1978, 1998 and 2017 were converted to point shape format. Using the spatial intersecting tool and a radius of 1 meter, DEM points that intersected the buildings and those that were within a distance of 1 meter from the building's edge were selected. The spatial join tool was used to assign one height value to each building. With this tool, all intersecting DEM point values were averaged and a single elevation value was assigned to each building. Using this method, area based point averaging was used to determine the height of buildings because buildings are surfaces and not point features. Therefore instead of using a single point such as the building's centroid to determine the height of the building, several points intersecting the buildings were selected.

On subtracting the DEM from the building polygon layer that has the building elevation above sea level, RMSE values were calculated in each of the years to derive the accuracy of buildings. The value obtained was used to correct all building heights within Upper Hill. Verification of building height accuracy was obtained from Emporis (2018) which is a database of buildings contained in cities around the world (Table 3.9). Only three buildings whose data is available from the internet were used to verify the 1998 dataset as shown in table 3.9 and these buildings were also observable in 2017 for analysis. To calculate the RMSE for 1998 buildings, the 2017 building heights were obtained using the 1998 DEM to determine the error of digitization of buildings observed in both images. For 1998 building dataset, three sets of buildings were used: three buildings with known height and were observed in 2017 image; three buildings observed in 1998 and in 2017 but actual heights not known; three buildings observed in 2017, but not 1998 and actual heights are known (Table 3.9). Mean height obtained was 1.12 meters. The mean

height of 1 meter was added to all buildings within the study area so that no building has negative values. Mean height calculation was carried out for 2017 using known building heights (Table 3.9).

Table 3.9: Mean Height Accuracy Assessment for 1998 Buildings in Upper Hill, Nairobi

Building Name	**AGH (m) (Emporis, 2018)**	**Measured Height (m)**		**Height Differences (m)**		
		1998	**2017**	**1998-AGH**	**1998-2017**	**2017-AGH**
Social security House	103.0	103.32	96.80	0.32	+6.52	-6.20
Ministry of Transport	42.67	26.06	35.70	-16.61	-9.64	-6.97
Chancery Building	40.71	26.18	33.19	-14.53	-7.00	-7.52
Milimani Court House	N/A	18.81	20.89	-	-2.08	-
Maji House	N/A	23.31	26.17	-	-2.86	-
Nairobi Club	N/A	3.02	2.25	-	+0.76	-
CTDL	67.84	N/A	59.81	-	-	-8.03
Flamingo towers	47.49	N/A	47.87	-	-	+0.38
KCB plaza	99.00	N/A	126.56	-	-	+27.56
SUM					**-14.30**	**-0.78**

AGH Actual Ground Height N/A Not Available

Mean building height in 2017 was 0.007292. However there were buildings with negative values. Therefore a height of 1 meter was added to all buildings within the study area (Table 3.10). This was done for the 1978 buildings where a value of 1 meter was added to all buildings. Scanned stereo-aerial photos used to derive the building footprints aided in verifying that buildings having negative values were not under construction and the negative results were due to human error.

Building heights are classified into three groups namely: low-rise, middle-rise and high-rise buildings (Table 3.11) as per the Kenyan building codes (RoK, 2009).

Table 3.10: Mean Height Accuracy Assessment for 2017 Buildings in Upper Hill, Nairobi

Building	**Actual Height(m) (Emporis, 2018)**	**No. of floors**	**2017_Height**	**Difference**
Chancery Building	40.71	12	33.698663	-7.011337
CTDLT Towers	67.84	20	57.476347	-10.363653
Flamingo Towers	47.49	14	47.895832	0.405832
Kasneb Towers II	47.49	14	44.870168	-2.619832
KCB Plaza	99	23	126.607844	27.607844
Landmark Plaza	47.49	14	51.464845	3.974845
Ministry of Transport	42.67	14	35.099649	-7.570351
Nachu Plaza	50.88	15	54.169979	3.289979
Rahimtulla Tower	61.06	18	84.589924	23.529924
Social Security House	102.72	28	94.691726	-8.028274
Taj Towers	44.1	13	46.065313	1.965313
Victoria Towers	40.71	12	15.617214	-25.092786
Zep-Re Place	40.71	12	40.38637	-0.32363
SUM				**-0.236126**

This harmonizes building morphology attributes as discrepancies are noted in the ordinance between different parts of the city.

Table 3.11: Classification of Building Heights in Kenya

Name	**Height**	**Floors**
Low-rise	$\leq$ 10 meters	3
Middle-rise	$10 > h \leq 30$ meters	3 to 10
High-rise	$>$ 30 meters	$>$ 10

(Source: (RoK, 2009)

Low-rise buildings refer to buildings whose uppermost storey floor does not exceed 10 m above the point of staircase discharge at the ground floor level. High-rise buildings are those whose uppermost storey or floor exceeds 30 m above the point of staircase discharge at the ground floor level. Middle-rise buildings are those whose height exceeds 10 m but not greater than 30 m. The height of each floor, measured from the floor to the ceiling, should be at least 2.4 m as this is the minimum height of a room (RoK, 2009). A height of 3 m is used to determine the number of floors, which includes the width of a floor in a storey building and height of the roof. 3D visualization of buildings was carried out using ArcScene 10.7 where buildings were classified as low, middle or high-rise. LoD1 was used to reconstruct the buildings to have flat roofs with no texture on the wall or roof.

3.5.8 Splitting of Buildings and Roads

Grids of 30 meter, 60 meter and 90 meter spatial resolution were created using the create grid feature, where grid lines were defined by the Landsat imagery grids. This ensured that building datasets and satellite derived results were stacked within a common spatial extent. In order to analyze the data sets within each of the grid polygons, the building and road data were split along the grid lines in 30 meter, 60 meter and 90 meter grid resolution. Roads were analyzed as polygons where the road center line created buffers of equal dimension as road widths. Different parts of a building could be in two or more parts of a grid. Using the merge tool, the split buildings and roads were merged together without any loss of any shape or area of each of the features.

3.5.9 Development of Built-up Volumes and Ground Coverage Ratio

New areas and volumes of buildings were calculated but the height did not change on each building during the splitting process. The road buffer was split into each of the grids and areas in each grid were calculated. Volume of roads was calculated by multiplying the area by the thickness, which was determined as 0.3 meters. This comprises: 100mm as the sub-base layer; 150mm for the base layer; and 50mm as the asphalt-concrete (A/C) layer. Thickness of 0.3 meters is the minimum value of road thickness.

A spatial join was done between the building dataset and the grid, where the areas and volumes were summed up in each grid. The data output is in grid format and not the same polygon feature of each building. Within each grid, the weighted average height of buildings was calculated as (Equation 3.16):

$$h_{w,g} = \frac{\sum_{i=1}^{m} A_i h_i}{\sum_{i=1}^{m} A_i} \quad \text{.....Equation 3.16}$$

Where:

A_i is the area of building i

h_i is the height of building i

m is the total number of buildings in the grid

$h_{w,g}$ is the average weighted height of all buildings in each grid g

The volume of each building was calculated and totaled in each grid after splitting along the grid line (Equation 3.17).

$$VB_g = \sum_{i=1}^{m} A_i h_i \quad \text{.....Equation 3.17}$$

Where:

VB_g is the total volume of buildings in a grid g

A_i is the area of building i

h_i is the height of building i

m is the total number of buildings in the grid

Volume of roads was calculated by obtaining the area of the split road in each grid and the width of the impervious surfaces using the recommended standard minimum thickness of a road (Equation 3.18).

$$VR_g = \sum_{r=1}^{n} A_r T_r \quad \text{.....Equation 3.18}$$

Where:

VR_g is the total volume of roads in a grid g

A_r is the area of the road r

T_r is the thickness of the road r

n is the total number of roads in the grid

The building and road data were merged into one dataset using a spatial join where the total area and volume was calculated in each grid cell for 1978, 1998 and 2017 datasets. The built-up volume density in each grid was calculated by dividing the built-up volume in each grid cell by the area of the total area by the grid area of 30m * 30m, 60m * 60m and 90m * 90m (Equation 3.19).

$$BVD_g = \frac{VB_g + VR_g}{A_g} \quad \text{.....Equation 3.19}$$

Where:

BVD_g is the built-up volume density of buildings and roads within a grid g

A_g is the area of the grid cell g

The rate of 3D built-up intensity expansion (Longyu *et al*., 2009) in the area of study within a time period T was calculated as equation 3.20:

$$ULI_g = \frac{BV_{v,t+s} - BV_{v,t}}{A_g} * \frac{1}{T} * 100\% \ldots\ldots\ldots\ldots\ldots\ldots\ldots\ldots\ldots\ldots\ldots\ldots\ldots\ldots\ldots\ldots \text{ Equation 3.20}$$

Where:

ULI_g is the intensity of urban expansion at grid g

$BV_{v,t+s}$ is the built-up volume in time $t+s$

$BV_{v,t}$ is the built-up volume in time t

A_g is the area of grid g

T is time period between the years

BVD and GCR was determined by dividing the total volume, which was the sum of road and building volumes, and the total area, which was the sum of buildings and roads, by the size of each grid cell area of 900 m^2, 3600 m^2 and 8100 m^2. The units of the resulting calculation is in m^3/m^2 for built-up volume densities and unitless for ground coverage ratio. The relationship between BVD and floor area ratio (FAR) was determined as equation 3.21:

$$x * FAR = BVD \ldots\ldots\ldots\ldots\ldots\ldots\ldots\ldots\ldots\ldots\ldots\ldots\ldots\ldots \text{ Equation 3.21}$$

Where x is the height of the floor, BVD is the building volume density and FAR is the floor area ratio

GCR, FAR and BVD were classified into three groups, low, medium and high density and were derived from the Nairobi Ordinance guiding principles (NCC, 2006). The height of the floor is

taken as 3 m therefore, BVD is three times greater than FAR. Plot ratio (PR) is the term used in the Nairobi Ordinance which is synonymous with FAR, hence these values are used to determine BVD ratios (Table 3.12).

Table 3.12: Classification of GCR, FAR and BVD in Kenya

Ratio	**Low density (%)**	**Medium density (%)**	**High density (%)**
GCR	$0 > GCR \leq 25$	$25 > GCR \leq 60$	> 60
FAR	$0 > FAR \leq 75$	$75 > FAR \leq 200$	> 200
BVD	$0 > BVD \leq 225$	$225 > BVD \leq 600$	> 600

(Source: Author, 2019)

The term 'high' or 'low' density is relative as it differs between communities and countries (Sokido, 2016).

3.6 Spatial Modelling between Built-up Morphology and Land Surface Temperature

Hotspot analysis was undertaken on LST datasets at 90 meters grid for 1978, 1998 and 2017 to determine areas where clustering of low values or high values are located in Upper Hill. It shows areas of spatial association with the lowest and highest temperatures and the confidence levels of the probability of this occurrence. Statistically significant z-score values are obtained when the differences between the local sum of a feature and its neighbours and the expected local sum are different and not a result of random chance. Z-score and p-values are used to determine whether to reject the null hypothesis (Ord & Getis, 2010). Areas that are statistically significant and are considered hot spots have high values and are surrounded by high values. A cold spot means that the incidence of the spatial unit under analysis is low, while a hot spot regions is the opposite.This method identifies statistically significant clustering using Getis-Ord Gi* statistic.

This statistic produces both p and z-scores, where a high or low z-score indicates high or low spatial clustering. Hot spots occur in areas where a feature had a high z-score and a small p-value, while a cold spot indicates areas with low negative z-scores and small p-values. Areas that do not have any spatial clustering have a z-score of near zero value (CEHI, 2018). The Getis-Ord local statistic equation is indicated as equation 3.22 to 3.24:

$$G_i^* = \frac{\sum_{j=1}^{n} w_{ij}x_{j-} \bar{X} \sum_{j=1}^{n} w_{ij}}{s\sqrt{\frac{[n\sum_{j=1}^{n} w_{ij}^2 - (\sum_{j=1}^{n} w_{ij})^2]}{n-1}}} \quad \text{Equation 3.22}$$

Where x_j is the attribute value for feature j, w_{ij} is the spatial weight between feature i and j, n is equal to the total number of features and:

$$\bar{X} = \frac{\sum_{j=1}^{n} x_j}{n} \quad \text{Equation 3.23}$$

$$S = \sqrt{\frac{\sum_{j=1}^{n} x_j^2}{n} - (\bar{X})^2} \quad \text{Equation 3.24}$$

The output of the results indicate confidence level bi (Gi_Bin) for each feature, together with p-values and z-scores for each feature class (Ord & Getis, 2010).

Data modelling was undertaken using two methods i.e. OLS and GWR in ArcMap. Datasets that used were in the 30 meter and 90 meter grid for comparison. Datasets used in spatial modelling were NDVI (unitless), albedo (unitless), aspect (degrees), BVD (m^3/m^2), GCR (unitless) and height (m), each used as explanatory variables to determine how each varied with land surface temperature (^{0}C). Model assumption was that land cover did not change significantly from 1978 to 1986 and therefore built-up datasets 1978 could be analyzed together with 1986 datatsets.

Aspect was transformed into eastness (Equation 3.21) to mitigate the circular property of the data by transforming the angles into rectangular polar coordinates (Tian *et al*., 2012; Marr, 2014).

$$E_\theta = sin(rad_\theta) \quad \text{Equation 3.25}$$

Where: $E_{\boldsymbol{\theta}}$ is Eastness

$rad_{\boldsymbol{\theta}}$ is the angle in radians where $\boldsymbol{\pi}=180^0$

$\boldsymbol{\theta}$ is the angle in degrees

Values range between -1 and 1, with '-1' designated to the west and '+1' designated to the east. NDVI was used as a proxy to land cover as it varies from -1 to 1, with -1 indicative of water and 1 indicative of vegetation. OLS was used to determine how well each of the explanatory variables modeled with land surface temperature fit. GWR was carried out on each of the datasets to determine the spatial variation of each explanatory variable with land surface temperature in both 30 meter and 90 meter grids. In the GWR dialogue box, the kernel type chosen was "fixed" as the dataset consists of regular gridded data and the bandwidth method chosen is "Akaike Information Criterion (AICc)", which identifies an optimal fixed distance for the model. The bandwidth method normally determines the degree of smoothing of the model (Esri, 2016). Other parameters were left as default. More than one explanatory variable was used to model the relationship with land surface temperature. For this to be done, feature scaling was undertaken to have all LST, NDVI, albedo, aspect, BVD, GCR and height data in the same comparable units or to standardize the range. This was done using the 'min-max normalization' method which standardized the range from 0 to 1 for all datasets (Equation 3.22).

$$Y' = \frac{Y - Y_{min}}{Y_{max} - Y_{min}} \quad \text{Equation 3.26}$$

Where Y' is the normalized value, Y is the original value, Y_{min} is the minimum value, Y_{max} is the maximum value.

Before modelling any variable in OLS, exploratory regression was done with the scaled data with LST as the dependable variable and NDVI, aspect, BVD, GCR and height selected as explanatory variables. This method determines all possible combinations of explanatory variables with the dependent variable applied before undertaking OLS to determine the best combination of datasets. The OLS and GWR modelling process was undertaken where the results from modelling each variable separately in OLS and GCR was determined as an input and each observed to analyze how each related with LST. A table was generated that provided diagnostic statistics on the accuracy of the models and also the reliability of the data generated. Spatial autocorrelation, which is a method that analyses spatial attribute patterns on the standard residuals, was done for final models for both GWR and OLS to determine whether the residuals showed a scattered, random or clustered pattern in ArcMap. To conceptualize the patterns 'Inverse Distance' was used and distances between neighbouring features was calculated using 'Euclidean Distance'. Moran's Index (Moran's I) is a test of significance statistics that indicates the relationship between the location of spatial objects and the attribute values (Murayama & Rajesh, 2011). Values range between -1 to +1, with -1 having a checkered pattern and indicates a negative spatial autocorrelation, +1 shows perfect clustering of high or low values and 0 showing perfect randomness (Fu *et al*., 2014). Z-score indicates whether the null hypothesis will be accepted, which is the variables are spatially scattered, or rejected.

CHAPTER FOUR: RESULTS AND DISCUSSIONS

This chapter presents results on the influence and relationship of variables that affect land surface temperature using time series data. The variables include land cover, urban morphological features which are building height, ground coverage ratio, built-up density and topological features. The results are based on research objectives which are:

1. To determine the relationship between land cover and land surface temperature changes in time space continuum between 1986 and 2017 in Upper Hill, Nairobi.
2. To evaluate the effects of built-up morphology on land surface temperature between 1986 and 2017 in Upper Hill, Nairobi.
3. To model the spatial relationship between built-up volumes and land surface temperature in Upper Hill, Nairobi.

4.1 Land Surface Temperature vis-à-vis Land Cover Changes in Upper Hill, Nairobi

4.1.1 Mean Rainfall and Mean Air Temperature

The mean rainfall for the months of January and February of Nairobi from Dagoretti Meteorological Station shows that the month of January receives a high amount of rainfall in the years 1993, 1998 and 2001 compared to the month of February (Figure 4.1). In 1993 and 1998 high rainfall is received in the month of February. Little or no rainfall is received for January and February in the years 1997, 2000 and 2012. The month of February receives high amounts of rainfall than in the month of January in 2007, 2011 and 2015. This may be attributed to global change in climate where rainfall patterns have been changing, with the amounts and intensity increasing over the years. February 2000 receives no rainfall while January 2005 receives high rainfall. A comparison is carried out between the mean, minimum and maximum air temperature over Nairobi from the Wilson Meteorological Station (Figure 4.2).

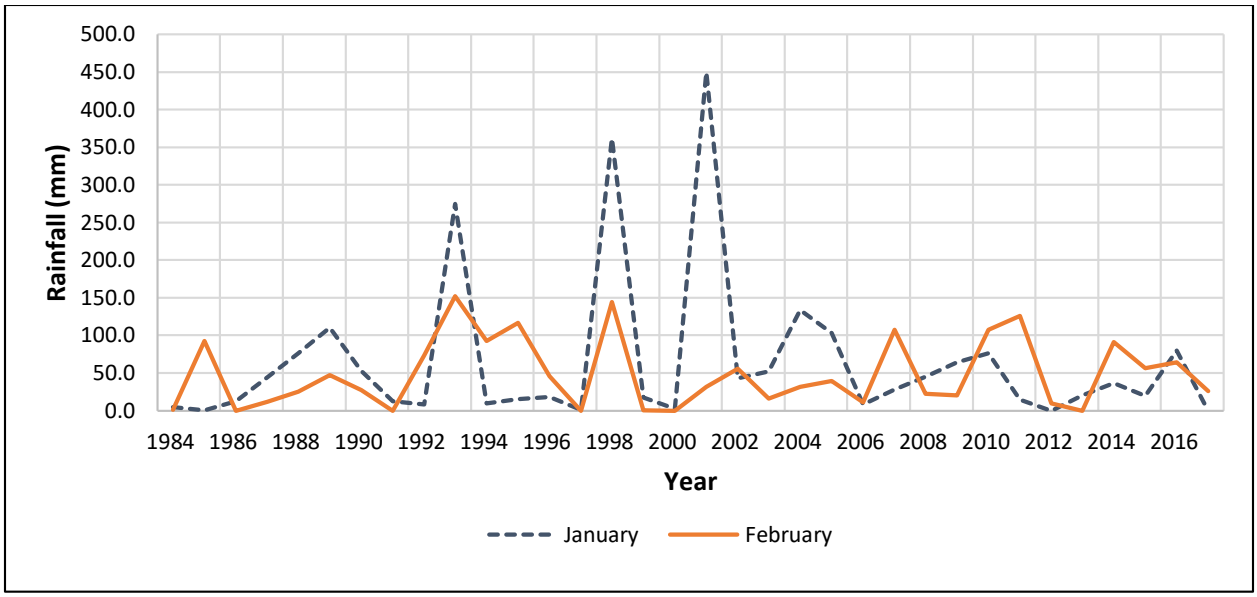

Figure 4.1: Mean Rainfall of January and February from Nairobi Wilson Station

Minimum temperatures within the months of January and February fluctuate with no defined month having the lowest temperature, unlike the maximum temperature where February has high values.

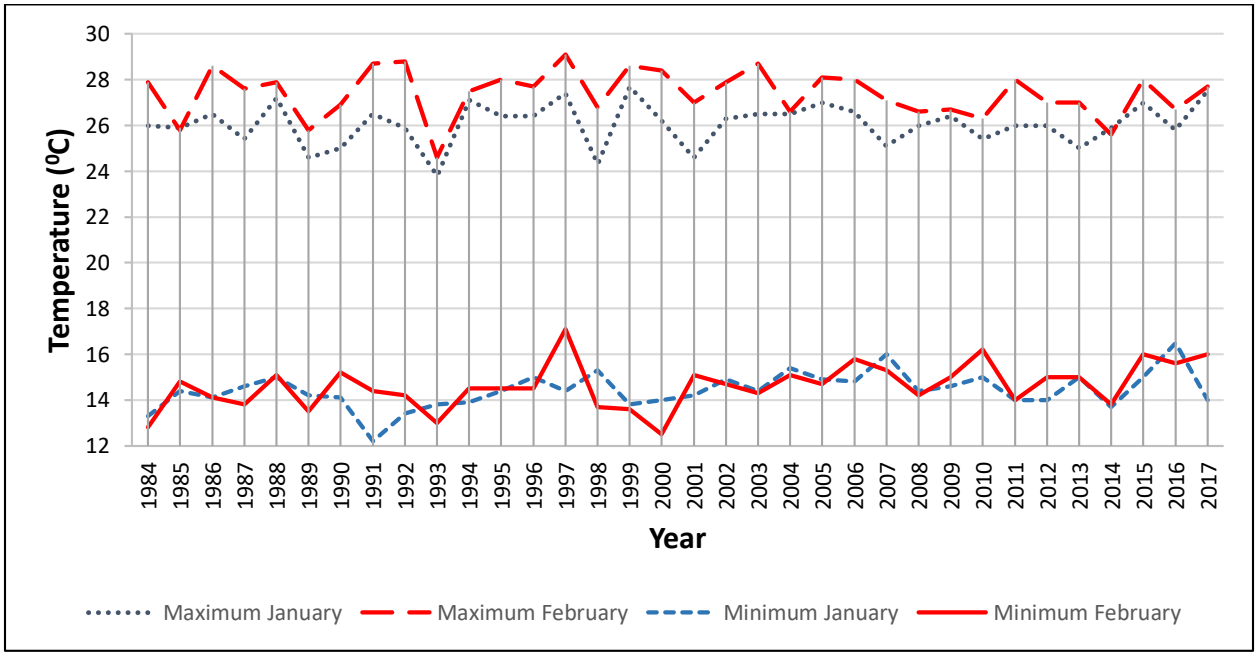

Figure 4.2: Mean Air Temperature from Nairobi Wilson Station

During the years when the remotely sensed data is analyzed, February 2000 has low minimum and high maximum temperature than the other observed years. Temperatures decline in average maximum temperatures from the year 2005 to 2014, with an increase in 2017. The maximum temperature from 1986 to 2017 is not consistent.

The minimum mean temperature in the study area has experienced an increase within the months of January and February. This resonates with Ongoma *et al*., (2013a) findings of annual mean air temperatures in Nairobi from 1975 to 2010 measured at six meteorological stations where the mean minimum temperature increased. The increase in minimum temperature is attributed to global warming and land cover changes such as urbanization that alter evapotranspiration rates. The maximum temperature within the same months does not show any significant increase in temperature, but the fluctuations could be as a result of climatic changes. Changes in land cover tend to affect mean minimum temperatures more than the mean maximum temperature (Ongoma et al., 2013a).

The minimum, maximum and mean land surface temperature analyzed from 1986 to 2017 in the months of January and February indicate that January 2005 has a warmer temperature (Figure 4.3). Morning temperatures recorded at 10:00 am indicate an increase in LST from 1986 to 2017 for both minimum and maximum temperatures. Observed high temperatures between the years 2000 and 2011 may have been related to drought conditions, which claimed millions of lives (Mbogo *et al*., 2015). Drought in the years 1999 to 2000 was the worst Kenya had experienced in 37 years. These dry conditions occurred again in 2005 and 2010 to 2011, which was the worst drought in 60 years (Mbogo *et al*., 2015).

Afternoon temperatures recorded at 1:30 pm indicate a drop in temperatures in 2011 from 2005 but increases in 2017. The observed LST in the morning and afternoon indicates that they follow the same trend with a reduction in average temperature in 2011. Night-time temperatures recorded at 10:30 pm decrease from 2000 to 2017 with an increase in maximum temperature in 2017. Under cloudless skies LST tends to be warmer in the afternoon than in the morning due to links in the solar peak time and the maximum skin temperature (Coops *et al*., 2007). Warming levels have been increasing at 0.3 ^{0}C to 0.7 ^{0}C every 30 years, though the warming rate in 2017 was 0.15 ^{0}C to 0.35 ^{0}C higher than average warming from 1988 to 2017 (Allen *et al*., 2018).

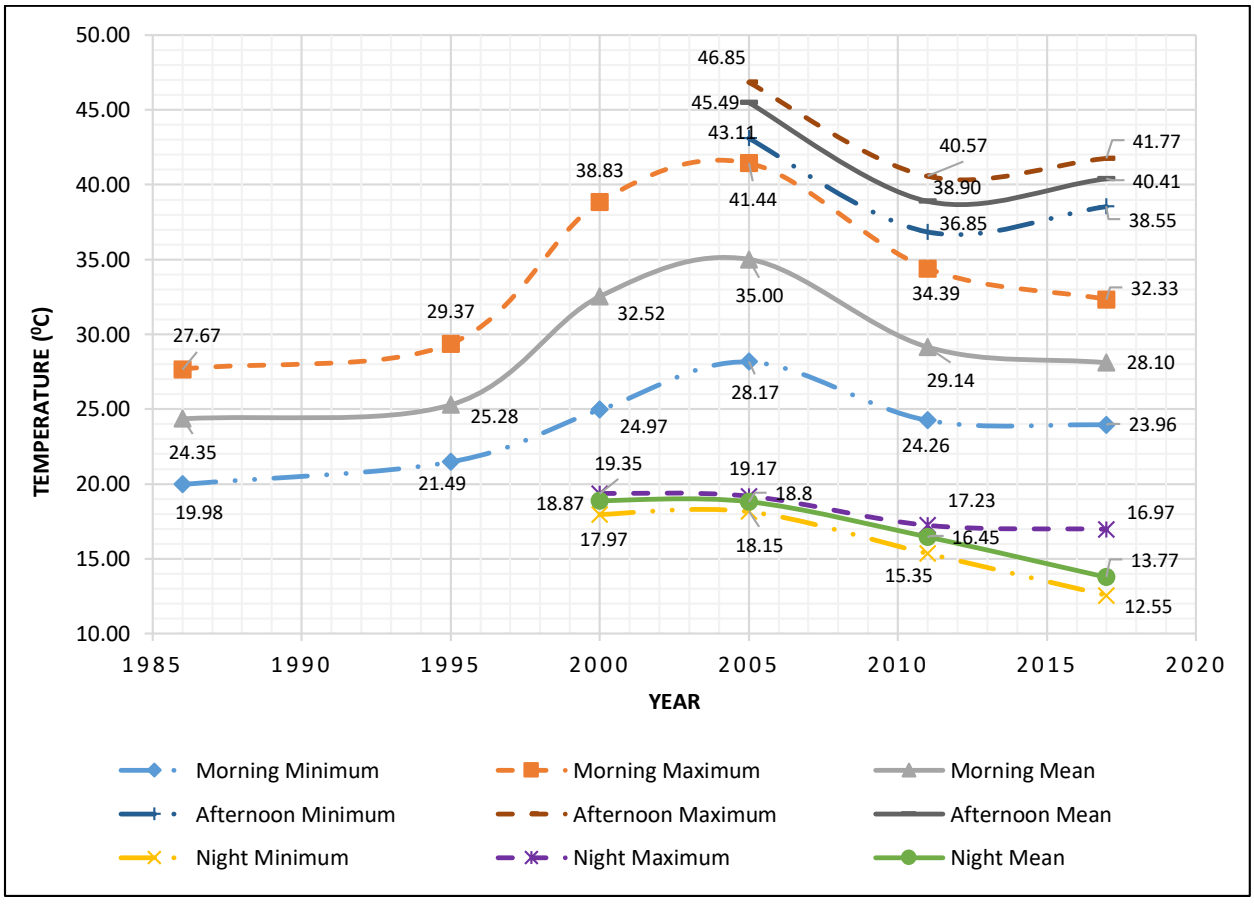

Figure 4.3: Day & Night LST from 1986 to 2017 in Upper Hill, Nairobi

Increase in the morning average land surface temperatures and LST peaks from 1986 to 2017 is an indication of effects of change of land cover, interacting with climate variability such as *la nina* which affect the vegetative health cover in an area (RoK , 2010). The heat emitted from the land surface heats up the air over the surface. When there is no movement of air due to wind caused by high rise buildings, the air temperature increases thus reducing the physiological equivalent temperature (PET) which is a measure of outdoor comfort of pedestrians. The UHI effect varies with the time of day and location of an area within a city (Mirzaei, 2015). The increase in built-up areas affects the microclimate of an area and can have adverse effects on health. The difference between air and surface temperatures on rooftops and pavements during summer can vary between 27 ^{0}C to 50 ^{0}C, while in shaded surfaces or rural areas, air and surface temperatures can nearly be the same (EPA, 2008a).

4.1.2 Land Cover Classification in Upper Hill, Nairobi

Land cover classification in Upper Hill indicate that significant changes from 1986 to 2017 is the increase in built-up areas, with forest reducing within the same period (Figure 4.4). Accuracy assessment in each year has an overall accuracy of more than 80% which is acceptable (Appendix 5). Areas that were previously covered by forest are built-up, sparse or open grassland. Commercial development in earlier years of 1986 are mostly around Upper Hill because of the proximity to highways due to accessibility. The land uses such as recreational fields in Upper Hill High School, Nairobi Sports Club and Uhuru Park have not changed. Areas previously classified as forest decreased from January 1986 to February 2017 due to land use changes. In January 1986, Upper Hill had mostly residential areas in the central part of Upper Hill, surrounded by heavy vegetation hence not easily detectible on satellite imagery. The land

use has changed from residential to commercial use, with larger buildings and expansion of impervious surfaces, pavements, parking lots and roads (Figure 4.4).

Urban areas in January 1986 and February 1995 are mostly concentrated towards the edge of the study area in the north and western parts along the major roads. Open grassland areas are mainly located in Uhuru Park in the eastern part and in Kenyatta National Hospital staff houses in the western part. Due to the size of the buildings and vegetation, the individual houses cannot be detected by sensors at 15 meter and 30 meter resolution hence they are classified as open grassland. Sparse grassland are located in areas with sport fields such Upper Hill High School, Nairobi club and Public Service club having sports fields and tennis courts, which are all located in the central part of the study area. In the south, open grounds are also mapped as sparse grassland. The urban areas in expand in the south eastern part of Upper Hill in 1995.

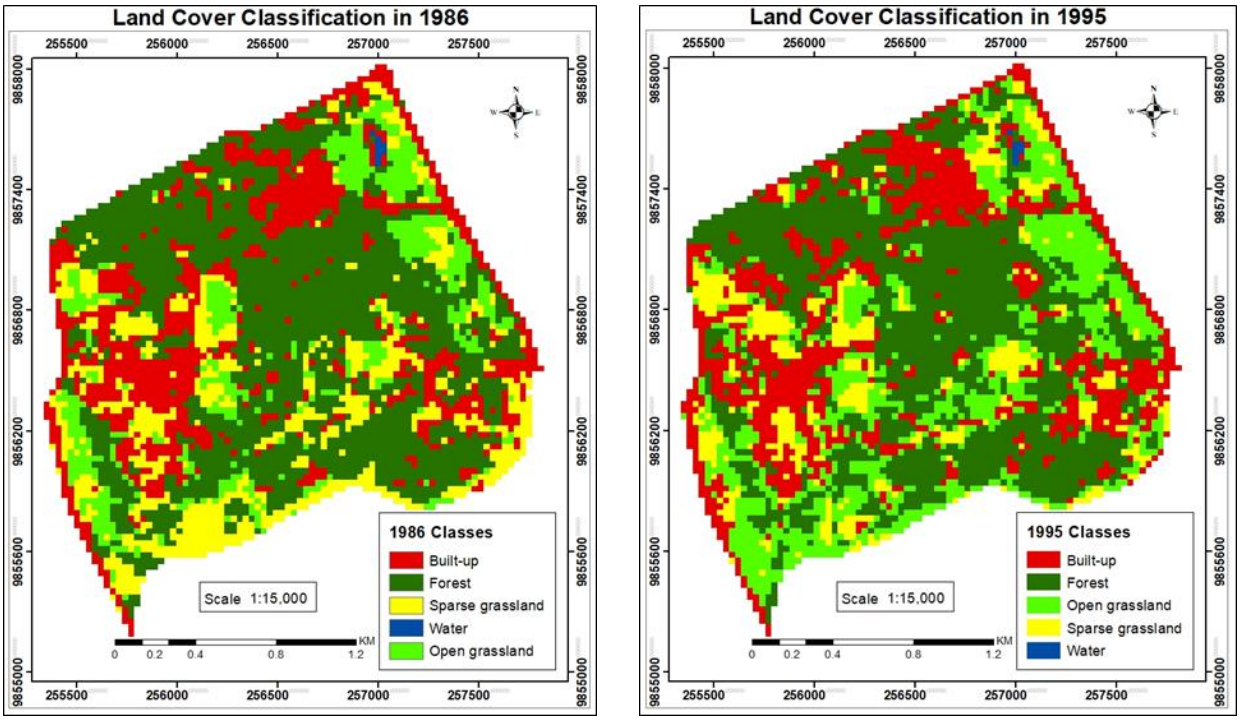

a. **b.**

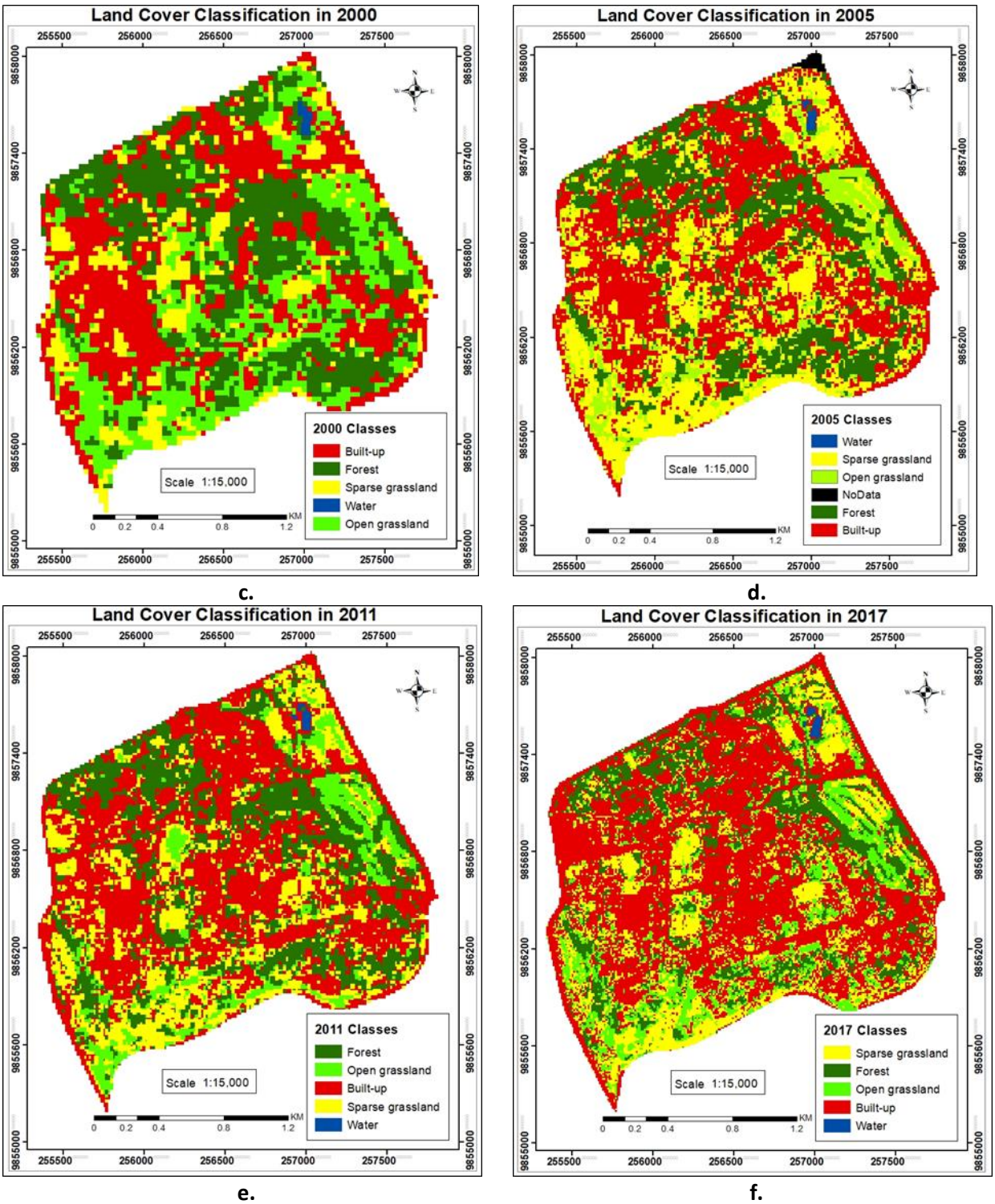

Figure 4.4: Land Cover Classification for 1986(a), 1995(b), 2000(c), 2005(d), 2011(e) and 2017(f), in Upper Hill, Nairobi

Central parts of Upper Hill in the year 2000 reduced in the amount of forest cover and built-up areas have increased significantly by 2005. This may have been fueled by proposed re-planning and rezoning of Upper Hill area and other parts in 1993 (NTPLC, 1993) and 2003 (NCC, 2006). This has led to the construction of commercial buildings, with many residential houses being demolished for commercial use thus increasing the plot ratio. Urban areas in 2011 have increased and land cover has changed with parts previously sparse grassland becoming open grassland. By 2017, the total amount of forest cover has reduced significantly in the central and northern parts of Upper Hill. Urban activities bringing about air pollution affect vegetation health where pollutants are absorbed into the leaf as dust or as chemical contaminants into the stomata, and also settling as particulate matter on the leaf's surface. These weaken the tree and can lead to its death (CoM, 2011). Air pollution also leads to acidic rainfall which causes damage to buildings and vegetation whereas climate change influences the presence and health of vegetation due to factors such as changing temperature and rainfall (JICA, 2014). Therefore, choosing trees that avoid the uptake or absorbs these chemicals and metabolize them into less harmful or toxic substances would be important in Upper Hill (CoM, 2011).

Percentage land cover of each class show trends of increase and decrease from 1986 to 2017 (Figure 4.5). Built-up areas increase from 1986 to 2017, with a high rate between 1995 to 2000 and 2011 to 2017. This is the period when policy reviews were undertaken in 1993 and 2004 that increased the ground coverage and plot ratio for residential, office, commercial, institutional and mixed land uses (Table 3.1). Developers had a preference for office block buildings in the Upper Hill area, therefore it was divided into six blocks with different development intensities during the zonal review of 1993 (NTPLC, 1993). Forest cover reduces in percentage coverage with

greater changes occurring between the periods 1995 to 2000 and 2011 to 2017. This change in forest land cover can be observed in the NDVI values which decrease in the same period of 1995 to 2000 and 2011 to 2017 (Figure 4.6).

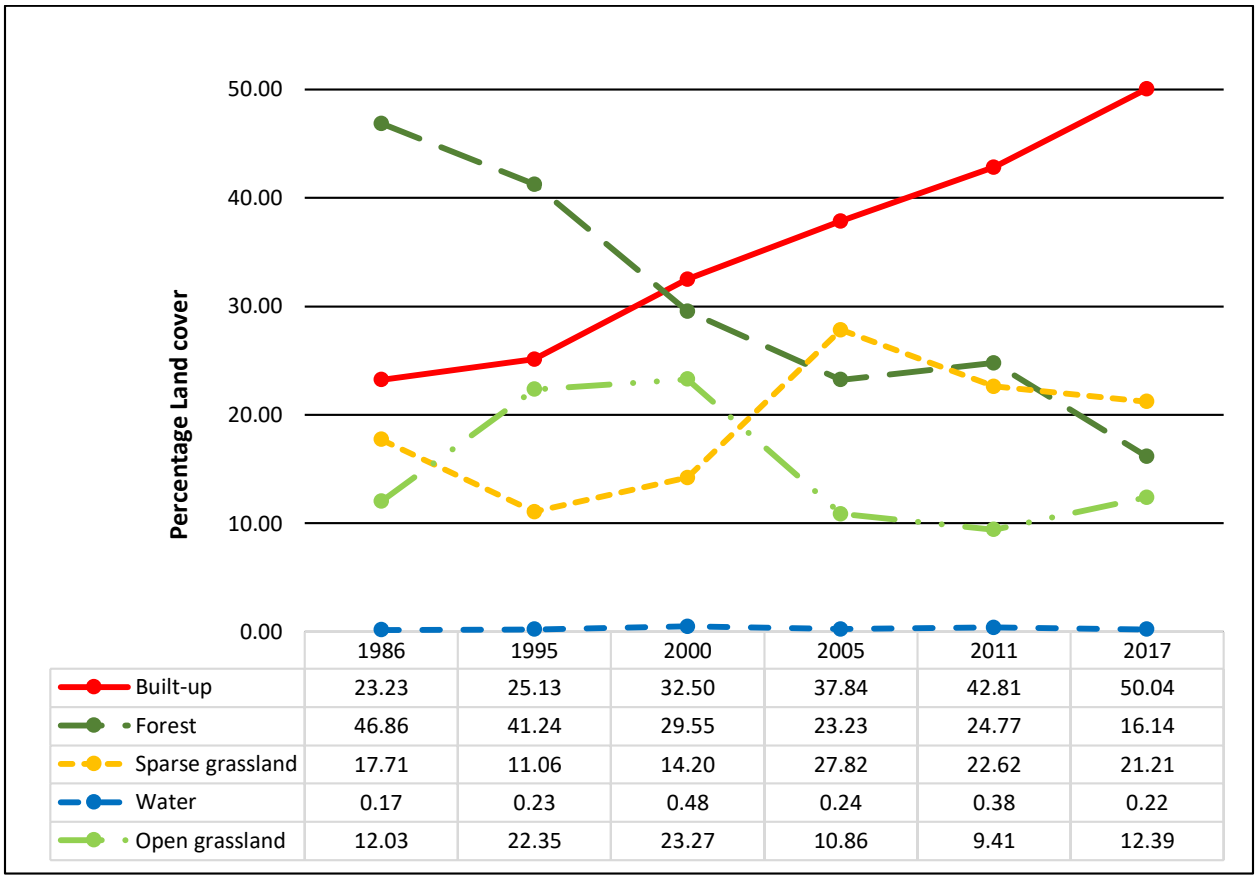

	1986	1995	2000	2005	2011	2017
Built-up	23.23	25.13	32.50	37.84	42.81	50.04
Forest	46.86	41.24	29.55	23.23	24.77	16.14
Sparse grassland	17.71	11.06	14.20	27.82	22.62	21.21
Water	0.17	0.23	0.48	0.24	0.38	0.22
Open grassland	12.03	22.35	23.27	10.86	9.41	12.39

Figure 4.5: Percentage of Land Cover Coverage from 1986 to 2017 in Upper Hill, Nairobi

Wetangula & Mazurewicz, (2017) determined that building and construction has increased immensely in Kenya within the last ten years. This corresponds to the period when built-up land cover increased with the greater change between 2011 and 2017 (Figure 4.5). Sparse grassland and open grassland reduce and increase interchangeably between the years 1986 to 2005, with sparse grassland having a greater coverage than grassland between 2005 and 2017. The percentage coverage of grassland decreases from the year 2000 with sparse grassland increasing

indicating reduced vegetative cover induced by land cover changes due to urbanization. Drought conditions experienced in the years 2000, 2005 and 2011 may have exacerbated the decrease in vegetation land cover. The water body in Upper Hill is only located in Uhuru Park in all years and changes in percentage coverage is due to vegetation growing on the water, or tree canopy covering parts of the water body, hence reducing its area. Some of the land cover changes in Nairobi that occurred between 2003 and 2012 were conversion from grassland to residential areas and detached houses to apartments or offices (NCC *et al*., 2014).

Urban development increased immensely from early 2000 as the country recovered from an economy slump that occurred in the 1990s which slowed down development (Mwaura, 2006). Increased development spurred by policy changes was not accompanied by improved infrastructural services leading to challenges: blocked and burst sewer lines, increased surface runoff during in heavy rains, water shortages, impeded traffic flow, inadequate parking at plot level resulting to indiscriminate parking by road-sides hence loss of greenery (Mwaura, 2006). To decongest Upper Hill road upgrading projects funded by the government were initiated to ease movement of people, goods and services, with an inclusion of footpaths and cycling lanes (UHDA, 2017). Mushrooming road-side kiosks and informal economic activities has led to trampling and hardening of vegetated ground along the road reserves (UHDA, 2015). A comprehensive environmental management plan needs to be formulated that will address issues dealing with conservation of flora and fauna which would promote beautification and greening in urban areas. This legal framework that would enforce policies and regulations and ensure more concerted efforts in collaborations between neighborhood committees and the county government (Mwaura, 2006). Upper Hill District Association (UHDA) founded in 2001

represents views and addresses issues of property owners, residents and business people while working with the Nairobi County Government (UHDA, 2015) to ensure Upper Hill develops sustainably.

4.1.3 Average NDVI Values

The average NDVI values in 1986, 1995, 2000, 2005, 2011 and 2017 (Appendix 7) are averaged and the mean NDVI value over the study area decreases from 1986 to 2017 (Figure 4.6).

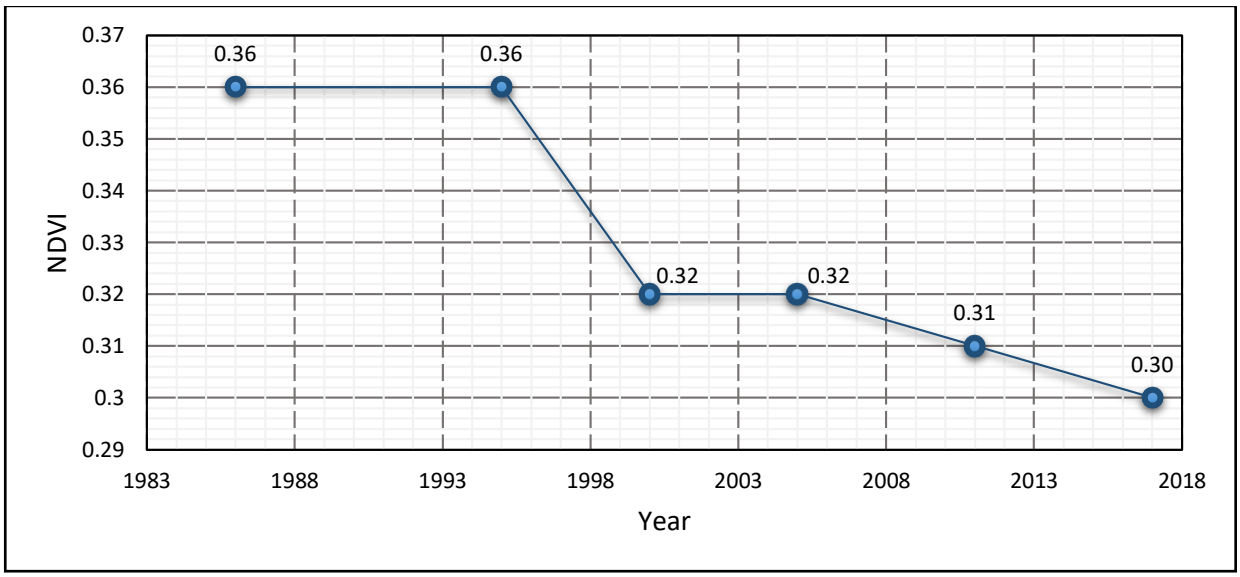

Figure 4.6: Average NDVI Values of 1986 to 2017 in Upper Hill, Nairobi

A reduction in average NDVI values results where vegetated areas are replaced by non-vegetated land cover such as impervious surfaces or bare-ground. The main reduction in NDVI values is between 1995 and 2000 as indicated in figure 4.5 where forest cover reduces by 12% and built-up areas increase by 7%. The years 2005 to 2017 has a decrease in NDVI values of 0.02 which coincides with the increase in built-up areas and reduction in vegetated areas (Figure 4.5). Sparse grassland land cover increases between the period 1995 to 2005 due to changes in vegetation cover i.e. from open ground or forest land cover. The quality of the vegetation cover also has an

effect on the average NDVI values calculated. Vegetation exposed to pollutants such as emissions from vehicles or acid rain due to pollutants have low value as these affect the vegetation health (Zupancic *et al*., 2015; JICA, 2014). Surface urban heat islands (SUHI) are influenced by seasonal variations of NDVI (Yuan & Bauer, 2007).

4.1.4 Land Cover versus Land Surface Temperature

The minimum, maximum and mean LST in each of the land covers indicates the interaction of each of the changing land covers with temperature (Figure 4.7). Low and high mean surface temperature in all land classes is recorded in 1986 and 2005 respectively, as this corresponds to the mean surface temperature in Upper Hill as indicated in figure 4.3. The thermal gradient indicates that sparse grassland has a higher mean LST, followed by built-up, open grassland, forest and water, except in 2011 where it has similar mean temperature with built-up.

Water has a low mean surface temperature in all years due to its high heat capacity, which makes it an important climatological material (Oke, 2014). Water is considered a good storer of energy compared to other materials since a similar rise in temperature in water would need much more energy, while it does not cool rapidly even if there is a reduction of energy over its surface (Oke, 2014). During the day it absorbs in-coming radiation while at night the effect is different as it emits the radiation absorbed during the day. SUHI is normally present both day and night, but mostly intense during the day during hot weather. This is contrary to CLUHI, which is mostly intense at night or just before dawn (EPA, 2008a). Sparse grassland records a higher mean temperature amongst the five land cover classes, except in 2011 where it has similar mean temperature with built-up.

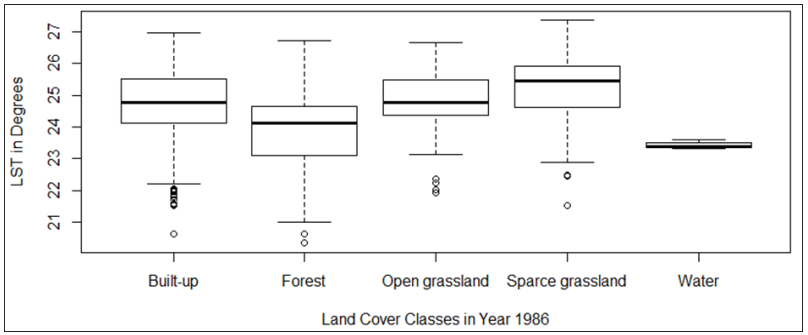

a.

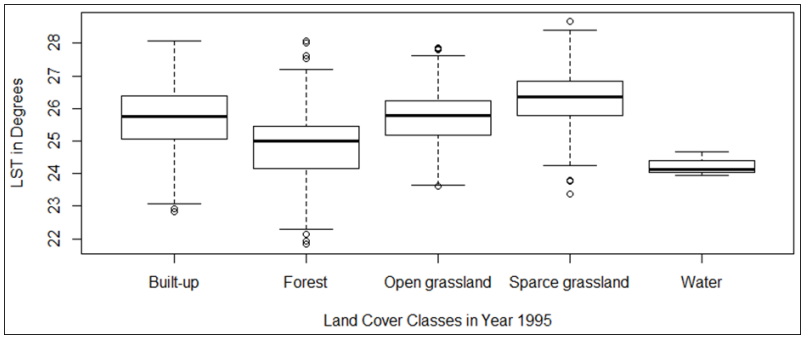

b.

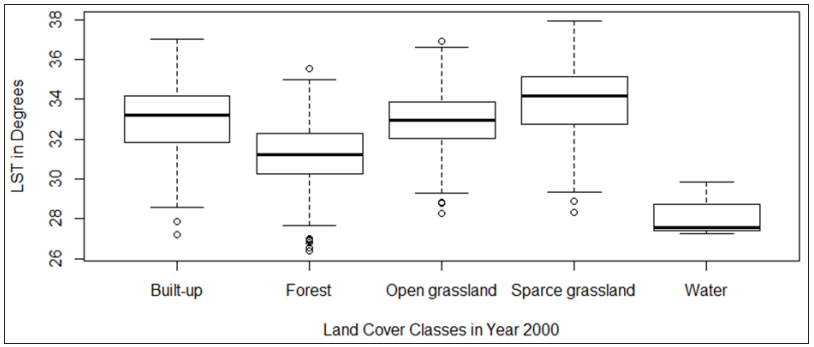

c.

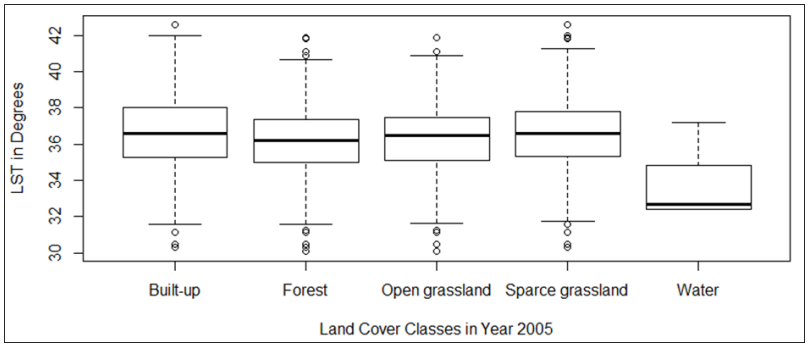

d.

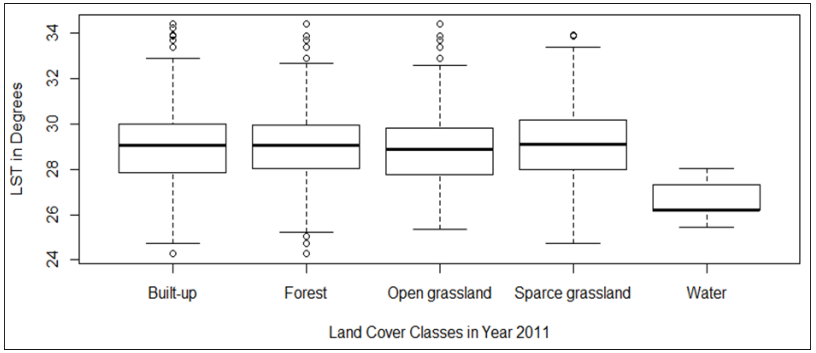

e.

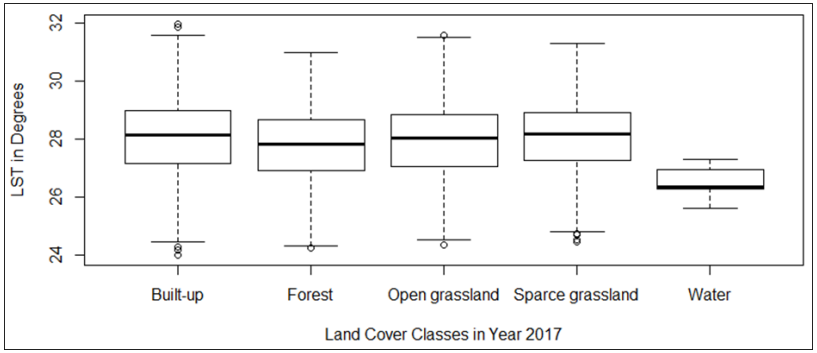

f.

Figure 4.7: Land Cover Analysis versus LST for 1986(a), 1995(b), 2000(c), 2005(d), 2011(e) and 2017(f) in Upper Hill, Nairobi

Bare ground or ground that does not have much vegetative cover heats up faster than other land covers because it reflects the incoming radiation. During the day heat is conducted downwards and conducted upwards at night in soils. The amount of moisture influences the surface temperature recorded on a land cover in raising the temperature (Tian *et al*., 2012). The soils thermal climate is determined by four thermal properties, including: thermal diffusivity, thermal admittance, heat capacity and thermal conductivity (Oke, 2014). The measure of the ability to conduct heat is referred to as thermal conductivity. Heat capacity is the ability of a material to store heat (Oke, 2014).

Built-up has a similar mean surface temperature with open grassland except in 2011 where built-up LST is higher by 1 ^{0}C. Forest land cover has similar mean LST with water in 1986 and 1995, while in other years it has a higher mean than water. The mean LST in Upper Hill in 1986 and 1995 is low, indicating the negative effect of vegetation in lowering the surface temperature. Forest land cover has low minimum LST while water has low maximum LST amongst the five land covers from 1986 to 2017. Therefore water and forest land cover have the lowest and highest temperature range respectively during the study period. Water absorbs incoming radiation hence its low temperature range and low values compared to the other land cover classes.

Land cover responds differently with land surface temperature in different study areas within a region or country due to the land cover distribution, geographical attributes, seasons, climatic conditions, resolution of sensor and time of data capture (Xiao *et al*., 2018). Land cover analysis of Vienna and Madrid indicated that built-up areas had lower surface temperature than

agricultural and natural greenery land in Madrid, while in Vienna the reverse was true (Xiao *et al*., 2018). Therefore, land cover and their characteristics such as composition and shape have a direct influence on LST.

Analysis of afternoon and night-time LST from MODIS for the years 2005 and 2011 and night-time Landsat 8 OLI/TIRS for 2017 indicates that of the five land covers, water has the highest LST due to its high thermal capacity (Figure 4.8). Landsat 8 has a higher temperature range due to its higher spatial resolution at 30 m compared to MODIS which gives coarser results over land cover at 1Km spatial resolution. Water has high temperatures in the afternoon compared to other land cover classes due to its thermal capacity. It emits the highest amount of radiation during the night compared to other land cover classes, emitting it in form of long-wave radiation, therefore having the highest mean and maximum surface temperature. This is in contrast to temperatures in the morning where water has low LST compared to other land covers. Built-up areas absorb incoming short-wave radiation during the day, emitting it at night as long-wave radiation therefore having a high LST at night than land. During the day forested areas are cooler than urban areas with open grounds being warmer, especially dry ground. At night this is reversed with urban areas having high temperatures than open grassland and sparsely vegetated areas which are cooler due to their lower thermal capacity. Forests have a higher LST than open and sparse grassland, though this warming effect at night tends to be lower than the cooling effect during the day. Forests tend to be warm as they release heat energy stored during the day (Li *et al*., 2015). Cool day-time temperatures and warmer night-time temperatures of forests are a result of trapped humidity and heat within the urban canopy layer (Sodoudi *et al*., 2018).

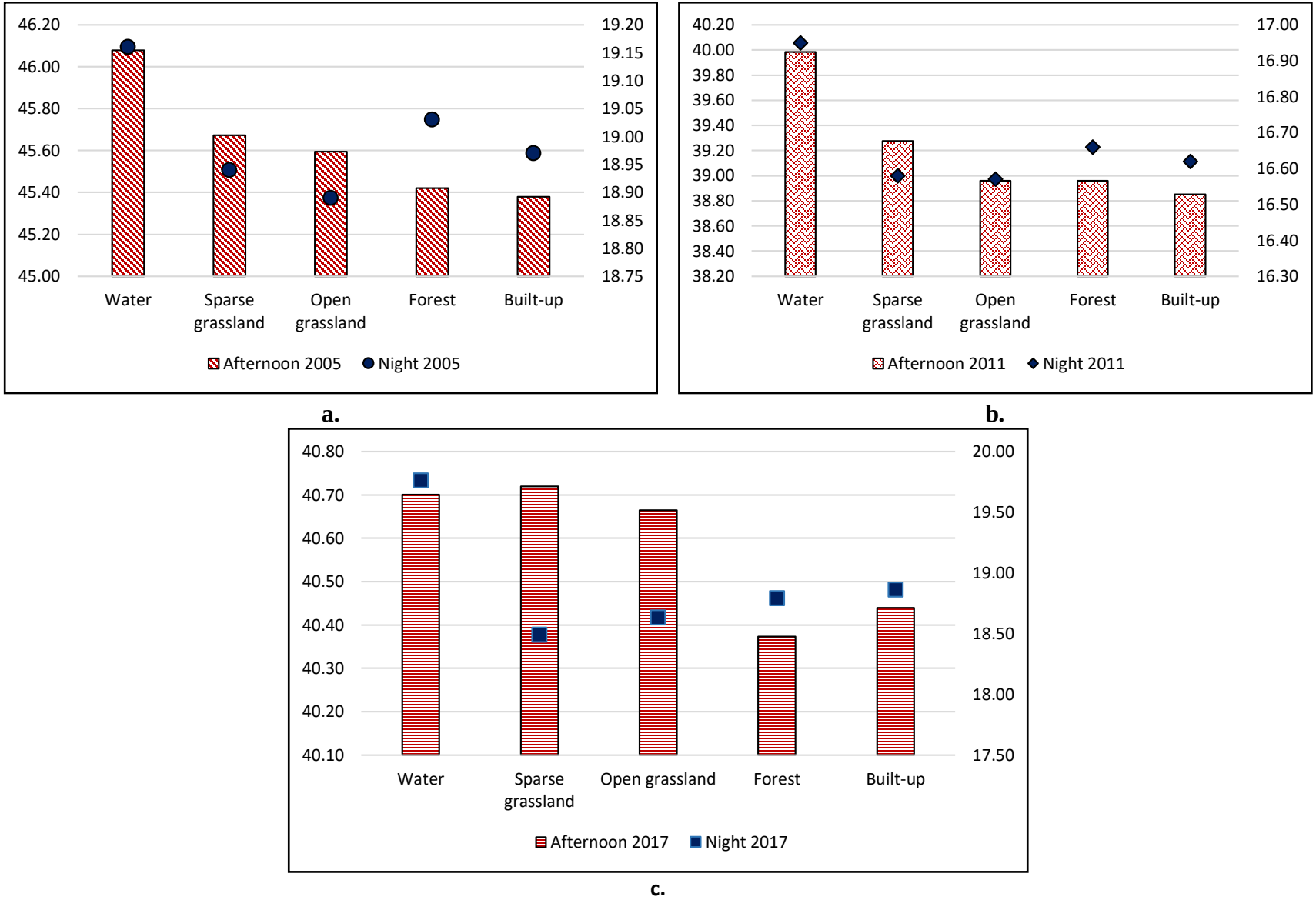

Figure 4.8: Afternoon & Night LST for 2005(a), 2011(b) and 2017(c) in Upper Hill, Nairobi

Sparse and open grassland have low land surface temperatures as open land cools faster at night (Sodoudi *et al*., 2018). Night-time land surface temperature does not have much discrepancy with urban canopy temperature hence can be used to determine the UHI effect at night (Sobrino *et al*., 2013; EPA, 2008b). The SUHI effect is demonstrated by the differences in LST or skin temperature in Upper Hill as it comprises of urban and open ground with vegetated areas that are typical of rural areas.

Distribution patterns of land cover and percentage changes between the years indicate greater changes occur with forest to built-up, mainly within the central parts of Upper Hill (Figure 4.9). Land cover change (LCC) from vegetated, i.e. forest, open and sparse grassland, to built-up has low values of 8% in 1986 to 1995 and high values of 18% in 2011 to 2017. LCC from forest to open and sparse grassland has low vales of 2% in 2005 to 2011 and high values of 9% in 1995 to 2000. These changes correspond to figure 4.5 where built-up areas increase greatly in 2011 to 2017 while forest land cover reduces largely between the years 1995 to 2000. Areas that experience no change in land cover have low values of 77% in 2011 to 2017 and high values of 86% in 1986 to 1995. Positive temperature changes in land cover occur in the period 1986 to 2005 as mean LST increases in this period, while negative temperature changes occur in the period 2005 to 2017 as mean LST decreases in this period (Figure 4.3).

High positive and negative temperature changes on land cover are experienced in the years 1995 to 2000 and 2005 to 2011 respectively as they experience high temperature differences between these years.

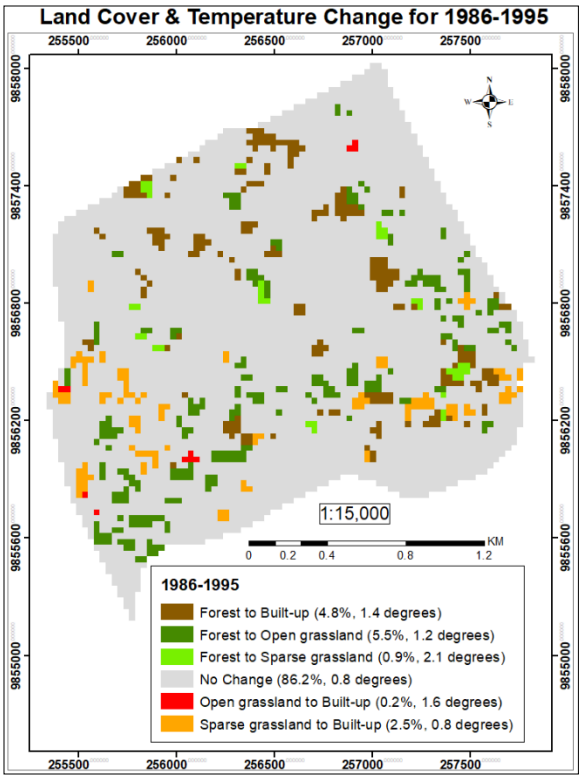
Land Cover & Temperature Change for 1986-1995
1:15,000
KM
0 0.2 0.4 0.8 1.2
1986-1995
Forest to Built-up (4.8%, 1.4 degrees)
Forest to Open grassland (5.5%, 1.2 degrees)
Forest to Sparse grassland (0.9%, 2.1 degrees)
No Change (86.2%, 0.8 degrees)
Open grassland to Built-up (0.2%, 1.6 degrees)
Sparse grassland to Built-up (2.5%, 0.8 degrees)

a.

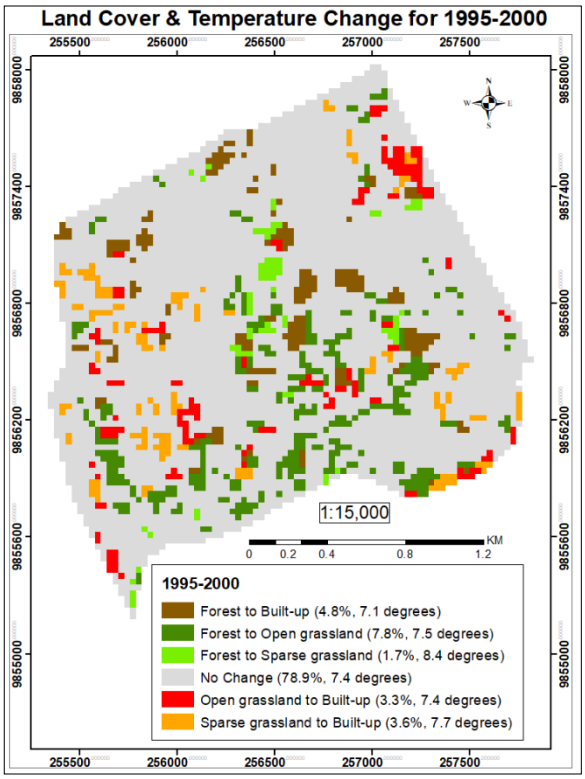
Land Cover & Temperature Change for 1995-2000
1:15,000
KM
0 0.2 0.4 0.8 1.2
1995-2000
Forest to Built-up (4.8%, 7.1 degrees)
Forest to Open grassland (7.8%, 7.5 degrees)
Forest to Sparse grassland (1.7%, 8.4 degrees)
No Change (78.9%, 7.4 degrees)
Open grassland to Built-up (3.3%, 7.4 degrees)
Sparse grassland to Built-up (3.6%, 7.7 degrees)

b.

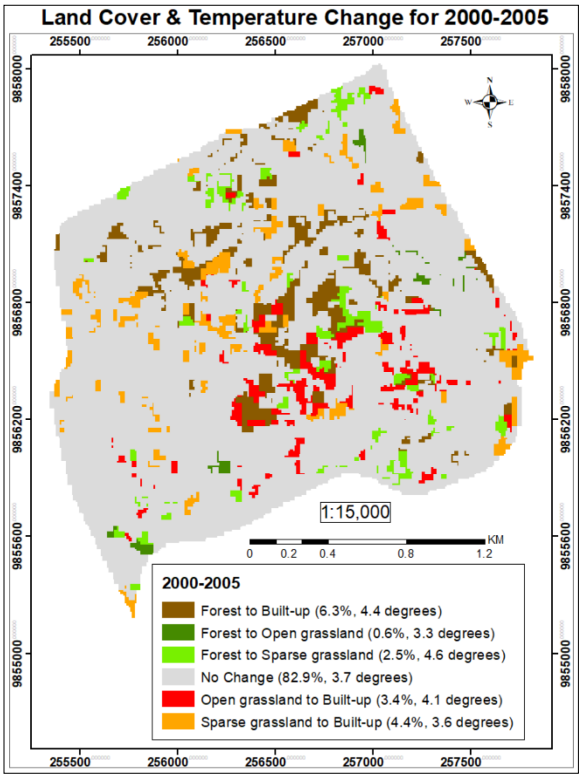
Land Cover & Temperature Change for 2000-2005
1:15,000
KM
0 0.2 0.4 0.8 1.2
2000-2005
Forest to Built-up (6.3%, 4.4 degrees)
Forest to Open grassland (0.6%, 3.3 degrees)
Forest to Sparse grassland (2.5%, 4.6 degrees)
No Change (82.9%, 3.7 degrees)
Open grassland to Built-up (3.4%, 4.1 degrees)
Sparse grassland to Built-up (4.4%, 3.6 degrees)

c.

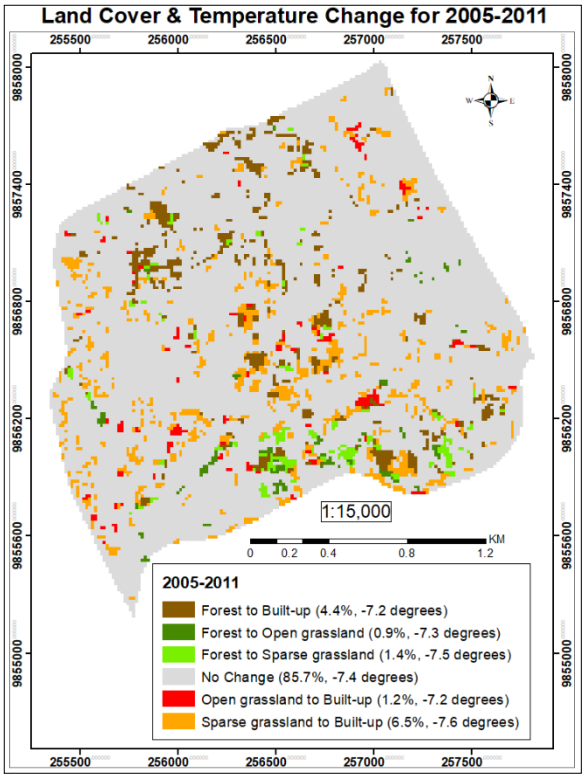
Land Cover & Temperature Change for 2005-2011
1:15,000
KM
0 0.2 0.4 0.8 1.2
2005-2011
Forest to Built-up (4.4%, -7.2 degrees)
Forest to Open grassland (0.9%, -7.3 degrees)
Forest to Sparse grassland (1.4%, -7.5 degrees)
No Change (85.7%, -7.4 degrees)
Open grassland to Built-up (1.2%, -7.2 degrees)
Sparse grassland to Built-up (6.5%, -7.6 degrees)

d.

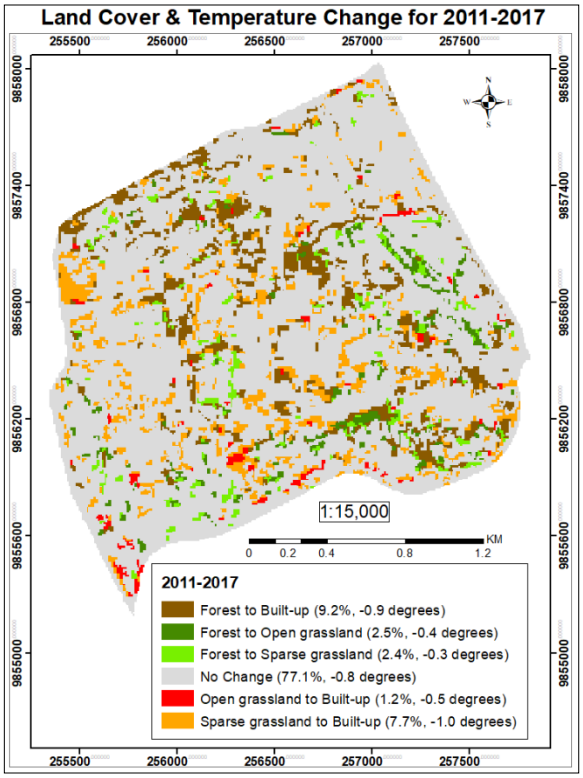

e.

Figure 4.9: Temperature and Percentage LCC from 1986 to 2017 in Upper Hill, Nairobi

The land cover changes that record high temperature change of 8.4 ^{0}C is forest to sparse grassland in 1995 to 2000. Areas that have not changed land cover types, referred to as 'no change' have low temperature changes in 1986 to 1995 and 2011 to 2017. The difference in the cooling effect of forests and warming effect of sparse grassland as indicated by their contribution index (Figure 4.11) results in high temperature changes.

The period 1986 to 2017 has low land cover changes while 2011 to 2017 has high land cover changes due to increased demand for office space and expansion from the central business district. High changes observed between 2011 and 2017 (Figure 4.9) is synonymous with an increase in the construction industry observed within that period (Wetangula & Mazurewicz, 2017). These developments occurred in places that were previously vegetated. Two important

factors that contribute to temperature differences in urban fabric include decreased evapotranspiration rate and differences in thermal properties of impervious surfaces, as blue and green urban spaces regulate local temperatures (Inostroza, 2014).

Studies undertaken in the tropics indicate that deforestation results to biophysical warming, with changes from shrub-land to crop-land or bare-ground having a warming effect of $\pm 0.5\ ^{0}C$ and $\pm 0.55\ ^{0}C$ respectively (Lucia *et al*., 2017). Amongst the three generalized land covers namely vegetation i.e. forest, open and sparse grassland to built-up, forest to grassland and no change, vegetation to built-up has higher LST changes. This shows that LCCs of vegetation to built-up do have a great impact on LST compared to changing from one vegetation type to another. The percentage change of vegetation to built-up is also higher than forest to grassland indicating that there is a relationship between types of land cover change and LST. This indicates that different land covers affect LST differently thereby having climatic effects. Effect on climate through LCC occurs through two processes: surface energy budget variations mediated by evapotranspiration, surface roughness and albedo; and net influx modifications of greenhouse gases such as carbon dioxide due to changes in soil carbon and vegetation (Lucia *et al*., 2017). In early 2015, ground breaking activities commenced along the junction of Upper Hill road and Haile Selassie road by Jabavu Village Limited, to start construction of a mixed-use, 45 story building with a built-up area of 100,000 m^2 (Frank, 2015). The area under this activity was forested and cleared to pave way for this new development.

Land cover and land surface temperature changes that have occurred reflect the ecologic economic theory where land use changes induced by demands for office space and provision

made by changed policies has contributed to increased land surface temperatures. Land conversion is a human induced stressor and in Upper Hill reduction of forests has changed the urban landscape. Policies on urban development as elaborated in 2.4.3 focus on sustainable development but need to specify the amount of vegetative coverage per acre or lot. Tree protection mandates protect trees based on their size, location or species and penalties are imposed on developers who remove them unless exceptional cases occur such as diseased trees. Landscaping ordinances incorporate standards and requirements such as specific number of trees per acre or lot and vegetation coverage (Hoverter, 2012). Identification and protection of natural and green systems is a very crucial element in fostering liveable cities, especially if they're compact (UN-Habitat, 2012).

4.1.5 Albedo Trends of Land Cover

The mean albedo in Upper-Hill has reduced with increased urbanization where built-up areas have high albedos and forested areas have low albedos (Figure 4.10), with their ranges within general observations in literature (Table 2.2). The albedo of a city or a town depends on the surfaces' arrangement, materials used for roofs, paving, coatings, and solar position (Bouyer *et al*., 2009). There has been significant changes in albedo values from 1986 to 2017 in all land cover due to changes in land cover coverage in Upper Hill, with years 1986 having a mean of 0.192, 2000 at 0.150 and 2017 at a mean of 0.153. Figure 4.10 indicates a relationship between mean surface temperature and albedo with water having low temperature and low albedo values, while sparse grassland and open grassland have high mean albedo and LST. The albedo values in all land covers have decreased from 1986 to 2017 with an exception of sparse grassland which

reduced by 0.3. Open grassland albedo reduced by 0.07, forest and water albedo reduced by 0.05, sparse grassland and built-up reduced by 0.03.

The solar heat gain in in urban areas is higher than in rural areas as the albedo is smaller than in rural areas (Yang *et al*., 2017). Conversion of vegetated to built-up surfaces creates a shift in local climate referred to as urban heat island effect therefore making the albedo an important parameter as it controls the local energy budget (Trlica *et al*., 2017) and determines how much solar insolation is reflected back into the atmosphere (Odunuga & Badru, 2015).

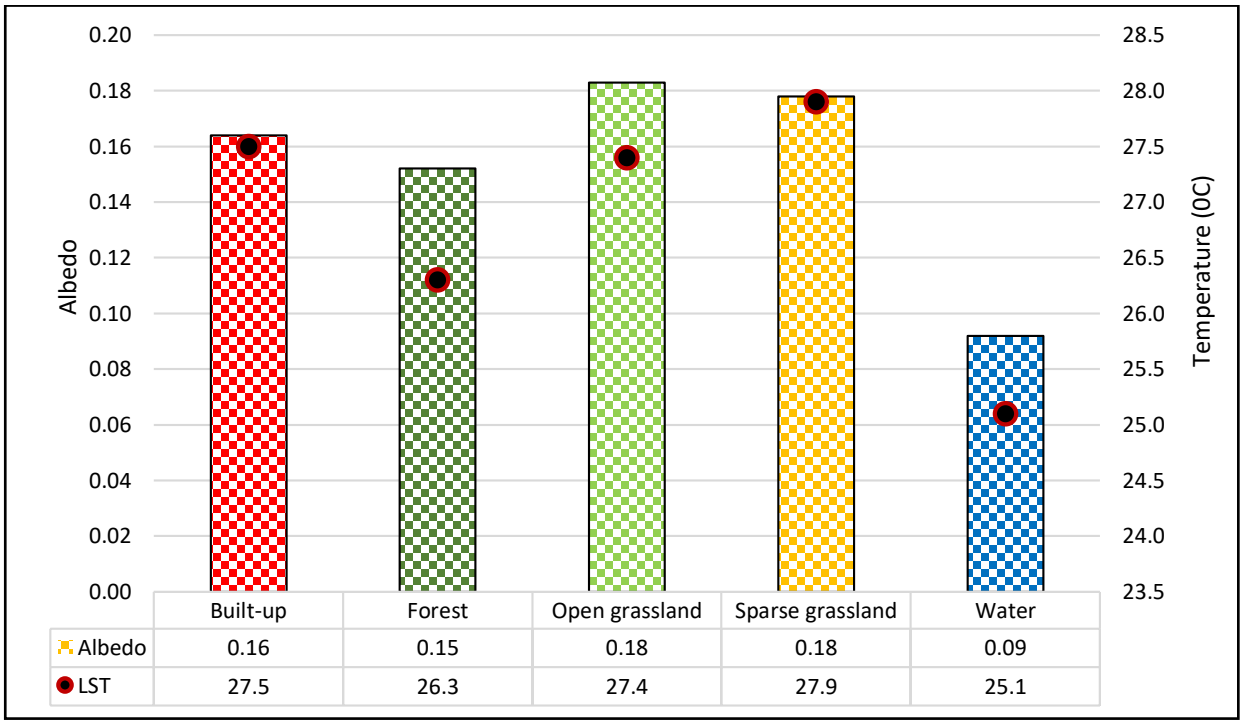

Figure 4.10: Mean Temperature and Albedo of Land Cover in Upper Hill, Nairobi

Odunuga & Badru, (2015) investigation on albedo in six different regions in Nigeria determined a similar trend between LST and albedo with high LST associated with high albedo values on different land cover. LST is key in surface energy balance influencing sensible and latent heat

fluxes (Tian *et al*., 2012). A material's colour is correlated with solar reflectance where lighter surfaces have higher solar reflectance than darker surfaces (EPA, 2008b). Averagely 20 to 25 percent of a city's land cover is comprised of roofs (Hoverter, 2012). Roofing materials are thin therefore main factors to consider are emissivity and reflectance due to the low heat capacity of well insulated roofs. Pavements are on the ground and are thicker therefore making considered factors more complex where they include density, heat capacity and thermal conductivity (EPA, 2008b). The albedo ranges for standard roofing materials is 0.10 to 0.25 with average values of 0.20 and can be increased to about 0.55 to 0.60 to increase reflectance (Bhargava & Bhargava, 2018). Increasing the albedo of roofing materials can reduce use of cooling energy, reduce urban temperatures and improve the urban air quality but increases the heating loads during the cold seasons (Bhargava & Bhargava, 2018). Interactions between pavements and buildings is complicated and use of highly reflective pavement increases the cooling requirements of buildings while low-albedo ground surfaces reduces the transfer of short-wave radiation to near-by buildings from ground surfaces (Bhargava & Bhargava, 2018). Porous and permeable pavements have been used as they cool the surface and the air around it by allowing air and water to pass through thus evaporation occurs through the pores (Hoverter, 2012). Surfaces tend to stay cool if they have high emittance values as they release heat readily (EPA, 2008b). It is imperative in urban planning and overall design that albedo be considered as an important parameter (Bhargava & Bhargava, 2018).

4.1.6 Contribution Index of Land Cover

The mean temperature of an area is a culmination of differences in emissivity of different land surface materials. The contribution index (Figure 4.11) for each land cover show that forest and

sparse grassland have higher negative and positive contribution index respectively than other land covers. Forest land cover reduces the amount of thermal heat emitted into the atmosphere as shown by its negative value, therefore reducing the surface urban heat islands. Forest land cover reduces in the contribution index from 2005 to 2017 due to the decrease in forest cover in Upper Hill. Water has a negative contribution index in all years due to its thermal properties thus acting as a coolant over the surface. Therefore forest and water surfaces tend to be cooler compared to sparse grassland or built-up areas due to latent heat transfer.

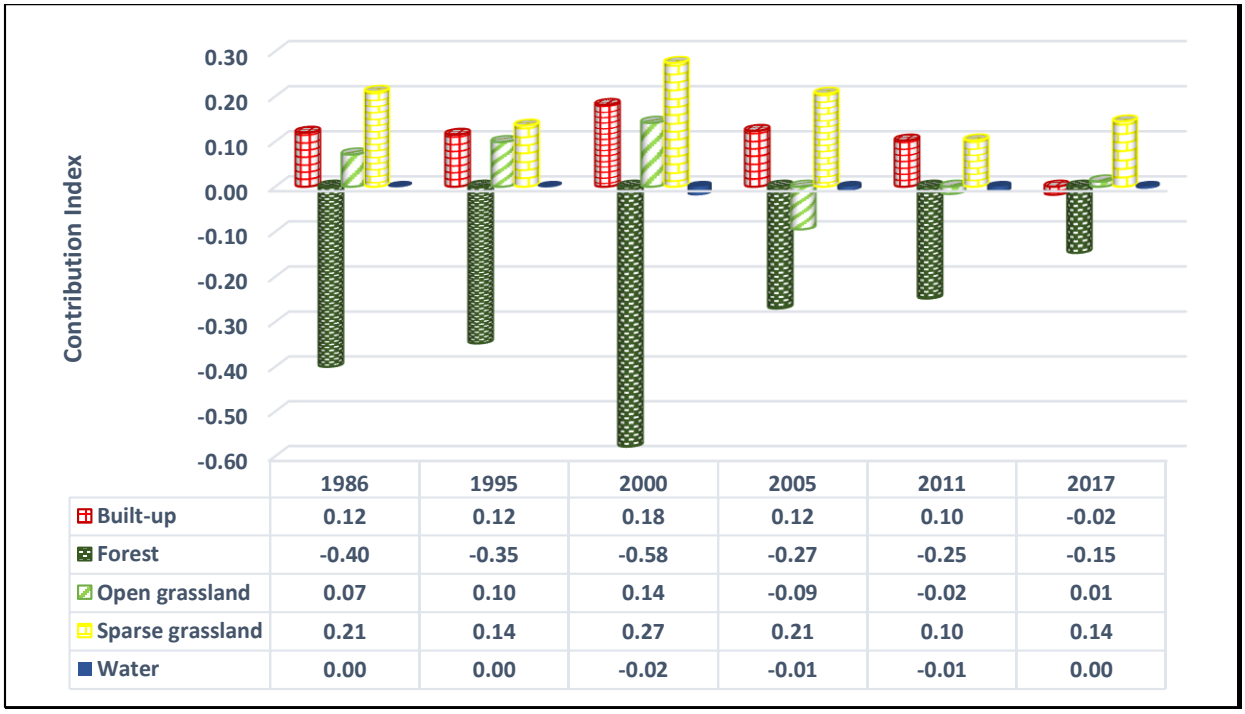

	1986	1995	2000	2005	2011	2017
Built-up	0.12	0.12	0.18	0.12	0.10	-0.02
Forest	-0.40	-0.35	-0.58	-0.27	-0.25	-0.15
Open grassland	0.07	0.10	0.14	-0.09	-0.02	0.01
Sparse grassland	0.21	0.14	0.27	0.21	0.10	0.14
Water	0.00	0.00	-0.02	-0.01	-0.01	0.00

Figure 4.11: Contribution Index of Land Covers in Upper Hill, Nairobi

Built-up land cover absorbs and stores thermal heat during the day hence reduction in contribution index from the year 2000 to 2017 with increased development. Due to impervious surfaces such as buildings and streets, there is more thermal storage in urban areas than in rural areas (Yang *et al*., 2017). Built-up areas contribution index increases from 1995 to 2000 due to

high LST in the year 2000 but decreases from 2005 to 2017 with a negative contribution index in 2017, where its mean LST is lower than the mean in Upper Hill. This has resulted from an increased amount of impervious surfaces in Upper Hill which increases its thermal heat capacity as it absorbs incoming radiation and is demonstrated by night-time LST (Figure 4.8 c) where built-up areas have a higher LST than forest compare to other years. Open grassland has a positive contribution in all years except in 2005 and 2011 where it has a negative index as the mean LST of open grassland is lower than the mean LST over Upper Hill. February 2000 records high contribution index in all land covers due to the large differences between mean LST in each land cover and mean LST in Upper Hill of up-to -2 ^{0}C (Figure 4.3).

Rural materials like sand and dry soil have lower heat capacities compared to building materials such as stone and steel which increases their ability to store heat (EPA, 2008b). Increasing artificial impervious surfaces increases the thermal capacity of a city and therefore the urban temperature and effect of global warming (Tarawally *et al*., 2018). Tarawally *et al*., (2018) comparative analysis between Bo town and Freetown determined that contribution index between the same land cover differs in magnitude and effect. Agricultural areas in Freetown had both negative and positive contribution index while Bo town had positive effects. The loss of ecological services and destruction of natural capital brings into focus the need of transitioning our cities into having sustainable urban development and greener economies (Mccormick *et al*., 2015). This encompasses the preservation of “blue” and “green” features in urban areas so as to create environments that stimulate social interactions and are healthy (Mccormick *et al*., 2013).

4.2 Effects of Built-up Morphology on Land Surface Temperature in Upper Hill, Nairobi

4.2.1 Height, Ground Coverage Ratio and Built-up Volume Densities Distribution

Figure 4.12 to figure 4.14 shows classified 3D building heights and GCR distributions. The mean GCR in 1978 in 1978 is 0.76 with a mean height of 9.8 meters and are at Kenyatta National Hospital which is one of the two high-rise buildings (Figure 4.12).

Figure 4.12: 3D Visualization of 1978 Buildings in Upper Hill, Nairobi

The mean medium density GCR in 1978 is 0.31 with a mean building height of 6.3 m and are located in the north and western parts of Upper Hill. Buildings include middle-rise buildings such as Ardhi House which has a mean height of 23.8 m in the north of Upper Hill, Nairobi Hospital, buildings along Mawenzi Road, Social Security House to the north which was completed in 1973; Community area with buildings such as Milimani Law Courts, Ministry of Water and Sanitation. Mean of low density GCR is 0.09 and has buildings with a mean height of 5.2 meters. Upper Hill has maintained low-rise buildings from 1978 to 1998 (Figure 4.13).

Distribution patterns of development from 1978 to 1998 indicate densification along public transport routes and around government institutions mostly in the northern and western parts of Upper Hill.

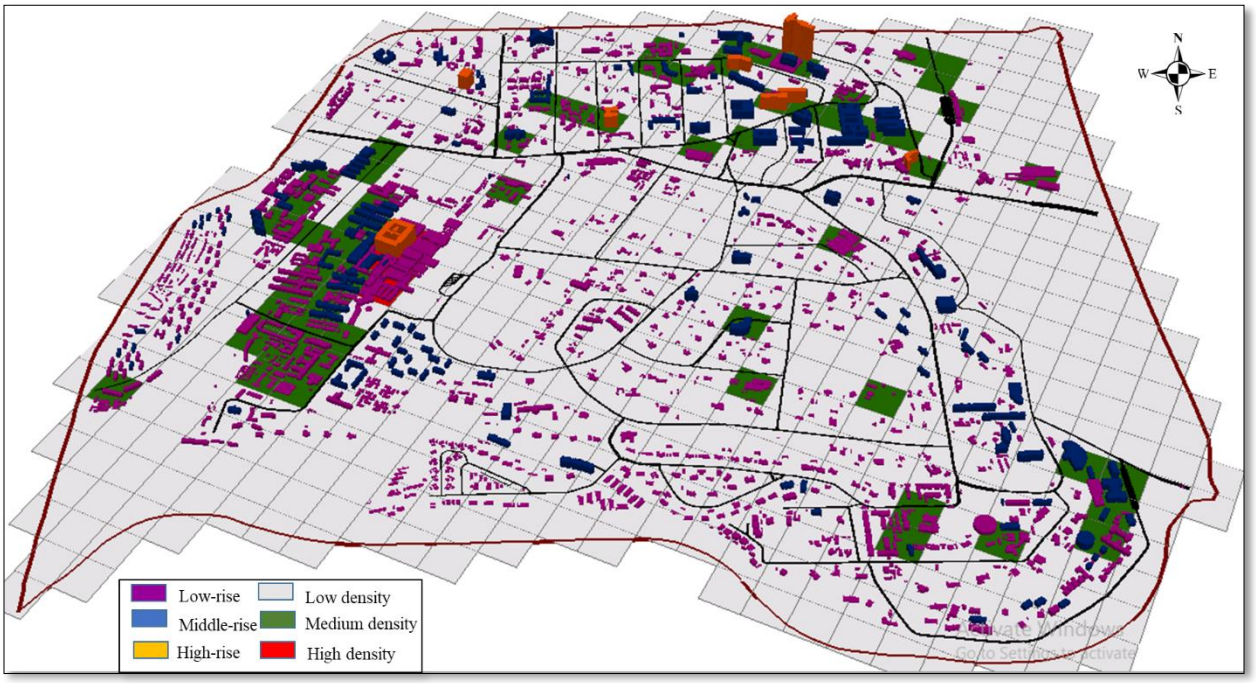

Figure 4.13: 3D Visualization of 1998 Buildings in Upper Hill, Nairobi

The mean high density GCR in 1998 is 0.73 with a mean height of 9.6 m and is at Kenyatta National Hospital and surrounding buildings (Figure 4.13). GCR medium-density areas have a mean of 0.27, buildings with a mean height of 5.4 m and mean road width of 6m which are distributed in the north, west and south-eastern parts of Upper Hill. Medium density buildings include National Industrial Credit (NIC) Bank completed in 1992 with a height of 13.57 m, Railways Club, Bishop's Garden buildings completed in 1992 at 27.14 m and Kenyatta National Hospital buildings. Medium and high-density buildings are located in blocks whose land-use is classified as institutional, commercial, office and residential while the mean height ranges between high and middle-rise buildings. Low-density GCR mean is 0.07 and buildings have a

mean height of 5.9 m while the mean width of roads is 6 m. The land-use in which low-rise buildings are located spans across all land use zones.

The mean high density GCR in 2017 is 0.68 which is high-density (Figure 4.14). There is an increase in middle-rise and high-rise buildings with low-rise buildings still being the majority (Figure 4.14).

Figure 4.14: 3D Visualization of 2017 Buildings in Upper Hill, Nairobi

Mean height of buildings in high density GCR areas is 18.9 meters including Kenyatta National Hospital, Nairobi Hospital, National Hospital Insurance Fund building, UAP-Old Mutual building and KCB Plaza completed in 2014 at 99 m. Mean GCR of medium density is 0.31 with mean building height of 7.6 m and mean road width of 6 m. Land-use of medium-density built-up areas are commercial offices, residential, institutional. Buildings include Victoria towers and Old Mutual building both completed in 2000 with a height of 40.71 m and 16.96 m respectively,

Landmark plaza completed in 2006 at 47.49 m, Blue Shield Towers I and IKM place both completed in 2007 at 23.75 m and 16.96 m respectively, Nachu Plaza completed in 2014 at 50.88 m, CTDLT and Flamingo towers completed in 2016 at 67.84 m and 47.49 m respectively. Low density GCR mean is 0.07 with mean building height of 4.8 meters and mean road with of 9 meters. The period between 1998 and 2017, land use changed with areas that were previously residential now having commercial, institutional and office use. The mean number of floors of buildings constructed is three floors (Table 4.1).

Summary results of the sum total of buildings and roads in Upper Hill in 1978, 2000 and 2017 are presented in table 4.1. Total density covered by built-up areas has increased due to changing building heights. The mean ground coverage ratio and built-up density ratios are within the low density range in 1978, 1998 and 2017, though there are medium and high-density buildings spread in Upper Hill. GCR and BVD increases more in 1998 to 2017 than 1978 to 1998 indicating increased urban development.

Table 4.1: Mean GCR, BVD and Height in Upper Hill, Nairobi

Mean Measure	**Year**			**Difference**		**Percentage Increase**	
	1978	**1998**	**2017**	**1978-1998**	**1998-2017**	**1978-1998**	**1998-2017**
GCR	0.11	0.12	0.19	0.01	0.07	9	58
BVD (m^3/m^2)	0.55	0.77	1.85	0.22	1.08	40	140
Height (m)	5.23	5.40	7.88	0.17	2.48	3	46
Road Width (m)	6.35	6.35	9.34	0	2.99	0	47

High-rise buildings in 1978, 1998 and 2017 have a maximum height of 49.67 m, 104.32 m and 135.04 m respectively. Widening of roads has contributed to increased ground coverage of built-up areas. Processional way, located in Uhuru Park, has the widest road width at 31 m in 1978

and 1998 and 39 m in 2017. Areas designated as recreational or open space land use such as Uhuru Park, Nairobi Safari Club, Upper Hill High School, Public Service Club and Nairobi Area Traffic Police Headquarters field have buildings that are mostly one (1) storey (less than or equal to 3 m) in 1978, 1998 and 2017. The percentage of buildings in 1978, 1998 and 2017 that are low-rise are 91.6%, 90.5%, 79.8% respectively, middle-rise are 8%, 9%, 15.7% respectively and high rise are 0.4%, 0.5%, 4.5% respectively. The percentage of buildings in 1978, 1998 and 2017 whose GCR is low density is 96.6%, 89.7%, 66.6% respectively, medium density is 14%, 18.9%, 45.5% respectively, high density is 0.2%, 0.7% and 1.6% respectively.

There is an expectation of taller buildings in larger cities due to concentration in space of infrastructure, economic activity and population due to the competition of land where compensation is made by making buildings taller (Schläpfer *et al*., 2015). Land use zones have encouraged mixed-use development and according to the classification of densities (Table *3.11*), Upper Hill should be a medium-density area based on GCR and medium-high density based on FAR. However, high density low-rise built-forms with high GCR tend to negatively influence the quality of spatial elements such as open and green spaces, day-light access, ventilation and accessibility (Sokido, 2016). Land use changes always have implications on transportation and issues that emerged with rezoning in Upper Hill was poor accessibility due to increased traffic, with vehicles parking by the road-side which further aggravated traffic congestion (Karoki, 2004). Rezoning of Upper Hill required a change in location of parking spaces for developers such that parking spaces were to be in-built or on-lot (Karoki, 2004). Increasing road widths and thickness increases the heat storage capacity hence the importance of including roads in urban heat island studies.

Built-up volume density distribution of built-up areas within Upper Hill indicates clusters of high values around the north and eastern parts of Upper Hill in 1978, increasing within the same region in 1998 and spreading towards the central parts of Upper Hill in 2017. High density BVD in 1978 (Figure 4.15 a) has a mean of 9.10 m^3/m^2 at Ministry of Transport, then referred to as Ministry of Works completed in 1968 and Kenyatta National Hospital with a mean building height of 17.5 meters. BVD medium density mean is 3.14 m^3/m^2 with buildings at 8.4 m mean height such as Social Security House, Milimani Law Courts, Ministry of Water and Sanitation. The mean width of roads in medium-density areas is 6 m while in high-density areas, no roads pass through. Low density built-up areas have a mean of 0.35 m^3/m^2 with buildings of a mean-height of 4.4 m. The pattern of development of medium and high-density is along public transport routes and are in land uses defined as institutional and office. High-rise high-density urban forms tend to be favorable due to their compactness but it should have quality urban spaces and amenities. However, the level of density should be determined in each area as one level of density may not be favorable or acceptable in another (UN-Habitat, 2012).

BVD high-density mean in 1998 (Figure 4.15 b) is 8.08 m^3/m^2 and a mean building height of 11.32 m which include Kenyatta National Hospital, Ministry of Transport and Social Security House. BVD medium density has a mean of 3.32 m^3/m^2 with mean building height of 7.0 m and includes the British Embassy and Chancery Building at 40.71 m. BVD low-density has a mean of 0.42 m^2/m^3 with mean building heights of 4.4 meters. Mean high density BVD in 2017 (Figure 4.15 c) is 9.5 m^3/m^2 with mean height of buildings at of 19.5 m with a mean road width of 9 m. These are located north, central, west and south-eastern parts of Upper Hill.

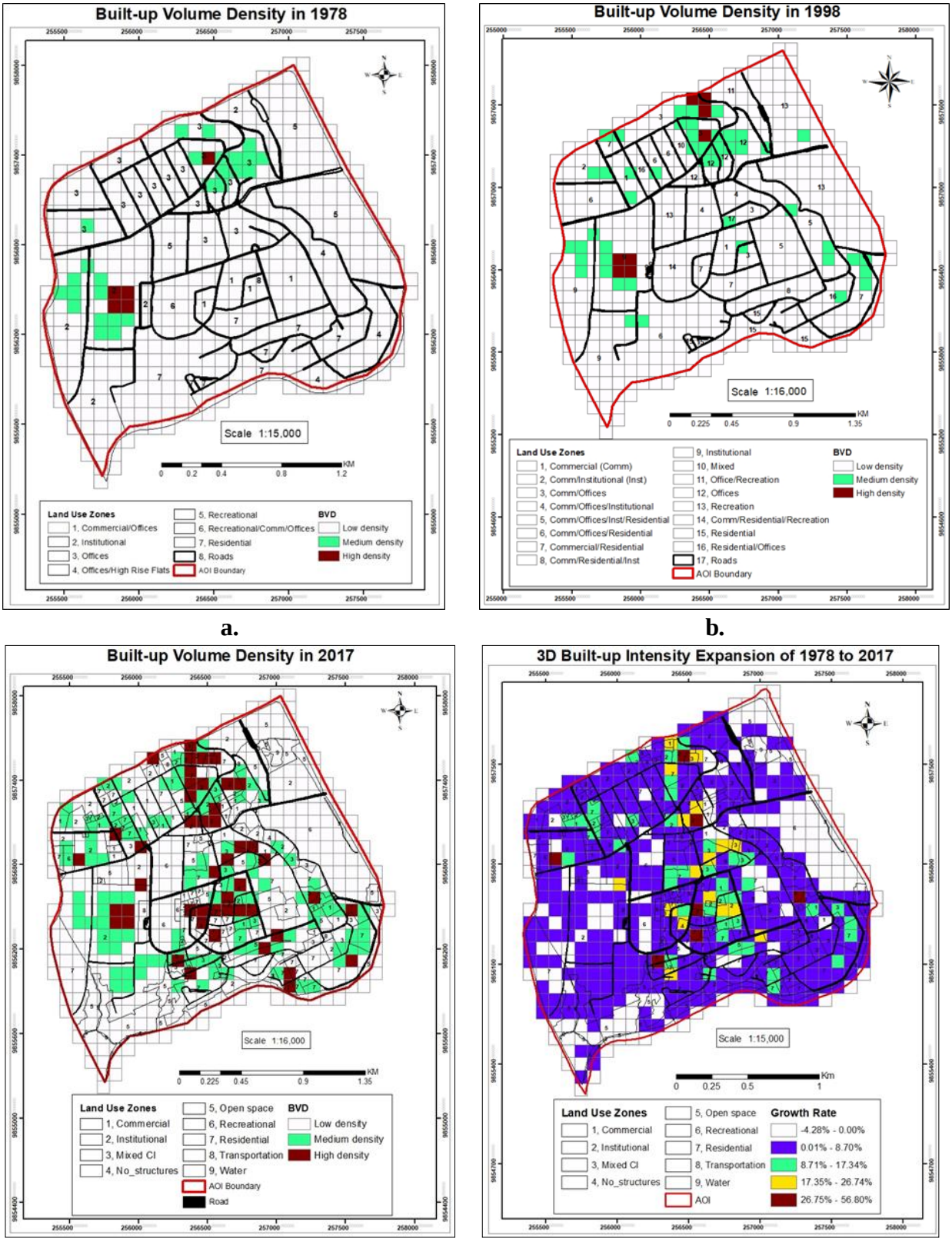

Figure 4.15: BVD and 3D Urban Intensity Expansion in Upper Hill, Nairobi

High- density built-up areas Kenyatta National Hospital and Nairobi Hospital, KCB Towers, UAP Towers and National Housing and Insurance Fund (NHIF) building. The land-use of high-density built-up areas commercial, institutional and residential. Medium-density built-up areas have spread and are in the north, central, west and south-eastern parts of Upper Hill and have a mean of 3.5 m^3/m^2 with mean building heights of 8.0 m and mean road width of 5.5 m. BVD low density buildings have a mean height of 4.0 m and a mean density of 0.55 m^3/m^2. The percentage of buildings in 1978, 1998 and 2017 whose BVD is low-density is 94.5%, 90.27%, 73.10% respectively, medium-density is 4.6%, 8.32%, 18.58% respectively, high-density is 0.88%, 1.42% and 8.32% respectively. Low density, both GCR and BVD built up areas in 1978, 1998 and 2017 have low-rise buildings. Medium density built-up in 1978 and 1998 has low and middle rise buildings while 2017 has middle-rise buildings. High-density built-up areas in 1978 are middle-rise, 1998 has middle and high-rise buildings and 2017 has high-rise buildings. Compared to ground coverage ratio (GCR), building volume density (BVD) has a different distribution than GCR due to the height of buildings (Zhan *et al*., 2015).

3D urban intensity expansion indicates the percentage increase of built-up areas in Upper Hill from 1978 to 2017 is at a mean of 3.3% per annum (Figure 4.15 d). Negative percentages occur in areas where buildings have been demolished or reconstruction has occurred. Grids with zero percentage cover 13% of Upper Hill where no construction has been undertaken such as recreational open spaces and if the building existed in 1978. Urban expansion has resulted from densification, reconstruction of buildings and expansion of roads. 57% of the study area has a 3D intensity mean growth rate of 2% which is indicated by areas that have a range of between 0 to 8.7%. 7% of Upper Hill area has a 13% mean growth rate, concentrated within the central part.

Land uses in these areas are commercial, offices, institutional and residential use in 1978 and have changed to mixed use by 2017 due to changed zoning policies. 3% of the Upper Hill has a 22% growth rate indicated by yellow grids and is located in the central and northern parts of Upper Hill. 1% of Upper Hill has a mean growth rate of 45% per annum whose buildings are institutions and where UAP-Old Mutual building, currently the tallest building in Upper Hill stands. A shortfall of the current system of data management in construction is when determining spatial development statistics of construction trends in Nairobi. They are wholistic and not broken into their spatial locations rendering it difficult to compare and determine which parts are growing faster than others spatially and which ones are decaying (K'Akumu, 2007).

The economic supply, defined as land units being used in a particular manner due to stimulus's such as institutions and prices, within a certain period can be increased by ways such as intensively utilizing areas in use and also area that are unused being brought into production (Hubacek & Vazquez, 2014). The development that has occured in Upper Hill is infill development where vacant or underdeveloped parcels are developed. Redevelopment has occured where existing buildings, mostly residential use with small plot ratios, have been demolished and commercial or office use buildings constructed to have high plot ratios and population densities. Widening of roads mostly along strategic routes has been done to improve mobility and accessibility. Road rehabilitation and upgrading in Upper Hill has been undertaken in phases with expansion of roads of major concern. This has been undertaken in phases with the first phase including Elgon, Kilimanjaro and parts of Mara, Hospital, Lower Hill, Upper Hill, and Bunyala Roads (KURA, 2016). Phase II roads comprise of Mawenzi road, Menengai road, Matumbato road, Masaba road, Chyulu road, link road between Chyulu and Mara road and

improve roads in KNH (Kinoti, 2017). Challenges cited during this process include poor planning, lack of adequate space for road expansion, unwillingness to surrender land for road reserves by land owners leading to lack of access relocation of services such as power-lines, data cables, sewer and water lines (KURA, 2016; Kinoti, 2017).

4.2.2 Land Surface Temperature Hot Spots

Hotspot analysis for 1986, 2000 and 2017 shows that the coolest area in the study is in the northern parts for day LST while at night these areas are warmer. The coolest areas in 1986 (Figure 4.16 a & b) have temperatures of between 20.36 ^{0}C to 23.5 ^{0}C, which is below the mean LST of 24.53 ^{0}C (Figure 4.3) and are cold spots of 99% confidence. The southern areas have cold spots at 95% confidence which is forest land cover. Hot spots are located along the major roads that bound the study area which are Uhuru highway and Mbagathi way. In the southern area is an open field that has high temperatures of between 26.5 ^{0}C and 28.0 ^{0}C. Other blocks that have hot spots of 95% to 99% are Kenyatta National Hospital, Nairobi Hospital and Nairobi Club. Kenyatta National Hospital whose built-up area comprises not only the buildings that cover large areas, but also parking spaces, which are not considered in the calculation of BVD or GCR.

Cold spots in 2000 are located in the north and southern parts of Upper Hill (Figure 4.16 c & d), though the extent has reduced from 1978. These areas have temperatures of between 26.5 ^{0}C to 31.0 ^{0}C, which is below the mean LST of 32.52 ^{0}C (Figure 4.3) and are cold spots of 99% confidence. Hot spot areas of between 90% to 99% confidence are along Haile Selassie road and Uhuru Park, Nairobi Hospital, Kenyatta National Hospital, Nairobi Club, Upper Hill High School field and open grounds in the south of Upper Hill.

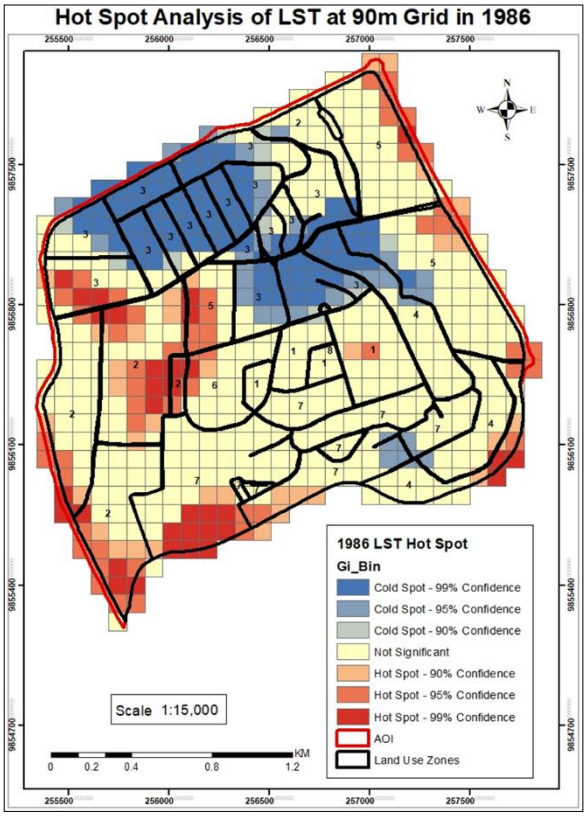
Hot Spot Analysis of LST at 90m Grid in 1986
1986 LST Hot Spot
Gi_Bin
Cold Spot - 99% Confidence
Cold Spot - 95% Confidence
Cold Spot - 90% Confidence
Not Significant
Hot Spot - 90% Confidence
Hot Spot - 95% Confidence
Hot Spot - 99% Confidence
AOI
Land Use Zones
Scale 1:15,000
KM
0 0.2 0.4 0.8 1.2

a.

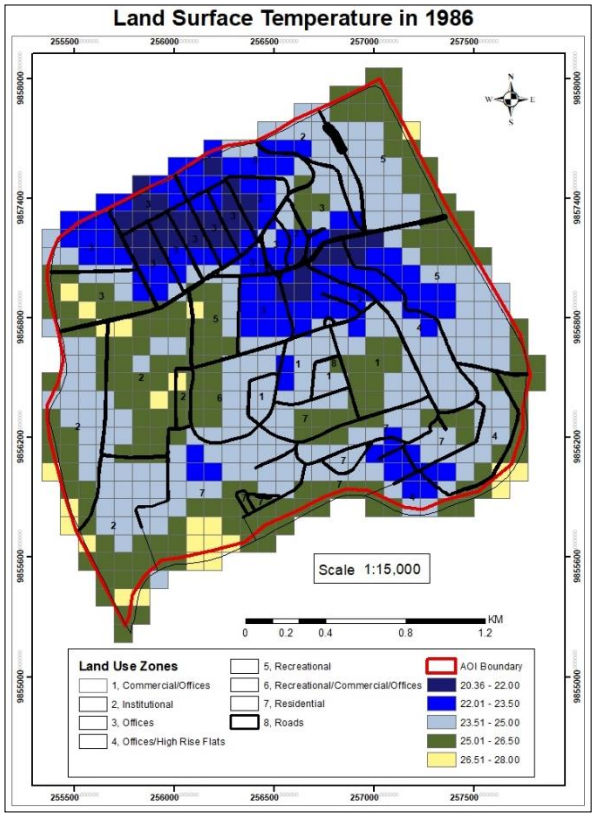
Land Surface Temperature in 1986
Scale 1:15,000
KM
0 0.2 0.4 0.8 1.2
Land Use Zones
1, Commercial/Offices
2, Institutional
3, Offices
4, Offices/High Rise Flats
5, Recreational
6, Recreational/Commercial/Offices
7, Residential
8, Roads
AOI Boundary
20.36 - 22.00
22.01 - 23.50
23.51 - 25.00
25.01 - 26.50
26.51 - 28.00

b.

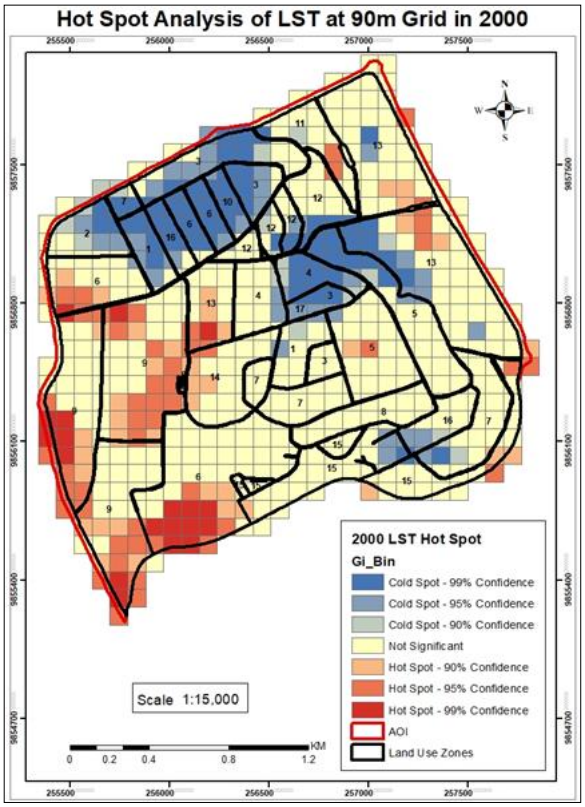
Hot Spot Analysis of LST at 90m Grid in 2000
2000 LST Hot Spot
Gi_Bin
Cold Spot - 99% Confidence
Cold Spot - 95% Confidence
Cold Spot - 90% Confidence
Not Significant
Hot Spot - 90% Confidence
Hot Spot - 95% Confidence
Hot Spot - 99% Confidence
AOI
Land Use Zones
Scale 1:15,000
KM
0 0.2 0.4 0.8 1.2

c.

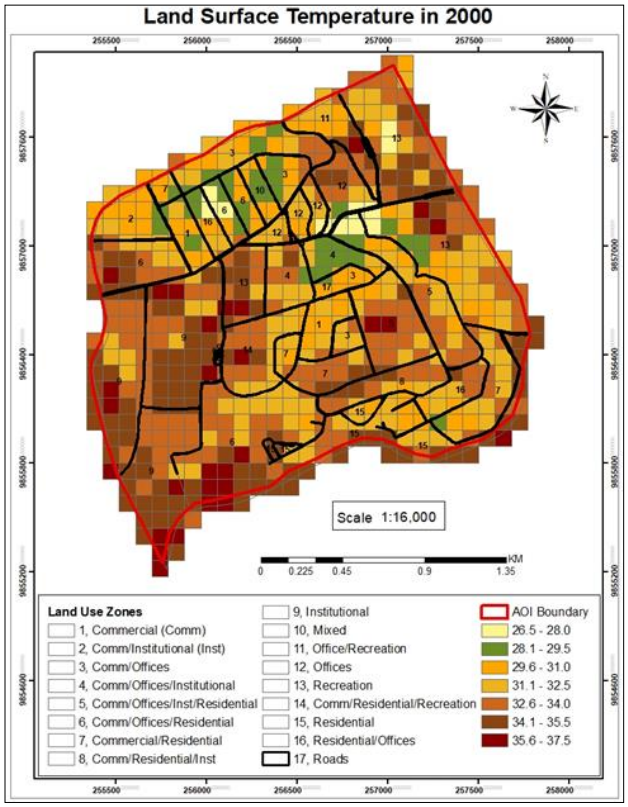
Land Surface Temperature in 2000
Scale 1:16,000
KM
0 0.225 0.45 0.9 1.35
Land Use Zones
1, Commercial (Comm)
2, Comm/Institutional (Inst)
3, Comm/Offices
4, Comm/Offices/Institutional
5, Comm/Offices/Inst/Residential
6, Comm/Offices/Residential
7, Commercial/Residential
8, Comm/Residential/Inst
9, Institutional
10, Mixed
11, Office/Recreation
12, Offices
13, Recreation
14, Comm/Residential/Recreation
15, Residential
16, Residential/Offices
17, Roads
AOI Boundary
26.5 - 28.0
28.1 - 29.5
29.6 - 31.0
31.1 - 32.5
32.6 - 34.0
34.1 - 35.5
35.6 - 37.5

d.

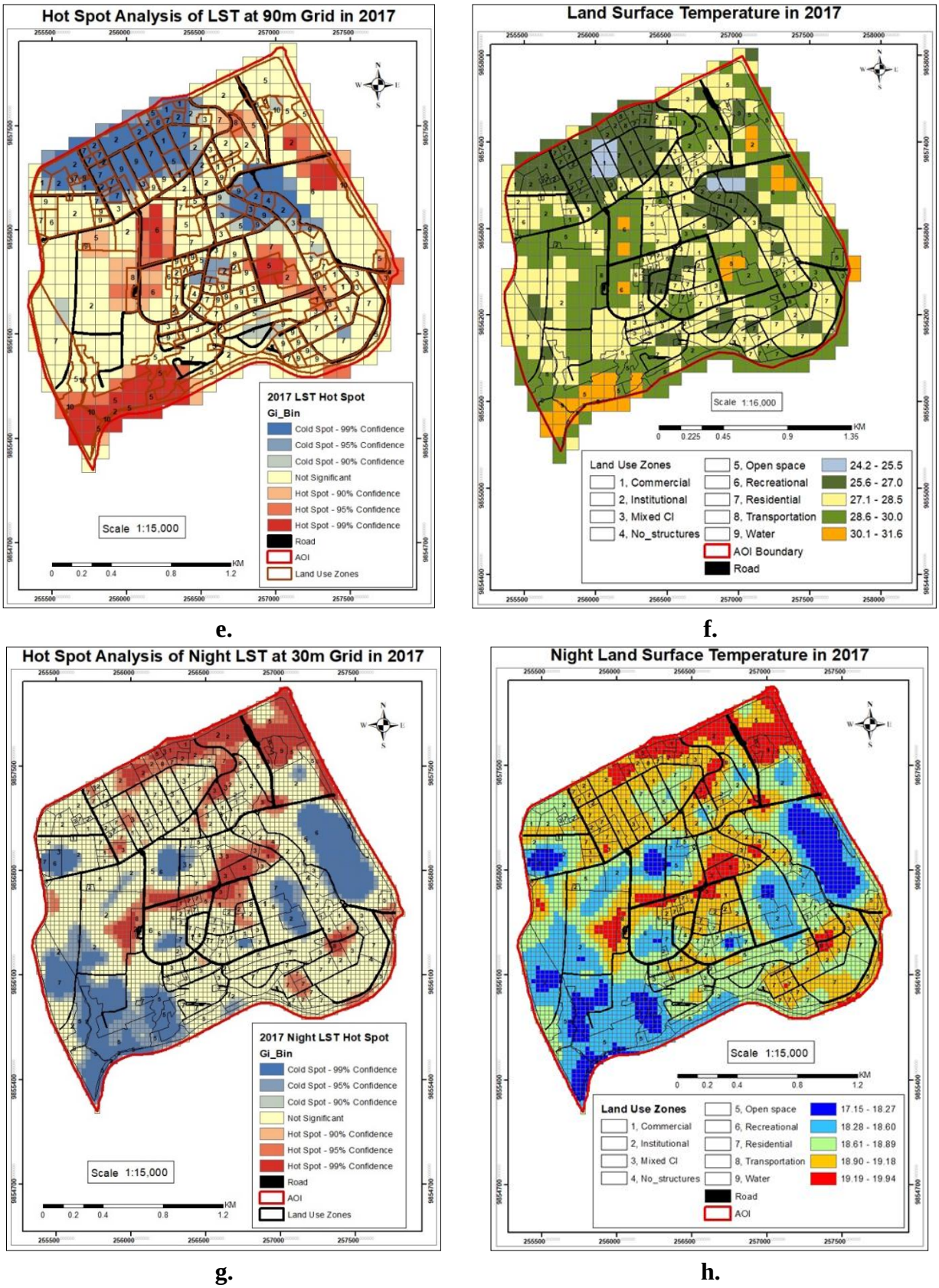

Figure 4.16: Hotspot Analysis and LST for 1986, 2000, 2017 in Upper Hill, Nairobi

The temperature range is between 34.0 ^{0}C and 37.5 ^{0}C, which is the highest temperature amongst the three years. Kenyatta National Hospital is the only hot spot that has high GCR and BVD values. Other hot spot areas do not have high density buildings but consist of open grounds that have sparse grassland. Kenyatta National Hospital staff house location is a hot spot area as the houses are widely spaced from each other and the surrounding land cover is sparse grassland. The contribution index for areas that have sparse grassland is positive and it tends to have the highest temperature amongst the other land covers. This explains why these areas are hot spots despite having low to no built-up densities. Cold spots in 2017 of 99% confidence are in the northern parts of Upper Hill (Figure 4.16 e & f) where there is forest land cover. Other cold spots have a confidence level of 90% and are scattered grids. The cold spot temperatures are between 24.0 ^{0}C and 27.0 ^{0}C which is below the mean LST of 28.10 ^{0}C (Figure 4.3). The area that has high BVD and GCR values is the institutional block that has Social Security House and parts of community area. The other cold spot of 99% interval is near Railways Club which has forest cover. The hot spots have temperatures of between 28.5 ^{0}C and 31.6 ^{0}C and are at Kenyatta National Hospital and National Industrial Credit (NIC) Bank and Bunyala road area which are built-up, Nairobi Club, Upper Hill High School, south of the study area and the area between Uhuru Park and Railways Golf Club which are all open grounds with minimal built-up values and have sparse grassland.

Night-time analysis indicates cold spots occurring in areas that have hotspots during the day in 2017 (Figure 4.16 g & h) signifying a cooling at night. These are open grounds that have open or sparse grassland land cover since they cool faster at night (Figure 4.8). Hotspots occur in the north, central and southern parts of Upper Hill signifying warmer areas with high temperatures.

These are also areas that have high 3D urban intensity expansion of averagely 23.66% per annum. Areas include open space in Uhuru Park due to the presence of a water body that emits heat at night, institutional, commercial and mixed use. High temperatures are also along roads such as Mara road, Upper Hill road, Hill lane, Ngong road, Cathedral road and Processional Way. Roads are also contributors to the emitted heat at night and not buildings, which indicates it is imperative to include them in urban heat studies and in planning. The land cover under and surrounding trees in urban areas is most often tarmacked and contributes to warm temperatures in areas whose land cover is indicated as forest. Hotspot areas with more than 90% confident interval have BVD of 2.3 m^3/m^2 with a GCR of 0.23. Mean height of buildings is 6.4 m with a maximum height of 96.7 m. These are low-rise buildings, low density GCR and medium density BVD. Cold spots with 90% confidence interval have BVD of 0.79 m^3/m^2, GCR of 0.11 and mean height of buildings at 2.83 m with a maximum height of 46.5 m. These are low-rise buildings with low density BVD and GCR.

Summary hot-spot analysis results of LST with BVD in Upper Hill in 1978, 2000 and 2017 are presented in Table 4. *2*. At night in 2017, both LST and BVD values in hot-spot regions are high compared to cold-spot areas. This indicates that during the day, areas with low BVD are warmer than areas with high BVD, while at night areas with high BVD are warmer as they are emitting already absorbed energy. Confidence interval categorized as ‘hot-spot’ has high LST and low BVD values compared to areas categorized as ‘cold spot’ using data collected from morning LST. The size and form of UHI in an urban area differs in time and places because of differences in urban, regional and meteorological characteristics (Shahmohamadi *et al*., 2012).

Table 4. 2: Hot-Spot LST Analysis with BVD

Confidence		1978		1998		2017			
		Morning LST (C^0)	**BVD m^3/m^2**	**Morning LST (C^0)**	**BVD m^3/m^2**	**Morning LST (C^0)**	**BVD m^3/m^2**	**Night LST (C^0)**	**BVD m^3/m^2**
Cold Spot	99%	22.04	0.38	29.05	1.26	26.00	2.28	18.19	0.73
	95%	22.82	0.43	30.40	1.11	26.64	9.23	18.41	0.74
	90%	23.38	0.82	30.80	1.41	26.92	3.42	18.48	1.19
Not Significant		24.56	0.30	32.81	0.68	28.14	1.96	18.81	2.36
Hot Spot	99%	26.62	0.45	35.80	0.13	30.30	0.12	19.35	1.89
	95%	25.98	0.20	35.02	0.67	29.57	0.86	19.14	2.62
	90%	25.72	0.28	34.47	0.64	29.27	0.69	19.06	2.55

Land cover plays an important role in land surface temperature as shown through the hot spot analysis (Figure 4.16). However the role of each land cover over an area depends on the time of day due to differences in materials and texture. Areas that are adjacent to dense forest cover have low surface temperatures than surrounding non-vegetated areas or those that have open grassland as a land cover. Areas whose land use is commercial or institutional have high surface temperatures due to intensity of built-up surfaces such as building blocks, pavement and parking areas. Though area and density of parking lots and pavements are not included in the analysis, they are important in understanding their influence on land surface temperatures. The effect of rezoning Upper Hill has resulted to an increase in built-up surfaces such as buildings, pavements and expansion of roads to accommodate the growing population (NTPLC, 1993). This has led to an increase in demand for parking spaces and the number of vehicles transiting through Upper Hill especially during peak hours. The net effect on the temperature is the increase in the mean surface temperature from 24.4 ^{0}C in 1986 to 32.6 ^{0}C in 2000 and 28.1 ^{0}C in 2017 indicating that

construction of modern buildings for office space or commercial use on land that was forested does influence local climatic conditions. The increase in ground coverage ratio over plots without the provision for vegetative cover has seen such areas having high temperatures at night (Figure 4.8) making the area warmer.

Urban forests are known to improve the thermal comfort of its citizens by reducing the UHI effect, people's well-being and social cohesion (Sodoudi *et al*., 2018). Incorporating green roofs to buildings also reduces the ambient temperature while reducing air pollution. Strategies identified in Melbourne, Australia on managing urban forests are increasing tree canopies, having a diversity of tree species, improving the urban ecology while consulting with the local community on its management (CoM, 2012). Figure 4.16 indicates that the cooling effect of trees in Uhuru Park is not significant to indicate a cold spot as they are not densely located as compared to the areas that are cold spots. Tree forms in urban areas should have a pyramid, vase or umbrella shape which is different from those found in rural settings (Crabtree & Hall, 2016). Basic urban design principles of choosing trees include selection of large trees, a limitation on the variety of tree species due to the harsh urban environment and that trees be planted close together in a grid or geometric pattern which is visually appealing (Crabtree & Hall, 2016). Plant species with massive canopies and dense leaves have higher transpiration rates and attenuation effects as a tree canopy temperature is determined by transpiration and the physical traits of the leaf where the amount of radiation that penetrates depends on the tree species (Sodoudi *et al*., 2018). Trees grown in parks may not be suitable along streets due to differences in adaptability to differences in urban conditions. Park trees are suitable in areas with large open spaces without restrictions under or above ground, while consideration for street trees include tree litter,

tolerance to pollution and having a low potential as an allergen (CoM, 2011). Tree species such as *Ficus benjamina* (weeping fig) which grows up-to 20 meters when mature was considered suitable in regulating ambient and surface temperatures (Sodoudi *et al*., 2018). Therefore, trees that would be recommended in an urban area are those that have a large and dense canopy and foliage that would cast a shadow to improve thermal effect and reduce wind effect (Sodoudi *et al*., 2018; CoM, 2011). A site assessment should be done that consider the above ground limitations such as wires, structure proximity; soil factors; climate factors such as hardiness, wind, heat; below ground limitations such as space for rooting , utilities. Once these as well as others are considered then a suitable species can be recommended at each location (Bassuk *et al*., 2009), while still understanding that there is no perfect one tree for an urban area (CoM, 2011).

4.3 Spatial Relationship between Built-up Volume Densities & Land Surface Temperature

4.3.1 Regression Analysis of Land Surface Temperature

Single-factor models in two scales at 30 meters and 90 meters show that depending on which regression analysis one is using, the scale affects the results (Table 4.3). OLS and GWR perform well at scales of 90 m compared to the 30 m grid for height, GCR and BVD while NDVI, aspect and albedo perform better at 30m grids. In 2017 height, GCR and BVD perform better at 30 m grid but results are shown at 90 m grids for comparison purposes with 1978 and 1998 results. GWR results for albedo did not run at 30 m grid in 1978 due to the range of variables between grid cells hence results are displayed for 90 m grids while 30 m grid results are shown for 1998 and 2017. GWR is used to explore the relationships between variables which global methods such as OLS are not able to explain or demonstrate. The spatial variability between LST and other variables and the local determinants of this variability are in table 4.3.

Table 4.3: LST and Explanatory Variables at 30 m and 90 m Grids in Upper Hill, Nairobi

Variables	Grid	Model	AICc			Adjusted R^2			F		
			1978	1998	2017	1978	1998	2017	1978	1998	2017
Height	30m	OLS	16513.12	20630.67	15716.42	0.01	0.03	0.05	30.86	132.35	229.31
		GWR	9501.00	16635.31	8198.82	0.77	0.58	0.81			
	90m	OLS	1932.96	2356.56	1806.40	0.04	0.06	0.08	25.98	34.16	52.71
		GWR	1056.82	1860.48	1068.80	0.82	0.65	0.81			
GCR	30m	OLS	16513.98	20743.75	15852.90	0.01	0.00	0.02	29.99	17.53	88.33
		GWR	9705.85	16705.98	7265.85	0.77	0.58	0.84			
	90m	OLS	1930.50	2378.74	1829.70	0.05	0.02	0.05	28.55	11.17	27.84
		GWR	1077.21	1855.27	1044.62	0.81	0.65	0.82			
BVD	30m	OLS	16522.70	20729.57	15835.02	0.00	0.01	0.02	21.22	31.79	106.58
		GWR	9679.62	16757.50	7347.86	0.77	0.57	0.84			
	90m	OLS	1957.40	2377.40	1823.14	0.00	0.02	0.06	1.05	12.53	34.73
		GWR	1028.50	1843.69	1031.95	0.83	0.66	0.82			
NDVI	30m	OLS	15665.73	19463.35	15849.18	0.17	0.24	0.02	964.21	1492.01	92.13
		GWR	132.50	8288.16	-159.36	0.97	0.94	0.97			
	90m	OLS	1808.98	2222.80	1825.80	0.23	0.25	0.05	170.50	193.66	31.93
		GWR	1154.37	1538.30	976.48	0.77	0.83	0.85			
Aspect	30m	OLS	16506.08	20754.52	15934.85	0.01	0.00	0.00	37.94	6.74	5.61
		GWR	8783.22	16370.02	7660.78	0.81	0.61	0.83			
	90m	OLS	1957.06	2386.57	1856.83	0.00	0.00	0.00	1.38	3.27	0.13
		GWR	1038.86	1867.23	1115.61	0.84	0.64	0.78			
Albedo	30m	OLS	15925.43	19629.83	15187.46	0.12	0.21	0.15	660.27	1277.08	815.65
		GWR	-	17279.72	12327.15	-	0.52	0.53			
	90m	OLS	1865.98	2221.18	1721.87	0.15	0.26	0.21	100.11	195.84	140.12
		GWR	1736.89	2095.46	1595.12	0.33	0.41	0.38			

GWR gives varied results from OLS as it is a local model rather than global model. The Akaike Information Criterion (AICc) with the GWR model improves by more than a value of three and is of a lower than the OLS value, indicating an improvement in the model when using GWR. The AICc is normally used as a relative measure for comparison between models that have the same independent variables. It measures relative distances between the unknown 'true' model and the fitted model, with low value models being preferable than those with high values of AICc (Fischer *et al*., 2010). The negative sign in the AICc value is not an indicator of any relationship and thus considered insignificant.

The NDVI explanatory variable has the lowest AICc value compared to OLS and other explanatory variables, which indicate that it is a much better predictor than the other explanatory variables. The spatial relationship between LST and each explanatory variable from 1978 to 2017 varies as indicated by the r^2 value in each of the three years, with 1978 having low r^2 variable. NDVI adjusted r^2 value at 30 m scale are high compared to height, GCR, BVD, albedo and aspect for all years showing that it best explains the spatial relationship with LST. Aspect affects the amount of solar radiation incident on Upper Hill hence the LST due to the direction of the slope and this effect reduces from 1978 to 2017. Scale effect on aspect is not significant with little variation in r^2 values except in the year 2017. GWR for albedo in 1978 at 30 m scale does not run due to the little variation in variables across Upper Hill. Albedo has better results in OLS compared to other variables but has lower r^2 values with GWR. Changes in the r^2 values in BVD and GCR from 1978 to 2017 is as a result of the increasing development over the area. This supports the notion that urban geometry one factor that leads to the modification of local urban climate (JICA, 2014).

The value of r^2 in 1978, 1998 and 2017 of height, BVD and GCR are within the same range indicating that their interaction and impact with LST is nearly the same in Upper Hill. However the spatial variance of each of these variables is best described using the coefficient, which indicates the nature of relationship between the variables and the strength i.e. positive or negative. In urban areas, incoming radiation received depends on shade provided by buildings, air pollution, orientation of street network and cloud cover (Rad *et al*., 2017).

The 90 meter grid (Table 4.1) show an improvement in the OLS results compared to the same at 30 meters. This is because OLS performs better with fewer points over an area as this reduces the range of values and affects the regression line. However, with GWR the effect is different where the results do not show much variation between 1978 and 2017, with low r^2 values obtained in 1998. This is a result of the "scale effect" where the scale at which an analysis is undertaken on non-stationary variables influences the model in terms of the direction and parameter values, strength of the relationship, accuracy of the prediction and others (Propastin *et al*., 2008). This indicates that these variables and processes operated at different spatial scales. The AICc values at 90 m were more than the AICc values in the 30 m grids. The AICc values reduced when using the GWR analysis compared to OLS in 90 m grids. These values are also smaller than the values obtained at 30 meters due to the reduced number of grids in the analysis.

OLS results at 90 m grid indicate that the modelled relationship between the explanatory variables and LST varies across the years. All r^2 values in all years, except NDVI and albedo, indicate a weak relationship due to low values tending to zero. Height and BVD are the only explanatory variables that increases from 1978 to 2017. Height increases progressively by 2%

while BVD shows no relationship with LST in 1978. GCR shows a decrease in r^2 value in 1998 and has the same value of 5% in 1978 and 2017. NDVI indicates that in 2017, the relationship between LST and NDVI is low in this year. Elevation is not analyzed with LST using GWR as a model error is obtained in both 30 m and 90 m grid while with OLS it is statistically insignificant with r^2 values of less than 1%. NDVI is a better explanatory variable in explaining variance in surface temperature than other variables in 1978 and 1998, while in 2017, height is a better explanatory variable.

Results for each of the individual variables with LST using the GWR model are explained in detail using the r^2 and coefficients (Figure 4.17 to Figure 4.22). Coefficients have positive and negative values indicating mixed effects on LST by the predictor. Local multicollinearity is not observed as the conditional number in each analysis is less than 30 and not less than or equal to zero. Presence of multicollinearity would indicate that the results are unstable (Esri, 2018). GWR results show non-stationary relationship between LST and NDVI across the study area with parts have positive and negative coefficients since NDVI values range between -1 and 1, varying with the presence or absence of vegetation (Figure 4.17). Pearson's correlational analysis between LST and NDVI indicates a negative relationship in 1978, 1998 and 2017 (Appendix 13). Negative coefficient indicates that as NDVI values increase in value LST reduces. Positive coefficients indicate that as the NDVI values increase LST also increases and they have a positive relationship. At the zero value, there's little influence that changes in NDVI have on LST.

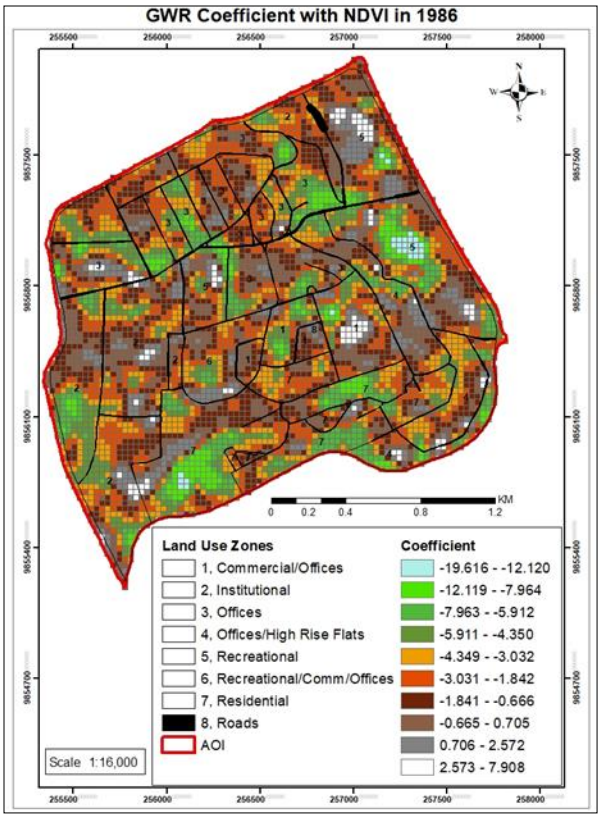
GWR Coefficient with NDVI in 1986
Land Use Zones
1, Commercial/Offices
2, Institutional
3, Offices
4, Offices/High Rise Flats
5, Recreational
6, Recreational/Comm/Offices
7, Residential
8, Roads
AOI
Coefficient
-19.616 - -12.120
-12.119 - -7.964
-7.963 - -5.912
-5.911 - -4.350
-4.349 - -3.032
-3.031 - -1.842
-1.841 - -0.666
-0.665 - 0.705
0.706 - 2.572
2.573 - 7.908
Scale 1:16,000
KM
0 0.2 0.4 0.8 1.2

a.

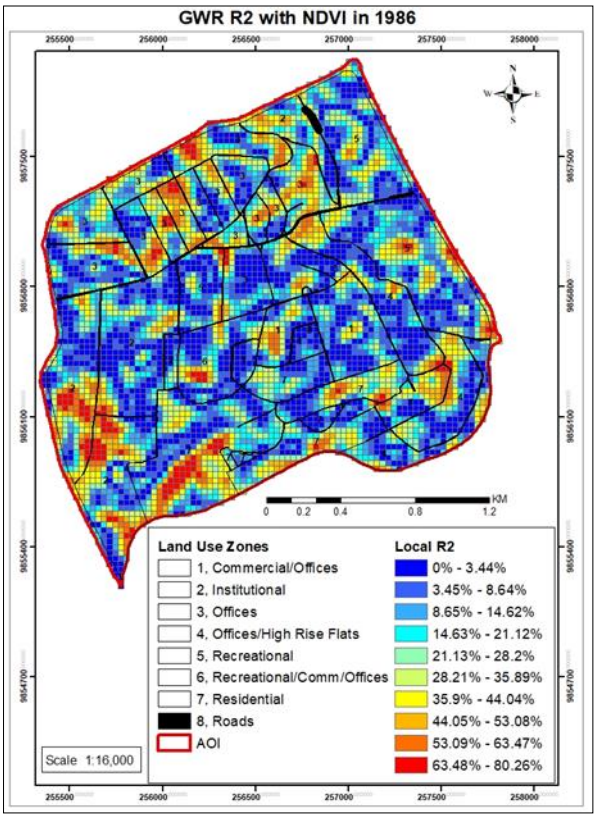
GWR R2 with NDVI in 1986
Land Use Zones
1, Commercial/Offices
2, Institutional
3, Offices
4, Offices/High Rise Flats
5, Recreational
6, Recreational/Comm/Offices
7, Residential
8, Roads
AOI
Local R2
0% - 3.44%
3.45% - 8.64%
8.65% - 14.62%
14.63% - 21.12%
21.13% - 28.2%
28.21% - 35.89%
35.9% - 44.04%
44.05% - 53.08%
53.09% - 63.47%
63.48% - 80.26%
Scale 1:16,000
KM
0 0.2 0.4 0.8 1.2

b.

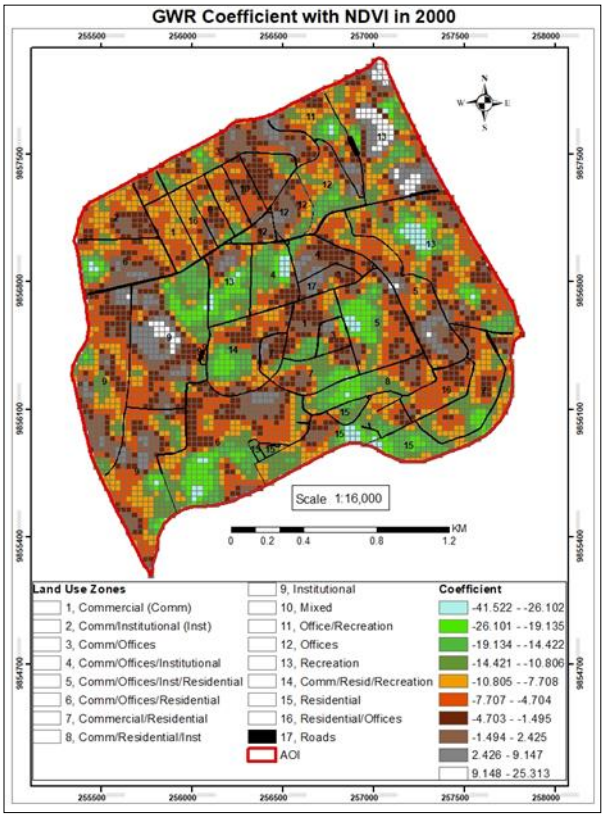
GWR Coefficient with NDVI in 2000
Land Use Zones
1, Commercial (Comm)
2, Comm/Institutional (Inst)
3, Comm/Offices
4, Comm/Offices/Institutional
5, Comm/Offices/Inst/Residential
6, Comm/Offices/Residential
7, Commercial/Residential
8, Comm/Residential/Inst
9, Institutional
10, Mixed
11, Office/Recreation
12, Offices
13, Recreation
14, Comm/Resid/Recreation
15, Residential
16, Residential/Offices
17, Roads
AOI
Coefficient
-41.522 - -26.102
-26.101 - -19.135
-19.134 - -14.422
-14.421 - -10.806
-10.805 - -7.708
-7.707 - -4.704
-4.703 - -1.495
-1.494 - 2.425
2.426 - 9.147
9.148 - 25.313
Scale 1:16,000
KM
0 0.2 0.4 0.8 1.2

c.

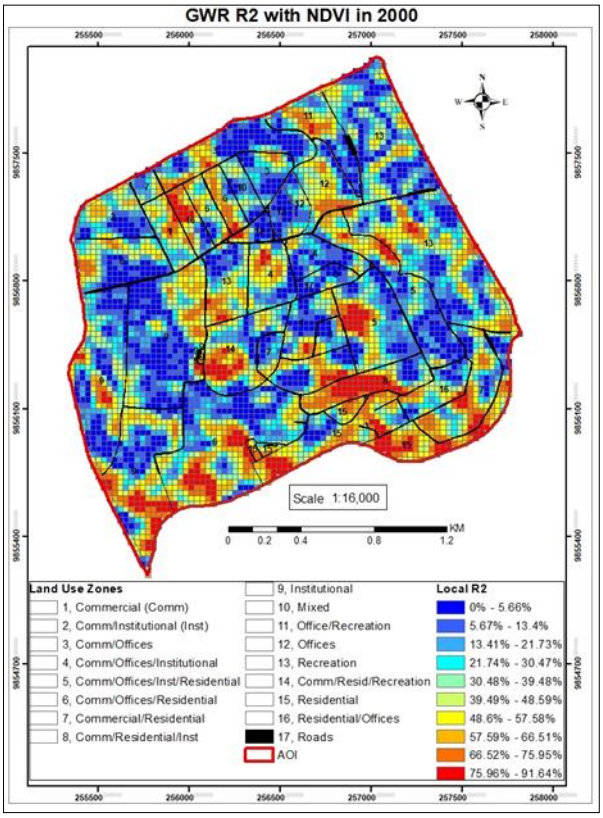
GWR R2 with NDVI in 2000
Land Use Zones
1, Commercial (Comm)
2, Comm/Institutional (Inst)
3, Comm/Offices
4, Comm/Offices/Institutional
5, Comm/Offices/Inst/Residential
6, Comm/Offices/Residential
7, Commercial/Residential
8, Comm/Residential/Inst
9, Institutional
10, Mixed
11, Office/Recreation
12, Offices
13, Recreation
14, Comm/Resid/Recreation
15, Residential
16, Residential/Offices
17, Roads
AOI
Local R2
0% - 5.66%
5.67% - 13.4%
13.41% - 21.73%
21.74% - 30.47%
30.48% - 39.48%
39.49% - 48.59%
48.6% - 57.58%
57.59% - 66.51%
66.52% - 75.95%
75.96% - 91.64%
Scale 1:16,000
KM
0 0.2 0.4 0.8 1.2

d.

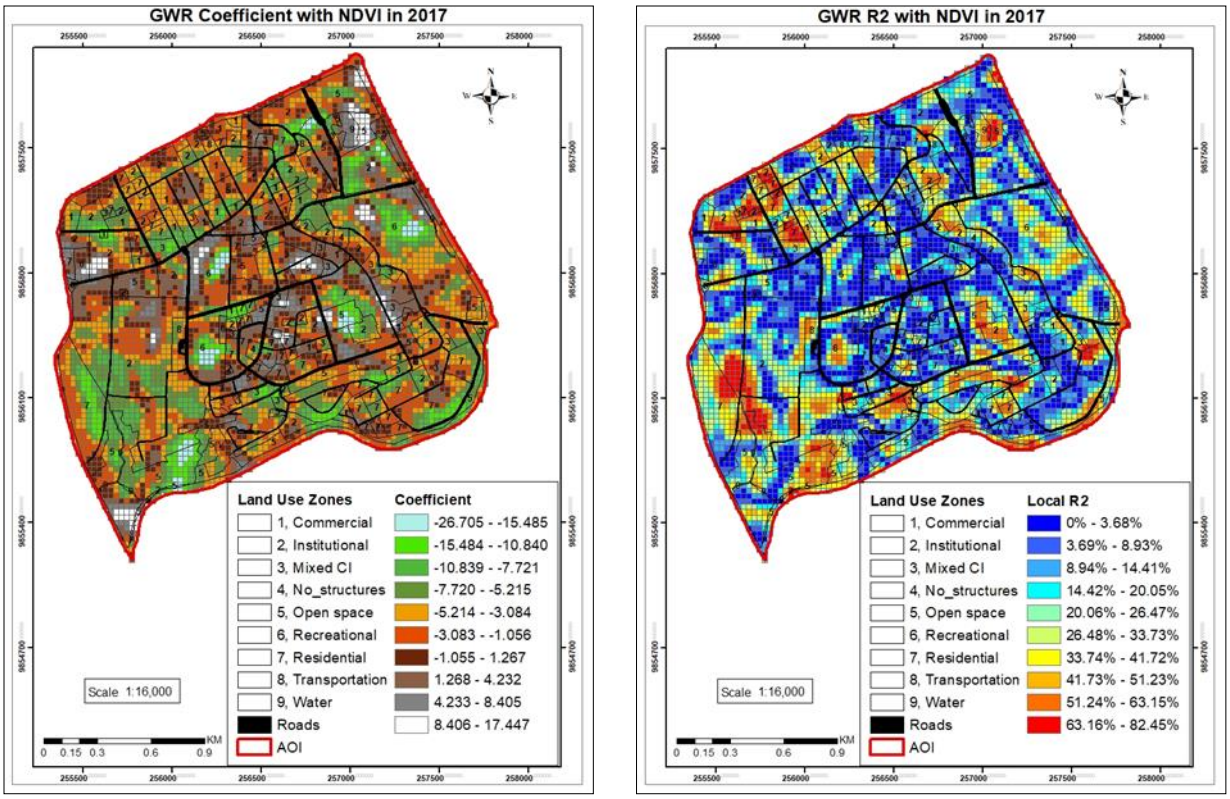

e. **f.**

Figure 4.17: NDVI Coefficient and R^2 Values in 1986, 2000, 2017 in Upper Hill, Nairobi

The variation in temperature reduction is a result of the type and presence of vegetation, leading to an increase or reduction of LST. Mean coefficient values from GWR analysis in 1978, 1998 and 2017 are -2.56, -7.53 and -2.79 respectively indicating a negative relationship with LST as seen using OLS and Pearson's correlational analysis. 1978 negative coefficients of -19.6163 to 0 had an NDVI value of 0.288 while positive coefficients of 0 to 7.9076 had NDVI value of 0.26. R^2 values of more than 20% in 1978 covers 40% of the Upper Hill at NDVI average values of value of 0.29. 1998 negative coefficients of -41.5218 to 0 have NDVI values of -0.079 while positive coefficients of 0 to 25.3122 have NDVI values of -0.149. R^2 values of more than 20% in 1998 covers 60% of Upper Hill with average NDVI values of -0.08. 2017 negative coefficients of -26.7051 to 0 have NDVI values of 0.180 while positive coefficients have NDVI values of

0.15. This indicates areas having high NDVI values i.e. presence of vegetation, have a negative relationship with LST while areas less vegetated have positive values. R^2 values of more than 20% in 2017 covers 42% of Upper Hill with average NDVI values of 0.18. The range effect in 1998 (-41.52 to 25.31) is large compared to 2017 (-26.71 to 17.45) and 1978 (-19.62 to 7.91) indicating the relationship between NDVI and LST is stronger in 1998, followed by 2017 than in 1978. This is indicated in figure 4.3 where the temperature is high and figure 4.11 where the contribution index is high compared to 1986 and 2017.

Land use, soil type and the geographical location affect the relationship between vegetation and its spatial predictors (Propastin *et al*., 2008). The relationship between NDVI and any climatic factor under study varies within different land over types. There have been cases under study where the same vegetation cover type has a non-stationary relationship in space with climatic factor (Propastin *et al*., 2008). This spatial relationship is not visible in previous analysis such as using hot spots as environmental physical factors are spatially auto-correlated. R^2 is calculated across Upper Hill and it varies areas having high r^2 being more reliable than areas with low r^2 values. Tian *et al*., (2012) studies with GWR and NDVI determines that an increased leaf area index (LAI) results to reduced LST as the surface net radiation is partitioned into latent heat flux than sensible heat flux.

Table 4.1 indicates a reduction in the strength of the relationship between LST and aspect from 1978 to 2017. The direction a slope of land faces does not generally change, however, the interaction between slope direction and LST changes in 1978, 1998 and 2017 (Figure 4.18) as aspect affects the intensity of incoming solar radiation on a surface.

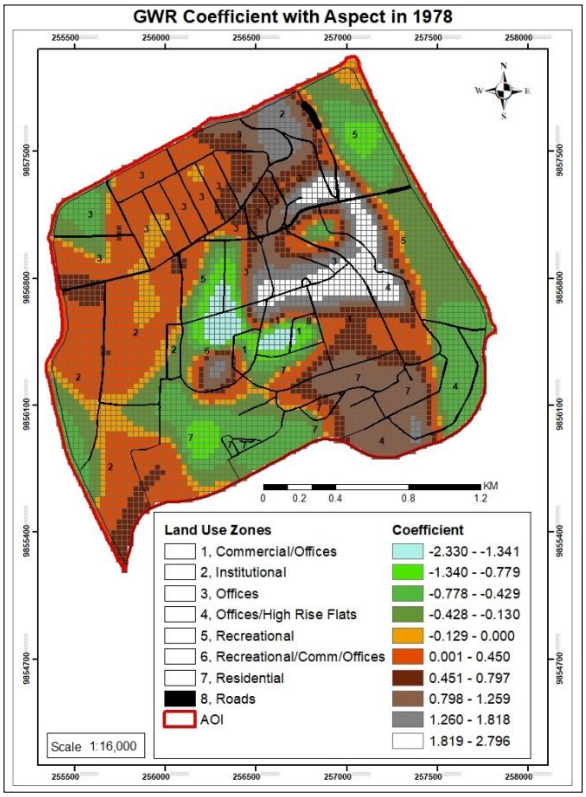
GWR Coefficient with Aspect in 1978
Land Use Zones
1, Commercial/Offices
2, Institutional
3, Offices
4, Offices/High Rise Flats
5, Recreational
6, Recreational/Comm/Offices
7, Residential
8, Roads
AOI
Coefficient
-2.330 - -1.341
-1.340 - -0.779
-0.778 - -0.429
-0.428 - -0.130
-0.129 - 0.000
0.001 - 0.450
0.451 - 0.797
0.798 - 1.259
1.260 - 1.818
1.819 - 2.796
Scale 1:16,000
KM
0 0.2 0.4 0.8 1.2

a.

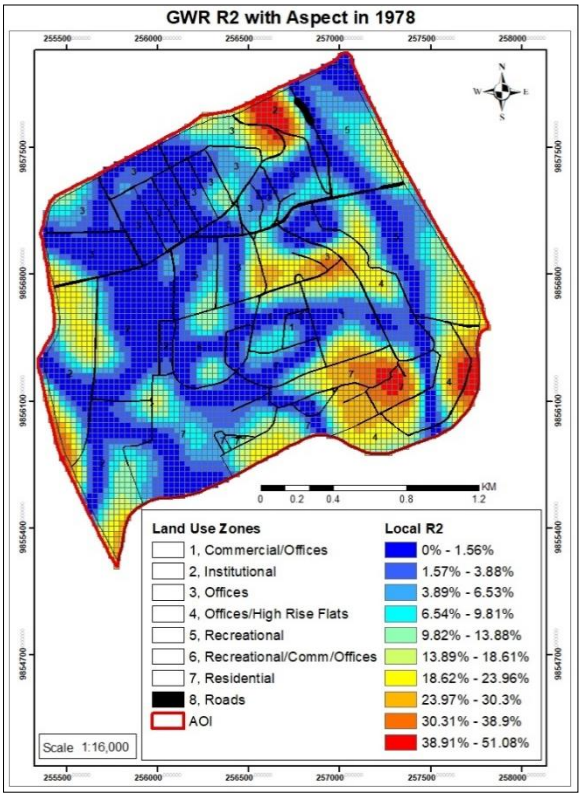
GWR R2 with Aspect in 1978
Land Use Zones
1, Commercial/Offices
2, Institutional
3, Offices
4, Offices/High Rise Flats
5, Recreational
6, Recreational/Comm/Offices
7, Residential
8, Roads
AOI
Local R2
0% - 1.56%
1.57% - 3.88%
3.89% - 6.53%
6.54% - 9.81%
9.82% - 13.88%
13.89% - 18.61%
18.62% - 23.96%
23.97% - 30.3%
30.31% - 38.9%
38.91% - 51.08%
Scale 1:16,000
KM
0 0.2 0.4 0.8 1.2

b.

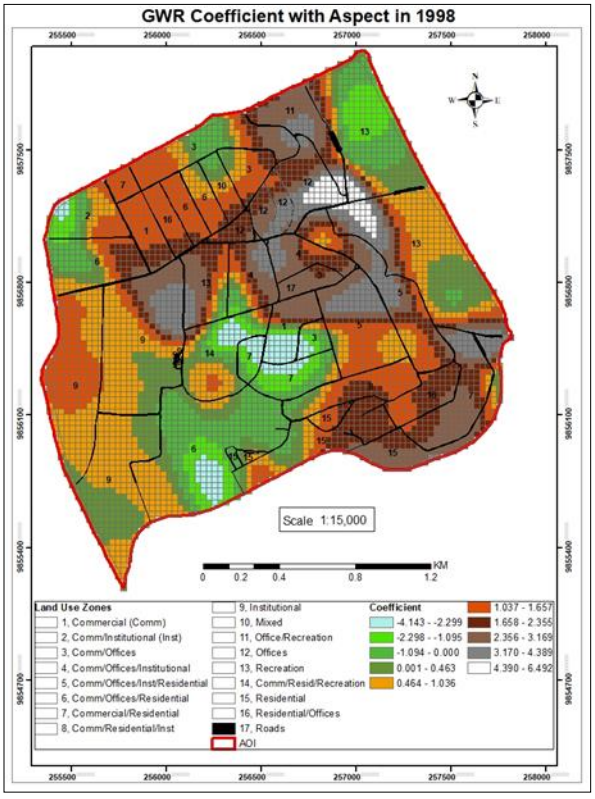
GWR Coefficient with Aspect in 1998
Land Use Zones
1, Commercial (Comm)
2, Comm/Institutional (Inst)
3, Comm/Offices
4, Comm/Offices/Institutional
5, Comm/Offices/Inst/Residential
6, Comm/Offices/Residential
7, Commercial/Residential
8, Comm/Residential/Inst
9, Institutional
10, Mixed
11, Office/Recreation
12, Offices
13, Recreation
14, Comm/Resid/Recreation
15, Residential
16, Residential/Offices
17, Roads
AOI
Coefficient
-4.143 - -2.299
-2.298 - -1.095
-1.094 - 0.000
0.001 - 0.463
0.464 - 1.036
1.037 - 1.657
1.658 - 2.355
2.356 - 3.169
3.170 - 4.389
4.390 - 6.492
Scale 1:15,000
KM
0 0.2 0.4 0.8 1.2

c.

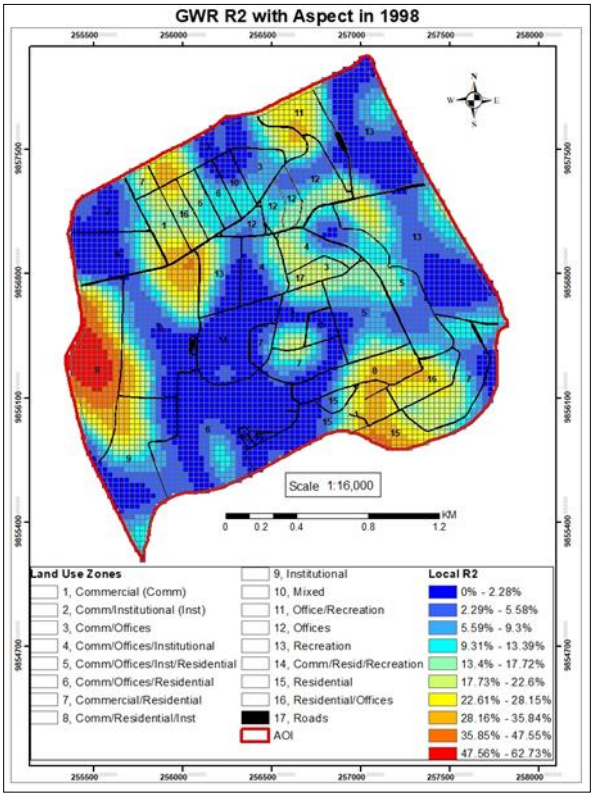
GWR R2 with Aspect in 1998
Land Use Zones
1, Commercial (Comm)
2, Comm/Institutional (Inst)
3, Comm/Offices
4, Comm/Offices/Institutional
5, Comm/Offices/Inst/Residential
6, Comm/Offices/Residential
7, Commercial/Residential
8, Comm/Residential/Inst
9, Institutional
10, Mixed
11, Office/Recreation
12, Offices
13, Recreation
14, Comm/Resid/Recreation
15, Residential
16, Residential/Offices
17, Roads
AOI
Local R2
0% - 2.28%
2.29% - 5.58%
5.59% - 9.3%
9.31% - 13.39%
13.4% - 17.72%
17.73% - 22.6%
22.61% - 28.15%
28.16% - 35.84%
35.85% - 47.55%
47.56% - 62.73%
Scale 1:16,000
KM
0 0.2 0.4 0.8 1.2

d.

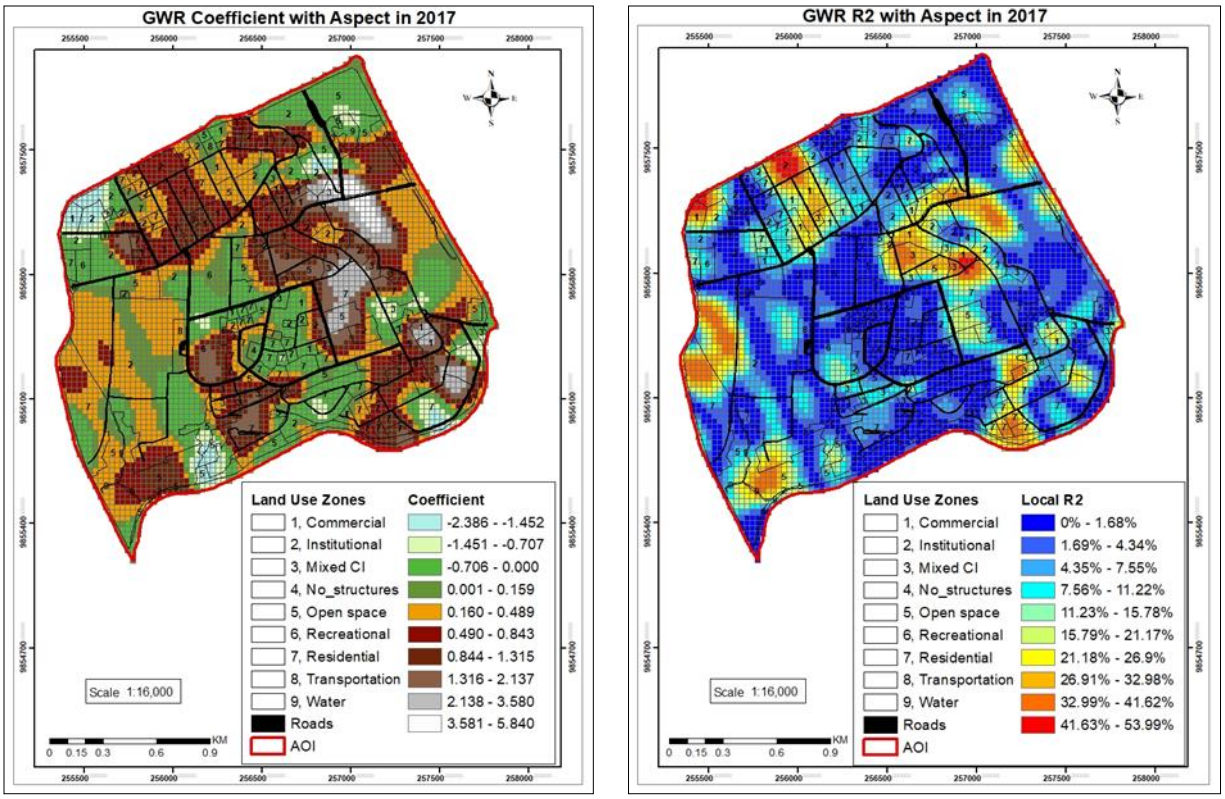

e. **f.**

Figure 4.18: Aspect Coefficient and R^2 Values in 1978, 1998, 2017 in Upper Hill, Nairobi

Pearson correlational analysis indicates a positive relationship with aspect in 1978, 1998 and 2017 (Appendix 13). Negative coefficients of -2.330 to 0 in 1978 have an average value of 122.06 degrees which are south east facing slopes while positive coefficients have an average value of 99.37 degrees which are east facing slopes. Eastern facing slopes have a strong relationship with aspect than western facing slopes therefore warming up faster. Across Upper Hill a reduction and increase in LST with changes in aspect, indicated by negative and positive coefficients respectively, differs (Figure 4.18 a). R^2 values vary across the study area indicating different model fit with r^2 values of more than 20% mainly in the eastern and also some western parts of Upper Hill. These are south eastern facing slopes at 132.62 degrees (Figure 4.18 b).

Mean correlation values from GWR in 1978, 1998 and 2017 are 0.001, 1.11 and 0.39 respectively indicating a positive relationship. Negative coefficients in 1998 of -4.143 to 0 have average aspect values of 126.66 degrees which is south eastern facing slopes in the southern and north eastern parts of Upper Hill and is 18% of the study area. Positive coefficients of 0 to 6.492 have average aspect values of 95.26 degrees, eastern facing slopes and 82% of Upper Hill and it has different warming rates (Figure 4.18 c). The range of values between the positive and negative coefficients indicate a strong and nearly equal positive and negative relationship with LST with greater areas having a positive relationship with LST. R^2 values of more than 20% in are south eastern facing slopes at 133.41 degrees and are in the north, western and southern parts of Upper Hill (Figure 4.18 d).

Negative coefficients in 2017 of -2.386 to 0 have average aspect values of 108.74 degrees which are east facing slopes while positive coefficients of 0 to 5.840 have average aspect values of 100.16 degrees which are east facing slopes. Positive coefficient values where LST has a positive relationship with aspect comprise about 72% of Upper Hill (Figure 4.18 e). Negative coefficients where LST has a negative relationship covers 28% of the Upper Hill. The range of coefficients between the positive and negative coefficients indicate a stronger influence on LST with positive coefficients than with negative coefficients. R^2 values of more than 20% are in the north, east and western parts of the Upper Hill and are averagely south east facing slopes of 128.4 degrees (Figure 4.18 f). 1998 has a large range of coefficient values -4.143 to 6.49) compared to 1978 (-2.33 to 2.80) and 2017 (-2.39 to 5.84) indicating that in 1998 the relationship between aspect and LST was strong. Mainly the eastern facing slopes have high positive coefficients and r^2 values indicating that eastern facing slopes warm up faster than other slopes as the sun rises in the east.

This is an important characteristic as thermal comfort and surface temperature are determined by the direction a building faces (Yang *et al*., 2017).

Coefficient of albedo for 1978, 1998 and 2017 have mean positive values of 25.94, 34.45 and 17.91 respectively, indicating a positive relationship between LST and albedo. Pearson correlational analysis between LST and albedo values indicate a positive relationship with albedo in the three years. Negative coefficient values of -6.336 to 0 in 1978 (Figure 4.19 a) which are in the southwestern part of Upper Hill have mean albedo values of 0.20 with minimum and maximum values of 0.18 and 0.21 respectively. Positive coefficient values of 0 to 25.522 which are in the eastern and western parts have mean albedo values of 0.20 with minimum and maximum values of 0.10 and 0.26 respectively.

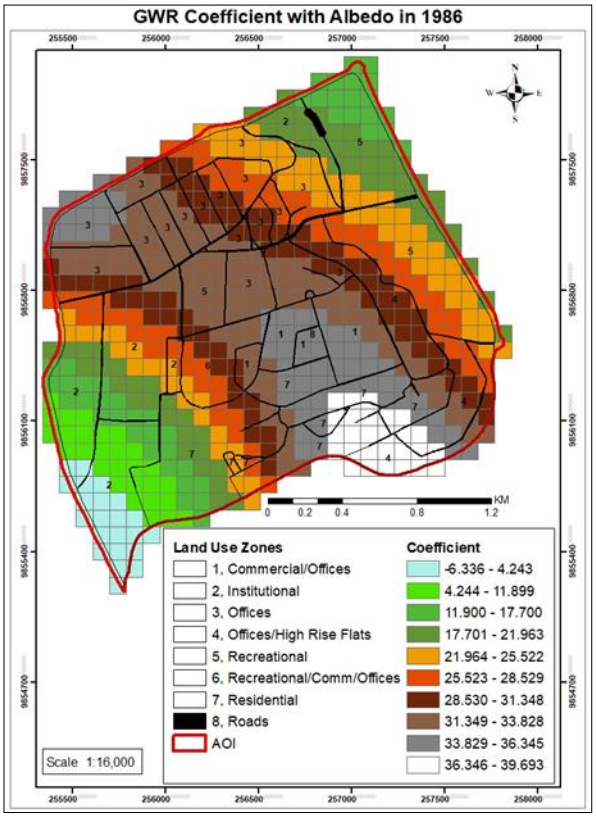

a.

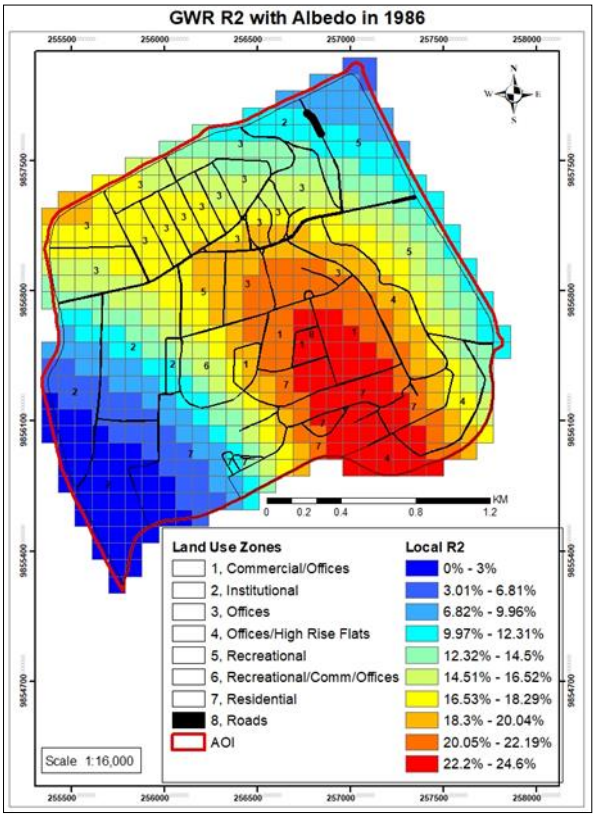

b.

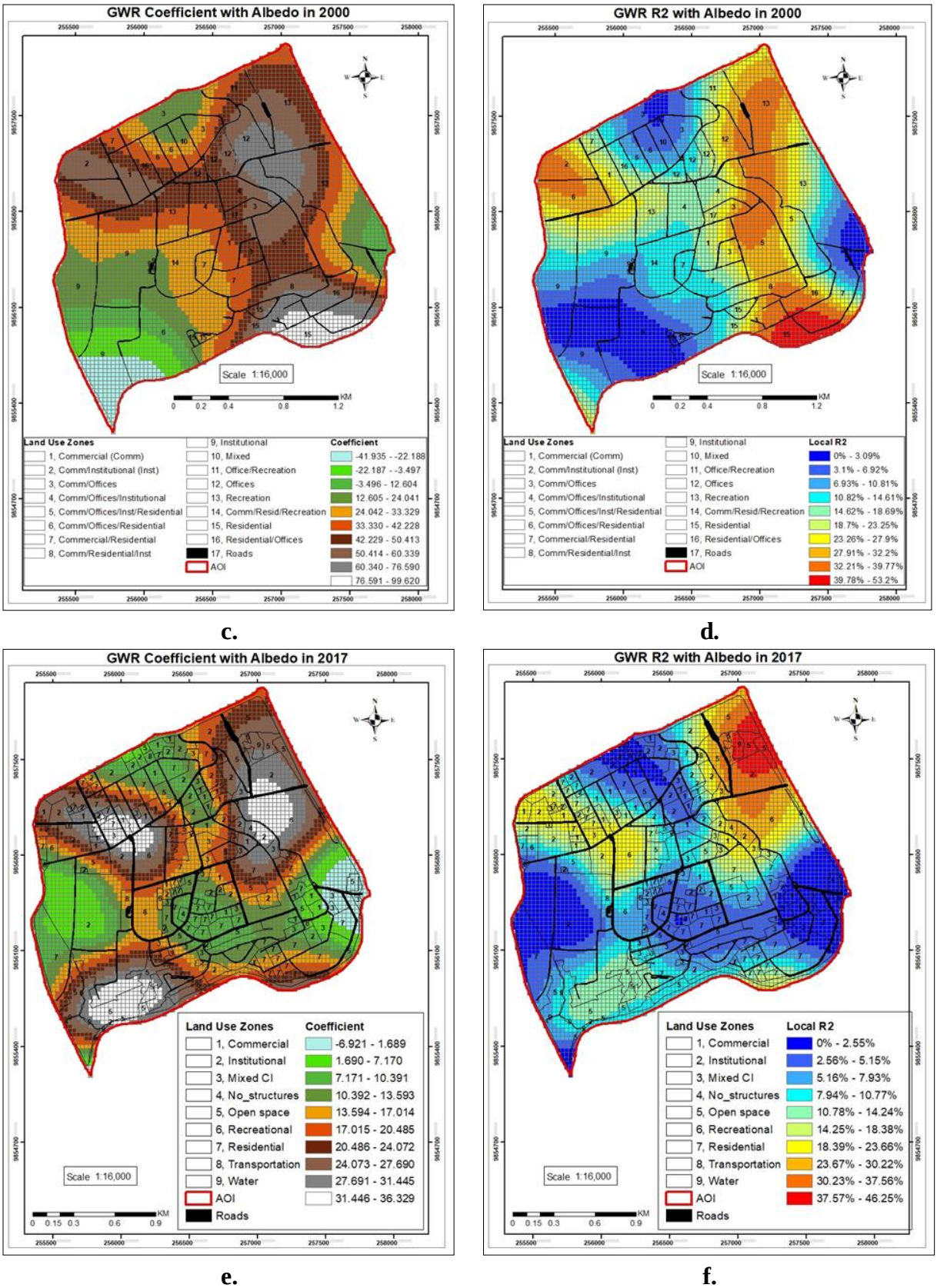

Figure 4.19: Albedo Coefficient and R^2 Values in 1986, 2000, 2017 in Upper Hill, Nairobi

Positive coefficients of 25.523 to 39.693 which is mainly in the central parts of Upper Hill have a mean of 0.19 with minimum and maximum values of 0.15 and 0.26 respectively. R^2 greater than 20% is mainly in the southern-central parts of Upper Hill with a mean albedo of 0.19 whereas r^2 of 10% to 20% has a mean albedo of 0.19 while less than 10% has mean albedo of 0.20 (Figure 4.19 b). The mean albedo with positive and negative coefficients and r^2 values is nearly the same as it is either 0.19 or 0.20 as the area has a high percentage of vegetation cover therefore material types do not differ much in 1978.

Negative coefficients of -41.935 to -22.188 in 1998 (Figure 4.19 c) are in the southwestern part of Upper Hill and has a mean albedo value of 0.153 with minimum and maximum albedo values of 0.123 and 0.186 respectively. Positive coefficients of -22.187 to 0 are in the southwestern part and have mean albedo value of 0.157 with minimum and maximum values of 0.123 and 0.197 respectively. Coefficients of 0 to 42.228 have a mean value of 0.152 with minimum and maximum values of 0.07 and 0.251 respectively. Coefficients of 42.227 to 99.620 have mean albedo values of 0.147 with minimum and maximum values of 0.056 and 0.240 respectively. R^2 values greater than 50% have a mean albedo value of 0.164, r^2 of between 20% and 50% has a mean of 0.149 and covers 41.8% of Upper Hill and r^2 of less than 20% has a mean of 0.151 and covers 57.9% of Upper Hill (Figure 4.19 d). Albedo values reduce from 0.16 where r^2 is greater than 50% to 0.15 where r^2 is less than 50% indicating areas with lower albedo do not have a strong relationship with LST.

Negative coefficients in 2017 (Figure 4.19 e) of -6.921 to 0 are in the southeastern parts of Upper Hill and have mean albedo values of 0.148 with minimum and maximum values of 0.126 and

0.188 respectively. Positive albedo values of 0 to 17.014 are in the northwestern to southeastern parts and have mean albedo values of 0.152 with minimum and maximum values of 0.07 to 0.261. Coefficient values of 17.013 to 36.329 have mean albedo values of 0.154 with minimum and maximum values of 0.058 and 0.258. R^2 greater than 20% are in the eastern part having a mean albedo values of 0.155 and cover 15% of Upper Hill while r^2 of less than 20% have a mean albedo of 0.153 (Figure 4.19 f).

Mean LST and albedo of negative coefficients is higher than LST and albedo of positive coefficients. The range of coefficients in 1998 (-41.935 to 99.620) is large compared to 1978 (-6.336 to 39.693) and 2017 (-6.921 to 36.329) indicating influence of albedo on LST is strong in 1998 compared to 1978 or 2017. Mean albedo values reduce from 1978 to 2017 due to land cover changes where vegetated areas are replaced with built-up areas therefore a variation in albedo values in 2017 than 1978 with the coefficients. The effective albedo is reduced by multiple reflections in urban canyons (Shahmohamadi *et al*., 2012). Roof structure and the building thermal balance affects the cooling load of a building (Shahmohamadi *et al*., 2012).

Pearson's correlational analysis between LST and height indicates a negative relationship (Appendix 13). Mean correlation values from GWR analysis in 1978, 1998 and 2017 are -0.09, -0.10 and -0.03 respectively indicating a negative relationship between LST and height. Height variation influence on LST across the three years differs (Figure 4.20).

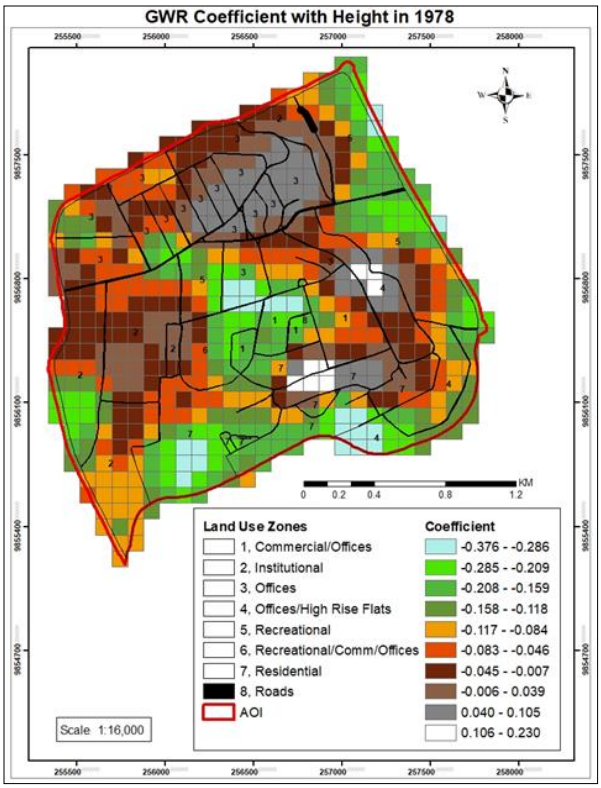
GWR Coefficient with Height in 1978
Land Use Zones
1, Commercial/Offices
2, Institutional
3, Offices
4, Offices/High Rise Flats
5, Recreational
6, Recreational/Comm/Offices
7, Residential
8, Roads
AOI
Coefficient
-0.376 - -0.286
-0.285 - -0.209
-0.208 - -0.159
-0.158 - -0.118
-0.117 - -0.084
-0.083 - -0.046
-0.045 - -0.007
-0.006 - 0.039
0.040 - 0.105
0.106 - 0.230
Scale 1:16,000
KM
0 0.2 0.4 0.8 1.2

a.

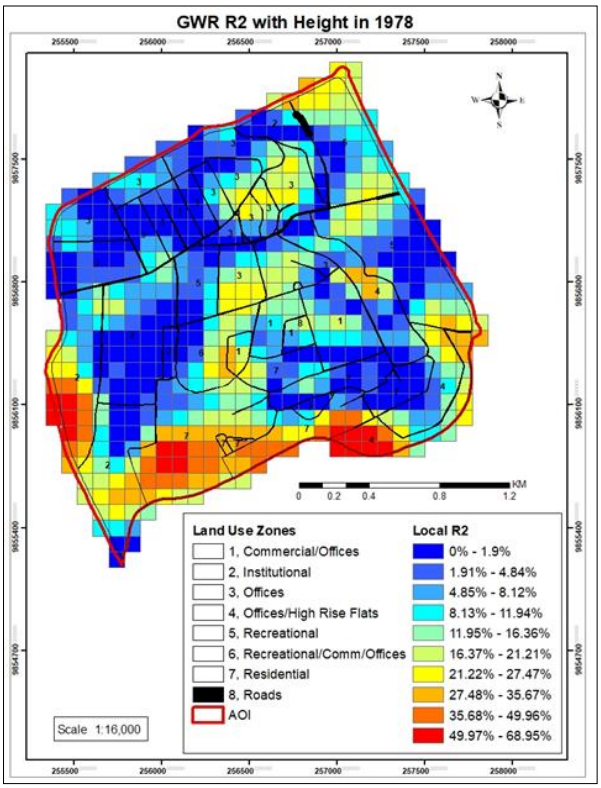
GWR R2 with Height in 1978
Land Use Zones
1, Commercial/Offices
2, Institutional
3, Offices
4, Offices/High Rise Flats
5, Recreational
6, Recreational/Comm/Offices
7, Residential
8, Roads
AOI
Local R2
0% - 1.9%
1.91% - 4.84%
4.85% - 8.12%
8.13% - 11.94%
11.95% - 16.36%
16.37% - 21.21%
21.22% - 27.47%
27.48% - 35.67%
35.68% - 49.96%
49.97% - 68.95%
Scale 1:16,000
KM
0 0.2 0.4 0.8 1.2

b.

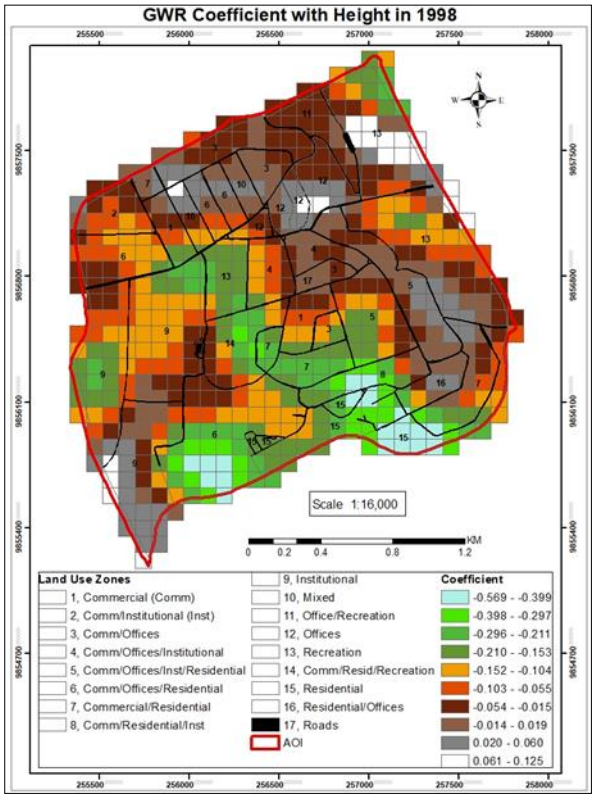
GWR Coefficient with Height in 1998
Land Use Zones
1, Commercial (Comm)
2, Comm/Institutional (Inst)
3, Comm/Offices
4, Comm/Offices/Institutional
5, Comm/Offices/Inst/Residential
6, Comm/Offices/Residential
7, Commercial/Residential
8, Comm/Residential/Inst
9, Institutional
10, Mixed
11, Office/Recreation
12, Offices
13, Recreation
14, Comm/Resid/Recreation
15, Residential
16, Residential/Offices
17, Roads
AOI
Coefficient
-0.569 - -0.399
-0.398 - -0.297
-0.296 - -0.211
-0.210 - -0.153
-0.152 - -0.104
-0.103 - -0.055
-0.054 - -0.015
-0.014 - 0.019
0.020 - 0.060
0.061 - 0.125
Scale 1:16,000
KM
0 0.2 0.4 0.8 1.2

c.

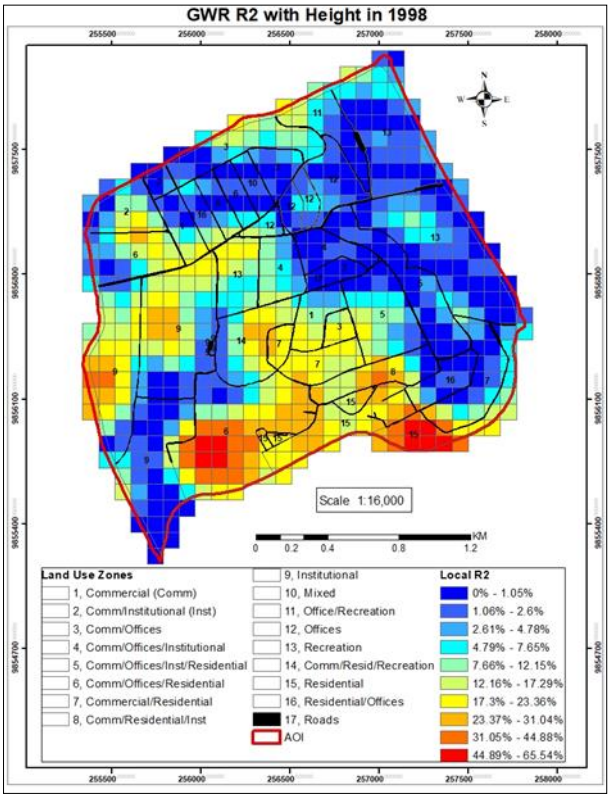
GWR R2 with Height in 1998
Land Use Zones
1, Commercial (Comm)
2, Comm/Institutional (Inst)
3, Comm/Offices
4, Comm/Offices/Institutional
5, Comm/Offices/Inst/Residential
6, Comm/Offices/Residential
7, Commercial/Residential
8, Comm/Residential/Inst
9, Institutional
10, Mixed
11, Office/Recreation
12, Offices
13, Recreation
14, Comm/Resid/Recreation
15, Residential
16, Residential/Offices
17, Roads
AOI
Local R2
0% - 1.05%
1.06% - 2.6%
2.61% - 4.78%
4.79% - 7.65%
7.66% - 12.15%
12.16% - 17.29%
17.3% - 23.36%
23.37% - 31.04%
31.05% - 44.88%
44.89% - 65.54%
Scale 1:16,000
KM
0 0.2 0.4 0.8 1.2

d.

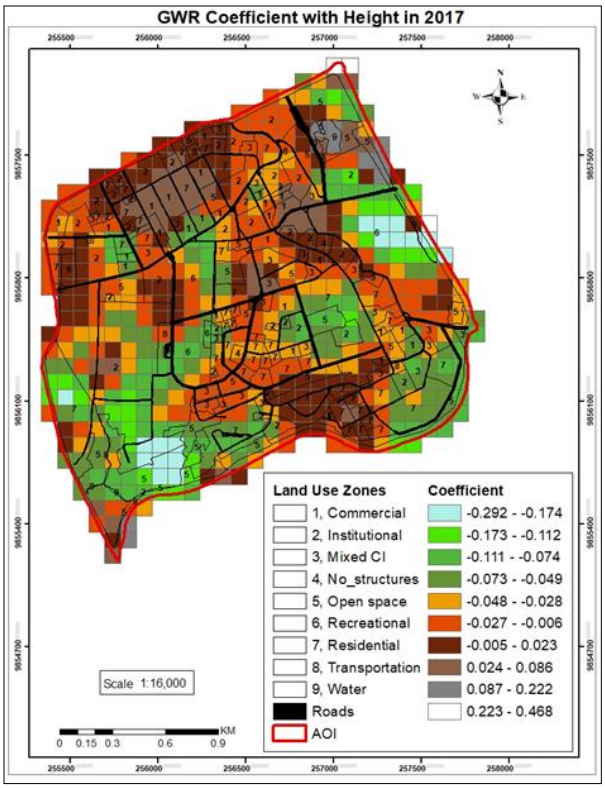

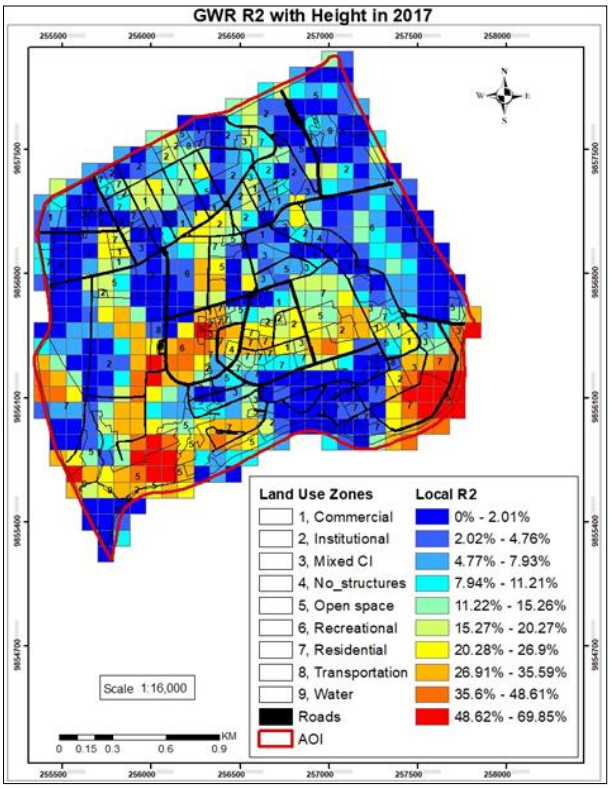

e. **f.**

Figure 4.20: Height Coefficient and R^2 Values in 1978, 1998, 2017 in Upper Hill, Nairobi

Areas in 1978 that have negative coefficients of -0.376 to -0.118 are in the central, southern and eastern parts of Upper Hill and have buildings whose mean height is 2.79 m (Figure 4.20 a) with a maximum height of 10.80 m. Negative coefficients from -0.117 to 0 has mean height of 5.01 m with a maximum height of 24 m. Positive coefficients of 0 to 0.23 has buildings that have a mean height of 6.34 m with maximum height of 25.97 m and are mainly located at the northern, eastern and western parts of Upper Hill. The average mean height of buildings within the negative coefficients is 3.9 m and 6.34 m for positive coefficients where the mean temperature with negative coefficients is higher than positive coefficients. Increasing building heights casts shadows thus lowering LST due to reduced absorption of solar radiation by the ground (Zheng *et al.*, 2019). R^2 values greater than 50% in 1978 are in the southern parts of Upper Hill where

negative coefficient values are obtained and have a mean building height of 2.30 m with other land cover as forest, open and sparse grassland. R^2 values less than 50% comprise buildings of mean height of 4.52 m and is 97% of Upper Hill (Figure 4.20 b). Predominant buildings in 1978 are low-rise buildings with high percentage of forest cover compared to 1998 and 2017. The maximum height within each coefficient range from negative to positive increases, with negative coefficients associated with low-rise buildings while positive coefficients have buildings within the high-rise range.

Negative coefficients in 1998 of -0.569 to -0.211 are located in the southern part of the study area with mean height of buildings as 3.40 m with a maximum height of 9.49 m (Figure 4.20 c). Coefficients of -0.210 to 0 have buildings whose mean height is 6.13 m with a maximum height of 104.32 m. Positive coefficients of 0 to 0.125 have buildings whose mean height is 6.81 m with a maximum height of 27.18 m. The mean height of buildings with negative and positive coefficients is low-rise with high-rise buildings in coefficients that tend towards zero and are positive indicating a mixed influence by different heighted buildings on LST. The average mean height of buildings within the negative coefficients is 4.77 m and 6.81 m for positive coefficients. R^2 values greater than 50% are located in the southern parts of Upper Hill with mean building height of 2.02 m while r^2 values of less than 50% have a mean building height of 5.90 m and covers 99% of Upper Hill (Figure 4.20 d).

Negative coefficient in 2017 of -0.292 to -0.049 is located in the eastern and western parts of Upper Hill with mean height of 6.26 m and maximum height of 38.81 m (Figure 4.20 e). Coefficients from -0.048 to 0 has buildings that have a mean height of 11.04 m, with maximum

height of 91.12 m. Coefficient of 0 to 0.468 has buildings that have a mean height of 9.16 m, with maximum height of 44.10 m. The average mean height of buildings within the negative coefficients is 8.65 m and 9.16 m for positive coefficients. R^2 values of more than 50% are in the southern parts of the study area with a mean height of 7.32 m while areas with less than 50% have mean building heights of 9.04 m and cover 96.3% of Upper Hill (Figure 4.20 f).

R^2 is not homogenously distributed as values vary across Upper Hill indicating that there are other covariates that need to be considered that will explain the LST variability as indicated by a large part of Upper Hill having r^2 of less than 50%. The LST energy distribution in an urban area can be affected by changing their spatial arrangement (Zheng *et al*., 2019). Results from 1978 and 1998 indicate that positive and negative coefficients are associated with low-rise buildings while in 2017 buildings tend towards middle-rise. Middle-rise buildings have negative coefficients in 2017 with high-rise building as maximum height indicating their high negative influence on LST compared to low-rise buildings. The mean height of buildings with positive coefficient values increases from 6.34 m in 1978 to 9.16 m in 2017. The coefficient ranges in 2017 (-0.292 to 0.468) are larger than in 1998 (-0.569 to 0.125) and 1978 (-0.376 to 0.23) indicating a stronger influence by building height on LST. High negative coefficients are obtained with low-rise buildings in 1978, 1998 and 2017 indicating a reduction in LST with increased building heights. Zheng *et al*., (2019) studies on the effects of building height and density in residential areas in Beijing showed a variation of LST, with high-rise residential areas having low LST than low-rise neighborhoods. Deep street canyons have low day-time temperatures but high night-time air temperatures. In an urban area where building heights are not uniform, building roofs have an important interaction with adjacent buildings. If there are

taller buildings adjacent to a shorter building, the roof of the shorter building acts as a reflective surface that also traps radiation (Yang & Li, 2015). High rise buildings tend to produce strong wind convection and cast shadows. Urbanization in Nairobi has not altered wind direction, which are easterlies, but has reduced their speeds (Ongoma *et al*., 2013b). Effects on the thermal environment can differ when the heights of buildings are different but the building density is the same (Yang *et al.*, 2017).

Figure 4.21 indicates variation in coefficient and r^2 values with ground coverage ratio across the three years. Pearson's correlational analysis between LST and GCR indicates a negative relationship (Appendix 13). Mean coefficient values from GWR analysis in 1978, 1998 and 2017 are -3.67, -2.72 and -0.94 respectively indicating a negative relationship between LST and GCR.

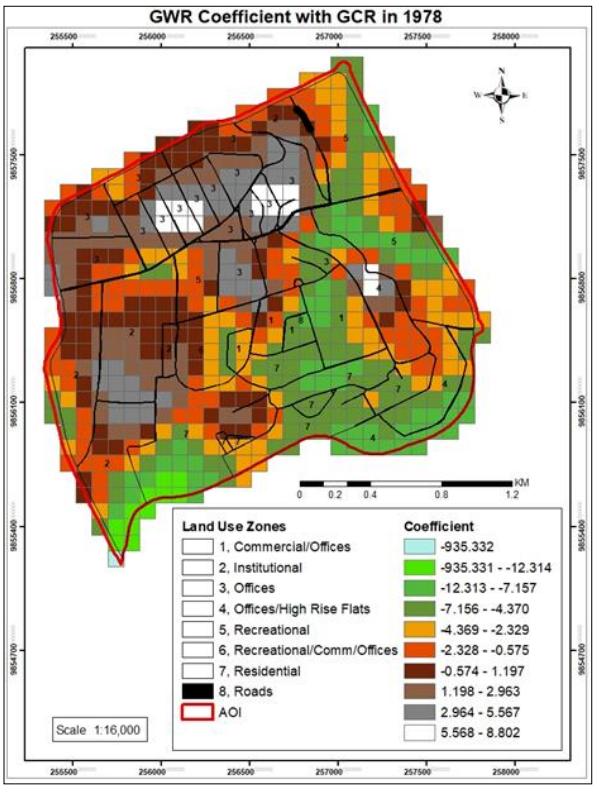

a.

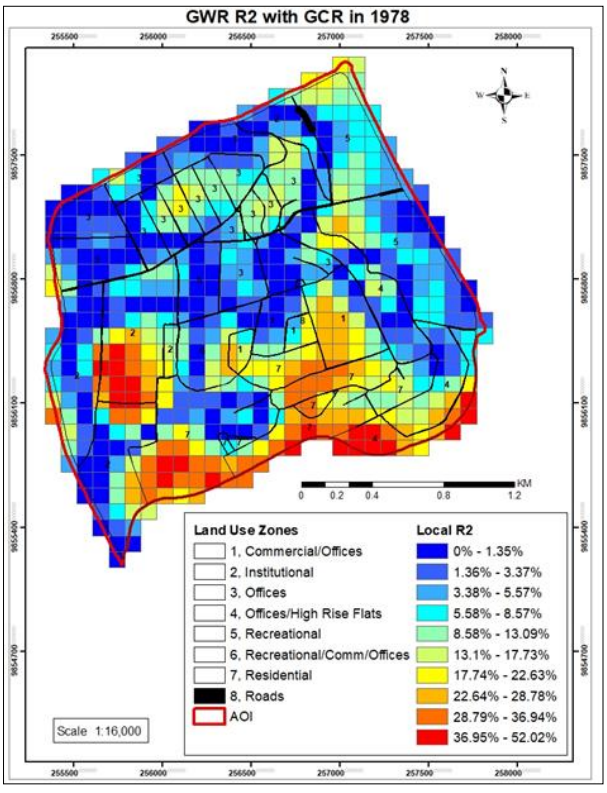

b.

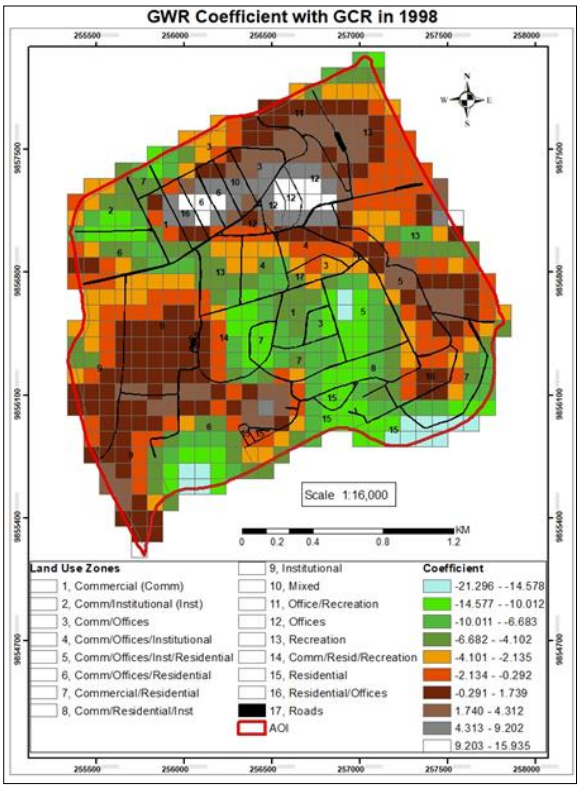

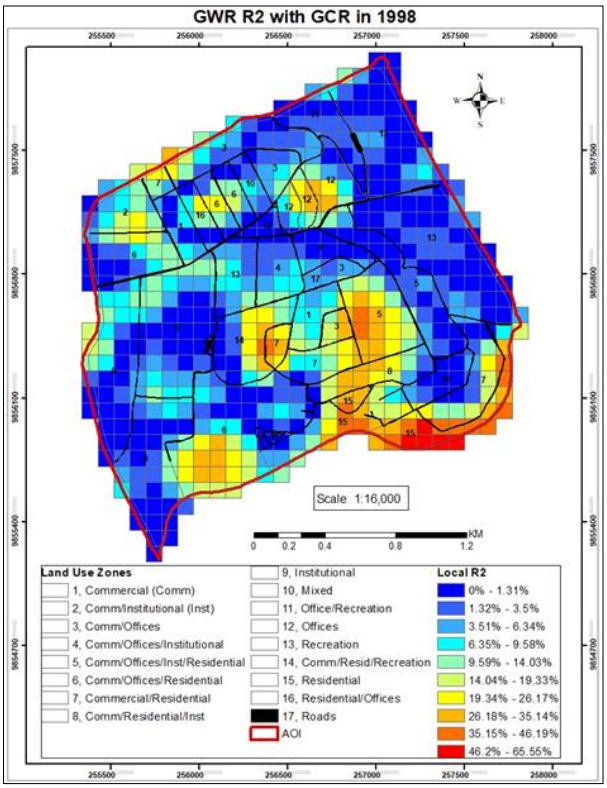

c. **d.**

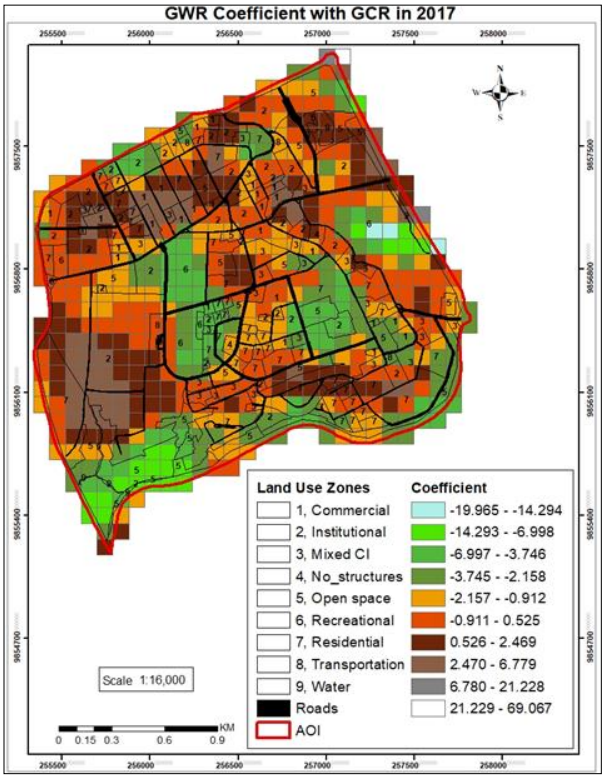

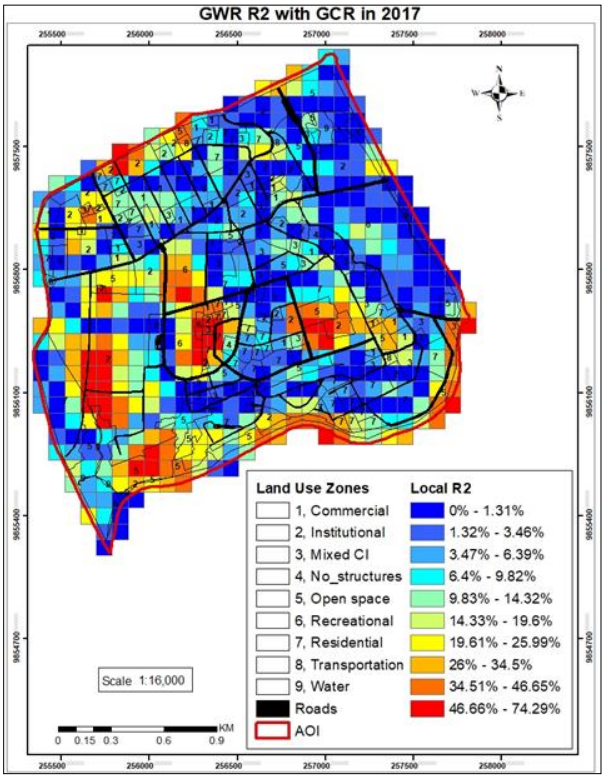

e. **f.**

Figure 4.21: GCR Coefficient and R^2 Values in 1978, 1998, 2017 in Upper Hill, Nairobi

Negative coefficients of -935.332 to -4.370 in 1978 have a GCR mean value of 0.06, with maximum values of 0.24 (Figure 4.21 a). Negative coefficients of -4.369 to 0 have mean GCR value of 0.08, with maximum GCR values of 0.30. Positive coefficient value of 0 to 8.802 has a mean GCR value of 0.17, with a maximum value of 0.82. Mean value increases from negative to positive coefficients and are all low density built-up areas. R^2 values greater than 50% is one pixel only and is only at Kenyatta National Hospital with a mean GCR of 0.35. Areas whose r^2 is less than 50% has a mean of GCR of 0.11 (Figure 4.21 b).

Negative coefficients of -21.296 to -4.102 in 1998 are from the northern to southern parts of Upper Hill with a mean GCR of 0.09 and maximum value of 0.31 (Figure 4.21 c). Negative coefficients of -4.101 to 0 has a mean GCR of 0.11, with maximum GCR value of 0.09. Positive coefficients of 0 to 15.935 has a mean GCR of 0.15 with maximum GCR value of 0.82. Mean density increases from positive to negative coefficients and are low density whereas the mean temperature reduces. R^2 values greater than 50% are located within a small region in the southern part of the study area with a mean GCR of 0.02 while areas with r^2 less than 50% have a mean GCR of 0.12 which comprise of 99% of Upper Hill (Figure 4.21 d). This indicates that the relationship between GCR and land surface temperature is not strong and that there may be other factors that would need to be studied on the surface temperature. Areas that have r^2 values of 10% to 23% are areas that do not have any buildings and also have high negative coefficients indicating a better model fit than areas having buildings. This also indicates the influence of land cover on LST as these are classified as open grassland.

Areas having negative coefficients of -19.965 to -2.158 in 2017 are mainly in the central and southern part of Upper Hill with mean GCR value of 0.12 and maximum value of 0.54 (Figure 4.21 e). Negative coefficients of -2.157 to 0 have a mean GCR value of 0.21 with maximum value of 0.64. Positive coefficient of 0 to 6.779 have a mean GCR value of 0.23 with maximum value of 0.84. Positive coefficients of 6.780 to 69.067 are edge pixels with no buildings. Low density built-up areas have a positive and negative correlation with LST. R^2 values greater than 50% are in the western part of Upper Hill with a mean GCR of 0.16 while r^2 values less than 50% comprise 97% of Upper Hill and have a mean GCR of 0.19 (Figure 4.21 f). Surface temperature is impacted by increased ground coverage ratio as indicated by the increase in mean GCR values of 0.17 in 1978, 0.15 in 1998 and 0.23 in 2017 within the positive coefficient range. Mean LST with negative coefficients is high compared to mean LST for GCR with positive coefficients therefore LST has a negative correlation with GCR. Increased impervious surfaces implies large absorption surface area due to thermal conductivity hence a negative contribution index (Figure 4.11).

BVD coefficient and r^2 values in 1978, 1998 and 2017 differs with low negative and high positive coefficient values in 2017. Pearson's correlational analysis between LST and BVD indicates a negative relationship (Appendix 13). Mean correlation values from GWR analysis in 1978, 1998 and 2017 are -0.65, -0.52 and -0.07 respectively indicating a negative relationship between LST and BVD. High r^2 values are also recorded in 2017 (Figure 4.22). Negative coefficients of -97.591 to -1.044 in 1978 have a mean BVD values of 0.12 m^3/m^2 with maximum BVD values of 1.05 m^3/m^2 mainly in the southern parts of Upper Hill (Figure 4.22 a).

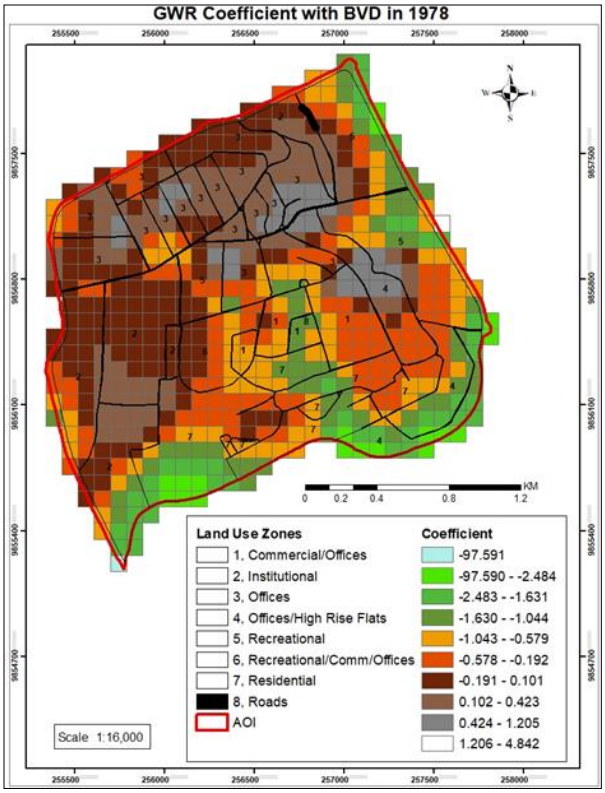
GWR Coefficient with BVD in 1978
Land Use Zones
1, Commercial/Offices
2, Institutional
3, Offices
4, Offices/High Rise Flats
5, Recreational
6, Recreational/Comm/Offices
7, Residential
8, Roads
AOI
Coefficient
-97.591
-97.590 - -2.484
-2.483 - -1.631
-1.630 - -1.044
-1.043 - -0.579
-0.578 - -0.192
-0.191 - 0.101
0.102 - 0.423
0.424 - 1.205
1.206 - 4.842
Scale 1:16,000
KM
0 0.2 0.4 0.8 1.2

a.

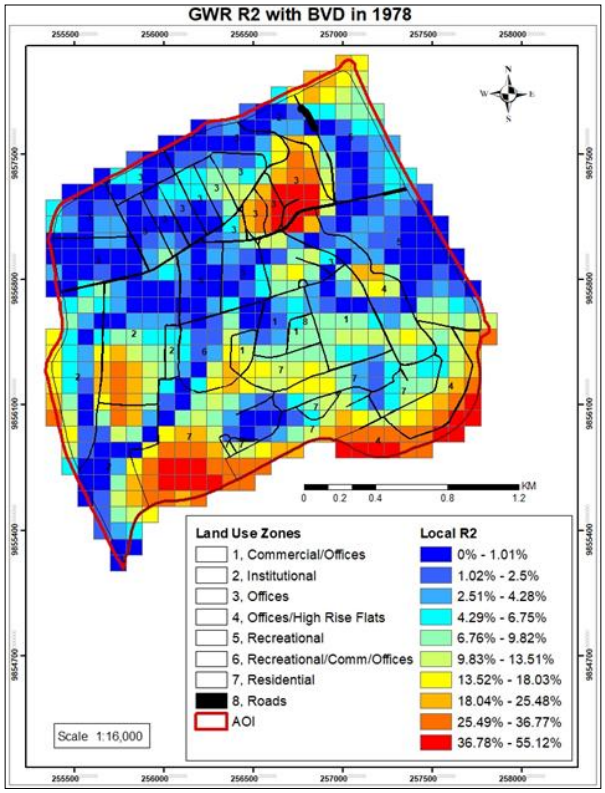
GWR R2 with BVD in 1978
Land Use Zones
1, Commercial/Offices
2, Institutional
3, Offices
4, Offices/High Rise Flats
5, Recreational
6, Recreational/Comm/Offices
7, Residential
8, Roads
AOI
Local R2
0% - 1.01%
1.02% - 2.5%
2.51% - 4.28%
4.29% - 6.75%
6.76% - 9.82%
9.83% - 13.51%
13.52% - 18.03%
18.04% - 25.48%
25.49% - 36.77%
36.78% - 55.12%
Scale 1:16,000
KM
0 0.2 0.4 0.8 1.2

b.

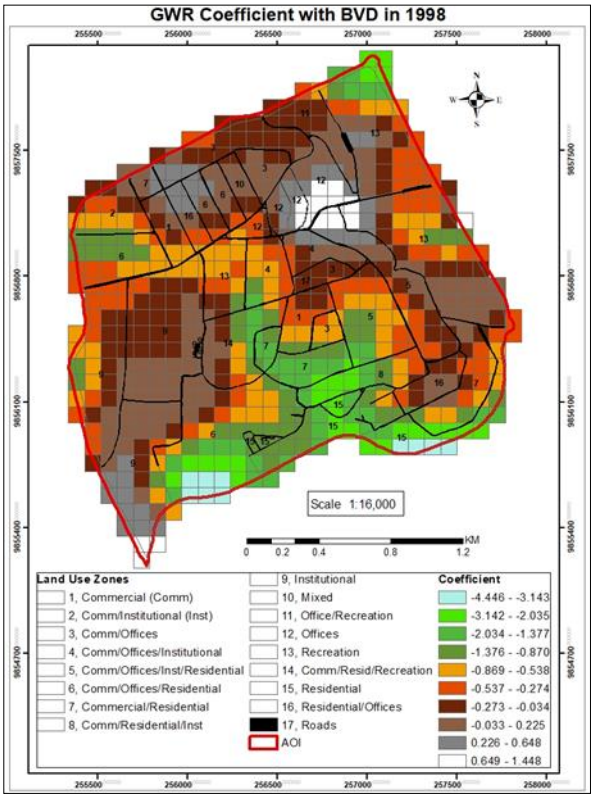
GWR Coefficient with BVD in 1998
Land Use Zones
1, Commercial (Comm)
2, Comm/Institutional (Inst)
3, Comm/Offices
4, Comm/Offices/Institutional
5, Comm/Offices/Inst/Residential
6, Comm/Offices/Residential
7, Commercial/Residential
8, Comm/Residential/Inst
9, Institutional
10, Mixed
11, Office/Recreation
12, Offices
13, Recreation
14, Comm/Resid/Recreation
15, Residential
16, Residential/Offices
17, Roads
AOI
Coefficient
-4.446 - -3.143
-3.142 - -2.035
-2.034 - -1.377
-1.376 - -0.870
-0.869 - -0.538
-0.537 - -0.274
-0.273 - -0.034
-0.033 - 0.225
0.226 - 0.648
0.649 - 1.448
Scale 1:16,000
KM
0 0.2 0.4 0.8 1.2

c.

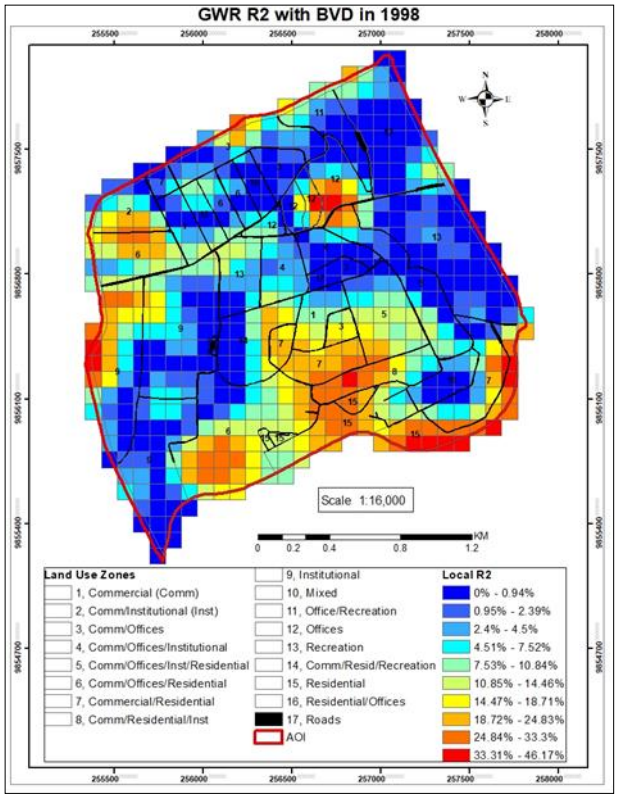
GWR R2 with BVD in 1998
Land Use Zones
1, Commercial (Comm)
2, Comm/Institutional (Inst)
3, Comm/Offices
4, Comm/Offices/Institutional
5, Comm/Offices/Inst/Residential
6, Comm/Offices/Residential
7, Commercial/Residential
8, Comm/Residential/Inst
9, Institutional
10, Mixed
11, Office/Recreation
12, Offices
13, Recreation
14, Comm/Resid/Recreation
15, Residential
16, Residential/Offices
17, Roads
AOI
Local R2
0% - 0.94%
0.95% - 2.39%
2.4% - 4.5%
4.51% - 7.52%
7.53% - 10.84%
10.85% - 14.46%
14.47% - 18.71%
18.72% - 24.83%
24.84% - 33.3%
33.31% - 46.17%
Scale 1:16,000
KM
0 0.2 0.4 0.8 1.2

d.

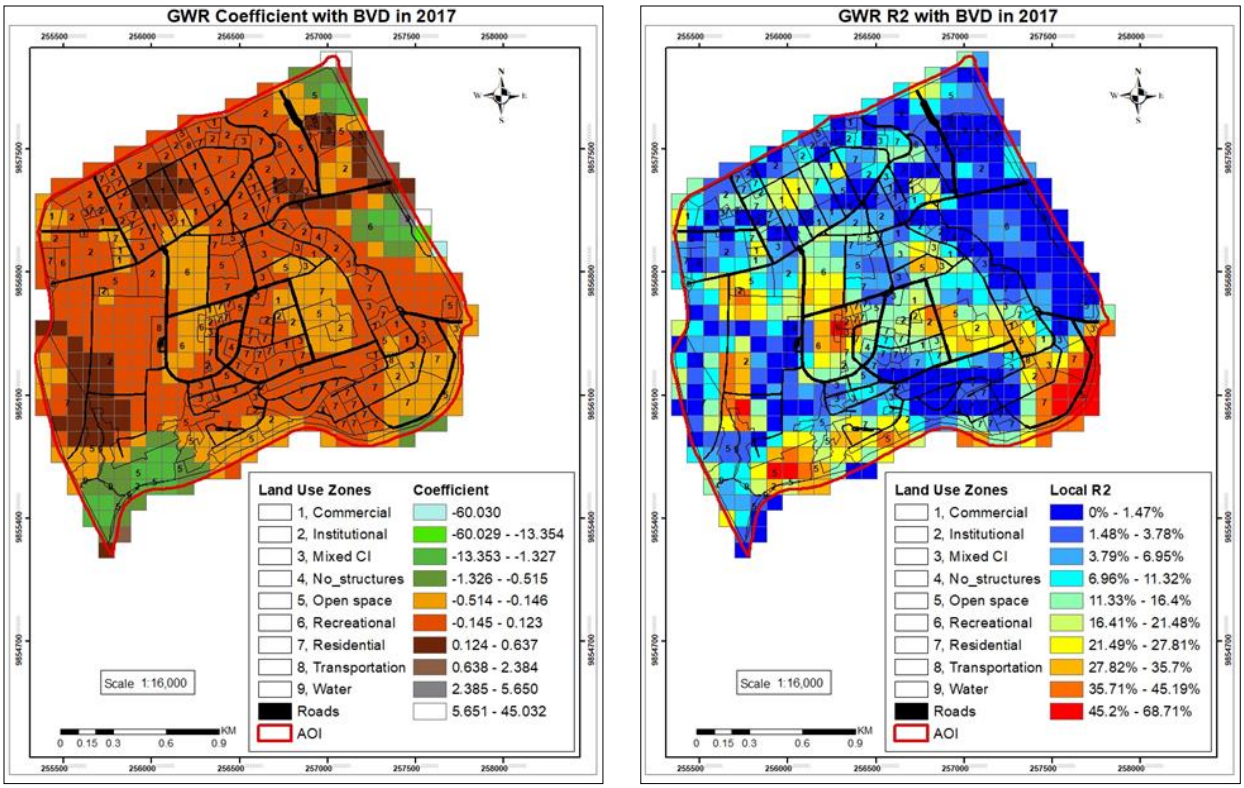

e. **f.**

Figure 4.22: BVD Coefficients and R^2 Values in 1978, 1998, 2017 in Upper Hill, Nairobi

Negative coefficient of -1.043 to 0 has a mean BVD value of 0.38 m^3/m^2 with maximum BVD values of 2.45 m^3/m^2 mainly in the central parts of Upper Hill. Positive coefficients of 0 to 4.842 have a mean BVD value of 1.09 m^3/m^2 with maximum BVD value of 11.24 m^3/m^2 mainly in the north and western parts of Upper Hill. Built-up areas that have large volumes contribute positively to the surface temperature as indicated by the increase in mean BVD values which is low-density. The maximum BVD values in all coefficients are high density built-up indicating a mixture of built-up areas influencing LST. R^2 values greater than 50% comprised of two pixels in eastern parts and have a mean BVD value of 0.83 m^3/m^2 while r^2 less than 50% has a mean BVD value of 0.55 m^3/m^2 (Figure 4.22 b).

Areas having high negative coefficients of -4.446 to -1.377 in 1998 are located in the southern parts of Upper Hill with mean BVD of 0.18 m^3/m^2 and maximum BVD value of 1.02 m^3/m^2 (Figure 4.22 c). Negative coefficient of -1.376 to 0 have a mean BVD value of 0.83 m^3/m^2 with maximum BVD value of 9.97 m^3/m^2. Positive coefficients of 0 to 1.448 have a mean BVD value of 0.95 m^3/m^2 with maximum BVD values of 6.65 m^3/m^2. Negative and positive coefficients have built-up areas that are low density but are mixed with high density built-up areas as indicated by the maximum values. R^2 values from 18% to 46% are mainly in the southern parts and has negative coefficient values of -1.39. Areas having r^2 values of less than 1% comprise 66% of Upper Hill and are along the northeastern and western parts of Upper Hill (Figure 4.22 d).

Low coefficients of -60.030 to -0.515 in 2017 are located in the southern and eastern edges of Upper Hill with mean BVD values of 0.08 m^3/m^2 and maximum values of 0.98 m^3/m^2 (Figure 4.22 e). Negative coefficients of -0.514 to 0 cover 63% of Upper Hill and have a mean BVD value of 2.11 m^3/m^2 with maximum values of 22.29 m^3/m^2. Positive coefficients of 0 to 45.032 have a mean BVD value of 1.84 m^2/m^3 with maximum BVD value of 9.57 m^3/m^2. Negative and positive coefficient values have low density built-up values with high-density built-up areas as indicated by the maximum values. R^2 values greater than 50% are mainly in the southern parts which is comprised of a mix of built-up, forest and open ground land cover and has a mean BVD of 1.06 m^3/m^2 (Figure 4.22 f). R^2 less than 50% has mean BVD values of 1.87 m^3/m^2 and cover 98% of Upper Hill.

Mean LST of buildings with negative coefficients is low compared to those with positive coefficients implying the negative relationship between LST and BVD due to lower reflectance of urban surfaces (EPA, 2008b). Large built-up densities have an influence on the surface temperature than areas that have smaller volumes of built-up materials. This can be seen in the increase in mean BVD values from negative to positive coefficients where mean BVD densities are 1.09 m^3/m^2, 0.94 m^3/m^2 and 1.84 m^3/m^2 in 1978, 1998 and 2017 respectively. Though the majority of buildings are low-density, the increase in values of maximum BVD in positive coefficients from 1978 to 2017 indicates that though spatially scattered, they have an influence. Larger blocks reduce wind speeds and alter the wind profile in the urban canopy (Guo *et al*., 2016). Wind flow over low-rise urban areas moves over and around the top of buildings, while for high-rise urban areas, drag is intensified as the air flow is only around buildings (Yang *et al*., 2017). Zheng *et al*., (2019) studies showed that building density had a positive relationship with LST, where high-rise residential buildings having low building densities reduced the LST.

4.3.2 Modelling Spatial Relationships

Exploratory regression analysis results undertaken for 1978, 1998 and 2017 at 30 and 90 meter grids before undertaking OLS and GWR show results of different combined models (Appendix 12). Model results with high r^2 value are obtained by combining explanatory variables i.e. albedo, NDVI, aspect, BVD, GCR and height. Various criteria for passing a model include adjusted r^2 value, VIF value, Jarque-Bera value, autocorrelation p-value and coefficient p-value (Fischer *et al*., 2010). Failure to satisfy any of these criteria, a model will not pass the test and therefore none of the model combinations in any of the years passed the model tests with OLS, hence GWR is used.

Table 4.4: GWR and OLS Model for Height, GCR and BVD in Upper Hill, Nairobi

Variable	**Scale**	**Model**	**AICc**			**Adjusted R^2**			**F**		
			1978	**1998**	**2017**	**1978**	**1998**	**2017**	**1978**	**1998**	**2017**
Height	30m	OLS	-5275.86	-7090.46	-5770.60	0.40	0.46	0.28	806.05	995.15	453.98
		GWR	-	-	-8471.88	-	-	0.59			
	90m	OLS	-741.45	-778.09	-706.12	0.60	0.56	0.41	203.37	179.71	99.70
		GWR	-971.67	-998.93	-1053.69	0.73	0.71	0.70			
GCR	30m	OLS	-5214.03	-6767.08	-5365.54	0.39	0.42	0.23	780.29	851.56	319.90
		GWR	-	-	-8213.25	-	-	0.57			
	90m	OLS	-712.96	-755.47	-655.11	0.57	0.54	0.36	186.48	167.17	79.01
		GWR	-943.06	-947.59	-998.40	0.72	0.68	0.67			
BVD	30m	OLS	-5117.29	-6937.54	-5656.09	0.38	0.44	0.26	740.63	926.03	414.91
		GWR	-	-	-8485.61	-	-	0.59			
	90m	OLS	-683.37	-805.66	-710.69	0.54	0.58	0.42	169.82	195.70	101.65
		GWR	-936.14	-1023.94	-1086.92	0.71	0.72	0.72			

The final modelling step NDVI, albedo and aspect are used as explanatory variables together with height, GCR and BVD, to understand the spatial variation and relationship that each has with surface temperature. OLS results indicate an improvement from previous results (Table 4.4) where individual explanatory variables are explored. GWR adjusted r^2 results have a better model fit than those obtained in OLS indicating that inclusion of other explanatory variables in the analysis improves the model.

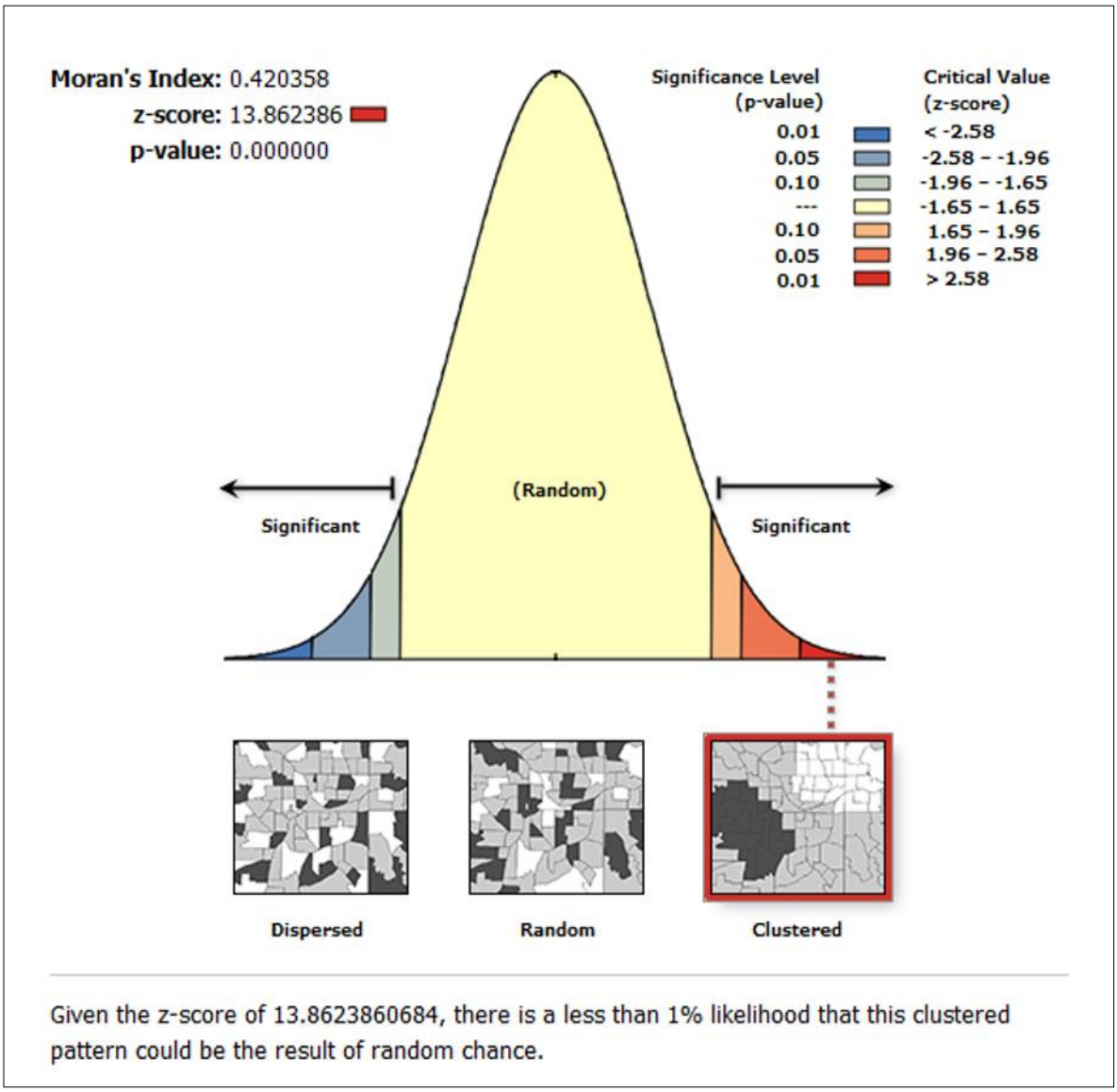

Figure 4.23: Spatial Autocorrelation Report in 1978 with Building Height at 90 m Grid

Spatial autocorrelation on standard residuals for both GWR and OLS at 90 m scales show a clustered pattern with less than 1% chance of the clustered pattern being a random chance (Figure 4.23). The p values (< 0.05) are significant and the results were adopted (Appendix 14). Tobler's first law of geography states that "Everything is related to everything else, but near things are more related than distant things" (Murayama & Rajesh, 2011) hence the positive z-score and Moran's I values that show that the spatial objects tend towards a clustered pattern. Geographical features have a strong relationship with features that are close to it than far features therefore it would be difficult for the variables used in this analysis to have a scattered or random pattern in the standard residuals.

R^2 and AICc results show an improvement in OLS when NDVI, aspect and albedo are analyzed together with each of the building morphology attributes, showing that building morphology interacts with other factors to influence LST. OLS and GWR models at 90 m scale perform better than 30 m scales and is adopted as the final result in analysis. Both models at 90 m scales have r^2 values of more than 50% signifying they perform well in explaining the relationship between LST and explanatory variables. GWR at 30m did not run for all 1978 and 1998 datasets. OLS r^2 values at 30 m increase in value from 1978 to 1998, but reduces in 2017 for height, GCR and BVD, while at 90 m scale the r^2 values reduce from 1978 to 2017, with a reduction of more than 0.15 between 1998 and 2017. OLS performance in 2017 indicate that the relationship becomes more non-linear as there could be other variables that are affecting LST. Causes of UHI due to rapid urban development include surface geometry, waterproofing of the surface, air pollution, fabric thermal properties and anthropogenic heat (Shahmohamadi *et al*., 2012). Air pollution changes the all-wave net radiation budget along the long-wave (infrared) and short

wave solar radiation by reducing incoming solar radiation or warming ambient air by absorbing infra-red radiation from urban surfaces (Shahmohamadi *et al*., 2012). Therefore there's no single factor that can be linked to warmer cities but it's a combination of factors.

R^2 values of height at 90 m scale in 1978 explain a high variation of surface temperature in OLS and GWR models than GCR and BVD. BVD r^2 values in 1998 and 2017 are high in OLS and GWR models showing it has more influence on LST compared to height and GCR. This implies that GCR and building height, constituting BVD, can have a positive impact on UHI and should therefore be viewed in tandem while planning for sustainable cities. R^2 values in 2017 are low compared to those in 1978 and 1998 showing there is a phenomena arising by 2017 which is not seen in previous years. There are other factors besides morphology and topology known to influence surface temperature, consequently urban heat island effect (Voogt, 2007). Therefore the importance of having monitoring stations in cities to assess changes in atmospheric conditions and pollution levels as they affect insolation.

Spatial patterns of local determination coefficients (r^2) in the GWR model show regional heterogeneity in all years modeled (Figure 4.24). Part of Upper Hill in 1978 with r^2 values less than 50% is in the west around Kenyatta National Hospital buildings. Mean building height, GCR and BVD with r^2 values of less than 50% is 5.96 m, 7.57 and 0.19 m^3/m^2 respectively and a mean road width of 5 m with a mean LST of 24.80 ^{0}C. These are low-rise buildings with high density GCR and low density BVD built-up areas. Mean values of explanatory variables analyzed are: albedo at 0.21 which is built-up, aspect at 151.19 which are southeast facing slopes, NDVI values of 0.34.

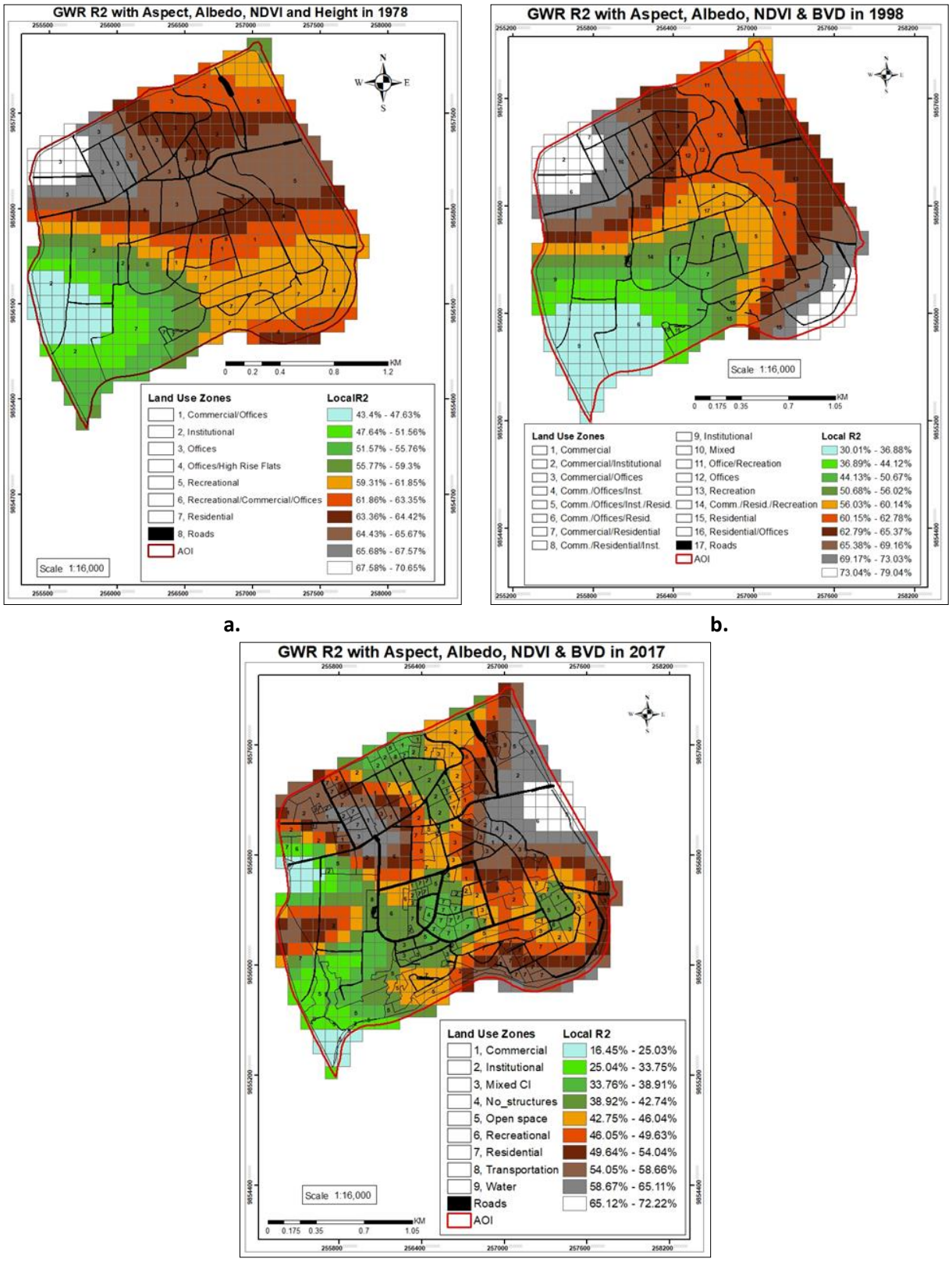

Figure 4.24: R^2 Values of BVD in 1978, Height in 1998 & 2017 in Upper Hill, Nairobi

The mean building height, GCR and BVD with r^2 values greater than 50% is 4.31 m, 0.10 and 0.12 m^3/m^2 respectively and a mean road width of 6 m with a mean LST of 24.37 ^{0}C. These are low-rise buildings with low-density GCR and BVD built-up areas. Mean values of explanatory variables analyzed are: albedo at 0.19 which is built-up, aspect at 110.81 which are east facing slopes, NDVI values of 0.35. Building morphology attributes in r^2 less than 50% have high values compared to areas with r^2 of more than 50%. This could be due to the negative relationship between height, GCR and BVD with LST due to thermal properties of urban materials. R^2 values of 63% to 71% have medium density GCR, with forest, open and sparse grassland land cover and whose land use of office and recreational.

BVD has a high influence on LST in 1998 compared to GCR and height with 23% of Upper Hill having r^2 values of less than 50% (Figure 4.24 b) in the south-western part. Mean height, GCR and BVD in areas with r^2 greater than 50% is 6.26 meters, 0.12 and 0.84 m^3/m^2 respectively and a mean road width of 7 m. The mean LST is 32.22 ^{0}C. These are low-rise buildings with low densities in both GCR and BVD. Mean values of explanatory variables analyzed are: albedo at 0.15 which is built-up, aspect at 102.54 which are east facing slopes, NDVI values of 0.32 where albedo and NDVI have reduced from 1978. R^2 values of less than 50% have mean height, GCR and BVD of 4.46 meters, 0.10 and 0.54 m^3/m^2 respectively and a mean road width of 5 m. The mean LST is 33.85 ^{0}C. Buildings are low-rise with low density BVD and GCR built-up areas. Mean values of explanatory variables analyzed are: albedo at 0.16 which is built-up, aspect at 139.26 which are southeast facing slopes, NDVI values of 0.32. This is in the southwestern part of Upper Hill with sparse grassland and little urban development, hence the high LST and low built-up morphological attributes compared to areas with an r^2 of more than 50%. R^2 values of

63% to 79% are in the northwest, east and southeastern parts of Upper Hill whose land use is defined as commercial, offices, institutional and residential and built-up, open grassland and forest land cover.

BVD has high influence on surface temperature compared to GCR and height in 2017. R^2 of less than 30% have mean height, GCR and BVD of 4.28 m, 0.08 and 0.51 m^3/m^2 with no roads in this area. Buildings are low-rise while GCR and BVD are low density. Mean LST in this areas is 29.33 ^{0}C and a mean 3D built-up intensity expansion of 2.32%. Mean values of explanatory variables are: 132.52 degrees for aspect which are southeast facing slopes, 0.16 for albedo and 0.26 for NDVI. R^2 of between 30% and 40% have mean height, GCR and BVD of 9.60 m, 0.21 and 2.15 m^3/m^2 with a road width of 8 m. Buildings are low-rise while GCR and BVD are low density. Mean LST in this areas is 28.20 ^{0}C and a mean 3D built-up intensity expansion of 13.46%. Mean values of explanatory variables are: 142.20 degrees for aspect which are southeast facing slopes, 0.16 for albedo and 0.29 for NDVI. R^2 of between 40% and 50% have mean height, GCR and BVD of 11.72 m, 0.25 and 2.60 m^3/m^2 with a road width of 8 m. Buildings are middle-rise while GCR and BVD are medium density. Mean LST in this areas is 28.10 ^{0}C and a mean 3D built-up intensity expansion of 25.86%. Mean values of explanatory variables are: 109.77 degrees for aspect which are east facing slopes, 0.15 for albedo and 0.28 for NDVI. R^2 of between 50% and 60% have mean height, GCR and BVD of 7.38 m, 0.16 and 1.20 m^3/m^2 with a road width of 9 m. Buildings are low-rise while GCR and BVD are low density. Mean LST in this areas is 27.80 ^{0}C and a mean 3D built-up intensity expansion of 13.60%. Mean values of explanatory variables are: 102.12 degrees for aspect which are east facing slopes, 0.15 for albedo and 0.31 for NDVI. Mean values of height, GCR and BVD in areas having r^2 values greater than

60% is 3.08 m, 0.09 and 0.57 m^3/m^2 and mean road width of 17m. Buildings are low-rise with low density in GCR and BVD. They comprise 10% of Upper Hill and are located in the eastern, southeastern and northwestern parts. The mean LST is 28.38 ^{0}C and a mean 3D built-up intensity expansion of 5.12%. The mean values of explanatory variables are: 115.46 degrees for aspect which are southeast facing slopes, 0.16 for albedo and 0.31 for NDVI. High values in 3D built-up intensity, height, BVD and GCR are found where r^2 are 30% to 60% with highest values between 40% and 50% whereas areas with more than 60% have high LST despite low morphology values. LST varies greatly with different built-up morphologies and spatial arrangement. Areas with r^2 values greater than 40% is where mitigation measures should be adapted to avert adverse effects resulting from increased temperatures, indoors due to heating and outdoors from emitted heat. These areas are within the threshold of a compact city which argues for medium to high density built-up developments (UN-Habitat, 2010), therefore showing impacts of developments differing with geographical locations. The level of vulnerability of inhabitants in Upper Hill to temperature changes is increasing with urban development due to its thermal capacity as indicated by r^2 values. Big data analytics and modelling not only indicates the temporal and spatial interactions but shows the interactions these changes and environment has on its populace (Cheng *et al.*, 2017).

Summary results of spatial variation of r^2 values in 1978, 1998 and 2017 are shown in Table 4.5. Areas having r^2 values of between 40% to 50% in 1978, 50% to 80% in 1998 and 30% to 50% in 2017 showed significant high values in height, GCR and BVD. In 2017, areas having r^2 values of 40% to 50% have high 3DBUI percentage values indicating these areas that have increased built-up intensity have significant relationship with LST.

Table 4.5: R^2 GWR values of GCR, Height and BVD

Measures	1978			1998					2017				
	40% - 50%	**50% - 60%**	**60% - 71%**	**30% - 40%**	**40% - 50%**	**50% - 60%**	**60% - 70%**	**70% - 80%**	**<30%**	**30% - 40%**	**40% - 50%**	**50% - 60%**	**60% - 72%**
Height (m)	5.96	4.06	4.37	3.66	5.61	4.98	6.68	6.64	4.28	9.60	11.72	7.38	3.08
GCR	0.15	0.11	0.10	0.08	0.12	0.13	0.12	0.12	0.08	0.21	0.25	0.16	0.09
BVD (m^3/m^2)	0.84	0.86	0.44	0.43	0.68	0.79	0.88	0.78	0.51	2.15	2.60	1.20	0.57
3DBUI (%)	-	-	-	-	-	-	-	-	2.32	13.46	25.86	13.60	5.12
LST (C^0)	24.80	25.37	24.11	34.22	33.32	32.61	32.10	32.07	29.33	28.20	28.10	27.80	28.38

Areas that have r^2 values of more than 50% from 1978 to 1998 have increased in mean building height by 1.95 m, in GCR by 0.02 and in BVD by 0.72 m^3/m^2. Slope direction remains the same as east-facing slopes while albedo and NDVI reduce by 0.04 and 0.03 respectively indicating a change in land cover due to increasing built-up areas. Areas with r^2 values of more than 50% in 1998 to 2017 showed a mean increase in GCR by 0.02, BVD by 0.19 m^3/m^2. Mean values of building heights, albedo and aspect remained the same at 6 m, 0.15 and eastern facing slopes respectively while NDVI reduced by 0.01. LST in areas where r^2 is less than 50% is high compared to areas with r^2 that is more than 50% in southeast facing slopes. Different scholars have differed on the relationship between LST and building height which could have resulted from certain variables not being included in the analysis (Zheng *et al*., 2019). Zheng *et al*., (2019) research shows that between building height, building and vegetation density, building height had a more significant effect on LST.

The energy flow of urban canyons is influenced by the surface and air temperature, which is turn is impacted by the height/width (H/W) ratio of the urban canyon (Nakata & Souza, 2013). The analysis from 1978 to 2017 indicates that an increase on impervious surfaces does have an influence on the surface temperature with different parts of Upper Hill having diverse interaction and intensity with LST in different years. Low-rise and low density buildings have high LST compared to middle to high-rise buildings and medium to high density built-up areas within Upper Hill as they warm up fast compared to high-rise high density built-up areas. This is attributed to the characteristic of buildings in Upper Hill which are majorly low-rise, though there has been a transformation of buildings in height, GCR and BVD between 1978 and 2017 (Table 4.1). High density buildings are scattered in the study area from 1978 to 2017 therefore it is difficult to determine their direct influence on LST. In the construction of buildings, energy

consumption is an important factor as it determines heat and cooling rates which contributes to anthropogenic heat.

One of the main reasons for UHI effect is the massive volume of buildings (Guo *et al*., 2016). High-rise high-density cities have warming and cooling rates which tend to be slower than low-rise low density cities due to their high thermal storage compared to low-rise low density cities (Yang *et al*., 2017). Low-rise low densities have larger surface temperature than high-rise high density cities as they have a larger sky-view factor (Yang & Li, 2015). This indicates that urban geometry plays an important role in the surface temperature of an area and that increasing density would increase the surface heat island effect. Perini & Magliocco, (2014) simulation of an urban environment using ENVI-met indicated that density and building heights had an influence on the mean radiant temperature. Larger potential temperatures were experienced in denser buildings while taller buildings had low temperatures due to the shading effect which improved the thermal comfort.

Zhan *et al*., 2015 studied the relationship between LST and GCR and BVD where buildings with low heights had a dense pattern and positive relationship with LST, while taller buildings were sparse and thus did not have a defined relationship with LST. He determined that GCR had a strong linear relationship with LST compared to BVD, which did not have a defined pattern. Sokido, (2016) determined that high-rise built-forms with low ground coverage have good quality spatial urban spaces due to provision of green spaces and other amenities. High-rise buildings are a preferred form of development due to its ability to allow high population densities and better use of space, while having a low density building footprint and increasing

green space coverage (Zheng *et al*., 2019). Landscaping surrounding built-up areas using different types of vegetation in horizontal and vertical layers can improve external climatic conditions (Shahmohamadi *et al.*, 2012).

An urban heat tool-kit designed for local governments for the built environment focuses on four key areas which are use of green roofs, urban forests, cool roofs and pavements to reduce urban heat islands, protect resident's health, reduce greenhouse gas emissions and improve air quality (Hoverter, 2012). Each of the methods have pros and cons which need to be considered before implementation. Green roofs require roofs that are either flat or have low slopes of up-to 30 degrees to support vegetation and also buildings that have good structural strength (Hoverter, 2012). Use of each of the different methods can be a requirement by local governments under certain circumstances or the general public can be encouraged to use them through education, demonstration programs and incentive programs (Hoverter, 2012). Green building programs can be implemented using building codes as they protect and preserve environmental and human health (Hoverter, 2012). Zoning codes have been used by local governments such as Seattle City council that passed the Green Ordinance in 2006 that requires newly constructed buildings in multifamily residential, neighborhood commercial and commercial zones to have additional planted areas such as green roofs (Hoverter, 2012). Areas identified as hotspots and having vulnerable residents should be prioritized as mitigation measures are implemented. Adverse effects of UHI on the environment, health and economy can be reduced through a built-environment strategy that focuses on the implementation of a combination of options to serve the government's objectives. It therefore imperative that current policy guidelines in the built environment are reviewed to determine sustainable densification guidelines for cities.

4.4 Reflection on Adopted Methodology

The modelling approach adopted has captured the surface physical characteristics of land cover, which as modification from Zhan *et al*., (2015) and Wu *et al*., (2013) who compared the 3D built-up morphology of urban areas with LST. The approach addresses complex relationships and interaction urban structures have with the natural environment unlike other models that focus on built-up densities as the only independent variable. The framework developed that classifies GCR, FAR and BVD into various densities eliminates the ambiguity in cities on magnitude of impervious surfaces desirable and contributes to a better understanding of the SUHI phenomena through the use of different models. Compact cities have been seen as an ideal form of sustainable development (Çalışkan, 2004) however from the modelling results, the idea of a compact city should be re-evaluated in light of the impacts this type of development has on LST and SUHI.

Open access data and freely available imagery has an important place in built-up and UHI studies where availability of older imagery allows for trend analysis. Their large resolution avails data over large expanses and their frequency in collecting data over an area is advantageous in studying land dynamics. High resolution data can provide detailed urban morphological information and provide LST data in wider ranges, which low resolution data does not give, though costs and frequency would be a limiting factor especially if area covered is large. Machine learning embedded in software and freely available is a robust tool in urban development, modelling urban phenomena with its capability to handle large data sets in determining an ideal physical form.

Implementation of ‘strong sustainability’ with economic growth needs to be enforced in urban areas as land cover changes indicate ‘weak sustainability’ in relation to natural resources. Human induced stressors are evident in land cover changes and their effect as indicated by LST changes in time space continuum. Lack of sufficient legal capacity to enforce green strategies indicates the gap between creation of policies that are meant to drive sustainable urban development to their implementation of conservation of non-renewable resources. The conceptual framework satisfies the theory that SUHI is influenced by built-up morphology and land cover and land use changes. Ecological economic theory and institutional theory therefore should be applied in tandem.

CHAPTER FIVE: SUMMARY, CONCLUSIONS AND RECOMMENDATIONS

5.1 Introduction

The primary purpose of this study was to develop a model that simulates' the impact of built-up morphology on land surface temperature in Upper Hill, Nairobi. The first objective was to evaluate the trend of land surface temperature and the relationship between land cover and land surface temperature. The second objective was to determine the relationship between built-up morphology and land surface temperature. The third objective was to determine the relationship between built-up volume densities and land surface temperature.

5.2 Summary of Findings

The land surface temperature affects both the urban canopy and urban boundary layer temperatures in an urban setting. The land surface temperature during the morning and afternoon follow the same trend as air temperature in the analyzed years. Mean air temperatures in the months of February are high with low rainfall compared to low temperatures and high rainfall in January. Land surface temperature is influenced by climatic events and conditions in the years 2000, 2005 and 2011 resulting to increased mean temperatures. Land covers that exist in Upper Hill are sparse grassland, open grassland, built-up, water and forest with built-up and forest land cover showing large increases and decreases in area respectively with time. NDVI reduces from 1986 to 2017 indicating that land cover changes have been influenced by increased urban development. Sparse and open grassland have high temperatures in the morning and low temperatures at night as they cool quickly. Water has high land surface temperatures in the afternoon and at night thus creating a warming effect in areas surrounding the water body. Forest land cover has low day-time and high nigh-time temperature creating a warming effect in

surrounding areas as it releases absorbed heat at night. Relationship between land cover and land surface temperature changes visibly indicate a correlation where changes from vegetated land cover to built-up have a great impact on the temperature change in Upper Hill. Land cover change defined as no-change has high percentage area and low temperature changes, while vegetation to built-up has high temperature changes in all years analyzed which affects the surface energy budget. Surface urban heat island effect is noted in Upper Hill due to differences in day and night temperatures between grassland and built-up areas where grasslands are high during the day and low at night compared to built-up land cover. There is a correlation between albedo and land surface temperature where high day-time temperatures occur on land cover having high albedo values and vice versa on land cover having low albedo. Forest and water land cover reduce land cover temperatures hence a negative contribution index while built-up, open and sparse grassland increase surface temperatures thus a positive contribution index.

Built-up volume density, ground coverage ratios and heights analyzed for the years 1978, 1998 and 2017 indicate an increase in values in time-series analysis. Mean heights in all years are less than 10 meters, which is low-rise, while densities are low densities both in ground coverage and built-up volume density. Low-rise buildings are the majority in all years compared to middle and high rise buildings with 1978 having a great percentage. Middle and high-rise buildings increase in 2017 while low-rise greatly reduce in between the year 1998 and 2017 due to different development patterns from 1978 such as in-filling with redevelopment on some blocks. Changes are high between the year 1998 and 2017 due to policy changes. Low density GCR reduces by a high percentage between the years 1998 and 2017 with a high increase in medium density in the same period. Low density BVD have a high reduction between the year 1998 and 2017 with an

increase in middle density BVD compared to high density BVD. Height of buildings in high density areas increases from low-rise in 1978 to high-rise in 2017 while low density are mostly low-rise buildings. 3D urban intensity expansion has resulted from densification, reconstruction of buildings and expansion of roads with high percentages in the central parts of Upper Hill. These are in land uses defined as residential, commercial, institutional and office. The land uses where high densities and high-rise built forms occur are mostly institutional, office, residential and commercial. Hot-spot analysis of day-time land surface temperature of the years 1978, 1998 and 2017 indicate that areas that have cold-spots are in forested parts of the study area while hot-spot areas are located in sparsely vegetated land cover. High-density built-up areas are hot-spots such as Kenyatta National Hospital. Night-time hot-spots occur in some parts that are cold-spots during the day especially with forested land cover. Cold-spots occur in open grounds while hot-spots occur along main roads in Upper Hill while have undergone expansion.

Ordinary linear regression and geographically weighted individual regression analysis between LST and aspect, NDVI, albedo, height, BVD and GCR at 30 meter and 90 meter grids indicates that GWR has a better model fit across the Upper Hill than OLS in both scales. GWR has better result at 90 m grid for built-up morphology indicating effect of scale. The influence of morphology on LST varies where BVD has high r^2 value in 1978, height and GCR have high r^2 in 1998 compared to BVD while in 2017 GCR and BVD have high r^2 values than height. Mean negative coefficients in height, GCR, BVD and NDVI indicates that an increase in each leads to a decrease in LST. Mean heights related with positive coefficients are low-rise while GCR and BVD have positive coefficients with low-density buildings. High-rise and high-density buildings are scattered in Upper Hill and therefore their pattern of influence cannot be mapped distinctly.

Low NDVI values which are sparsely vegetated have positive coefficients. Albedo and aspect have positive mean coefficients implying a corresponding increase in LST with each. East facing slopes have positive coefficients compared to west facing slopes as they are warmer. Range of coefficient values in 1998 tends to be high compared to 1978 and 2017 with albedo, NDVI and aspect while with height, GCR and BVD the coefficient range is low due to the high LST in 1998 compared to 1978 and 2017. Analysis combining NDVI, albedo, aspect with either building mean height, GCR and BVD shows an improvement in global method OLS in r^2 values compared to single-factor r^2 values. GWR performs better than OLS in r^2 values with both regression methods having high r^2 at 90 meter than at 30 meter scale. Based on overall r^2 values the best descriptors of variations of LST and urban morphological descriptors are height in 1978, BVD in 1998 and 2017. Spatial autocorrelation of standard residuals indicate the spatial objects have a clustered patterns in both GWR and OLS due to the strong relationship between close geographical features. Built-up morphological attributes in areas with r^2 values of more than 50% have increased from 1978 to 2017 due to increased urban development and has high 3D urban expansion intensity values in 2017. Range of r^2 values in 2017 indicate high relationship with LST in areas that have middle-rise buildings and medium density GCR and BVD. High density areas contribute positively to the changes in LST due to their thermal capacity. These findings are in agreement with the ecological and institutional theories that look at human induces stressors and the institutions that look into the development of sustainable environments.

5.3 Conclusions

Land cover changes in urban areas influences land surface temperature with a reduction in surface albedo which exacerbates the surface urban heat island effect. Land cover type impacts

day-time and night-time land surface temperatures, which affects its contribution in warming or cooling effect the environment. Policy reviews influence the rate and intensity of 3D urban expansion with high density and high rise developments being the current main form of development. Thermal heat storage increases with 3D urban expansion with effects being warming night-time temperatures thus increasing the urban heat island effect over the area. Geographically weighted regression is suitable for modelling the spatial relationship between variables having a non-linear relationship. Built-up volume densities have a greater relationship with land surface temperature compared to building height or ground coverage. Modelling built-up morphological attributes with topographical features and land cover characteristics captures the physical dynamics and interaction built-up forms have with land surface temperature.

5.4 Recommendations

1. Harmonization of institution policies addressing climate change with a need on focusing on integrating cities and urban development to their climate action and not only on rural development. This includes zoning regulations in urban areas in reference to building morphology and inclusion of performance zoning which is flexible, adaptive and dynamic. Development of a comprehensive environmental management plan that addresses issues of beautification and greening in urban areas is equally important.
2. There should be encouragement of green-roofs which would reduce the temperature within the urban boundary layer and also the radiation that is absorbed into the building from the roofs. Open spaces should be well defined, managed and protected as they are a key part of an ecosystem and contribute to the microclimate of an environment. Development of passive designs that take advantage of natural features in a site should be

encouraged and that seek to utilize green building technology for sustainability. Establishment of monitoring stations to collect meteorological and pollution data ensuring collection of accurate data to enable early mitigation of adverse effects of climate change.

3. Developing a national grid framework with standardized cell sizes for spatially analyzing land use changes in tackling climate change issues. Regular collection and use of 3D datasets on urban built forms for planning of cities and tackling climate change issues for climate resilient and smart city development. The use of geographically weighted regression in analyzing heterogeneous areas should be adopted to derive spatial variation between geographic entities.

5.5 Areas of Further Research

1. Measurement of air temperature in different seasons collected within the area for comparative analysis to determine the influence built-up forms have on the microclimate of the area.
2. Explore use of LiDAR to capture vegetation morphology to analyze their influence using high resolution thermal data, to enhance aspects of surface roughness and its impact on surface urban heat islands.
3. Analysis of the effects of different material types on air and land surface temperatures so as to recommend appropriate materials and albedos of pavements, roads and building materials.

REFERENCES

Abrams, M., & Hook, S. (2002). ASTER User Handbook Version 2. *Jet Propulsion, 2003*(23/09/2003), 135. https://doi.org/10.1017/CBO9781107415324.004

African Union Commission. (2014). *Agenda 2063: The Africa We Want*. *African Union*. https://doi.org/978-92-95104-23-5

AL_kinani, Y. H. K. (2015). Protect Digital Elevation Model (DTM) from Aerial Photographs by Using ERDAS IMAGINE. *Eng. & Tech. Journal*, *33*(8), 1890–1900.

Alhaddad, B., Roca, J., Burns, M., & Garcia, J. (2004). Satellite Imagery and Lidar Data for Efficiently Describing Structures and Densities in Residential Urban Land Uses Classification. *ISPRS XXXVII Congress*, 35–40. Retrieved from http://www.isprs.org/proceedings/XXXVII/congress/8_pdf/1_WG-VIII-1/07.pdf

Allen, M. R., Dube, O. P., Solecki, W., Aragón-Durand, F., Cramer, W., Humphreys, S., … Zickfeld, K. (2018). *Framing and Context. In: Global Warming of 1.5°C.*

Alobeid, A, Jacobsen, K., & Heipke, C. (2009). Building Height Estimation in Urban Areas from Very High Resolution Satellite Stereo Images. *ISPRS Hannover Workshop*, *5*, 2–5.

Alobeid, A, Jacobsen, K., Heipke, C., & Al Rajhi, M. (2011). Building Monitoring with Differential DSMs. *Isprs …*, *XXXVIII*(June), 14–17. Retrieved from http://www.int-arch-photogramm-remote-sens-spatial-inf-sci.net/XXXVIII-4-W19/7/2011/isprsarchives-XXXVIII-4-W19-7-2011.pdf

Alobeid, Abdalla. (2011). *Assessment for Matching Algorithms for Urban DSM Generation from Very High Resolution Satellite Stereo Images*. Leibniz University Hanover.

Argent, N. M. J. D., Beringer, J., Tapper, N., & Coutts, A. (2012). Planning for the Compact City ; An Assessment of Melbourne @ 5million. In *WSUD 2012: Water sensitive urban design; Building the water sensitive community; 7th international conference on water sensitive urban design* (pp. 781–785). Barton, ACT, Australia: Engineers Australia.

Association of Religion Data Archives. (2018). Institutional Theory , New and Old. Retrieved March 15, 2019, from http://wiki.thearda.com/tcm/theories/institutional-theory-new-and-old/

Bass, J. M., Nicholson, B., & Subrahmanian, E. (2013). A Framework Using Institutional Analysis and the Capability Approach in ICT4D. *Information Technologies & International Development*, *9*(1), 19–35.

Bassuk, N., Curtis, D., Marranca, B., & Neal, B. (2009). *Recommended Urban Trees: Site Assessment and Tree Selection for Stress Tolerance*. *Urban Horticulture Institute*. New york. Retrieved from http://www.hort.cornell.edu/uhi/outreach/recurbtree/pdfs/~recurbtrees.pdf

Bechtel, B., Zakšek, K., & Hoshyaripour, G. (2012). Downscaling Land Surface Temperature in an Urban Area: A Case Study for Hamburg, Germany. *Remote Sensing*, *4*(10), 3184–3200. https://doi.org/10.3390/rs4103184

Berger, C., Voltersen, M., Hese, S., Walde, I., & Schmullius, C. (2012). Using Geographic Object-Based Image Analysis (GEOBIA) for Urban Land Cover Mapping and Settlement

Density Assessment. *Proceedings of the 4th GEOBIA*, *49*(0), 503–508.

Bhargava, A., & Bhargava, S. (2018). Effects of Albedo in Urban Planning - Special Reference to Building Roofs. *Examines Mar Biol Oceanogr.*, *1*(2), 6–7. https://doi.org/10.31031/EIMBO.2018.01.000506

Blakely, E. J. (2007). *Urban Planning for Climate Change*. *Lincoln Institute of Land Policy Working Papers*. New Orleans.

Bottyan, Z., Kircsi, A., Szegedi, S., & Unger, J. (2005). The Relationship between Built-up Areas and the Spatial Development of the Mean Maximum Urban Heat Island in Debrecen, Hungary. *International Journal of Climatology*, *25*(3), 405–418. https://doi.org/10.1002/joc.1138

Bouyer, J., Musy, M., Huang, Y., & Athamena, K. (2009). Mitigating Urban Heat Island Effect by Urban Design: Forms and Materials. *Cities and Climate Change*, 164–181.

Çalışkan, O. (2004). *Urban Compactness : A Study of Ankara Urban Form*. Middle East Technical University.

Caltech/JPL. (2004). SWIR - ASTER User Advisory. Retrieved August 29, 2018, from https://asterweb.jpl.nasa.gov/swir-alert.asp

Carmin, J., Nadkarni, N., & Rhie, C. (2012). Progress and Challenges in Urban Climate Adaptation Planning: Results of a Global Survey, 33. Retrieved from http://resilient-cities.iclei.org/fileadmin/sites/resilient-cities/files/Resilient_Cities_2012/Urban_Adaptation_Report_23May2012.pdf

Cheng, J., Gould, N., Han, L., & Jin, C. (2017). Big Data for Urban Studies: Opportunities and Challenges: A Comparative Perspective. *2016 Intl IEEE Conferences on Ubiquitous Intelligence & Computing, Advanced and Trusted Computing, Scalable Computing and Communications, Cloud and Big Data Computing, Internet of People, and Smart World Congress*, (July), 1229–1234. https://doi.org/10.1109/UIC-ATC-ScalCom-CBDCom-IoP-SmartWorld.2016.0189

Children's Environmental Health Initiative. (2018). *Introduction to Hotspot Analysis*. Houston, Texas.

Chun, B., & Guldmann, J.-M. (2014). Spatial Statistical Analysis and Simulation of the Urban Heat Island in High-Density Central Cities. *Landscape and Urban Planning*, *125*, 76–88. https://doi.org/10.1016/j.landurbplan.2014.01.016

City of Melbourne. (2011). *Urban Forest Diversity Guidelines - Tree species selection strategy for the City of Melbourne*. Melbourne.

City of Melbourne. (2012). *Urban Forest Strategy: Making a Great City Greener 2012-2032*. *City of Melbourne*. Retrieved from https://www.melbourne.vic.gov.au/Sustainability/UrbanForest/Documents/Urban_Forest_Strategy.pdf

Coops, N. C., Duro, D. C., Wulder, M. A., & Han, T. (2007). Estimating Afternoon MODIS Land Surface Temperatures (LST) Based on Morning MODIS Overpass, Location and Elevation Information. *International Journal of Remote Sensing*, *28*(10), 2391–2396. https://doi.org/10.1080/01431160701294653

Crabtree, P., & Hall, L. (2016). *Trees in Urban Design*. *Landscape Journal* (Vol. 13). https://doi.org/10.3368/lj.13.1.64

Cristóbal, J., Jiménez-Muñoz, J. C., Prakash, A., Mattar, C., Skoković, D., & Sobrino, J. A. (2018). An Improved Single-Channel Method to Retrieve Land Surface Temperature from the Landsat-8 Thermal Band. *Remote Sensing*, *10*(3). https://doi.org/10.3390/rs10030431

Di Gregorio, A., & Jansen, L. J. M. (1998). Land Cover Classification System (LCCS): Classification Concepts and User Manual. *Fao*. Retrieved from http://www.fao.org/docrep/003/x0596e/x0596e00.htm

Diego, G., Euginia, C., David, H., & Pablo, R. (2013). Automated Urban Analysis Based on LiDAR Derived Building Models. *IEEE Transaction on Geoscience and Remote Sensing*, *51*(3), 1844–1851.

DuPuis, N., & Stahl, E. (2016). *Trends in Smart City Development*. *National League of Cities*.

Eckert, S. (2008). *3D-Building Height Extraction from Stereo IKONOS Data*. *JRC Scientific and Technical Reports*. Luxembourg. Retrieved from http://ses.jrc.it

Emporis. (2018). EMPORIS. Retrieved July 2, 2018, from https://www.emporis.com/buildings

EPA. (2008a). *Reducing Urban Heat Islands : Compendium of Strategies, Urban Heat Island Basics*. Retrieved from www.epa.gov/heatisland/resources/pdf/BasicsCompendium.pdf

EPA. (2008b). *Reducing Urban Heat Islands: Compendium of Strategies, Cool Pavements*. *Heat Island Reduction Activities*. https://doi.org/10.1175/1520-0450(2002)041<0792:THFIUA>2.0.CO;2

Esri. (2014). *3D Urban Mapping : From Pretty Pictures to 3D GIS*. *Esri*. Carlifornia. Retrieved from http://www.esri.com/library/whitepapers/pdfs/3d-urban-mapping.pdf

Esri. (2016). Interpreting GWR results—Help | ArcGIS for Desktop. Retrieved October 19, 2018, from http://desktop.arcgis.com/en/arcmap/10.3/tools/spatial-statistics-toolbox/interpreting-gwr-results.htm

Esri. (2018). Geographically Weighted Regression (GWR). Retrieved April 19, 2019, from https://pro.arcgis.com/en/pro-app/tool-reference/spatial-statistics/geographically-weighted-regression.htm

Fang, C., Liu, H., Li, G., Sun, D., & Miao, Z. (2015). Estimating the Impact of Urbanization on Air Quality in China using Spatial Regression Models. *Sustainability (Switzerland)*, *7*(11), 15570–15592. https://doi.org/10.3390/su71115570

FAO. (2018). Forests and Sustainable Cities. *Unasylva*, *69*(250), 88.

Feizizadeh, B., & Blaschke, T. (2013). Examining Urban heat Island Relations to Land Use and Air Pollution: Multiple Endmember Spectral Mixture Analysis for Thermal Remote Sensing. *IEEE Journal of Selected Topics in Applied Earth Observations and Remote Sensing*, *6*(3), 1749–1756. https://doi.org/10.1109/JSTARS.2013.2263425

Firl, G. J., & Carter, L. (2011). *Lesson 10 : Calculating Vegetation Indices from Landsat 5 TM and Landsat 7 ETM + Data*. *Natural Resources Ecology Laboratory, Colorado State Univeristy*.

Fischer, M. M., Getis, A., Wheeler, D. C., & Páez, A. (2010). Geographically Weighted Regression. *Handbook of Applied Spatial Analysis*, *47*(3), 461–486. https://doi.org/10.1111/1467-9884.00145

Forsyth, A. (2003). Measuring Density : Working Definitions for Residential Density and Building Intensity. *Design Center for American Urban Landscape*, *8*(8), 2–8.

Frank, K. (2015). *Kenya Market Update*. *Knight Frank*. Nairobi.

Fu, W. J., Jiang, P. K., Zhou, G. M., & Zhao, K. L. (2014). Using Moran's I and GIS to Study the Spatial Pattern of Forest Litter Carbon Density in a Subtropical Region of Southeastern China. *Biogeosciences*, *11*(8), 2401–2409. https://doi.org/10.5194/bg-11-2401-2014

Ge, Y., Song, Y., Wang, J., Liu, W., Ren, Z., Peng, J., & Lu, B. (2017). Geographically Weighted Regression-Based Determinants of Malaria Incidences in Northern China. *Transactions in GIS*, *21*(5), 934–953. https://doi.org/10.1111/tgis.12259

Georganos, S. (2016). Exploring the Spatial Relationship between NDVI and Rainfall in the Semi-Arid Sahel using Geographically Weighted Regression, (December). https://doi.org/10.13140/RG.2.2.10145.40803

Gorsevski, V., Taha, H., Quattrochi, D., & Luvall, J. (1998). Air Pollution Prevention through Urban Heat Island Mitigation: An Update on the Urban Heat Island Pilot Project, (x), 23–32. Retrieved from http://scholar.google.com/scholar?hl=en&btnG=Search&q=intitle:Air+Pollution+Prevention+Through+Urban+Heat+Island+Mitigation+:+An+Update+on+the+Urban+Heat+Island+Pilot+Project#0

Gowdy, J. M. (2000). Terms and Concepts in Ecological Economics. *Wildlife Society Bulletin*, *28*(1), 26–33. https://doi.org/10.2307/4617280

Guo-an, T., Strobl, J., Jian-ya, G., Mu-dan, Z., & Zhen-jiang, C. (2001). Evaluation on the Accuracy of Digital Elevation Models. *Journal of Geographical Sciences*, *11*(2), 209–216. https://doi.org/10.1007/BF02888692

Guo, G., Zhou, X., Wu, Z., Xiao, R., & Chen, Y. (2016). Characterizing the Impact of Urban Morphology Heterogeneity on Land Surface Temperature in Guangzhou, China. *Environmental Modelling & Software*, *84*(June), 427–439. https://doi.org/10.1016/j.envsoft.2016.06.021

Guzmán, J. M., Martine, G., Gordon, M., Daniel, S., & Cecilia, T. (2009). *Population Dynamics and Climate Change*.

HARRIS Geospatial Solutions Inc. (2019). Atmospheric Correction. Retrieved August 30, 2018, from https://www.harrisgeospatial.com/docs/AtmosphericCorrection.html

Hassani, H., Huang, X., & Silva, E. (2019). Big Data and Climate Change. *Big Data and Cognitive Computing*, *3*(1), 12. https://doi.org/10.3390/bdcc3010012

Hebbert, M. (2012). *Cities and Climate Change: Global Report on Human Settlements 2011*. *The Town Planning Review* (Vol. 83). https://doi.org/10.1787/9789264091375-en

Heldens, W., Esch, T., & Taubenböck, H. (n.d.). Climate Change in Cities – Can Remote

Sensing Help to Optimise Mitigation Strategies? In *RE-MIXING THE CITY- Towards Sustainability and Resilience?* (Vol. 1, pp. 121–128). REAL CORP.

Hoverter, S. P. (2012). *Adapting to Urban Heat: A Tool Kit for Local Governments*. Retrieved from http://66.39.13.15/sites/default/files/climate-adaptation-urban-heat.pdf%5Cnhttp://www.law.georgetown.edu/academics/academic-programs/clinical-programs/our-clinics/HIP/upload/Urban-Heat-Toolkit_RD2.pdf

Hubacek, K., & Vazquez, J. (2014). *The Economics of Land Use Change*. Laxenburg,.

Humanitarian Data Exchange. (2019). Kenya Admin Boundaries - Election Polling stations - Humanitarian Data Exchange. Retrieved June 3, 2019, from https://data.humdata.org/dataset/kenya-elections

Hunt, A., & Watkiss, P. (2011). Climate Change Impacts and Adaptation in Cities: A Review of the Literature. *Climatic Change*, *104*(1), 13–49. https://doi.org/10.1007/s10584-010-9975-6

Inostroza, L. (2014). Open Space and Urban Ecosystem Services. *Jornal of Land Use, Mobility and Environment*, 523–534.

JICA. (2014). The Project on Integrated Urban Development Master Plan for the City of Nairobi in the Republic of Kenya Final Report (Draft), (May), 221. Retrieved from http://citymasterplan.nairobi.go.ke/index.php/downloads/doc_download/132-draft-final-report-main1

Joshi, S., Saxena, S., Godbole, T., & Shreya. (2016). Developing Smart Cities: An Integrated Framework. *Procedia Computer Science*, *93*(September), 902–909. https://doi.org/10.1016/j.procs.2016.07.258

K'Akumu, O. A. (2007). Construction statistics review for Kenya. *Construction Management and Economics*, *25*(3), 315–326. https://doi.org/10.1080/01446190601139883

Kanuri, C., Revi, A., Espey, J., & Kuhle, H. (2016). *Getting Started with the SDGs in Cities*. Retrieved from http://unsdsn.org/wp-content/uploads/2016/07/9.1.8.-Cities-SDG-Guide.pdf

Karanja, F. N., & Matara, S. (2013). The Transformation from Green to Concrete Cities; A Remote Sensing Perspective. *International Archives of the Photogrammetry, Remote Sensing and Spatial Information Sciences - ISPRS Archives*, *40*(1W1), 163–166. Retrieved from http://www.scopus.com/inward/record.url?eid=2-s2.0-84924739749&partnerID=tZOtx3y1

Karoki, E. M. (2004). *Examination of Effects of Rezoning on the Transport Demand in Nairobi Hill Area*. (E. Karoki, Ed.). University of Nairobi. Retrieved from http://erepository.uonbi.ac.ke/bitstream/handle/11295/20133/Karoki_Examination Of Effects Of Rezoning On The Transport Demand In Nairobi Hill Area.pdf?sequence=3

Kenya Urban Roads Authority. (2016). *Rehabilitation and Upgrading of UpperHill Roads*. Nairobi.

Kiai, S. K. (2009). *Reversing Horizontal Sprawl: Towards More Compact City Neighbourhoods. Shelter Design & Development*.

Kinoti, S. . (2017). *Upgrading of Nairobi Urban Road Network*. Nairobi.

Koomen, E., Rietveld, P., & Bacao, F. (1998). The Third Dimension in Urban Geography: The Urban Volume Approach, 1–24.

Koukoulas, S., Vafeidisa, A. T., Vafeidis, G., & Symeonakis, E. (2008). The Role of Spatial Metrics on the Performance of an Artificial Neural-Network Based Model for Land Use Change. *The International Archives of the Photogrammetry, Remote Sensing and Spatial Information Sciences*, *37*(1), 1661–1666.

Krehl, A., Siedentop, S., Taubenböck, H., & Wurm, M. (2016). A Comprehensive View on Urban Spatial Structure: Urban Density Patterns of German City Regions. *ISPRS International Journal of Geo-Information*, *5*(6), 76. https://doi.org/10.3390/ijgi5060076

Lambin, E. F., Geist, H. J., & Lepers, E. (2003). Dynamics of Land-Use and Land-Cover Change in Tropical Regions. *Annual Review of Environment and Resources*, *28*(1), 205–241. https://doi.org/10.1146/annurev.energy.28.050302.105459

Lawrence, T. B., & Shadnam, M. (2008). Institutional Theory. In W. Donsbach (Ed.), *The International Encyclopedia of Communication* (V, pp. 2288–2293). Blackwell Publishing Ltd.

Li, Y., Zhao, M., Motesharrei, S., Mu, Q., Kalnay, E., & Li, S. (2015). Local Cooling and Warming Effects of Forests Based on Satellite Observations. *Nature Communications*, *6*, 1–8. https://doi.org/10.1038/ncomms7603

Liu, K., Su, H., Zhang, L., Yang, H., Zhang, R., & Li, X. (2015). Analysis of the Urban Heat Island Effect in Shijiazhuang, China using Satellite and Airborne Data. *Remote Sensing*, *7*(4), 4804–4833. https://doi.org/10.3390/rs70404804

Longyu, S., Guofan, S., Shenghui, C., Xuanqi, L., Tao, L., Kai, Y., & Jingzhu, Z. (2009). Urban Three-Dimensional Expansion and its Driving Forces - A Case Study of Shanghai, China. *Chinese Geographical Science*, *19*(4), 291–298. https://doi.org/10.1007/s11769-009-0291-x

Lowe, B., & Kulkarni, A. (2015). Multispectral Image Analysis Using Random Forest. *International Journal on Soft Computing*, *6*(1), 1–14. https://doi.org/10.5121/ijsc.2015.6101

Lucia, P., Luca, C., Sergio, M., Alessandro, C., Benjamin, Q., Nathalie de, N.-D., … Almut, A. (2017). Biophysical Effects on Temperature and Precipitation due to Land Cover Change. *Environmental Research Letters*, *12*(5), 53002. Retrieved from http://stacks.iop.org/1748-9326/12/i=5/a=053002

Luhmann, T., Robson, S., Harley, I., & Kyle, S. (2006). *Close Range Photogrammetry: Principles, Techniques and Applications*. Caithness: Whittles Publishing.

Macharia, E. (2012). Managing Expansion of Commercial Districts for Sustainable Development : A Case Study of Upper Hill Area in Nairobi , Kenya Managing Expansion of Commercial Districts for Sustainable Development : A Case Study of Upper Hill Area in Nairobi , Kenya, (May), 6–10.

Makokha, G. L., & Shisanya, C. A. (2010). Trends in Mean Annual Minimum and Maximum Near Surface Temperature in Nairobi City, Kenya. *Advances in Meteorology*, *2010*, 1–6. https://doi.org/10.1155/2010/676041

Marks, H. (2009). *The Impact of Asphalt Pavements on the Urban Heat Island*. Lanham.

Retrieved from http://co-asphalt.com/wp-content/uploads/documents/Environmental/napa_special_report_202_uhi1.pdf

Marr, P. G. (2014). Directional (Circular) Statistics. Retrieved from http://webspace.ship.edu/pgmarr/Geo441/Lectures/Lec 16 - Directional Statistics.pdf

Martensson, U. (2004). Map Accuracy Assessment. Retrieved from https://www.nateko.lu.se/sites/nateko.lu.se.sv/files/assessment_of_classification_accuracy2.pdf

Masson-Delmotte, V., Zhai, P., Pörtner, H.-O., Roberts, D., Skea, J., Shukla, P. R., … (eds), T. W. (2018). *IPCC, 2018: Summary for Policymakers. In: Global Warming of 1.5°C. IPCC Special Report*. Geneva: IPCC. https://doi.org/10.1017/CBO9781107415324

Mathews, B., & Weigle, B. (2015). Automated Feature Extraction from Aerial Imagery for Forestry Projects The Power of 4. *ESRI International User Conference 2015*. Retrieved from http://proceedings.esri.com/library/userconf/proc15/index.html

Mbogo, E., Inganga, F., & Maina, J. (2015). *Drought Conditions and Management Strategies in Kenya*. Nairobi. Retrieved from http://www.ais.unwater.org/ais/pluginfile.php/629/mod_page/content/6/Senegal_EN.pdf

Mccormick, K., Anderberg, S., Coenen, L., & Neij, L. (2013). Advancing Sustainable Urban Transformation. *Journal of Cleaner Production*, *50*, 1–11. https://doi.org/10.1016/j.jclepro.2013.01.003

Mccormick, K., Neij, L., & Anderberg, S. (2012). Sustainable Urban Transformation and the Green Urban Economy. *The Economy of Green Cities: A World Compendium on the Green Urban Economy*, 11.

Mccormick, K., Richter, J. L., & Pantzar, M. (2015). *Greening the Economy Compendium*. Lund University.

McWilliam. N, Teeuw .R, Whiteside .M, Z. . . (2005). Field Techniques Manual: GIS, GPS and Remote Sensing. In *GIS GPS and Remote Sensing Field Techniques Manual* (1st ed., pp. 153–176). London: Geography Outdoors Royal Geographical Society (with IBG). Retrieved from http://www.rgs.org/NR/rdonlyres/4F82496A-3CD1-4337-B644-00C8892B4174/0/Chapter5RemoteSensing.pdf%5Cnhttp://www.rgs.org/OurWork/Publications/EAC+publications/GIS+GPS+and+Remote+Sensing.htm

Memon, R. A., Leung, D. Y. C., & Chunho, L. I. U. (2008). A Review on the Generation, Determination and Mitigation of Urban Heat Island, *20*, 120–128.

Mennis, J. (2006). Mapping the Results of Geographically Weighted Regression. *The Cartographic Journal*, *43*(2), 171–179. https://doi.org/10.1179/000870406X114658

Mills, G. (2004). The Urban Canopy Layer Heat Island IAUC Teaching Resources. *IAUC Newsletter*, 1–5.

Mirzaei, P. A. (2015). Recent Challenges in Modeling of Urban Heat Island. *Sustainable Cities and Society*, *19*, 200–206. https://doi.org/10.1016/j.scs.2015.04.001

Mishra, S. (2009). An Exploration of Environmental Capital in Context of Multiple Deprivation:

A Case of Kalyan-Dombivli Kalyan, India.

Mohajeri, N., Gudmundsson, A., Upadhyay, G., & Assouline, D. (2015). Neighbourhood Morphology and Solar Irradiance in Relation to Urban Climate. *9th International Conference on Urban Climate Jointly with 12th Symposium on the Urban Environment*, (July 2015), 1–6.

Murayama, Y., & Rajesh, T. B. (2011). *Spatial Analysis and Modeling in Geographical Transformation Process: GIS-based Applications*. (R. B. T. Yuji Murayama, Ed.), *Springer*. https://doi.org/10.1007/978-94-007-0671-2

Mwangi, P. W., Karanja, F. N., & Kamau, P. K. (2018). Analysis of the Relationship between Land Surface Temperature and Vegetation and Built-Up Indices in Upper-Hill, Nairobi. *Journal of Geoscience and Environment Protection*, *06*(01), 1–16. https://doi.org/10.4236/gep.2018.61001

Mwaura, A. M. (2006). Policy Review for Zones 3 , 4 and 5 , Nairobi , Kenya. *ISoCaRP Congress*, 1–13.

Nairobi City County. (2006). *A Guide of Nairobi City Development Ordinances and Zones*. Nairobi.

Nairobi City County, Japan International Cooperation Agency, & Nippon Koei Co., L. (2014). *The Project on Integrated Urban Development Master Plan for the City of Nairobi in the Republic of Kenya Final Report Part II: The Master Plan Nairobi City County (NCC)*. https://doi.org/10.1016/B978-0-12-374849-2.00005-8

Nairobi Town Planning Liaison Committee. (1993). *Proposed Replanning and Rezoning of Hill and Kilimani Areas-Nairobi*. Nairobi.

Nakata, C. M., & de Souza, L. C. L. (2013). Verification of the Influence of Urban Geometry on the Nocturnal Heat Island Intensity. *Journal of Urban and Environmental Engineering*, *7*(2), 286–292. https://doi.org/10.4090/juee.2013.v7n2.286292

NASA. (2009). Landsat 7 science data users handbook. *National Aeronautics and Space Administration Landsat*, 186. Retrieved from http://glovis.usgs.gov/%0Ahttp://edcsns17.cr.usgs.gov/EarthExplorer/%0Ahttp://www.landcover.org/index.shtml%0Ahttp://landsathandbook.gsfc.nasa.gov/handbook/handbook_toc.html

NASA. (2018a). Landsat 4 « Landsat Science. Retrieved October 17, 2018, from https://landsat.gsfc.nasa.gov/landsat-4/

NASA. (2018b). Landsat 6 « Landsat Science. Retrieved October 17, 2018, from https://landsat.gsfc.nasa.gov/landsat-6/

National Environmental Management Authority. (2011). *Integrated National Landuse Guidelines*. Nairobi.

Nebiker, S., Lack, N., & Deuber, M. (2014). Building Change Detection from Historical Aerial Photographs using Dense Image Matching and Object-Based Image Analysis. *Remote Sensing*, *6*(9), 8310–8336. https://doi.org/10.3390/rs6098310

Neidhart, H., & Brenner, C. (2003). Automatic Calculation of Building Volumes for an Area-

Wide Determination of Heat Requirements. Retrieved from http://www.ikg.uni-hannover.de/fileadmin/ikg/staff/publications/Konferenzbeitraege_abstract_review/NeidhartBrenner_ISPRS2003.pdf%5Cnneidhart 02.07.2003 - Microsoft Word.pdf

Ng, E., & Ren, C. (2015). *The Urban Climatic Map for Sustainable Urban Planning* (1st ed.). New york: Routledge. Retrieved from www.routledge.com

Noi, P., Kappas, M., & Degener, J. (2016). Estimating Daily Maximum and Minimum Land Air Surface Temperature Using MODIS Land Surface Temperature Data and Ground Truth Data in Northern Vietnam. *Remote Sensing*, *8*(12), 1002. https://doi.org/10.3390/rs8121002

Nyaga, E. (2014a). *Air Quality as a Factor of Urban Heat Islands Phenomenena: A Case Study of Nairobi*. University of Nairobi.

Nyaga, E. (2014b). Air Quality as a Factor of Urban Heat Islands Phenomenena: A Case Study of Nairobi. *Environment and Urbanization*, *1*(1), 1–9. https://doi.org/10.1007/s13398-014-0173-7.2

Nyaura, J. E. (2014). Urbanization Process in Kenya : The Effects and Consequences in the 21 st Century, *1*(2), 33–42.

Odunuga, S., & Badru, G. (2015). Landcover Change, Land Surface Temperature, Surface Albedo and Topography in the Plateau Region of North-Central Nigeria. *Land*, *4*(2), 300–324. https://doi.org/10.3390/land4020300

Oke, T. (2014). *Boundary Layer Climates.* Routledge. Retrieved from https://books.google.co.ke/books/about/Boundary_Layer_Climates.html?id=vNAangEACAAJ&redir_esc=y

Ongoma, V., Muthama, J. N., & Gitau, W. (2013a). Evaluation of urbanization influences on urban temperature of Nairobi City, Kenya. *Global Meteorology*, *2*(1), 1. https://doi.org/10.4081/gm.2013.e1

Ongoma, V., Muthama, N. J., & Gitau, W. (2013b). Evaluation of Urbanization Influences on Urban Temperature of Nairobi City, Kenya. *Global Meteorology*, *2*(1), 1. https://doi.org/10.4081/gm.2013.e1

Ongoma, V., Muthama, N. J., & Gitau, W. (2013c). Evaluation of Urbanization Influences on Urban Winds of Kenyan Cities. *Ethiopian Journal of Environmental Studies and Management*, *6*(3), 223–231.

Ongoma, V., Otieno, G., & Omondi, O. A. (2014). An Investigation of the Transport and Dispersion of Atmospheric Pollutants over Nairobi City. *Journal of Environmental and Agricultural Sciences*, *1*(10), 1–10.

Opiyo, R. (2009). Metropolitan Planning and Climate Change in Nairobi : How Much Room To Manouvre ? In *FIFTH URBAN RESEARCH SYMPOSIUM* (p. 14).

Ord, J. K., & Getis, A. (2010). Local Spatial Autocorrelation Statistics: Distributional Issues and an Application. *Geographical Analysis*, *27*(4), 286–306. https://doi.org/10.1111/j.1538-4632.1995.tb00912.x

Parcher, J. (2012). Landsat History and Legacy. In *UNCOPUOS Special Panel for the 40th Anniversary of the Landsat Programme and the Worldwide Evolution of Remote Sensing from Space* (pp. 1–13). Vienna: United States Geological Survey.

Perini, K., & Magliocco, A. (2014). Effects of Vegetation, Urban Density, Building Height, and Atmospheric Conditions on Local Temperatures and Thermal Comfort. *Urban Forestry and Urban Greening*, *13*(3), 495–506. https://doi.org/10.1016/j.ufug.2014.03.003

Potsiou, C., Doytsher, Y., Paul, K., Khouri, R., McLaren, R., & Mueller, H. (2010). Rapid Urbanization and Mega Cities: The Need for Spatal Information Management. In *SIM in Support of Mega City Management* (pp. 109–119). Sydney: International Federation of Surveyors.

Prastacos, P., Chrysoulakis, N., & Kochilakis, G. (2011). Urban Atlas, Land Use Modelling and Spatial Metric Techniques. *ERSA Conference Papers*.

Propastin, P., Kappas, M., & Erasmi, S. (2008). Application of Geographically Weighted Regression to Investigate the Impact of Scale on Prediction Uncertainty by Modelling Relationship between Vegetation and Climate *. *International Journal of Spatial Data Infrastructures Research*, *3*(January), 73–94. https://doi.org/10.2902/1725-0463.2008.03.art6

Qin, J., Fang, C., Wang, Y., Li, G., & Wang, S. (2015). Evaluation of Three-Dimensional Urban Expansion: A Case Study of Yangzhou City, Jiangsu Province, China. *Chinese Geographical Science*, *25*(2), 224–236. https://doi.org/10.1007/s11769-014-0728-8

Rad, H. R., Rafieian, M., & Sozer, H. (2017). Evaluating the Effects of Increasing of Building Height on Land Surface Temperature. *Urban Management and Energy Sustainability*, *1*(1), 11–16.

Republic of Kenya. (2009a). *Building Code of the Republic of Kenya (2009 Edition)* (Vol. 169). Nairobi.

Republic of Kenya. (2009b). *Sessional Paper No. 3 of 2009 on National Land Policy*. Nairobi.

Republic of Kenya. (2010). NCCRS National Climate Change Response Strategy, (April), 1–122.

Republic of Kenya. (2013). *National Climate Change Action Plan 2013 -2017*. Nairobi.

Republic of Kenya. (2016). *National Spatial Plan: Optimal Productivity, Sustainability, Efficiency and Equity in the use of our Land and Territorial Space*. Nairobi.

Republic of Kenya. (2017). *Kenya's Popular Version of the New Urban Agenda: Towards Inclusive , Safe , Resilient and Sustainable Cities and Human Settlements*. Nairobi.

Satterthwaite, D. (2008). Climate Change and Urbanization: Effects and Impliactions for Urban Governance. *United Nations Expert Group Meeting on Population Distribution, Urbanization, Internatl Migration and Development. New York , 21-23 January 2008.*, (December 2007), 29. Retrieved from http://www.un.org/esa/population/meetings/EGM_PopDist/P16_Satterthwaite.pdf

Satterthwaite, D., & McGranahan, G. (2014). Urbanisation Concepts and Trends. *Urban*, (May), 1–28. https://doi.org/ISBN 978-1-78431-063-9

Schenk, T. (1999). *Digital Photogrammetry* (Volume 1). Ohio: TerraScience.

Schenk, T. (2005). Introduction to Photogrammetry. Retrieved from http://www.mat.uc.pt/~gil/downloads/IntroPhoto.pdf

Schipper, L., Liu, W., Krawanchid, D., & Chanthy, S. (2010). Review of Climate Change Adaptation Methods and Tools. *MRC Technical Paper No. 34*, (34), 76. Retrieved from http://www.mrcmekong.org/assets/Publications/technical/Tech-No34-Review-of-climate-change.pdf

Schläpfer, M., Lee, J., & Bettencourt, L. M. A. (2015). Urban Skylines: Building Heights and Shapes as Measures of City Size. Retrieved from http://arxiv.org/abs/1512.00946

Shahmohamadi .P, Che-Ani .A.I, Maulud K. N. A., Tawil N.M., & Abdullah .N. A.G. (2012). The Impact of Anthropogenic Heat on Formation of Urban Heat Island and Energy Consumption Balance. *Urban Studies Research*, *2011*, 1–9. https://doi.org/10.1155/2011/497524

Shahmohamadi, P., Cubasch, U., & Sodoudi, S. (2012). Mitigating Urban Heat Island Effects in Tehran Metropolitan Area. https://doi.org/10.5772/2591

Shirowzhan, S., & Lim, S. (2014). Three Dimensional Spatial Metrics for Compactness Assessment of Urban Forms. *31st International Symposium on Automation and Robotics in Construction and Mining, ISARC 2014 - Proceedings*, (Isarc), 884–889. Retrieved from http://www.scopus.com/inward/record.url?eid=2-s2.0-84912575406&partnerID=tZOtx3y1

Singh, S. P. (2013). Virtual 3D City Modeling: Techiques and Applications, *XL*(November), 27–29.

Sobrino, J. A., Oltra-carrió, R., Sòria, G., Jiménez-Muñoz, J. C., Franch, B., Hidalgo, V., … Marc, P. (2013). Evaluation of the Surface Urban Heat Island Effect in the City of Madrid by Thermal Remote Sensing. *International Journal of Remote Sensing*, *34:9-10*(January 2016), 3177–3192. https://doi.org/10.1080/01431161.2012.716548

Sodoudi, S., Wesonga, J. M., Matsaba, E. O., Njoroge, J. B., & Adimo, A. O. (2018). Attenuation Effect of Plant Canopy Sizes on Microclimate in Urban Greenspaces within Nairobi City, Kenya. *African Journal of Plant Science*, *12*(7), 129–140. https://doi.org/10.5897/ajps2018.1659

Sokido, D. L. (2016). Density in Relation to Patterns of Built-forms (Case Study: Addis Ababa, Ethiopia). *International Journal of Architecture and Urban Development*, *6*(3), 5–18.

Srivanit, M., & Kazunori, H. (2011). The Influence of Urban Morphology Indicators on Summer Diurnal Range of Urban Climate in Bangkok Metropolitan Area, Thailand. *International Journal of Civil & Environmental Engineering*, *11*(5), 34–46.

Stempihar, J., Pourshams-Manzouri, T., Kaloush, K., & Rodezno, M. C. (2013). Porous Asphalt Pavement Temperature Effects on Overall Urban Heat Island. *Journal of Chemical Information and Modeling*, *53*(9), 1689–1699. https://doi.org/10.1017/CBO9781107415324.004

Strømann-Andersen, J., & Sattrup, P. A. (2011). The Urban Canyon and Building Energy Use: Urban Density versus Daylight and Passive Solar Gains. *Energy and Buildings*, *43*(8), 2011–2020. https://doi.org/10.1016/j.enbuild.2011.04.007

Tack, F., Buyuksalih, G., & Goossens, R. (2012). 3D Building Reconstruction based on Given Ground Plan Information and Surface Models Extracted from Spaceborne Imagery. *ISPRS Journal of Photogrammetry and Remote Sensing*, *67*(1), 52–64. https://doi.org/10.1016/j.isprsjprs.2011.10.003

Tarawally, M., Xu, W., Hou, W., & Mushore, T. D. (2018). Comparative Analysis of Responses of Land Surface Temperature to Long-Term Land Use/Cover Changes between a Coastal and Inland City: A Case of Freetown and Bo Town in Sierra Leone. *Remote Sensing*, *10*(1), 1–18. https://doi.org/10.3390/rs10010112

Tian, F., Qiu, G. Y., Yang, Y. H., Xiong, Y. J., & Wang, P. (2012). Studies on the Relationships between Land Surface Temperature and Environmental Factors in an Inland River Catchment based on Geographically Weighted Regression and MODIS Data. *IEEE Journal of Selected Topics in Applied Earth Observations and Remote Sensing*, *5*(3), 687–698. https://doi.org/10.1109/JSTARS.2012.2190978

TP . Ho Chi Minh Land Use Change Detection and Analysis for the Megacity Ho Chi Minh City. (2013), (January), 2013.

Trlica, A., Hutyra, L. R., Schaaf, C. L., Erb, A., & Wang, J. A. (2017). Albedo, Land Cover, and Daytime Surface Temperature Variation Across an Urbanized Landscape. *Earth's Future*, *5*(11), 1084–1101. https://doi.org/10.1002/2017EF000569

U.S. Geological Survey (USGS), & National Aeronautics and Space Administration (NASA). (2016). *Landsat 8 (L8) Data Users Handbook*. *America* (2nd ed., Vol. 8). https://doi.org/http://www.webcitation.org/6mu9r7riR

UN-Habitat. (2010). *Planning Sustainable Cities: Global Report on Human Settlements 2009*. *United Nations Human Setlements Programme*. Earthscan.

UN-Habitat. (2012). *Urban Patterns for a Green Economy: Leveraging Density*. (V. Quinlan, Ed.) (1st ed.). Nairobi.

United Nations Development Program. (2015). *Kenya Natural Disaster Profile*. Retrieved from http://meteorology.uonbi.ac.ke/sites/default/files/cbps/sps/meteorology/Project on Disasters.pdf

United Nations Development Programme. (2016). Climate Change - United Nations Sustainable Development. Retrieved from http://www.un.org/sustainabledevelopment/climate-change-2/

United Nations Environment Programme, United Nations Centre for Human Settlements, & Republic of Kenya. (2009). *City of Nairobi Environment Outlook*. Nairobi. https://doi.org/10.1109/VS-GAMES.2015.7295756

United Nations Sustainable Development. (2015). Cities - United Nations Sustainable Development Action 2015. *United Nations Sustainable Development*. Retrieved from http://www.un.org/sustainabledevelopment/cities/#f3c52f92070201572

Upper Hill District Association. (2015). Upper Hill District Association. Retrieved February 21, 2019, from http://www.uhda.or.ke/

Upper Hill District Association. (2017). *UHDA Newsletter*. Nairobi.

USGS. (2013). Sea Level Rise and Coastal Regions | Climate and Land Use Change Research and Development Program. Retrieved May 8, 2015, from http://www.usgs.gov/climate_landuse/clu_rd/pt_sealevel_rise.asp

USGS. (2015). Sentinel-2 | The Long Term Archive. Retrieved October 17, 2018, from https://lta.cr.usgs.gov/sentinel_2

Vogelmann, J., Howard, S. . ., Yang, L., Larson, C. . ., Wylie, B. . ., & Driel, N. (2001). Completion of the 1990s National Land Cover Data Set for the Conterminous United States from LandSat Thematic Mapper Data and Ancillary Data Sources. *Photogrammetric Engineering & Remote Sensing*, *67*(June), 13. https://doi.org/10.1007/978-94-011-4976-1

Voogt, J. A. (2007). How Researchers Measure Urban Heat Islands. *Department of Geography*, 34. Retrieved from http://epa.gov/heatisland/resources/pdf/EPA_How_to_measure_a_UHI.pdf

Voogt, J. A., & Oke, T. R. (2003). Thermal Remote Sensing of Urban Climates. *Remote Sensing of Environment*, *86*(3), 370–384. https://doi.org/10.1016/S0034-4257(03)00079-8

Wan, Z., & Barbara, S. (2006). MODIS Land Surface Temperature Products Users' Guide. *Quality Assurance*, (March).

Wang, J., Zhan, Q., & Guo, H. (2016). The Morphology, Dynamics and Potential Hotspots of Land Surface Temperature at a Local Scale in Urban Areas. *Remote Sensing*, *8*(1). https://doi.org/10.3390/rs8010018

Wang, Y. (2016). Automatic Extraction of Building Outline from High Resolution Aerial Imagery. *International Archives of the Photogrammetry, Remote Sensing and Spatial Information Sciences - ISPRS Archives*, *41*(July), 419–423. https://doi.org/10.5194/isprsarchives-XLI-B3-419-2016

Wapwera, S. D. (2013). Spatial Planning Framework for Urban Development and Management in Jos Metropolis Nigeria, (October).

Wetangula, J., & Mazurewicz, M. (2017). *Market Research Preliminary Report: The Construction Market in Kenya*. Nairobi.

Wu, C.-D., & Lung, S.-C. C. (2016). Application of 3-D Urbanization Index to Assess Impact of Urbanization on Air Temperature. *Scientific Reports*, *6*, 24351. https://doi.org/10.1038/srep24351

Wu, C.-D., Lung, S.-C. C., & Jan, J.-F. (2013). Development of a 3-D Urbanization Index using Digital Terrain Models for Surface Urban Heat Island Effects. *ISPRS Journal of Photogrammetry and Remote Sensing*, *81*, 1–11. https://doi.org/10.1016/j.isprsjprs.2013.03.009

Wurm, M., D'Angelo, P., Reinartz, P., & Taubenböck, H. (2014). Investigating the Applicability of Cartosat-1 DEMs and Topographic Maps to Localize Large-Area Urban Mass Concentrations. *IEEE Journal of Selected Topics in Applied Earth Observations and Remote Sensing*, *7*(10), 4138–4152. https://doi.org/10.1109/JSTARS.2014.2346655

Xiao, H., Kopecká, M., Guo, S., Guan, Y., Cai, D., Zhang, C., … Yao, W. (2018). Responses of Urban Land Ssurface Temperature on Land Cover: A Comparative Study of Vienna and Madrid. *Sustainability (Switzerland)*, *10*(2). https://doi.org/10.3390/su10020260

Yang, X., & Li, Y. (2015). The Impact of Building Density and Building Height Heterogeneity on Average Urban Albedo and Street Surface Temperature. *Building and Environment*, *90*(August), 146–156. https://doi.org/10.1016/j.buildenv.2015.03.037

Yang, X., Li, Y., Luo, Z., & Chan, P. W. (2017). The Urban Cool Island Phenomenon in a High-Rise High-Density City and its Mechanisms. *International Journal of Climatology*, *37*(2), 890–904. https://doi.org/10.1002/joc.4747

Yang, Y., Zhang, X., Lu, X., Hu, J., Pan, X., Zhu, Q., & Su, W. (2017). Effects of Building Design Elements on Residential Thermal Environment. *Sustainability (Switzerland)*, *10*(1), 1–15. https://doi.org/10.3390/su10010057

Yuan, F., & Bauer, M. E. (2007). Comparison of Impervious Surface Area and Normalized Difference Vegetation Index as Indicators of Surface Urban Heat Island Effects in Landsat Imagery. *Remote Sensing of Environment*, *106*(3), 375–386. https://doi.org/10.1016/j.rse.2006.09.003

Zhan, J., Huang, J., Zhao, T., Geng, X., & Xiong, Y. (2015). Modeling the Impacts of Urbanization on Regional Climate Change : A Case Study in the Beijing-Tianjin-Tangshan Metropolitan Area, *2013*(2013), 1–7.

Zhan, Q., Meng, F., & Xiao, Y. (2015). Exploring the Relationships between Land Surface Temperature, Ground Coverage Ratio and Building Volume Density in an Urbanized Environment. *ISPRS - International Archives of the Photogrammetry, Remote Sensing and Spatial Information Sciences*, *XL-7/W3*(May), 255–260. https://doi.org/10.5194/isprsarchives-XL-7-W3-255-2015

Zhang, H., Jing, X.-M., Chen, J.-Y., Li, J.-J., & Schwegler, B. (2016). Characterizing Urban Fabric Properties and their Thermal Effect using QuickBird Image and Landsat 8 Thermal Infrared (TIR) Data: The Case of Downtown Shanghai, China. *Remote Sensing*, *8*(7), 541. https://doi.org/10.3390/rs8070541

Zhao, H., Ren, Z., & Tan, J. (2018). The Spatial Patterns of Land Surface Temperature and Its Impact Factors: Spatial Non-Stationarity and Scale Effects Based on a Geographically-Weighted Regression Model. *Sustainability*, *10*(7), 2242. https://doi.org/10.3390/su10072242

Zheng, Z., Zhou, W., Yan, J., Qian, Y., Wang, J., & Li, W. (2019). The Higher, the Cooler? Effects of Building Height on Land Surface Temperatures in Residential Areas of Beijing. *Physics and Chemistry of the Earth*. https://doi.org/10.1016/j.pce.2019.01.008

Zupancic, T., Westmacott, C., & Bulthuis, M. (2015). The Impact of Green Space on Heat and Air Pollution in Urban Communities : A Meta-Narrative Systematic Review, (March), 1–68.

APPENDICES

Appendix 1: Landsat Data Products

Landsat 5 Thematic Mapper (TM)

Bands	Wavelength (micrometers)	Resolution(meters)
Band 1 - Blue	0.45-0.52	30
Band 2 - Green	0.52-0.60	30
Band 3 - Red	0.63-0.69	30
Band 4 - Near Infrared (NIR)	0.76-0.90	30
Band 5 - Shortwave Infrared (SWIR) 1	1.55-1.75	30
Band 6 - Thermal	10.40-12.50	120 * (30)
Band 7 - Shortwave Infrared (SWIR) 2	2.08-2.35	30

Landsat 7 Enhanced Thematic Mapper Plus (ETM+)

Bands	Wavelength (micrometers)	Resolution(meters)
Band 1 - Blue	0.45-0.52	30
Band 2 - Green	0.52-0.60	30
Band 3 - Red	0.63-0.69	30
Band 4 - Near Infrared (NIR)	0.77-0.90	30
Band 5 - Shortwave Infrared (SWIR) 1	1.55-1.75	30
Band 6 - Thermal	10.40-12.50	60 * (30)
Band 7 - Shortwave Infrared (SWIR) 2	2.09-2.35	30
Band 8 - Panchromatic	.52-.90	15

Landsat 8 Operational Land Imager (OLI) and Thermal Infrared Sensor (TIRS)

Bands	Wavelength (micrometers)	Resolution(meters)
Band 1 - Ultra Blue (coastal/aerosol)	0.43 - 0.45	30
Band 2 - Blue	0.45 - 0.51	30
Band 3 - Green	0.53 - 0.59	30
Band 4 - Red	0.64 - 0.67	30
Band 5 - Near Infrared (NIR)	0.85 - 0.88	30
Band 6 - Shortwave Infrared (SWIR) 1	1.57 - 1.65	30
Band 7 - Shortwave Infrared (SWIR) 2	2.11 - 2.29	30
Band 8 - Panchromatic	0.50 - 0.68	15
Band 9 - Cirrus	1.36 - 1.38	30
Band 10 - Thermal Infrared (TIRS) 1	10.60 - 11.19	100 * (30)
Band 11 - Thermal Infrared (TIRS) 2	11.50- 12.51	100*(30)

Appendix 2: Sentinel-2A Data Products

Bands	Wavelength (micrometers)	Resolution(meters)
Band 1 - Coastal/aerosol	0.443	60
Band 2 - Blue	0.49	10
Band 3 - Green	0.560	10
Band 4 - Red	0.665	10
Band 5 – Vegetation Red Edge	0.705	20
Band 6 - Vegetation Red Edge	0.740	20
Band 7 - Vegetation Red Edge	0.783	20
Band 8 - NIR	0.842	10
Band 8A - Vegetation Red Edge	0.865	20
Band 9 – Water vapour	0.945	60
Band 10 – SWIR- Cirrus	1.375	60
Band 11 - SWIR	1.610	20
Band 12 - SWIR	2.190	20

Appendix 3: ASTER Data Products

Subsystem	**Bands**	**Wavelength (micrometers)**	**Resolution (meters)**
Visible and Near Infrared	Band 1 - Green	0.52 - 0.60	15
	Band 2 - Red	0.63 - 0.69	15
	Band 3N – Near Infrared	0.76 - 0.86	15
	Band 3B – Near Infrared	0.76 - 0.86	15
Shortwave Infrared (SWIR)	Band 4 - Shortwave Infrared	1.60 – 1.70	30
	Band 5 - Shortwave Infrared	2.145 – 2.185	30
	Band 6 - Shortwave Infrared	2.185 – 2.225	30
	Band 7- Shortwave Infrared	2.235 – 2.285	30
	Band 8 - Shortwave Infrared	2.295 – 2.365	30
	Band 9 - Shortwave Infrared	2. 2.360 – 2.430	30
Thermal Infrared (TIRS	Band 10 - Thermal Infrared)	8.125 – 8.475	90
	Band 11 - Thermal Infrared)	8.475 – 8.825	90
	Band 12 - Thermal Infrared)	8.925 – 9.275	90
	Band 13 - Thermal Infrared)	10.25 – 10.95	90
	Band 14 - Thermal Infrared)	10.95 – 11.65	90

Appendix 4: MODIS Data Product

SDS Name	Long Name	Number Type	Unit	Valid Range	Fill Value	Scale factor	Add offset
LST Day (1km)	Daily daytime 1km grid Land-surface Temperature	uint16	K	7500-65535	0	0.02	0.0
QC_Day	Quality control for daytime LST and emissivity	uint8	none	0-255	0	NA	NA
LST Night (1km)	Daily nighttime 1km grid Land-surface Temperature	uint16	K	7500-65535	0	0.02	0.0
QC_Night	Quality control for nighttime LST and emissivity	uint8	none	0-255	0	NA	NA

Appendix 5: Accuracy Assessment Results of Land Cover Classification

PrAc (Producer's accuracy) = 1 – Com (Commission errors)

UsAc (User's accuracy) = 1 – Om (Omission errors)

1986 Accuracy Assessment

Kappa ($\widehat{K}$)= 0.9859

	Reference Source							Accuracy	
Classified Map	**Class**	Urban	Forest	Sparse grassland	Water	Open grassland	Totals	Users Accuracy	Error of Omission
	Urban	20	0	0	0	0	20	1	0
	Forest	0	44	0	0	0	44	1	0
	Sparse grassland	1	0	12	0	0	13	0.92	0.08
	Water	0	0	0	5	0	5	1	0
	Open grassland	0	0	0	0	17	17	1	0
	Totals	21	44	12	5	17	99	-	
Accuracy	Producer's Accuracy	0.95	1	1	1	1	-	**Overall accuracy: 98.99%**	
	Error of Commission	0.05	0	0	0	0			

1995 Accuracy Assessment

Kappa ($\widehat{K}$)= 0.9573

	Reference Source							Accuracy	
Classified Map	**Class**	Urban	Forest	Sparse grassland	Water	Open grassland	Totals	Users Accuracy	Error of Omission
	Urban	50	0	0	0	0	50	1	0
	Forest	0	18	0	0	1	19	0.95	0.05
	Sparse grassland	2	0	19	0	0	21	0.90	0.10
	Water	0	0	0	5	0	5	1	0
	Open grassland	0	0	0	0	15	15	1	0
	Totals	52	18	19	5	16	110	-	
Accuracy	Producer's Accuracy	0.96	1	1	1	0.94	-	**Overall Accuracy: 97.27%**	
	Error of Commission	0.04	0	0	0	0.06			

2000 Accuracy Assessment

Kappa ($\hat{K}$)= 0.9593

	Reference Source							Accuracy	
Classified Map	**Class**	Urban	Forest	Sparse grassland	Water	Open grassland	Totals	Users Accuracy	Error of Omission
	Urban	105	0	0	0	0	105	1	0
	Forest	0	14	0	0	1	15	0.93	0.07
	Sparse grassland	2	0	18	0	0	20	0.90	0.10
	Water	0	0	0	4	0	4	1	0
	Open grassland	0	0	0	0	9	9	1	0
	Totals	107	14	18	4	10	153	-	
Accuracy	Producer's Accuracy	0.98	1	1	1	0.90	-	**Overall Accuracy: 98.04%**	
	Error of Commission	0.02	0	0	0	0.10			

2005 Accuracy Assessment

Kappa ($\hat{K}$)= 0.9542

	Reference Source							Accuracy	
Classified Map	**Class**	Urban	Forest	Sparse grassland	Water	Open grassland	Totals	Users Accuracy	Error of Omission
	Urban	290	1	5	0	0	296	0.98	0.02
	Forest	1	115	0	0	2	118	0.97	0.03
	Sparse grassland	7	0	76	0	0	83	0.92	0.08
	Water	3	0	0	19	0	22	0.86	0.14
	Open grassland	0	1	0	0	52	53	0.98	0.02
	Totals	301	117	81	19	19	572	-	
Accuracy	Producer's Accuracy	0.96	0.98	0.94	1	0.96	-	**Overall Accuracy: 96.50%**	
	Error of Commission	0.04	0.02	0.06	0	0.04			

2011 Accuracy Assessment

Kappa ($\widehat{K}$)= 0.9695

		Reference Source						Accuracy	
	Class	Urban	Forest	Sparse grassland	Water	Open grassland	Totals	Users Accuracy	Error of Omission
Classified Map	Urban	240	0	1	1	0	242	0.99	0.01
	Forest	1	79	0	0	1	81	0.98	0.02
	Sparse grassland	3	0	45	0	0	48	0.94	0.06
	Water	2	0	0	23	0	24	0.96	0.04
	Open grassland	0	0	0	0	64	64	1	0
	Totals	245	79	46	24	65	459	-	
Accuracy	Producer's Accuracy	0.98	1	0.98	0.96	0.98	-	**Overall Accuracy: 98.26%**	
	Error of Commission	0.02	0	0.02	0.04	0.02			

2017 Accuracy Assessment

Kappa ($\widehat{K}$)= **0.9320**

		Reference Source						Accuracy	
	Class	Urban	Forest	Sparse grassland	Water	Open grassland	Totals	Users Accuracy	Error of Omission
Classified Map	Urban	683	0	21	4	0	708	0.96	0.04
	Forest	0	85	1	0	0	86	0.99	0.01
	Sparse grassland	18	0	251	0	0	269	0.93	0.07
	Water	4	0	0	70	0	74	0.95	0.05
	Open grassland	0	1	0	0	58	59	0.98	0.02
	Totals	705	86	273	74	58	1196	-	
Accuracy	Producer's Accuracy	0.97	0.99	0.92	0.95	1	-	**Overall Accuracy: 95.90%**	
	Error of Commission	0.03	0.01	0.08	0.05	0			

Appendix 6: Random Forest Sample Code

```
install.packages("raster")
library(raster)
install.packages("rgdal")
library(rgdal)

rasterOptions(tmpdir = "D:/tmp")

#my satellite data for 1986
setwd("K:/PHD Imagery/SATELLITE IMAGERY/LANDSAT IMAGERY/1986")
compfb86<-stack("Composite_Clip/Arc60_Jn86.tif")
ndvifb86<-stack("Indices/NDW_NDVI/UUNDVIARC60_J_86.TIF")

stackfb86all<-stack(compfb86,ndvifb86)

writeRaster(stackfb86all, filename = "K:/PHD Imagery/SATELLITE IMAGERY/LANDSAT IMAGERY/Data Analysis Using
R/1986/Output/Spectral Bands/stackfb86all.tif",overwrite=TRUE)

#Put them together and give bands names
brUUfb86<-brick("K:/PHD Imagery/SATELLITE IMAGERY/LANDSAT IMAGERY/Data Analysis Using
R/1986/Output/Spectral Bands/stackfb86all.tif",overwrite=TRUE)
names(brUUfb86)<-c('Blue','Green','Red','SWIR1','NIR','SWIR2','Thermal','NDVI')
plot(brUUfb86)
brUUfb86

#reading files from training sites. Projection lat, long
trainfb86<-shapefile("Classification/Supervised/TrainSites/NDVI4_Jan86.shp")

#to view cropped area in different bands side by side
#nffb<-layout(matrix(c(1,0,2), 1, 3, byrow = TRUE), width = c(1,0.2,1), respect = TRUE)
#plotRGB(brUUfb86, r = 3, g = 2, b = 1, axes = TRUE, stretch = "lin", main = "Landsat True Color Composite")
#plotRGB(brUUfb86, r = 4, g = 3, b = 2, axes = TRUE, stretch = "lin", main = "Landsat False Color Composite")
#dev.off()  #turns off the display

#to extract values of a raster from vector data
extUUfb86<-extract(brUUfb86,trainfb86,df=TRUE)

#plots each  of the landclasses in the NDR and Thermal Bands
#plot(extUUfb86[,'Red'],extUUfb86[,'NDR'],xlab='Red',ylab='NDR',col=rainbow(5)[extUUfb86$ID])


#First compute the mean reflectance values for each class and band
msbUUfb86<-aggregate(. ~ ID,mean,data=extUUfb86)
msbUUfb86

#specify row and column
rownames(msbUUfb86)<-msbUUfb86[,1]
msbUUfb86<-msbUUfb86[,-1]
colnames(msbUUfb86)<-names(msbUUfb86)


#transforming msbUU from a data.frame to a matrix
msbUUfb86<-as.matrix(msbUUfb86)
```

```
rasterOptions(tmpdir = "D:/tmp")
library(raster)
install.packages("rgdal")
library(rgdal)

#classifying the image using a FOR loop for the selected training sites

clsfnfb86<-vector("list", length=length(trainfb86))

#for loop
for (i in 1:length(trainfb86)){
  cat("Polygon",i,"of",length(trainfb86),"is in,start processing.\n") #R to tell us where we are when it is iterating
  matUUfb86<-extract(brUUfb86,trainfb86[i,], df=TRUE)
  matUUfb86$ID<-trainfb86$Classname[i]
  names(matUUfb86)<-c("ID","B1","B2","B3","B4","B5","B6","B7","NDVI")#resetting the column names to each of the bands
to 0# obtain the raw radiance values from the polygons
  clsfnfb86[[i]]<-matUUfb86
}

valuesUUfb86<-do.call("rbind",clsfnfb86)  #combines classes to bands
head(matUUfb86)   #obtains the first six classes classified
tail(matUUfb86)   #obtains the last six classes classified
head(valuesUUfb86)
```

Appendix 7: NDVI Classification from 1986 to 2017

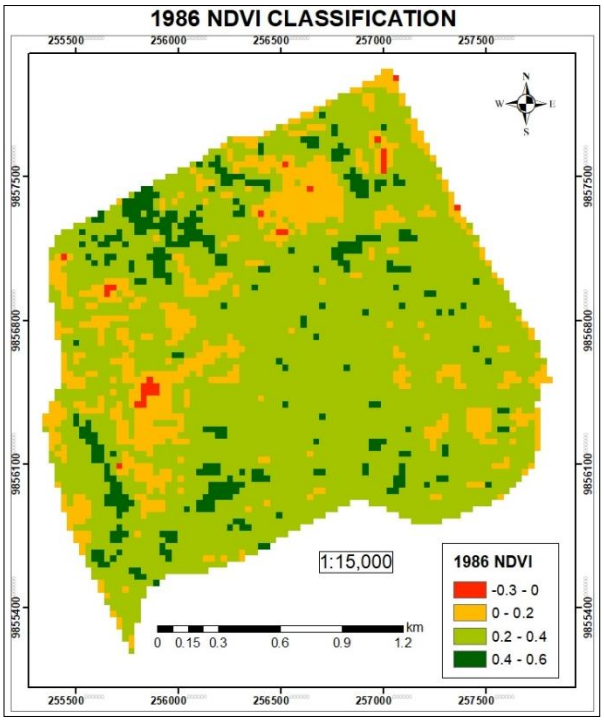

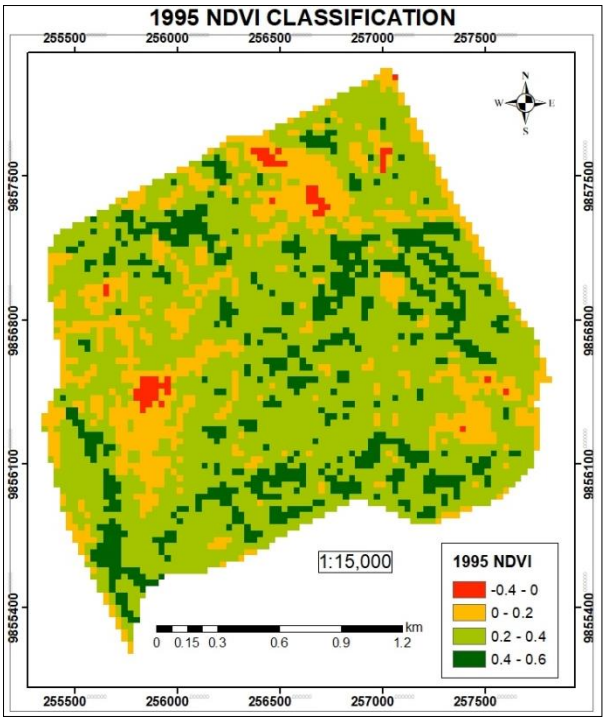

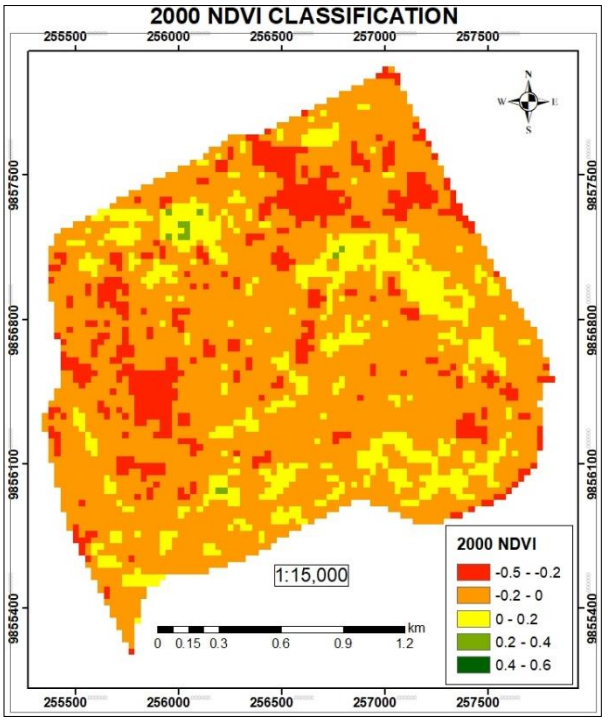

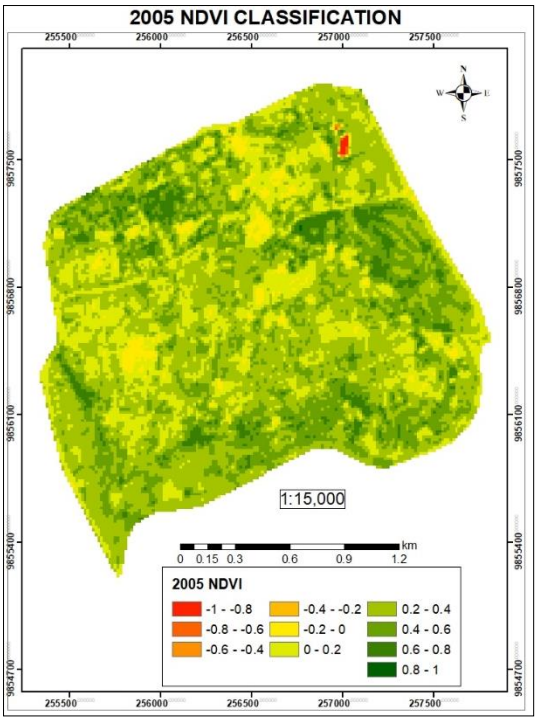

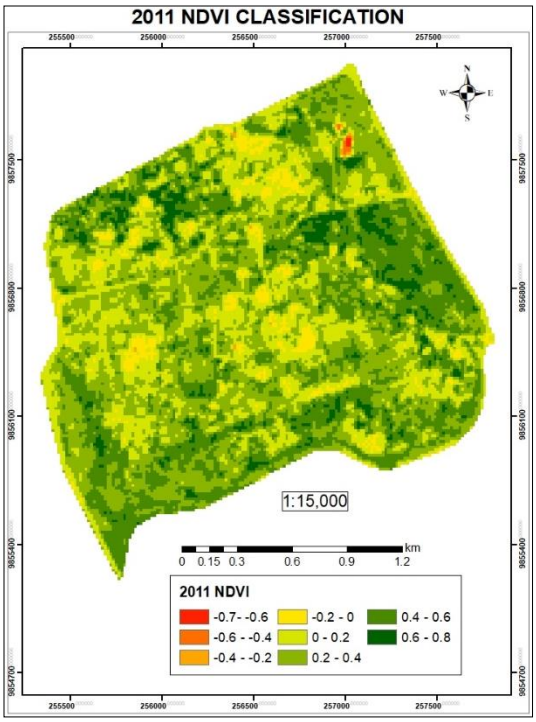
2011 NDVI CLASSIFICATION
255500
256000
256500
257000
257500
9857500
9856800
9856100
9855400
9854700
N
W
E
S
1:15,000
km
0 0.15 0.3 0.6 0.9 1.2
2011 NDVI
-0.7 - -0.6
-0.6 - -0.4
-0.4 - -0.2
-0.2 - 0
0 - 0.2
0.2 - 0.4
0.4 - 0.6
0.6 - 0.8

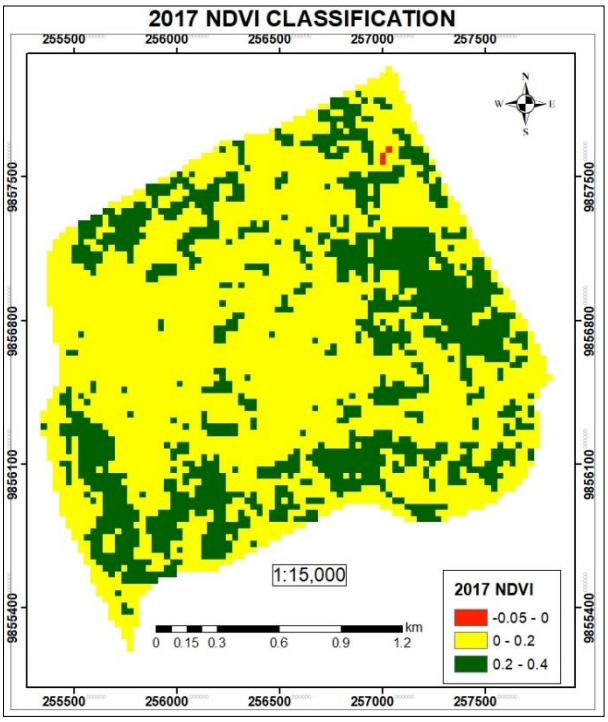
2017 NDVI CLASSIFICATION
255500
256000
256500
257000
257500
9857500
9856800
9856100
9855400
N
W
E
S
1:15,000
km
0 0.15 0.3 0.6 0.9 1.2
2017 NDVI
-0.05 - 0
0 - 0.2
0.2 - 0.4

Appendix 8: Ground Control Point Locations

Thirteen ground control points were selected and below are sample of the twelve collected. The point identified is marked by a red dot.

GCP 1

GCP 2

GCP 3

GCP 4

GCP 5

GCP 6

GCP 7

GCP 8

GCP 9 & 10

GCP 11

GCP 12

GCP 13

GCP 14

Appendix 9: Ground Control Point Distribution over Digital Imagery of 2017 in Nairobi

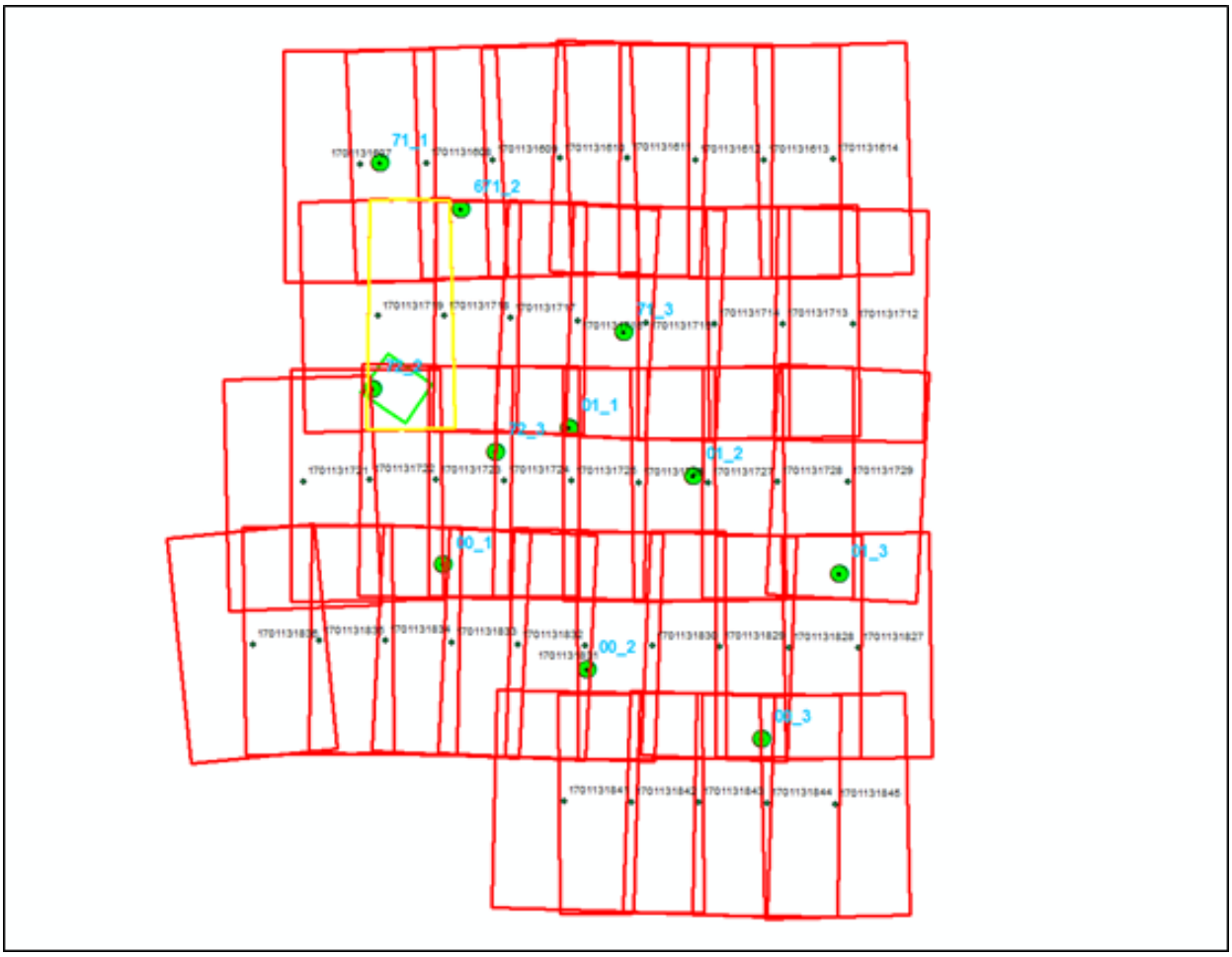

Appendix 10: Ground Control Collection

Center of manhole (GCP 5)

Top edge of culvert (GCP 6)

Top edge of slab (GCP 7)

Appendix 11: Exterior Orientation Coordinate List

ID	Name	Easting	Northing	Height	Omega	Phi	Kappa
21	1701131607	254103.8	9857554	3102.796	-0.20273	-0.13206	124.5583
22	1701131608	254444.7	9857795	3105.011	-0.18138	-0.14239	126.8227
23	1701131609	254781.4	9858045	3101.385	-0.13599	-0.11842	126.0006
24	1701131610	255123.1	9858292	3097.118	-0.21221	-0.18186	126.1862
25	1701131611	255473	9858535	3107.83	0.18559	-0.27175	122.4557
26	1701131612	255834.1	9858765	3114.129	-0.16616	-0.1609	123.9932
27	1701131613	256191.9	9859007	3113.234	-0.19784	-0.16402	124.2647
28	1701131614	256546.6	9859256	3106.742	-0.09917	-0.1336	125.7843
29	1701131712	257238.9	9858467	3102.797	-0.30913	0.38282	-56.7692
30	1701131713	256871.6	9858220	3104.639	0.50458	0.0274	-55.0997
31	1701131714	256512.9	9857979	3106.525	0.11954	0.12289	-55.6625
32	1701131715	256154.7	9857739	3108.348	0.1917	0.16858	-57.9861
33	1701131716	255793	9857510	3096.38	0.18785	0.14203	-59.2446
34	1701131717	255433.7	9857286	3100.942	0.19171	0.15157	-56.4354
35	1701131718	255078.3	9857061	3098.007	0.19067	0.1142	-56.5029
36	1701131719	254734.9	9856827	3094.45	0.15871	0.13618	-54.313
37	1701131721	254930.5	9855703	3092.932	-2.1639	-0.8883	126.3423
38	1701131722	255267.9	9855947	3100.138	-1.24008	0.01973	124.6778
39	1701131723	255619	9856182	3106.456	-0.22821	-0.04443	123.3057
40	1701131724	255971.5	9856418	3096.63	-0.0991	-0.0623	124.1442
41	1701131725	256324.7	9856653	3106.093	-0.36375	-0.06711	123.3894
42	1701131726	256684.7	9856886	3110.306	-0.18007	-0.14347	124.2656
43	1701131727	257041.3	9857129	3114.989	-0.17937	-0.13042	125.1408
44	1701131728	257402.3	9857381	3103.913	-0.14354	-0.07875	124.0912
45	1701131729	257767.1	9857631	3102.832	-0.29662	-0.09179	121.0516
46	1701131827	258406.9	9856804	3062.308	0.21631	0.20945	-54.7145
47	1701131828	258046.8	9856559	3048.154	0.16854	0.13138	-55.9701

48	1701131829	257683	9856316	3063.329	0.13238	0.12601	-58.1474
49	1701131830	257329.6	9856081	3076.005	0.1333	0.11047	-55.5067
50	1701131831	256980	9855844	3086.574	0.16759	0.13829	-57.8493
51	1701131832	256628.7	9855612	3069.582	0.19701	0.13242	-58.784
52	1701131833	256275.9	9855391	3068.417	0.19359	0.13647	-58.6312
53	1701131834	255923.9	9855166	3084.441	0.17256	0.14226	-56.564
54	1701131835	255580.3	9854929	3085.934	0.17113	0.13974	-55.1235
55	1701131836	255247.8	9854675	3071.173	0.20086	0.17457	-49.7654
56	1701131841	257419.2	9854961	3024.687	0.4663	-0.35806	122.7531
57	1701131842	257773.5	9855197	3036.844	-0.21114	-0.1325	124.7871
58	1701131843	258125.9	9855435	3038.333	-0.2458	-0.20475	122.2665
59	1701131844	258484.5	9855669	3046.669	-0.22513	-0.15177	123.332
60	1701131845	258842.4	9855907	3051.231	-0.21944	-0.15094	125.5153

Appendix 12: Results of Exploratory Regression

EXPLORATORY VARIABLE OF 1978 AT 30 METER GRID

```
**************************************************************************
********
Choose 1 of 5 Summary
      Highest Adjusted R-Squared Results
AdjR2     AICc   JB K(BP)  VIF   SA   Model
 0.17 -3697.41 0.00  0.34 1.00 0.00  -SCALE_NDVI***
 0.01 -2857.06 0.00  0.00 1.00 0.00  +SCALE_ASPE***
 0.01 -2850.02 0.00  0.00 1.00 0.00  -SCALE_HGHT***
       Passing Models
AdjR2 AICc JB K(BP) VIF SA   Model
**************************************************************************
********
Choose 2 of 5 Summary
              Highest Adjusted R-Squared Results
AdjR2     AICc   JB K(BP)  VIF   SA   Model
 0.21 -3941.52 0.00  0.00 1.09 0.00  -SCALE_HGHT***  -SCALE_NDVI***
 0.21 -3915.00 0.00  0.16 1.12 0.00  -SCALE_GCR***  -SCALE_NDVI***
 0.18 -3790.38 0.00  0.64 1.15 0.00  -SCALE_BVD***  -SCALE_NDVI***
       Passing Models
AdjR2 AICc JB K(BP) VIF SA   Model
**************************************************************************
********
Choose 3 of 5 Summary
                     Highest Adjusted R-Squared Results
AdjR2     AICc   JB K(BP)  VIF   SA   Model
 0.22 -4026.48 0.00  0.00 1.35 0.00  -SCALE_HGHT***  -SCALE_GCR***  -
SCALE_NDVI***
 0.22 -3969.67 0.00  0.00 1.09 0.00  -SCALE_HGHT***  +SCALE_ASPE***  -
SCALE_NDVI***
 0.21 -3953.83 0.00  0.02 1.12 0.00  +SCALE_ASPE***  -SCALE_GCR***  -
SCALE_NDVI***
       Passing Models
AdjR2 AICc JB K(BP) VIF SA   Model
**************************************************************************
********
Choose 4 of 5 Summary
                           Highest Adjusted R-Squared Results
AdjR2     AICc   JB K(BP)  VIF   SA   Model
 0.23 -4062.69 0.00  0.00 1.35 0.00  -SCALE_HGHT***  +SCALE_ASPE***  -
SCALE_GCR***  -SCALE_NDVI***
 0.23 -4058.82 0.00  0.00 2.63 0.00  -SCALE_HGHT***  +SCALE_BVD***  -
SCALE_GCR***  -SCALE_NDVI***
 0.22 -3967.80 0.00  0.00 2.02 0.00  -SCALE_HGHT***  +SCALE_ASPE***
+SCALE_BVD  -SCALE_NDVI***
       Passing Models
AdjR2 AICc JB K(BP) VIF SA   Model
**************************************************************************
********
```

```
Choose 5 of 5 Summary
                                        Highest Adjusted R-Squared
Results
AdjR2     AICc   JB K(BP)  VIF   SA   Model
 0.24 -4095.13 0.00  0.00 2.63 0.00  -SCALE_HGHT***  +SCALE_ASPE***
+SCALE_BVD***  -SCALE_GCR***  -SCALE_NDVI***
       Passing Models
AdjR2 AICc JB K(BP) VIF SA   Model
**********************************************************************
********
************* Exploratory Regression Global Summary (SCALE_LST)
**************

              Percentage of Search Criteria Passed
                   Search Criterion Cutoff Trials # Passed % Passed
             Min Adjusted R-Squared > 0.50     31        0     0.00
            Max Coefficient p-value < 0.05     31       25    80.65
                      Max VIF Value < 7.50     31       31   100.00
            Min Jarque-Bera p-value > 0.10     31        0     0.00
Min Spatial Autocorrelation p-value > 0.10     14        0     0.00

----------------------------------------------------------------------
--------

      Summary of Variable Significance
Variable   % Significant % Negative % Positive
SCALE_HGHT        100.00     100.00       0.00
SCALE_ASPE        100.00       0.00     100.00
SCALE_NDVI        100.00     100.00       0.00
SCALE_GCR          87.50     100.00       0.00
SCALE_BVD          75.00      25.00      75.00

----------------------------------------------------------------------
--------

   Summary of Multicollinearity
Variable    VIF Violations Covariates
SCALE_HGHT 1.90     0      --------
SCALE_ASPE 1.01     0      --------
SCALE_BVD  2.63     0      --------
SCALE_GCR  1.77     0      --------
SCALE_NDVI 1.17     0      --------

----------------------------------------------------------------------
--------

                Summary of Residual Normality (JB)
      JB    AdjR2         AICc    K(BP)      VIF       SA   Model
0.000000 0.000746 -2823.793013 0.031118 1.000000 0.000000
+SCALE_BVD**
0.000000 0.007722 -2857.056668 0.000000 1.000000 0.000000
+SCALE_ASPE***
```

```
0.000000 0.006250 -2850.017966 0.002150 1.000000 0.000000  -
SCALE_HGHT***

--------------------------------------------------------------------
--------

                                          Summary of Residual Spatial
Autocorrelation (SA)
      SA    AdjR2         AICc       JB    K(BP)      VIF   Model
0.000000 0.236127 -4095.126829 0.000000 0.000256 2.632730  -
SCALE_HGHT***  +SCALE_ASPE***  +SCALE_BVD***  -SCALE_GCR***  -
SCALE_NDVI***
0.000000 0.230728 -4062.691491 0.000000 0.000012 1.354279  -
SCALE_HGHT***  +SCALE_ASPE***  -SCALE_GCR***  -SCALE_NDVI***
0.000000 0.230101 -4058.821356 0.000000 0.001097 2.632714  -
SCALE_HGHT***  +SCALE_BVD***  -SCALE_GCR***  -SCALE_NDVI***

--------------------------------------------------------------------
--------

Table Abbreviations
AdjR2 Adjusted R-Squared
AICc  Akaike's Information Criterion
JB    Jarque-Bera p-value
K(BP) Koenker (BP) Statistic p-value
VIF   Max Variance Inflation Factor
SA    Global Moran's I p-value
Model Variable sign (+/-)
Model Variable significance (* = 0.10, ** = 0.05, *** = 0.01)

--------------------------------------------------------------------
--------
```

EXPLORATORY VARIABLE OF 1998 AT 30 METER GRID

```
**********************************************************************
********
Choose 1 of 5 Summary
      Highest Adjusted R-Squared Results
AdjR2     AICc   JB K(BP)  VIF   SA   Model
 0.24 -5501.12 0.00  0.00 1.00 0.00  -SCALE_NDVI***
 0.03 -4333.81 0.00  0.00 1.00 0.00  -SCALE_HGHT***
 0.01 -4234.91 0.00  0.00 1.00 0.00  -SCALE_BVD***
       Passing Models
AdjR2 AICc JB K(BP) VIF SA   Model
**********************************************************************
********
Choose 2 of 5 Summary
              Highest Adjusted R-Squared Results
AdjR2     AICc   JB K(BP)  VIF   SA   Model
 0.33 -6082.54 0.00  0.00 1.07 0.00  -SCALE_HGHT***  -SCALE_NDVI***
 0.30 -5893.23 0.00  0.00 1.11 0.00  -SCALE_BVD***  -SCALE_NDVI***
```

```
 0.29 -5819.16 0.00  0.00 1.11 0.00  -SCALE_GCR***  -SCALE_NDVI***
       Passing Models
AdjR2 AICc JB K(BP) VIF SA   Model
**********************************************************************
********
Choose 3 of 5 Summary
                      Highest Adjusted R-Squared Results
AdjR2     AICc   JB K(BP)  VIF   SA   Model
 0.34 -6189.49 0.00  0.00 1.27 0.00  -SCALE_HGHT***  -SCALE_GCR***  -
SCALE_NDVI***
 0.33 -6105.89 0.00  0.00 2.07 0.00  -SCALE_HGHT***  -SCALE_BVD***  -
SCALE_NDVI***
 0.33 -6099.96 0.00  0.00 1.07 0.00  -SCALE_HGHT***  +SCALE_ASPE***  -
SCALE_NDVI***
       Passing Models
AdjR2 AICc JB K(BP) VIF SA   Model
**********************************************************************
********
Choose 4 of 5 Summary
                               Highest Adjusted R-Squared Results
AdjR2     AICc   JB K(BP)  VIF   SA   Model
 0.35 -6212.97 0.00  0.00 1.28 0.00  -SCALE_HGHT***  -SCALE_GCR***
+SCALE_ASPE***  -SCALE_NDVI***
 0.34 -6187.49 0.00  0.00 2.69 0.00  -SCALE_HGHT***  -SCALE_GCR***  -
SCALE_BVD  -SCALE_NDVI***
 0.33 -6124.08 0.00  0.00 2.07 0.00  -SCALE_HGHT***  -SCALE_BVD***
+SCALE_ASPE***  -SCALE_NDVI***
       Passing Models
AdjR2 AICc JB K(BP) VIF SA   Model
**********************************************************************
********
Choose 5 of 5 Summary
                                     Highest Adjusted R-Squared Results
AdjR2     AICc   JB K(BP)  VIF   SA   Model
 0.35 -6210.96 0.00  0.00 2.69 0.00  -SCALE_HGHT***  -SCALE_GCR***
+SCALE_BVD  +SCALE_ASPE***  -SCALE_NDVI***
       Passing Models
AdjR2 AICc JB K(BP) VIF SA   Model
**********************************************************************
********
************* Exploratory Regression Global Summary (SCALE_LST)
**************

              Percentage of Search Criteria Passed
                   Search Criterion Cutoff Trials # Passed % Passed
             Min Adjusted R-Squared > 0.50     31        0     0.00
            Max Coefficient p-value < 0.05     31       21    67.74
                      Max VIF Value < 7.50     31       31   100.00
            Min Jarque-Bera p-value > 0.10     31        0     0.00
Min Spatial Autocorrelation p-value > 0.10     14        0     0.00
```

Summary of Variable Significance

Variable	% Significant	% Negative	% Positive
SCALE_HGHT	100.00	100.00	0.00
SCALE_NDVI	100.00	100.00	0.00
SCALE_BVD	87.50	68.75	31.25
SCALE_ASPE	75.00	0.00	100.00
SCALE_GCR	62.50	87.50	12.50

Summary of Multicollinearity

Variable	VIF	Violations	Covariates
SCALE_HGHT	2.00	0	--------
SCALE_GCR	1.66	0	--------
SCALE_BVD	2.69	0	--------
SCALE_ASPE	1.00	0	--------
SCALE_NDVI	1.14	0	--------

Summary of Residual Normality (JB)

JB	AdjR2	AICc	K(BP)	VIF	SA	Model
0.000000	0.006444	-4234.910606	0.000056	1.000000	0.000000	- SCALE_BVD***
0.000000	0.003471	-4220.722747	0.000552	1.000000	0.000000	- SCALE_GCR***
0.000000	0.026925	-4333.807402	0.000000	1.000000	0.000000	- SCALE_HGHT***

Summary of Residual Spatial Autocorrelation (SA)

SA	AdjR2	AICc	JB	K(BP)	VIF	Model
0.000000	0.345385	-6212.967332	0.000000	0.000000	1.276850	- SCALE_HGHT*** -SCALE_GCR*** +SCALE_ASPE*** -SCALE_NDVI***
0.000000	0.345247	-6210.961527	0.000000	0.000000	2.692966	- SCALE_HGHT*** -SCALE_GCR*** +SCALE_BVD +SCALE_ASPE*** - SCALE_NDVI***
0.000000	0.342000	-6189.488361	0.000000	0.000000	1.272954	- SCALE_HGHT*** -SCALE_GCR*** -SCALE_NDVI***

Table Abbreviations

```
AdjR2 Adjusted R-Squared
AICc  Akaike's Information Criterion
JB    Jarque-Bera p-value
K(BP) Koenker (BP) Statistic p-value
VIF   Max Variance Inflation Factor
SA    Global Moran's I p-value
Model Variable sign (+/-)
Model Variable significance (* = 0.10, ** = 0.05, *** = 0.01)

-------------------------------------------------------------------
--------
```

EXPLORATORY VARIABLE OF 2017 AT 30 METER GRID

```
**********************************************************************
********
Choose 1 of 5 Summary
      Highest Adjusted R-Squared Results
AdjR2     AICc   JB K(BP)  VIF   SA   Model
 0.05 -4461.54 0.00  0.00 1.00 0.00  -SCALE_HGHT***
 0.02 -4342.94 0.00  0.00 1.00 0.00  -SCALE_BVD***
 0.02 -4328.78 0.01  0.00 1.00 0.00  -SCALE_NDVI***
       Passing Models
AdjR2 AICc JB K(BP) VIF SA   Model
**********************************************************************
********
Choose 2 of 5 Summary
              Highest Adjusted R-Squared Results
AdjR2     AICc   JB K(BP)  VIF   SA   Model
 0.09 -4702.71 0.00  0.00 1.11 0.00  -SCALE_HGHT***  -SCALE_NDVI***
 0.06 -4539.50 0.00  0.00 1.13 0.00  -SCALE_BVD***  -SCALE_NDVI***
 0.06 -4529.63 0.00  0.00 1.17 0.00  -SCALE_GCR***  -SCALE_NDVI***
       Passing Models
AdjR2 AICc JB K(BP) VIF SA   Model
**********************************************************************
********
Choose 3 of 5 Summary
                     Highest Adjusted R-Squared Results
AdjR2     AICc   JB K(BP)  VIF   SA   Model
 0.10 -4759.68 0.00  0.00 1.37 0.00  -SCALE_HGHT***  -SCALE_GCR***  -
SCALE_NDVI***
 0.10 -4710.59 0.00  0.00 1.12 0.00  -SCALE_HGHT***  -SCALE_NDVI***  -
SCALE_ASPE**
 0.09 -4702.63 0.00  0.00 2.27 0.00  -SCALE_HGHT***  -SCALE_BVD  -
SCALE_NDVI***
       Passing Models
AdjR2 AICc JB K(BP) VIF SA   Model
**********************************************************************
********
Choose 4 of 5 Summary
                               Highest Adjusted R-Squared Results
AdjR2     AICc   JB K(BP)  VIF   SA   Model
```

```
 0.11 -4765.44 0.00  0.00 1.37 0.00  -SCALE_HGHT***  -SCALE_GCR***  -
SCALE_NDVI***  -SCALE_ASPE**
 0.11 -4762.34 0.00  0.00 2.80 0.00  -SCALE_HGHT***  +SCALE_BVD**  -
SCALE_GCR***  -SCALE_NDVI***
 0.10 -4710.42 0.00  0.00 2.27 0.00  -SCALE_HGHT***  -SCALE_BVD  -
SCALE_NDVI***  -SCALE_ASPE**
       Passing Models
AdjR2 AICc JB K(BP) VIF SA   Model
************************************************************************
********
Choose 5 of 5 Summary
                                      Highest Adjusted R-Squared Results
AdjR2     AICc   JB K(BP)  VIF   SA   Model
 0.11 -4767.96 0.00  0.00 2.80 0.00  -SCALE_HGHT***  +SCALE_BVD**  -
SCALE_GCR***  -SCALE_NDVI***  -SCALE_ASPE**
       Passing Models
AdjR2 AICc JB K(BP) VIF SA   Model
************************************************************************
********
************* Exploratory Regression Global Summary (SCALE_LST)
**************

              Percentage of Search Criteria Passed
                   Search Criterion Cutoff Trials # Passed % Passed
             Min Adjusted R-Squared > 0.50     31        0     0.00
            Max Coefficient p-value < 0.05     31       21    67.74
                      Max VIF Value < 7.50     31       31   100.00
            Min Jarque-Bera p-value > 0.10     31        0     0.00
Min Spatial Autocorrelation p-value > 0.10     15        0     0.00

------------------------------------------------------------------------
--------

      Summary of Variable Significance
Variable   % Significant % Negative % Positive
SCALE_HGHT        100.00     100.00       0.00
SCALE_GCR         100.00     100.00       0.00
SCALE_NDVI        100.00     100.00       0.00
SCALE_BVD          75.00      62.50      37.50
SCALE_ASPE         62.50     100.00       0.00

------------------------------------------------------------------------
--------

   Summary of Multicollinearity
Variable    VIF Violations Covariates
SCALE_HGHT 2.25     0      --------
SCALE_BVD  2.80     0      --------
SCALE_GCR  1.69     0      --------
SCALE_NDVI 1.21     0      --------
SCALE_ASPE 1.00     0      --------
```

Summary of Residual Normality (JB)

JB	AdjR2	AICc	K(BP)	VIF	SA	Model
0.010588	0.018835	-4328.782234	0.000982	1.000000	0.000000	- SCALE_NDVI***
0.004802	0.019673	-4331.838752	0.000000	1.000218	0.000000	- SCALE_NDVI*** -SCALE_ASPE*
0.002058	0.062783	-4544.356226	0.000000	1.130617	0.000000	- SCALE_BVD*** -SCALE_NDVI*** -SCALE_ASPE**

Summary of Residual Spatial Autocorrelation (SA)

SA	AdjR2	AICc	JB	K(BP)	VIF	Model
0.000000	0.106276	-4767.960519	0.000000	0.000000	2.800940	- SCALE_HGHT*** +SCALE_BVD** -SCALE_GCR*** -SCALE_NDVI*** - SCALE_ASPE**
0.000000	0.105613	-4765.444207	0.000000	0.000000	1.372592	- SCALE_HGHT*** -SCALE_GCR*** -SCALE_NDVI*** -SCALE_ASPE**
0.000000	0.105027	-4762.339383	0.000000	0.000000	2.800506	- SCALE_HGHT*** +SCALE_BVD** -SCALE_GCR*** -SCALE_NDVI***

Table Abbreviations
AdjR2 Adjusted R-Squared
AICc Akaike's Information Criterion
JB Jarque-Bera p-value
K(BP) Koenker (BP) Statistic p-value
VIF Max Variance Inflation Factor
SA Global Moran's I p-value
Model Variable sign (+/-)
Model Variable significance (* = 0.10, ** = 0.05, *** = 0.01)

Appendix 13: Pearson Correlational Analysis Results at 30m & 90m Scales

Scale	Value	Pearson (r)			P value		
		1978	**1998**	**2017**	**1978**	**1998**	**2017**
30m	NDVI	-0.411	-0.489	-0.138	0.000	0.000	0.000
	Aspect	0.089	-0.038	-0.034	0.000	0.009	0.018
	Albedo	0.349	0.460	0.383	0.000	0.000	0.000
90m	Mean Height	-0.241	-0.271	-0.312	0.000	0.000	0.000
	GCR	-0.125	-0.139	-0.217	0.03	0.001	0.000
	BVD	0.13	-0.148	-0.241	0.752	0.000	0.000

Appendix 14: Spatial Autocorrelation Results

a) GWR at 90 meters for final models in 1978, 1998 and 2017

Model Year	Albedo, Aspect, NDVI with:	P-values	Z-Score	Moran's Index
1978	Mean height	0.000000	13.862386	0.420358
1998	BVD	0.000000	15.409179	0.467047
2017	BVD	0.000000	12.865068	0.390283

b) OLS at 90 meters for final models in 1978, 1998 and 2017

Model Year	Albedo, Aspect, NDVI with:	P-values	Z-Score	Moran's Index
1978	Mean height	0.000000	19.309902	0.586645
1998	BVD	0.000000	19.158113	0.581541
2017	BVD	0.000000	21.241903	0.645717

Appendix 15: Upper Hill Development

a) Dilapidated buildings low rise building along Third Avenue, Ngong road

b) Middle & high rise buildings from Mara road with Coca Cola parking at the fore

c) Construction of high rise buildings along Fourth Ngong Avenue

d) Clearing of forest cover along Ngong road for the tallest building in Kenya

Appendix 16: PhD Substantive Registration

KENYATTA UNIVERSITY
OFFICE OF THE REGISTRAR (ACADEMIC)
P.O. BOX 43844 – 00100 NAIROBI
TEL: 8703222/23
Email: admissions-pg@ku.ac.ke

==========

Our Ref: N85/33297/2015 **Date:** 15th March, 2018

Mwangi Patricia Wanjiku
P.O BOX 20842 – 00202
NAIROBI

Dear Mr Mwangi,

RE: SUBSTANTIVE REGISTRATION (Ph.D)

Following the recommendation by the Dean, Graduate School, you are hereby granted substantive Ph.D. registration.

Please note that your registration number and all rules and regulations remain the same as per your admission letter.

Thank you.

N.O AJUOGAH
FOR: REGISTRAR (ACADEMIC)

CC Dean School of Environmental Studies
Dean, Graduate School
Chairman, Environmental Planning & Management

NOA/cm

Appendix 17: Research Permit

NACOSTI

NATIONAL COMMISSION FORSCIENCE, TECHNOLOGY ANDINNOVATION

Telephone: +254-20-2213471, 2241349,3310571,2219420
Fax: +254-20-318245,318249
Email: dg@nacosti.go.ke
Website: www.nacosti.go.ke
When replying please quote

9th Floor, Utalii House
Uhuru Highway
P.O. Box 30623-00100
NAIROBI-KENYA

Ref. No. **NACOSTI/P/17/10445/18870**

Date: **7th September, 2017**

Patricia Wanjiku Mwangi
Kenyatta University
P.O Box 43844-00100
NAIROBI.

RE: RESEARCH AUTHORIZATION

Following your application for authority to carry out research on ***"Modeling the spatial relationship between built-up densities and surface urban heat island in Upper-Hill, Nairobi, Kenya"*** I am pleased to inform you that you have been authorized to undertake research in **Nairobi County** for the period ending **5th September, 2018.**

You are advised to report to **the County Commissioner and the County Director of Education, Nairobi County** before embarking on the research project.

Kindly note that, as an applicant who has been licensed under the Science, Technology and Innovation Act, 2013 to conduct research in Kenya, you shall deposit **a copy** of the final research report to the Commission within **one year** of completion. The soft copy of the same should be submitted through the Online Research Information System.

GODFREY P. KALERWA MSc., MBA, MKIM
FOR: DIRECTOR-GENERAL/CEO

Copy to:

The County Commissioner
Nairobi County.

The County Director of Education
Nairobi County.

National Commission for Science, Technology and Innovation ISO9001:2008 Certified

THIS IS TO CERTIFY THAT:
MS. PATRICIA WANJIKU MWANGI
of KENYATTA UNIVERSITY, 20842-202
Nairobi,has been permitted to conduct research in *Nairobi County*

on the topic: *MODELLING THE SPATIAL RELATIONSHIP BETWEEN BUILT-UP DENSITIES AND SURFACE URBAN HEAT ISLAND IN UPPER-HILL, NAIROBI, KENYA*

for the period ending:
5th September,2018

Permit No : NACOSTI/P/17/10445/18870
Date Of Issue : 7th September,2017
Fee Recieved :Ksh 2000

.....
Applicant's Signature

.....
Director General
National Commission for Science, Technology & Innovation